

Development of Functionalised Carbon Based Substrates for Neuronal Cell Culture and Production of Carbon Nanoparticles for Bioimaging Applications



The
University
Of
Sheffield.

Andrew Hopper

Thesis submitted to the University of Sheffield for
the degree of Doctor of Philosophy

Department of Materials Science and Engineering

September 2014

Table of Contents

Table of Contents	0
Abstract	7
Acknowledgements	9
Publications	10
Abbreviations	11
Chapter One: Literature Review	15
1. Introduction	15
1.1 Diamond Functionalisation Routes	19
1.1.1 Non-Covalent Functionalisation.....	20
1.1.2 Covalent Functionalisation	22
1.2 Nanodiamond Films	25
1.3 Nanodiamond Films as Biocoatings.....	28
1.3.1 Surfaces Which Influence the Proliferation or Differentiation of Cells.....	28
1.3.2 Biosensors.....	30
1.3.3 Retinal and Neural Prostheses	32
1.4 Nanodiamond Particles	34
1.4.1 Nanodiamond Functionalisation Routes.....	38
1.4.2 Biocompatibility of Nanodiamond	39
1.4.3 Applications of Nanodiamond Particles	40
1.4.3.1 Nanocomposites	40
1.4.3.2 Protein Replicas	41
1.4.3.3 Biolabelling.....	42
1.4.3.4 Drug Delivery	44
1.4.3.5 Gene Delivery	47
1.4.3.6 Intracellular Antioxidant System	48
1.4.3.7 Influence upon cell attachment	48
1.5 Diamond-Like Carbon (DLC) as Biocoatings	49
1.5.1 Different Forms of DLC	49
1.5.1.1 Polymeric (Highly Hydrogenated) Amorphous Carbon (a-C:H).....	50

1.5.1.2 Soft [(Hydrogenated a-C:H) and (Non-Hydrogenated a-C)] Amorphous Carbon	50
1.5.1.3 Hard (Hydrogenated a-C:H) Amorphous Carbon and Tetrahedral (ta-C) Carbon	50
1.5.2 DLC Coating Methods	51
1.5.3 Properties of DLC	53
1.5.4 DLC Applications and its use as a Biocoating	54
1.5.4.1 Orthodontic Wires	55
1.5.4.2 Vascular Stents	56
1.5.4.3 Artificial Joint Implants	56
1.5.4.4 Biosensors and Bioarrays	58
1.5.4.5 Cell Growth Patterning	59
1.6 Carbon Nanoparticles	62
1.6.1 Applications of Carbon Nanoparticles	64
1.6.1.1 <i>In Vitro</i> Bioimaging	65
1.6.1.2 <i>In Vivo</i> Biolabelling	67
1.7 Conclusion	68
1.8 Thesis Aims and Objectives	69
Chapter Two: Materials and Methods	71
2.1 Diamond-Like Carbon (DLC) Study Methods	71
2.1.1 Preparation of Diamond-Like Carbon Substrates - Pulsed Laser Deposition of DLC	71
2.1.2 SEM Electron Beam Deposition of DLC	71
2.1.3 Synthesis of Trifluoroacetic acid protected-10-Aminodec-1-ene (TFAAD)	72
2.1.4 Determination of optimal UV radiation exposure for TFAAD grafting	72
2.1.5 Preparation of 10-amino-dec-1-ene Functionalised DLC	73
2.1.6 Preparation of 2-(10-Undecen-1-yl)-1,3-dioxolane	73
2.1.7 Preparation of 10-undecenal Functionalised DLC	74
2.1.8 NG108-15 Cell Culture Medium	74
2.1.9 NG108-15 Neuroblastoma Cell Culture	74
2.1.10 NG108-15 Cell Passaging	75
2.1.11 Resurrecting Cells	76
2.1.12 Primary Schwann Cell Isolation and Culture	76
2.1.13 Fluorescence Cell Staining	77

2.1.14 3-(4,5-dimethylthiazol-2-yl)-2,5-diphenyltetrazolium bromide (MTT) Cell Viability Assay	78
2.1.15 Contact Angle Measurements.....	79
2.1.16 X-Ray Photoelectron Spectroscopy (XPS).....	80
2.1.17 Scanning Electron Microscopy (SEM).....	81
2.2 Nanodiamond (ND) Study Methods	81
2.2.1 Fenton Treated Nanodiamond Synthesis.....	81
2.2.2 Non-Fenton Treated Nanodiamond Synthesis.....	82
2.2.3 Synthesis of Trifluoroacetic acid protected-10-Aminodec-1-ene (TFAAD)	82
2.2.4 Preparation of 10-Amino dec-1-ene functionalised Nanodiamond.....	83
2.2.5 Plasma Polymerisation of Acrylic Acid	83
2.2.6 Production of AAND Substrates	84
2.2.7 NG108-15 Cell Culture Medium.....	85
2.2.8 NG108-15 Neuroblastoma Cell Culture	85
2.2.9 Primary Schwann Cell Isolation and Culture	85
2.2.10 NG108-15 Neuroblastoma and Primary Schwann cell Co-Culture.....	86
2.2.11 Primary Dorsal Root Ganglion (DRG) isolation and dissociation	86
2.2.12 Fluorescence Cell Staining	87
2.2.13 Immunofluorescence Cell Staining	88
2.2.14 Transmission Electron Microscopy (TEM).....	88
2.2.15 Atomic Force Microscopy (AFM).....	89
2.2.16 Contact Angle Measurements.....	89
2.2.17 X-Ray Photoelectron Spectroscopy (XPS).....	89
2.3.1 Carbon Nanoparticle (CNP) Production.....	90
2.3.2 Primary Human Dermal Fibroblast Isolation	91
2.3.3 Cell Passaging.....	91
2.3.4 RN22 Cell Culture	92
2.3.5 NG108-15 Cell Culture Medium.....	92
2.3.6 NG108-15 Neuroblastoma Cell Culture	93
2.3.7 Primary Schwann Cell Isolation and Culture	93
2.3.8 Analysis of CNP Autofluorescence Within Cells.....	93
2.3.9 3-(4,5-dimethylthiazol-2-yl)-2,5-diphenyltetrazolium bromide (MTT) Assay	94
2.3.10 Live-Dead Assay	94
2.3.11 Dynamic Light Scattering (DLS)	94

2.3.12 Sodium Dodecyl Sulphate Polyacrylamide Gel Electrophoresis (SDS-PAGE) of CNP Solutions	95
2.3.13 Fluorescence Spectroscopy.....	97
2.3.14 Ultraviolet/Visible (UV/Vis) Spectroscopy.....	97
2.3.15 X-Ray Photoelectron Spectroscopy (XPS).....	97
Chapter Three: Diamond-Like Carbon (DLC) Study Results	98
3.1 Introduction	98
3.2 Surface Characterisation of DLC Coatings.....	99
3.2.1 Determination of Optimal Irradiation Time for TFAAD Grafting.....	100
3.2.2 Scanning Electron Microscopy of DLC-Amine Surface.....	101
3.2.3 Substrate contact angle measurements	103
3.2.4 X-ray Photoelectron Spectroscopy (XPS) Graphs.....	104
3.2.4.1 PLD-Derived Diamond-Like Carbon	105
3.2.4.2 TFAAD bound to PLD-DLC (5-20 minutes).....	106
3.2.4.3 10-undecenal bound to PLD-DLC (5-20 minutes)	108
3.2.4.4 TFAAD bound to PLD-DLC (1-4 hours)	112
3.3 Cell Culture upon DLC surfaces	116
3.3.1 NG108-15 MTT Cell Viability on Functionalised DLC Surfaces	118
3.3.2 Fluorescence Images of NG108-15 Cells Cultured upon DLC surfaces.....	119
3.3.3 Immunofluorescence Microscopy of Primary Schwann Cells Cultured upon DLC Surfaces	121
3.3.4 NG108-15 Neurite Lengths Upon Control/DLC Substrates.....	123
3.3.5 Mean Number of Neurites per NG108-15 Cell Across All Substrates.....	126
3.3.6 Neurite Plurality Across the Surfaces.....	129
3.4 Conclusion.....	131
Chapter Four: Nanodiamond (ND) Study Results	132
4.1 Introduction	132
4.2 Surface Characterisation of Nanodiamond Particles.....	133
4.2.1 Nanodiamond Functionalisation Routes.....	133
4.2.2 X-ray Photoelectron Spectroscopy (XPS) Graphs.....	135
4.2.2.1 XPS - Plasma Polymerised Acrylic Acid (ppAA)	135
4.2.2.2 XPS - 10-amino-dec-1-ene functionalised Nanodiamond bound to plasma polymerised acrylic acid (AAND)	137
4.2.2.3 XPS - 10-amino-dec-1-ene functionalised ND (Am-ND)	139

4.2.3 Nanodiamond Transmission Electron Micrographs (TEMs)	141
4.2.4 Atomic Force Microscopy (AFM) Images of ppAA and AAND.....	144
4.2.4.1 AFM Images - Plasma-Polymerised Acrylic Acid Coated Glass (ppAA).....	145
4.2.4.2 AFM Images - ppAA Coated with Amine Functionalised ND (AAND)	146
4.2.5 Water contact angle measurements	148
4.3 Cell Culture upon ND Surfaces.....	149
4.3.1 Fluorescence Microscopy Images	149
4.3.1.1 NG108-15 Cell Fluorescence Microscopy.....	149
4.3.1.2 Dissociated Rat Dorsal Root Ganglia Immunofluorescence Microscopy	151
4.3.1.3 Schwann Cell Immunofluorescence Microscopy	154
4.3.1.4 Neuronal & Primary Schwann Cells Co-Culture upon AAND	156
4.3.2 Neurite Length Measurement Analysis – NG108-15 cells.....	159
4.3.3 3-(4,5-dimethylthiazol-2-yl)-2,5-diphenyltetrazolium Bromide (MTT) Assay ...	166
4.4 Conclusion.....	168
Chapter Five: Carbon Nanoparticles (CNPs) Study Results.....	170
5.0 Introduction	170
5.1 Spectroscopy Analysis of CNPs.....	171
5.1.1 X-ray Photoelectron Spectroscopy (XPS) of Carbon nanoparticles and Precursor Solutions	171
5.1.1.1 XPS of Dried Glycerol/Glucose Solution upon Glass	172
5.1.1.2 XPS of Glucose CNPs upon Glass	172
5.1.1.3 XPS of Dried Glycerol/Sucrose Solution upon Glass.....	174
5.1.1.4 XPS of Sucrose CNPs upon Glass	174
5.1.2 Fluorescence Spectroscopy of CNPs.....	176
5.1.3 Absorbance (UV/Visible) Spectroscopy CNPs	179
5.2 Dynamic Light Scattering (Particle Sizing) Analysis of CNPs.....	181
5.3 Sodium dodecyl sulphate polyacrylamide gel electrophoresis (SDS-PAGE) of CNP solutions	185
5.4 Cell Culture	187
5.4.1 Fluorescence of CNPs within Cells.....	187
5.4.1.1 Glucose CNPs	188
5.4.1.2 Cell Autofluorescence – No CNPs present.....	191
5.4.1.3 Thermally-decomposed glycerol	193
5.4.1.4 Alginate CNPs	194

5.4.1.5 Sucrose CNPs.....	197
5.4.1.6 Alginate/Sucrose CNPs.....	201
5.4.1.7 Alginate/Glucose CNPs	203
5.4.2 Live / dead imaging of fibroblast cells incubated with CNPs	206
5.4.3 MTT assay of fibroblast cells incubated with CNPs	207
5.5 Conclusion.....	211
Chapter Six: Discussion.....	213
6.1 Introduction – DLC & ND discussion.....	213
6.1.1 Discussion of DLC and ND related data	213
6.2 Introduction – CNP Discussion.....	225
6.2.1 Discussion of Carbon Nanoparticle (CNP) Related Data.....	225
Chapter Seven: Thesis Summary	236
7.1 Introduction	236
7.2 Production of a neurocompatible substrate using diamond-like carbon (DLC) or nanodiamond (ND).....	236
7.3 Manufacture of carbon nanoparticles (CNPs) as bioimaging agents	237
7.4 Future Work	238
Appendix.....	241
References.....	256

Abstract

The desire to create an idealised substrate for the growth of neural based cells has been a research ambition for many years. Neural based cells are notoriously difficult to culture, normally requiring the creation of a specially prepared substrate to allow for their attachment, growth and differentiation. Although polylysine serves as an adequate functional treatment for this purpose *in vitro* its associated cytotoxicity present difficulties for *in vivo* applications. Although progress has been made in recent years with regards to the initial development of brain computer interfaces (BCIs) and the bionic eye research in the field could be significantly accelerated through the development of novel successful neurocompatible substrates. It is envisaged that the utilisation of amine-functionalised nanodiamond or diamond-like carbon may fulfil this role due to the ability for diamond surfaces to be neurocompatible, mechanically strong, readily applied as a surface coating, highly stable and easily functionalised.

Additionally, there also exists demand for the creation of nanoparticles to act as bioimaging agents which possess the fluorescence capabilities of quantum dots without the associated cytotoxicity issues. Research progression has unveiled that carbon nanoparticles produced swiftly and in large quantities, from the pyrolysis of carbohydrates, may eclipse quantum dots due to their superior biocompatibility, excellent fluorescence emission levels, environmentally friendly synthesis methods and lack of photobleaching. This area of research is still rapidly expanding, with many carbonaceous compounds still awaiting investigation for their potential as creating carbon nanoparticles (CNP) favourable for bioimaging purposes. It is envisaged the key to creating successfully fluorescent CNPs which can be translocated

within cells boils down to a number of factors, including surface functionality, CNP diameter, and carbon source.

One of the aims of this thesis was to investigate the suitability of amine-functionalised nanodiamond and diamond-like carbon derived substrates for the culture of neuronal cell lines and primary neural cells and also to investigate their effectiveness in comparison to conventional polylysine functionalised surfaces. These novel substrates were illustrated to support neural cells as effectively as conventional polylysine surfaces with cells displaying numerous neuritis of up to 300 μm in length. Furthermore, primary cells were supported on the functionalised substrates for up to three weeks without any indication of apoptosis or cell detachment and cell viability assays indicated no deviation in activity from cells cultured on functionalised and control samples.

In addition, a further aim was to identify the suitability of CNPs derived from multiple saccharide sources (i.e. glucose, sucrose and alginate) as potential bioimaging replacements for presently used quantum dots / fluorescent dyes which are unfortunately subject to photobleaching or cytotoxicity issues. Those CNPs derived purely from either glucose, sucrose or alginate were shown to have luminescence capabilities similar to conventional fluorescent tags, clearly allowing for the morphology of the cells tested to be recorded after cells were exposed to the CNPs for a 2 hour period. This luminescence was shown to still be visually detectable three years post CNP synthesis and the particles were shown to have no significant effect upon cell viability illustrating their widespread potential within scientific research.

Acknowledgements

Firstly I would like to give many thanks to my supervisor, Dr. Frederik Claeysens, for his advice, assistance and supervision with the completion of this thesis and his motivation for helping me to persevere with my research. I am also exceptionally grateful to all my colleagues and friends at the University of Sheffield who have helped and supported me during my years in the tissue culture labs. Everyone at the Kroto Institute has helped my time pass much more quickly than I would have liked and it does not seem a week since I first started my first experiment as a PhD student! In particular, I would like to thank Dr. Rossukon Kaewkhaw for teaching me the basics of cell culture and Dr. Andrew Gill for helping me with polymer synthesis. I would also like to thank Dr. Katie Smith for her invaluable help with the plasma polymerisation rigs and members of the Haycock research group including Dr. Juliet Bell for assisting me with culturing primary Schwann cells and DRGs. In addition I would like to especially thank Dr. James Dugan for his great contribution to my first journal publication and his helpful advice regarding thesis writing.

I would also like to thank my parents, Brenda and Maurice, my brother, Stephen, and my sister, Sara, for their help, understanding and patience through what has sometimes been a stressful five years! Throughout all the good and bad times you have all been there for me and I could not ask for more. Thank you so much for supporting me and helping me to progress to the stage where I am today.

Publications

Journal Articles:

Hopper, A. P.; Dugan, J. M.; Gill, A. A.; Fox, O. J.; May, P. W.; Haycock, J. W.; Claeysens, F., **Amine Functionalised Nanodiamond Promotes Cellular Adhesion, Proliferation and Neurite Outgrowth** *Biomedical Materials*, 2014, 9 (4)

Book Chapters:

Hopper, A. P.; Claeysens, F., **Diamond and Related Materials for Biological Applications** *Diamonds: Properties, Synthesis and Applications*, 2011; pp 155 – 194

Oral and Poster Presentations:

Hopper, A. P.; Claeysens, F., **Morphological Influence of Functionalised Nanodiamond Surfaces on Neuronal Cells** Poster Presentation, TCES 2011, Leeds

Hopper, A. P.; Claeysens, F., **Amine Functionalised Nanodiamond for Neuronal Cell Culture** Oral Presentation, BiTEG 2011, Sheffield

Hopper, A. P.; Claeysens, F., **Amine Functionalised Nanodiamond as a Neuronal Cell Substrate** Oral Presentation, TCES 2012, Liverpool

Hopper, A. P.; Claeysens, F., **Amine Functionalised Nanodiamond for Neuronal Cell Culture** Poster Presentation, TERMIS 3rd World Congress 2012, Vienna

Abbreviations

AAND	10-amino-dec-1-ene functionalised nanodiamond treated acrylic acid coated glass
AAND-H	Hydrogenated nanodiamond treated acrylic acid coated glass
a-C	Non-hydrogenated amorphous carbon
a-C:H	Hydrogenated amorphous carbon
AFM	Atomic force microscope
Am-ND	10-amino-dec-1-ene functionalised nanodiamond
APS	Ammonium persulphate
ArF	Argon fluoride
ATCC	American Type Culture Collection
BCI	Brain computer interface
BDNF	Brain derived nerve factor
BOC	Di-tert-butyl dicarbonate
BSA	Bovine serum albumin
BS	Bottenstein & Sato
C	Celsius
C-Dots	Carbon dots
cdMEM	Completed Dulbecco's modified Eagle's medium
cm	Centimetre
CNP	Carbon nanoparticle
CVD	Chemical vapour deposition
DAPI	4',6-diamidino-2-phenylindole
°	Degree
Dex	Dexamethasone
DLC	Diamond-like carbon
DLC-Aldehyde	10-undecenal functionalised diamond-like carbon
DLC-Amine	10-amino-dec-1-ene functionalised diamond-like carbon
DLD	Delay –line detector
DLS	Dynamic light scattering
DMSO	Dimethyl sulphoxide
DNA	Deoxyribonucleic acid
DRG	Dorsal root ganglion
dDRG	Dissociated dorsal root ganglion
EAC	Ehrlich ascites carcinoma
EBID	Electron beam induced deposition
ECM	Extracellular matrix
EG	Ethylene glycol
Erk	Extracellular signal-regulated kinases

eV	Electron volt
Fak	Focal adhesion kinase
FCS	Foetal calf serum
FEG	Field emission gun
FITC	Fluorescein isothiocyanate
FTIR	Fourier transform infrared spectroscopy
FND	Fluorescent nanodiamond
g	Gram
g	Standard gravity
GFAP	Glial fibrillary acidic protein
GFP	Green fluorescent protein
Glass-ND	10-amino dec-1-ene functionalised nanodiamond treated glass
GPa	Gigapascal
H-ND	Hydrogenated nanodiamond
H-UNCD	Hydrogen-terminated ultrananocrystalline diamond
hBM-MSC	Human bone marrow derived mesenchymal stem cells
HFCVD	Hot filament chemical vapour deposition
HO-ND	Hydroxylated nanodiamond
HRTEM	High-resolution transmission electron microscopy
HXLPE	Highly crosslinked polyethylene
Hz	Hertz
IgG	Immunoglobulin G
IL	Interleukin
IR	Infrared
J	Joule
λ	Wavelength
λ_{em}	Emission wavelength
λ_{ex}	Excitation wavelength
M	1 mole / litre
mbar	Millibar
MEA	Microelectrode array
MEMs	Microelectromechanical devices / systems
ml	Millilitre
μ l	Microlitre
mm	Millimetre
μ m	Micrometre
mol	Mole
MRI	Magnetic resonance imaging
MTT	3-(4,5-Dimethylthiazol-2-yl)-2,5-diphenyltetrazolium bromide
MWCNT	Multi-walled carbon nanotubes
MWPCVD	Microwave plasma chemical vapour deposition
n=3 (N=1)	Three repeat experiments were conducted (n = 3) using a single batch of cells (N=1)
n=9 (N=3)	Three triplicate repeat experiments were conducted (n = 9) with each

	triplicate using a different batch of cells (N=3)
NCD	Nanocrystalline diamond
ND	Nanodiamond
NGC	Nerve guidance conduit
NGF	Neuronal growth factor
nm	Nanometre
nM	1 nanomole / litre
NO	Nitric oxide
N/S	Not significant (data)
NSC	Neural stem cell
NV	Nitrogen vacancy
O:DLC	Oxygen-terminated DLC
O-UNCD	Oxygen-terminated ultrananocrystalline diamond
P:DLC	Phosphate-doped diamond-like carbon
PACVD	Plasma-assisted chemical vapour deposition
PAGE	Polyacrylamide gel electrophoresis
PBS	Phosphate buffered saline
PCD	Polycrystalline diamond
%	Percent
PET	Polyethylene terephthalate
PEG	Polyethylene glycol
PEI800	Polyethylenimine 800
PL	Poly-L-lysine / Poly-L-lysine treated tissue culture plastic
PLD	Pulsed laser deposition
Poly-C	Polycrystalline
ppAA	Plasma polymerised acrylic acid
PPEI-EI	Poly(propionyl-ethylenimine- <i>co</i> -ethylenimine)
QD	Quantum dot
RNA	Ribonucleic acid
ROS	Reactive oxygen species
RT-PCR	Reverse transcription polymerase chain reaction
rpm	Revolutions per minute
sccm	Standard cubic centimetres per minute
SDS	Sodium dodecyl sulphate
SEM	Scanning electron microscope
SiRNA	Small interfering RNA
SSMCC	Sulpho-(succinimidyl 4-[N-maleimidomethyl] cyclohexane-1-carboxylate)
STSG	Split thickness skin graft
SWCNT	Single-walled carbon nanotubes
ta-C	Tetrahedral amorphous carbon
TCP	Tissue culture plastic
TEM	Transmission electron microscope
TEMED	Tetramethylethylenediamine
TFAAD	Trifluoroacetic acid protected 10-amino-dec-1-ene

θ	Contact angle
TNT	Trinitrotoluene
Tris	2-amino-2-hydroxymethyl-propane-1,3-diol
TTDDA	4,7,10-trioxa-1,13-tridecanediamine
U	Unit of penicillin (0.0006 mg)
UHMWPE	Ultra high molecular weight polyethylene
UNCD	Ultrananocrystalline diamond
UV	Ultraviolet
UV/Vis	Ultraviolet / visible
v/v	Concentration of liquid solute within solution (solute volume/solution volume)
wt%	Weight percent
w/v	Concentration of solid solute within solution (mass weight/solution volume)
V	Volt
W	Watt
XPS	X-ray photoelectron spectroscopy
XRD	X-ray diffraction

Chapter One: Literature Review

Adapted from the book chapter “Diamond and Related Materials for Biological Applications” by Andrew Hopper and Frederik Claeysens

1. Introduction

Diamond and its related amorphous carbon derivatives of graphite and graphene are allotropes of carbon that are currently being researched and considered for use in a variety of biological applications [2-17]. The many unique properties that diamond possesses are unparalleled in the natural world. For example, the short carbon-carbon distance (1.54 Å) of bulk diamond crystal results in it possessing one of the highest atomic densities of any solid [5]. Furthermore, the exceptionally high bond energy between the carbon atoms and the associated directionality of the respective tetrahedral bonds in the material's structure conveys diamond's impressive strength [18]. Additionally, the unusually low coefficient of friction further adds to the list of diamond's tribological advantages, an asset utilised by Nissan to reduce friction between engine parts by more than 45 % [19]. These factors outline the importance diamond holds within current research and why investigations into its possible future applications continues to progress.

Recently, advances in the chemical surface functionalisation of diamond have enabled the covalent binding of biomolecules onto diamond surfaces and has opened up exciting novel biomedical applications [20-24]. Diamond can be rendered semiconducting via doping with boron and phosphorous, making it well suited as a biosensing material; indeed important progress has recently been made in this area [5]. Diamond substrates have been functionalised with oligonucleotides to form biologically active DNA biosensors which

exhibit greater stability and selectivity than those constructed from more conventional materials such as gold coated glass substrates [20]. The lack of cytotoxicity associated with diamond and amorphous carbon, such as DLC, also opens the possibility of them being utilised in more widespread *in vivo* applications. Nanocrystalline diamond is currently being heavily investigated as a material for retinal prostheses [7, 25].

Temperature sensitive substrates (e.g. silicon or glass based devices) can be surface coated with an amorphous form of carbon (diamond-like carbon, DLC) under much milder regimes compared to diamond itself. Diamond-like carbon (DLC) can be fabricated under ambient conditions as a thin film (typically having a thickness 10-100 nm) via plasma coating, pulsed laser deposition (PLD) or cathodic arc deposition, thus providing a low-temperature route to surface modification and chemical stability. DLC was initially used for its anti-wear and haemocompatible properties as a surface coating for orthopaedic joints and surgical instruments [26]. For example, DLC has been applied as a coating to the articulating surface of joint prostheses [27]. The application of a DLC coating to such areas creates a hard, wear-resistant layer, which would significantly increase the longevity of these implants and thus requiring fewer revision operations. In addition, this coating can be surface functionalised via the same routes as diamond creating, with relative ease, effective biosensors or biomolecule arrays.

A nanoparticulate form of diamond (nanodiamond, ND) has also been widely investigated for its possible biological applications [2, 3, 6, 8, 15, 17, 23, 28-36]. ND can exist as individual particles of diameter 5-10 nm or as thin surface films/monolayers. It has been illustrated that ND particles or films can be functionalised via covalent or non-covalent surface modification, both of which have yielded encouraging results [37-42]. Enzymes such as lysozyme and luciferase have been attached to ND particles by non-covalent

functionalisation, and have been shown to retain their catalytic activity following immobilisation [28, 30]. In addition, DNA strands can be grafted onto hydroxylated or oxidised ND films via covalent modification [20, 43]. ND particles have also been studied for their suitability as gene carriers into living cells whereby DNA has been coupled with biological molecules such as antibodies [2, 13]. Of further interest, ND particles which have been doped with certain elements have been shown to luminesce due to the presence of point defects. Following nitrogen doping, for example, ND particles exhibit fluorescence at far-red / near infra-red wavelengths, between 638-780 nm. Such particles may then be introduced into cells, enabling them to be visualised via fluorescence microscopy [35, 44]. No discernible photobleaching or cytotoxicity have been known to occur following such procedures, illustrating the advantages such particles possess over conventional fluorescence labels for imaging living cells.

Furthermore the widespread use of nanoparticles for biolabels and imaging purposes is becoming ever more widespread, with new and exciting areas emerging, such as the use of carbon nanodots for *in vivo* and *in vitro* bioimaging. These are thought to have great potential as safer alternatives to quantum dots which are produced from heavy metals including cadmium. These metals are toxic and carcinogenic, exemplifying the need for suitable replacements as biological imaging markers [17]. Similarly, fluorescent nanodiamonds (FNDs) can be taken up and individually detected in cells, allowing their movements to be monitored and the tracking of cellular metabolism pathways [36].

Furthermore, recent work has uncovered the efficiency of diamond nanoparticles as drug carriers for insulin [2]. The enzyme remained dormant as it was non-covalently bound to nanodiamond particles, whilst regaining biological functionality following release in an alkaline environment. These findings could produce innovative applications in the field of

drug delivery for all patients, allowing more comfortable and easier drug administration methods in the near future.

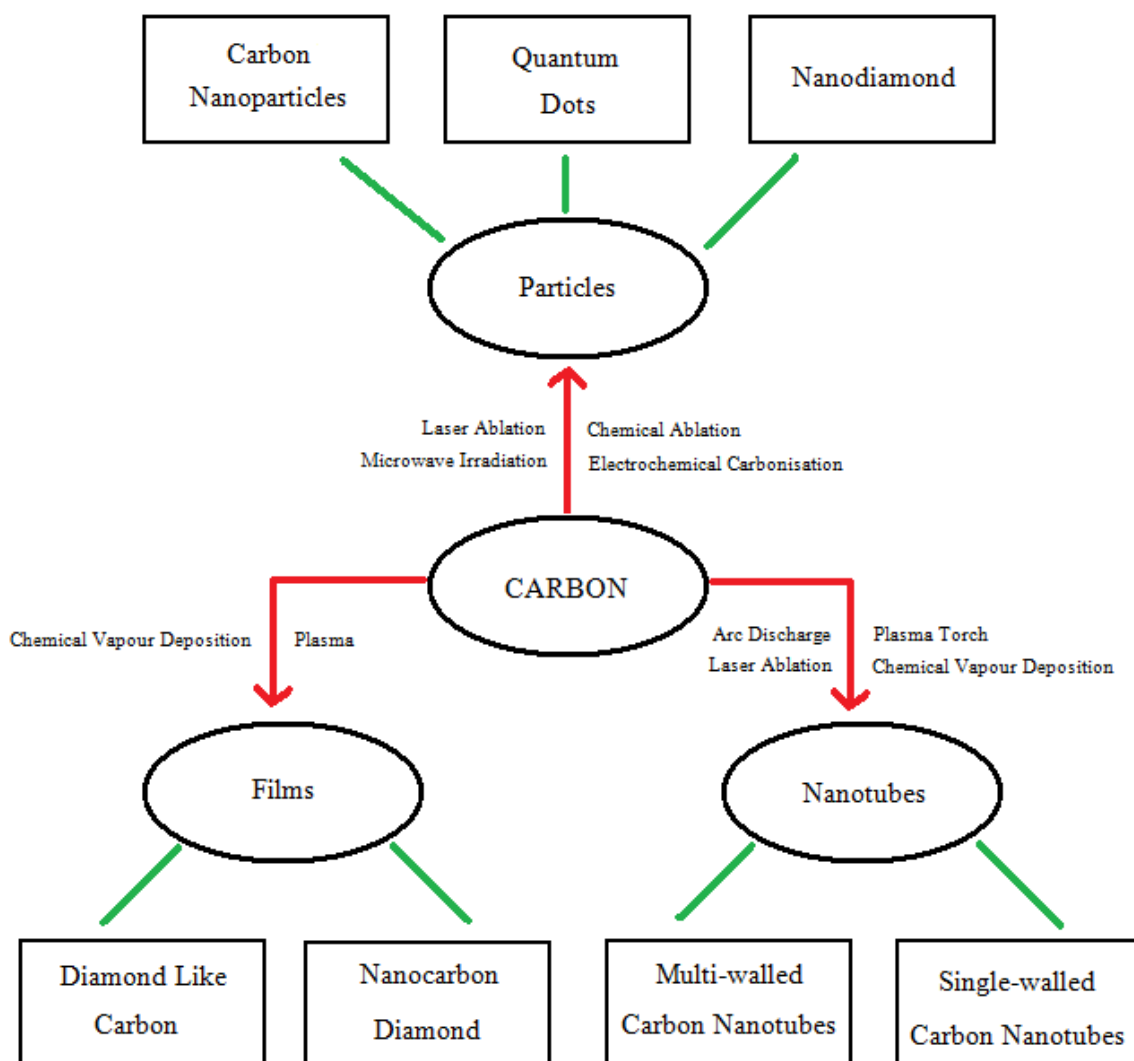


Figure 1: Some of the different forms of carbon that are currently being researched and their respective production methods.

This chapter aims to provide an overview to the current biological research being conducted into diamond and amorphous carbon films and nanoparticles (figure 1). In order to provide an understanding as to what applications may be available (table 1) to these unique classes of

materials this review will first outline the various functionalisation routes which are applicable to diamond and amorphous carbon coatings.

Carbon Biomaterial Example	Suitable Applications
Carbon Nanotubes (Single Walled and Multi Walled)	<ul style="list-style-type: none"> - Scaffold material for bone and neural regeneration [45] - Drug delivery system [46] - Cancer cell imaging [47]
Diamond-Like Carbon (DLC)	<ul style="list-style-type: none"> - Biocoating upon: <ul style="list-style-type: none"> - Orthodontic wires [12] - Vascular stents [48] - Artificial implants [49] - Biosensors [50] - Cell growth surfaces [51]
Nanocrystalline Diamond (NCD)	<ul style="list-style-type: none"> - Biosensors [20] - Retinal / neural prostheses [52] - Influence cell proliferation / differentiation [53]
Nanodiamond Particles (ND)	<ul style="list-style-type: none"> - Drug / gene delivery [2] - Biolabelling [44] - Protein replicas [54] - Nanocomposites [55] - Intracellular antioxidant system [14] - Cell attachment [8]
Carbon Nanoparticles (CNPs)	<ul style="list-style-type: none"> - <i>In vivo</i> and <i>in vitro</i> bioimaging [56, 57]

Table 1: Examples of different carbon-based biomaterials and their respective applications

1.1 Diamond Functionalisation Routes

As indicated in the introduction, both DLC and diamond exhibit numerous advantageous properties. One important characteristic for their use as a biomaterial is the ability to

chemically graft moieties onto their surfaces via well-defined and easily accessible functionalisation routes. Through these procedures it is possible to optimally exploit the bulk properties of diamond and its related materials in biomedical applications, enabling the manufacture of diamond based biosensors, gene/drug delivery vehicles and biolabelled particles. The functionalisation of these materials also chemically homogenises the surface allowing further modification to occur more easily and effectively. Such functionalisation of amorphous carbon and diamond-based materials can take place either through covalent or non-covalent means producing surfaces which have a variety of uses for biological purposes.

1.1.1 Non-Covalent Functionalisation

Although amorphous carbon surfaces prove to be particularly inert under ambient conditions the adsorption of biological molecules, such as proteins [23, 28, 58-60], can nevertheless occur. This is true for oxidised amorphous carbon surfaces, whose terminal-groups (hydroxide, aldehyde/ketone and carboxylate moieties) are able to participate in polar interactions, including hydrogen bonds which bind with enzymes such as luciferase [28] and lysozyme [30]. These functionalised surfaces were shown to be biologically active, with the activity of the adsorbed enzymes being conserved. It is possible to attach further molecules on to the functionalised surface as demonstrated by Huang *et al* [59]. Their research illustrated that it was permissible to covalently immobilise fluorescent dyes to poly-L-lysine coated nanodiamond particles, allowing for use in labelling applications (Figure 2).

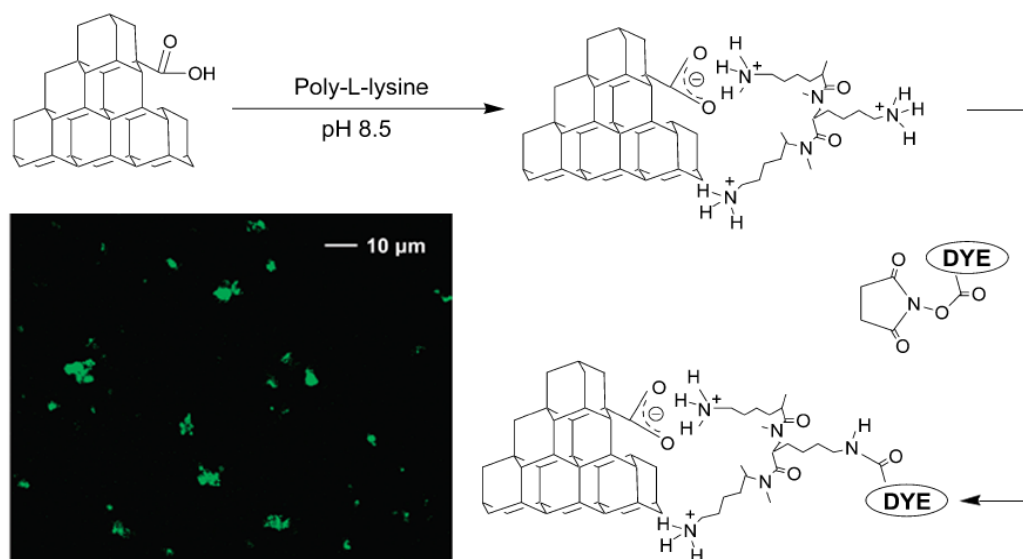


Figure 2: Non-Covalent surface modification of nanodiamond particles using poly-L-lysine. A fluorescent dye was then covalently bound to the amino group of the poly-L-lysine. Inset is a fluorescence image of the nanodiamonds labelled with Alexa Fluor 488 [59].

Nanodiamond has also shown the ability to non-covalently bind with antibodies [29] and peptides [21]. Wang *et al* [61] confirmed the suitability of nanodiamond as a protein carrier via non-covalent adsorption. This was illustrated using the example of bovine serum albumin (BSA) which is known as a ‘soft’ protein due to its low internal stability. This translates to it being one of the most susceptible proteins to undergo conformational alteration following environmental change. Although slight conformational changes to the protein structure were observed following immobilisation, these were thought to be unlikely to result in protein denaturation. The nanodiamond was shown to preserve most of the BSA structural features and exhibited a high affinity for adsorption.

1.1.2 Covalent Functionalisation

A plethora of covalent functionalisation strategies exist for the surface modification of carbon substrates, with the number of functionalisation routes continuously expanding [32, 62]. One set of methods is based on photochemical surface functionalisation. This method utilises ultraviolet radiation (λ ranging from 254 nm to 360 nm) to facilitate the binding of organic molecules possessing a terminal vinyl functional group to a hydrogenated amorphous carbon surface. The stable C-C bonds which form to these alkenes create a base on to which additional functional moieties can be bound. The advantage of using photochemical techniques is that arrays of biomolecular functional groups can be precisely attached through simple shadow mask techniques [63].

The photochemical reaction involving organic alkenes is initiated by photo-electron ejection from the sample. This creates radicals in the solution which cleave hydrogen atoms from the diamond surface, creating highly reactive sites that react with the alkenes [64]. One such alkene which has particular interest to biological research is trifluoroacetamide-protected 10-aminodec-1-ene (TFAAD). Following adsorption, and the deprotection of the TFAAD molecule, a free amine functional group is yielded, upon which further biological moieties such as DNA or enzymes can be bound to form highly sensitive and stable biosensors [65]. Additional chemical methods of functionalising hydrogenated diamond films include the electrochemical or radical grafting of diazonium salts and azo-perfluoroalkyl compounds respectively. Further information on these procedures has been detailed in a number of studies [66-70].

In contrast with diamond and diamond-like-carbon deposited thin films, diamond nanoparticles produced by detonation methods are initially difficult to surface modify without chemical refinement [32, 71, 72]. The chemical inhomogeneity of detonation diamond

nanoparticles is one of the first stumbling blocks towards effective surface functionalisation. The particles are coated in soot, graphitic carbon and metal impurities causing the particles to coalesce into micron-sized aggregates (Figure 3). These impurities can be removed by oxidising the nanodiamond in an acid solution, concurrently causing deaggregation.

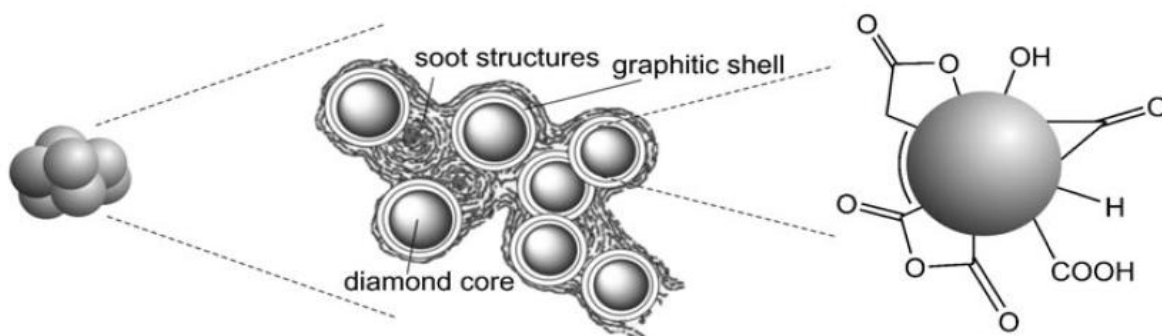


Figure 3: Structure of detonation nanodiamond aggregates and surface functional groups [32].

Upon oxidation, it is then possible to chemically homogenise the nanoparticles through a variety of different functional routes. One such method utilises reactive gases, including ammonia, hydrogen, chlorine and carbon tetrachloride [72] (Figure 4). This treatment, whilst improving the purity of the nanoparticles, also establishes homogeneous functional groups (NH_2 , C-H and Cl) on their surfaces. Further research has discovered that chlorinated nanodiamonds can undergo amination following exposure to ammonia [73]. Similar results were obtained using fluorine in the presence of hydrogen [37]. The fluorinated surface coating could then be further functionalised through the binding of amino acids or amines. In addition to the use of reactive gases, more easily accessible wet chemistry routes exist for the chemical surface homogenisation of diamond nanoparticles. The surface of oxidised nanodiamond powder consists of a mixture of hydroxyl, anhydride, carboxyl (ester and acid) and carbonyl (anhydride and ketone) moieties (Figure 3). These surface moieties (except for hydroxyl groups) can be reduced using borane to produce a uniform hydroxylated surface.

Hydroxyl groups allow for further modification through the grafting of trialkoxysilane molecules [62]. Once adsorbed, the amino groups of these silane molecules, such as trimethoxy and triethoxy 3 amino-propyl-silane, can be used for further surface modification. The successful adsorption of biotin through this process was accomplished, with its biological activity maintained to permit binding to streptavidin [74]. Research has also been conducted into the beneficial procedure of functionalising nanodiamond particles using ‘click chemistry’ [42]. This involves the copper (I) catalysed cycloaddition of azides and alkynes, to which additional organic moieties can be bound or ‘clicked’. This can produce multifunctional diamond nanoparticles, leading them to exhibit both carboxylic and alkyne functional groups. Such a method permits the concomitant binding of two biomolecules at different binding sites through orthogonal coupling linkers. This procedure is biologically significant since the technique is highly efficient and selective, possibly allowing for nanodiamond particles to be utilised as multifunctional biolabels and drug delivery vehicles [42].

An alternative method for producing hydroxylated nanodiamond particles directly from detonated diamond has been devised using Fenton chemistry. This significantly increases the density of hydroxyl groups upon detonation nanodiamond (figure 4) producing highly reactive hydroxyl radicals that can cause partial oxidation of any exposed carbon atoms on the nanodiamond [13]. Concurrently, the reaction also causes the degradation of any adsorbed soot on the surface, forming carbon dioxide, thus exposing greater numbers of carbon atoms to oxidation. This eventually forms a surface layer of –OH groups upon the ND, onto which a high density network of functional groups can be covalently bound. X-ray diffraction (XRD) of the fenton treated particles reveals diamond XRD peaks, indicating that the method preserves the diamond crystal structure whilst increasing functionality [75].

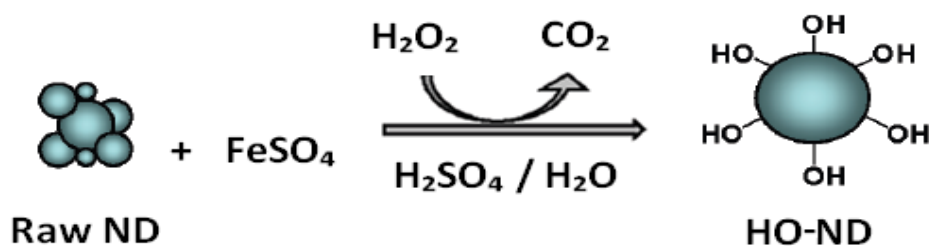


Figure 4: Fenton reaction route to functionalise nanodiamond particles with hydroxyl groups (HO-ND) [13].

Additionally, it is possible to functionalise nanodiamond with aryl organic molecules by Suzuki coupling reactions [39]. This reaction route is useful for producing fluorescent particles, through the Suzuki coupling of pyrene, which generates a fluorescent nanodiamond-pyrene complex. Importantly, nanodiamond functionalised in this manner demonstrates greater resistance to aggregation, and improved dispersion in ethanol and hexane.

Further surface chemistry reaction routes for nanodiamond particles are discussed in section 1.4.1. The functionalisation strategies in this section illustrate the huge range of possible applications which diamond and related carbon materials are suited for. Research continues to progress in identifying further functionalisation methods and applications which could prove useful for future applications. Past and present biological uses of diamond related materials will now be discussed in the following sections.

1.2 Nanodiamond Films

Another form of diamond which has been shown to have uses in biological research, as well as in electrical applications is nanocrystalline (NCD) diamond. Discovered in the early 1960s in the Soviet Union [76], the material can be obtained as a film by chemical vapour techniques (CVD) (Figure 5) [1] and can be distinguished from other forms of amorphous

carbon by its grain size, which is usually in the range of 100 – 300 nm. The growth mechanism for NCD films requires hydrogen-rich growth chemistry, whereby crystal growth results in a columnar morphology oriented in the growth direction. As the film increases in thickness, the grain size subsequently increases also, however it is possible to maintain grain sizes in the NCD range for films several microns in thickness by controlling the nucleation density and growth parameters [5].

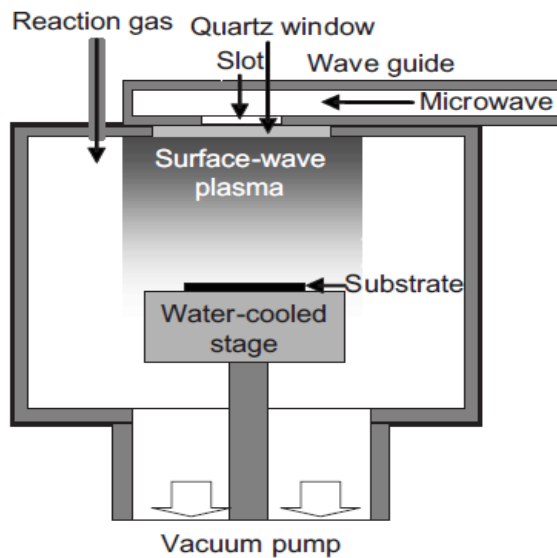


Figure 5: The typical components of a microwave plasma CVD system used for the low temperature deposition of nanocrystalline diamond films [1].

NCD shares many of the desirable properties associated with natural diamond such as a wide band gap, negative electron affinity, exceptional hardness and remarkable biocompatibility. Notably NCD also possesses negative electron affinity, whereby the addition of an electron to the material will require energy, rather than cause the release of energy. Although such a property has remained relatively unutilised at present, it may offer advantageous properties within the semiconductor industry [77]. Such advantages have garnered accelerating research interest, opening the door to a possibly wide range of suitable applications. However, fabrication techniques such as CVD, which can often require temperatures in excess of 400°C for the production of NCD, may limit the range of substrates to which it could be applied [78].

Efforts have therefore been made to attempt the low temperature synthesis of NCD films. Hot-filament CVD (HFCVD) can deposit diamond particles on a silicon substrate at a temperature of 135°C [79], whereas microwave plasma CVD (MWPCVD) can fabricate NCD films at temperatures as low as 86°C on plastic substrates [1]. At such low temperatures, the crystal size of the diamond was measured on average to be 5 nm which is in keeping with normal NCD films.

However, in the past decade a new form of nanodiamond film, known as ultrananocrystalline diamond (UNCD), has been developed. It was patented and first produced at the Argonne National Laboratory [80] and has since been suggested as having possible biological applications [7, 81]. UNCD possesses a much finer grain size, in the region of between 3 -5 nm [82], in comparison to nanocrystalline diamond (typically 100 – 300 nm) [83]. This provides UNCD films with a larger surface area for the grafting of functional molecules, and a smoother surface topography which can permit a greater cellular surface contact area [83]. Such films can be produced using a plasma which has a comparatively low hydrogen content, typically consisting of 97% argon, 2% hydrogen and 1% methane [84]. This is in contrast to the hydrogen-rich plasmas used for the synthesis of conventional nanodiamond films (99% hydrogen and 1% methane). It is possible to produce UNCD films of any thickness with little variation in the surface roughness due to a high re-nucleation rate [82]. This contrasts with NCD, whose surface roughness increases with film thickness. NCD eventually resembles microcrystalline diamond above certain thicknesses [82]. It has also been discovered that the bias-enhanced nucleation process for UNCD synthesis offers greater efficiency and enhanced substrate adhesion compared to other processes producing UNCD such as mechanical polishing. Furthermore, a technique has been finalised that permits the deposition of UNCD layers of uniform grain size (3 – 5 nm), low compressive stress, ultra-smooth surfaces and

high growth rates which could progress UNCD as a potential material for microelectromechanical (MEMs) devices [85].

1.3 Nanodiamond Films as Biocoatings

Research into the uses of NCD and UNCD as biomaterials have resulted in the development of several applications as outlined below:

1.3.1 Surfaces Which Influence the Proliferation or Differentiation of Cells

Being able to control the surface properties of substrates for cell culture is of great scientific importance. Cell adhesion molecules, such as integrins, serve as interconnecting bridges between cells and the extracellular matrix (ECM) or cellular growth substrate [86, 87]. These integrins trigger signalling cascades (Figure 6) which determine cellular phenotype and differentiation capabilities. It has been demonstrated that the nanoroughness and surface charge distribution of a substrate can determine cell attachment efficiency, proliferation rates and differentiation [88].

In turn, it would be beneficial to control the differentiation and proliferation of stem cells *in vivo*. This is particularly important in the case of neural stem cells (NSCs) since injuries to the peripheral or central nervous system originate from the loss or damage of neural cells, which often fail to regenerate spontaneously [89, 90]. However, neural stem cells cultured on UNCD have been found to differentiate into different cell types depending on the surface termination of the film [53]. For example, NSCs cultured on O-UNCD films in serum-free media showed a preference to differentiate towards oligodendrocytes, whilst those cells cultured on H-UNCD films were more likely to differentiate towards neuronal cells. These different responses are directly related to the surface chemical properties both of these films exhibit. H-UNCD films have negative electron affinity, possess p-type surface conductivity

and are hydrophobic. Meanwhile, O-UNCD films are electrically insulating, hydrophilic and display a positive electron affinity [91]. The changes in cellular behaviour that have been documented have been quantified by the reverse-transcriptase polymerase chain reaction (RT-PCR) through the expression of specific neuronal cell markers and immunofluorescence staining [53].

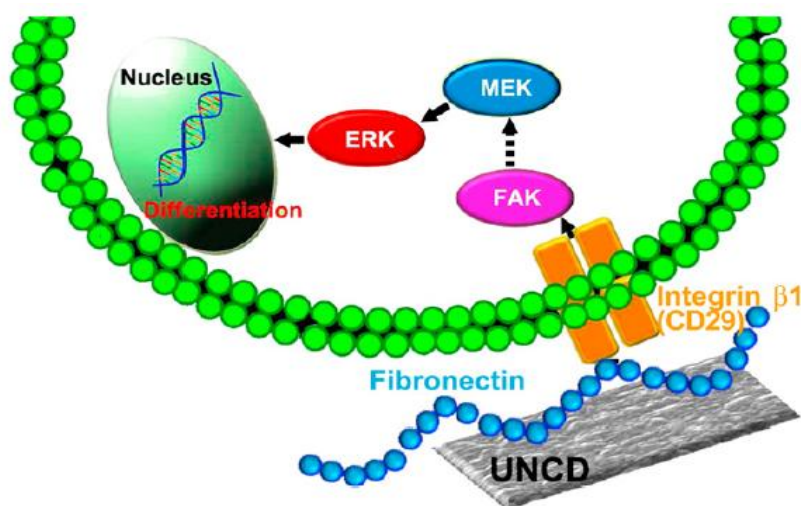


Figure 6: Schematic diagram summarising the influence of hydrogenated ultra-nanocrystalline diamond films (H-UNCD) in mediating neuronal differentiation from NSCs. Adsorbed fibronectin on H-UNCD activates integrin, focal adhesion kinase (Fak) and extracellular signal-regulated kinases 1/2 (Erk1/2) pathways culminating in neural stem cell (NSC) neuronal differentiation [81].

H-UNCD films have also been shown to favour the adhesion and proliferation of mesenchymal stem cells, whereas oxygen and fluorine terminated UNCD coatings have generally resisted stem-cell adhesion [92]. However, one biological application where O-UNCD films have proved to be biocompatible is for the growth of murine embryonic fibroblasts [93], whose proliferation was observed to be of a similar rate on both tissue culture plastic (TCP) and O-UNCD surfaces. Similarly no cytotoxicity was observed when fibroblast cells were cultured on NCD-coated ceramics, proving the substrate to be a suitable

surface for cell attachment and growth in this situation. After a few days the cells were observed to form a confluent surface layer, with proliferation rates observed to be slightly higher than those observed on TCP [94].

Furthermore, cell lines have been shown to favour O-UNCD (hydrophilic) surfaces also, due to the presence of a plethora of interaction sites for media components and adhering cells. Such sites originate from local variations in electric field gradients across the UNCD films, caused by oxygen termination, polarity and surface alterations. Cellular adhesion has been shown to be significantly greater than that displayed on glass. In contrast H-UNCD films were shown not to be appropriate for the culture of cell lines due to the absence of sufficient interaction sites [91].

UNCD films can also be functionalised in such a way as to reduce cellular activity [95]. It is possible to coat carboxylated-UNCD with collagen to which dexamethasone (Dex), an anti-inflammatory therapeutic, can be bound. Dex, a glucocorticoid which can attenuate inflammatory gene expression, could have useful applications as a surface coating for artificial implants and materials to reduce potential inflammation and biofouling. The presence of Dex has been shown to reduce the incidence of pro-inflammatory cytokines such as IL-6 and suppress inflammatory gene expression [96].

1.3.2 Biosensors

One major hurdle for the integration of microelectronics and biotechnology is the requirement to develop interfaces that are compatible with current processing methods, but which also permit satisfactory selectivity and *in vivo* stability. Conventional microelectronic materials, such as silicon, can be biologically functionalised but surface degradation affecting the efficiency of the biosensor can be problematic. Attention has therefore shifted to the use

of diamond, in particular NCD, for the construction of integrated biosensors. The aforementioned chemical and physical properties, in addition to the ability of NCD to be deposited as a thin, robust film, make the material amenable for biosensor construction. Indeed, previously, DNA molecules have been attached to hydrogenated NCD films which had been photochemically functionalised with TFAAD [20]. This produced a biosensor which possessed excellent selectivity and stability, exceeding that of conventional microelectronic substrates such as silicon and gold [20]. The potential for using UNCD as a biosensor platform has been previously reported whereby a hydrogen peroxide sensor based on catalase was covalently bound onto NCD [97]. The biosensor produced thus displayed excellent activity with minimal denaturation of the enzyme upon binding to the NCD surface.

It has also been discovered that diamond surfaces functionalised with ethylene glycol groups (EG) discourage the non-specific binding of proteins. So effective was the surface that it reduced the detection of adsorbed fibrinogen beyond the detection range capability of XPS, a decrease of 97% in comparison to hydrogenated-diamond samples [98]. Such data explains the improved signal:noise ratio evident from biosensors created from diamond substrates in comparison to those manufactured using gold or glass. Encouragingly, it was discovered that the roughness of the diamond surface (nanocrystalline diamond films exhibiting greater roughness than single crystal diamonds) had little effect upon covalent binding ability [98]. Furthermore, the binding of *E.Coli* antibodies to diamond thin films has also been shown to be particularly stable, whereas glass substrates struggle. The hydrolysis of Si-O-Si bonds at the antibody interface is the main disruptive factor in this instance. The biological activity of antibodies attached to diamond surfaces is noticeably greater than the equivalent on glass, illustrating that biosensors created from diamond have the potential for greater longevity [98]. This was corroborated in a further independent study where antibody-based biosensors were able to withstand repeated antigen binding cycles without activity loss [99]. Suitable

applications for such biosensors include the monitoring of food and water supplies for contaminating bacteria including *salmonella*, *E. Coli* and *Campylobacter* [98].

Immunosensors incorporating nanocrystalline diamond, including one capable of physically adsorbing anti-C reactive protein antibodies to a hydrogenated NCD film surface [100]. It is possible to monitor these proteins in real-time, permitting the detection of micromolar quantities within a 30 minute timeframe.

1.3.3 Retinal and Neural Prostheses

Retinal microchips may be widely deployed in the future to help restore a patient's vision following retinal degeneration due to diseases such as age-related macular degeneration. It is envisaged an optical microchip could be connected to the inner retina of a patient's eye to substitute damaged photoreceptors [7, 25, 52]. To ensure success it would be a requirement for the prosthesis material to be constructed of, or coated with, a bioinert material to prevent inflammation of the retina. The release of toxic or irritable by-products would need to be negligible.

Although silicon would normally be a suitable structural and functional material for the microchip, its unfortunate ability to slowly dissolve in physiological fluids would require the use of a coating material, such as UNCD, to protect the chip's integrity. This coating procedure has already been investigated, and it was realised that deposition of NCD films by PECVD at temperatures between 400 – 800 °C did not adversely affect the Si substrate [7]. Implantation of these UNCD coated Si chips into the eyes of rabbits over a 6 month period elicited no immune response, thus confirming the bioinertness and biostability of UNCD coatings and the importance of such forms of diamond to this biological application [7].

Additionally, detailed research into the production of a diamond-penetrating microelectrode array (MEA) which could in future restore at least partial vision to blind patients has been undertaken [25]. It was possible to implant models of the array into rat retinas without causing significant damage to the diamond electrodes (95% of which survived the procedure intact). In a model retinal prosthesis the diamond electrodes would need to be embedded in the patient's retina, residing in the ganglion cell layer in close proximity to the optic nerve. Images captured by a remote video camera worn by the patient would be processed and relayed wirelessly to a microchip within the retinal device. The electrodes which would penetrate the retina could then electrically stimulate the ganglion cells, which in turn would then stimulate the patient's optic nerve. Retinal cells have been shown to survive and proliferate on NCD equally as well as on glass [52] and it has been possible to fabricate diamond MEAs upon soft substrate materials such as polyimide and parylene to produce flexible implants. Following implantation in blind rats, no gliosis was observed in the retinal tissue, proving that the implant did not damage the optic nerve [52].

Similarly, findings have been published relating to the production of polycrystalline-diamond (poly-C) based microprobes, which may have future applications in neural prostheses [101]. Boron-doped diamond was used as the electrode material in this instance to provide a stable surface for the detection of chemical and electrical stimuli, with a supporting structure composed of undoped polycrystalline diamond. It was possible to detect levels of norepinephrine, a neurotransmitter which acts as a stress hormone, at concentrations as low as 10 nM. *In vivo* studies, whereby microprobes were inserted into the auditory cortex of guinea pig brains to monitor neural activity were also completed. Broadband sound signals were applied to stimulate the brain, and neural activity within the cortex was monitored. Although the probe was capable of recording the stimulated neural signal, the signal to noise ratio was low. The large surface area of poly-C diamond has been known to enhance

background noise, so adaptations to the device design would need to be considered before further *in vivo* studies are undertaken.

In conclusion, nanodiamond films have been researched in numerous applications in biotechnology and bioengineering. Its biocompatibility and electrical properties and its ability to be deposited as a coherent film, enable it to be of particular use as a biosensor substrate. Indeed the work which has been completed already with respect to retinal prostheses illustrates the future potential such a material can unlock.

1.4 Nanodiamond Particles

Detonation nanodiamond particles remained relatively obscure from their initial production in 1960s Soviet Russia until approximately thirty years later when interest in their research uses began to gather pace [102, 103]. Gradually, greater applications for nanodiamond were realised, beginning with the production of colloidal suspensions of individual nanodiamond particles [104]. Later, fluorescent nanodiamonds were discovered that could be utilised as non-toxic alternatives to quantum dots whilst magnetic nanoscale sensors, also based on ND, were developed [105-107]. It was later realised that tuneable ND surface properties made it possible for functionalisation to occur via various wet and dry chemistry routes, further widening their possible applications to include drug / biomolecule delivery [2, 72, 108-111]. In addition, the lower cytotoxicity associated with ND when compared to other forms of nanocarbon such as carbon nanotubes has opened up further possible applications within biomedicine and bioengineering [112, 113]. One advantage of ND production is that it can be used to dispose of superfluous munitions which would otherwise remain unused, including Composition B, rendering the production route both environmentally friendly and economically viable [71, 114]. The explosives utilised act as both a source of carbon and

energy for the conversion required to produce diamond, which occurs in a pressurised vessel containing either an inert gas or water-based coolant [71, 114]. Although the temperatures and pressures produced in the reaction chamber are insufficient to synthesise bulk liquid carbon, they are high enough to produce nanoscale liquid carbon droplets, which are thought to condense and crystallise to create ND particles (figure 7) [114].

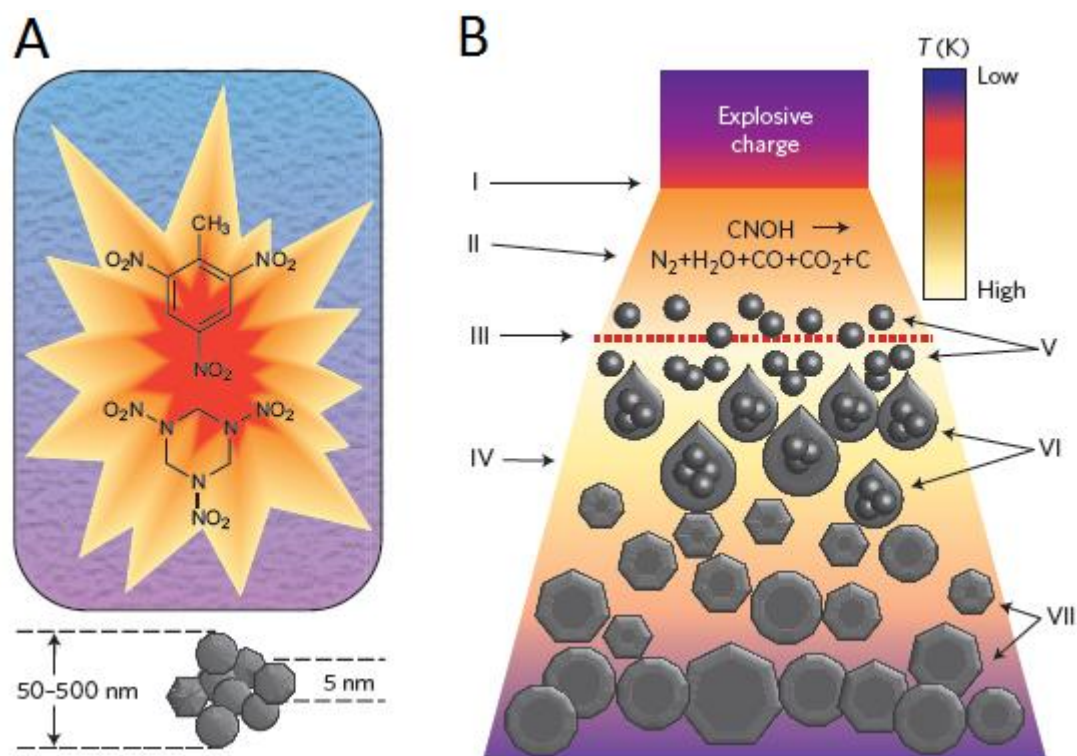


Figure 7: The synthesis of detonation nanodiamond. (A) Nanodiamonds are produced by detonating a mixture of explosives such as trinitrotoluene (TNT) and hexogen within a sealed metallic container under vacuum. (B) Detonation wave propagation illustrating (i) the explosive shock wave; (ii) decomposition of explosive molecules within chemical reaction zone; (iii) Chapman-Jouguet plane whereby temperature and pressure conditions are amenable to forming liquid nanocarbon droplets; (iv) detonation products expand; (v) carbon nanocluster formation; (vi) liquid nanodroplet coagulation; and (vii) the crystallisation and aggregation of nanodiamonds [115].

Although the resulting detonation soot can contain up to 75 wt% of diamond, the actual carbon yield represents at most only 10 wt% of the explosive used [71]. Additionally present in the detonation soot are graphitic carbons (25 - 85 wt%) and numerous metal and oxide impurities (1 - 8 wt%) which originate from the igniter utilised to initiate detonation (usually azides of silver, copper or lead) and the steel walls of the detonation vessel [71, 76, 115]. Since these impurities can be found attached to the interior and outer surface of ND aggregates it is paramount to separate out the aggregates in order to remove all the impurities present [115]. The harsh nature of the synthesis pathway of detonation nanodiamond results in a particle surface littered with myriad functional groups, rendering it initially difficult to characterise raw nanodiamond due to the unique assortment of chemical functionalities present on each particle [115].

However, both liquid (incorporating either nitric or sulphuric acid with hydrogen peroxide) and gaseous (through the use of oxygen or hydrogen) purification methods are available, the latter of which is preferred due to it being a cost-effective and simple process which does not harm the environment [71, 76, 116]. Oxygen/hydrogen purified NDs have also been noted as forming smaller aggregates in aqueous solutions (160-180 nm) and significantly greater quantities of free particles compared to ND exposed to acidic surface treatments [115].

Nanodiamonds may also be separated by centrifugation to produce fractions based on weight and size [117]. This ensures that nanodiamonds of certain dimensions can be separated for distinct applications; for example, aggregate sizes below 10 nm are preferable for drug delivery [22]. Once purified, the ND particles achieve surface chemistry homogeneity (figure 8), making the process of subsequent functionalisation far more effective and efficient. This functional dexterity is one of many advantages which nanodiamond holds, the others namely being biocompatibility, chemical stability and exceptional toughness and hardness [115].

Indeed, these various surface functionalisations can occur without detriment to the beneficial properties of the diamond core.

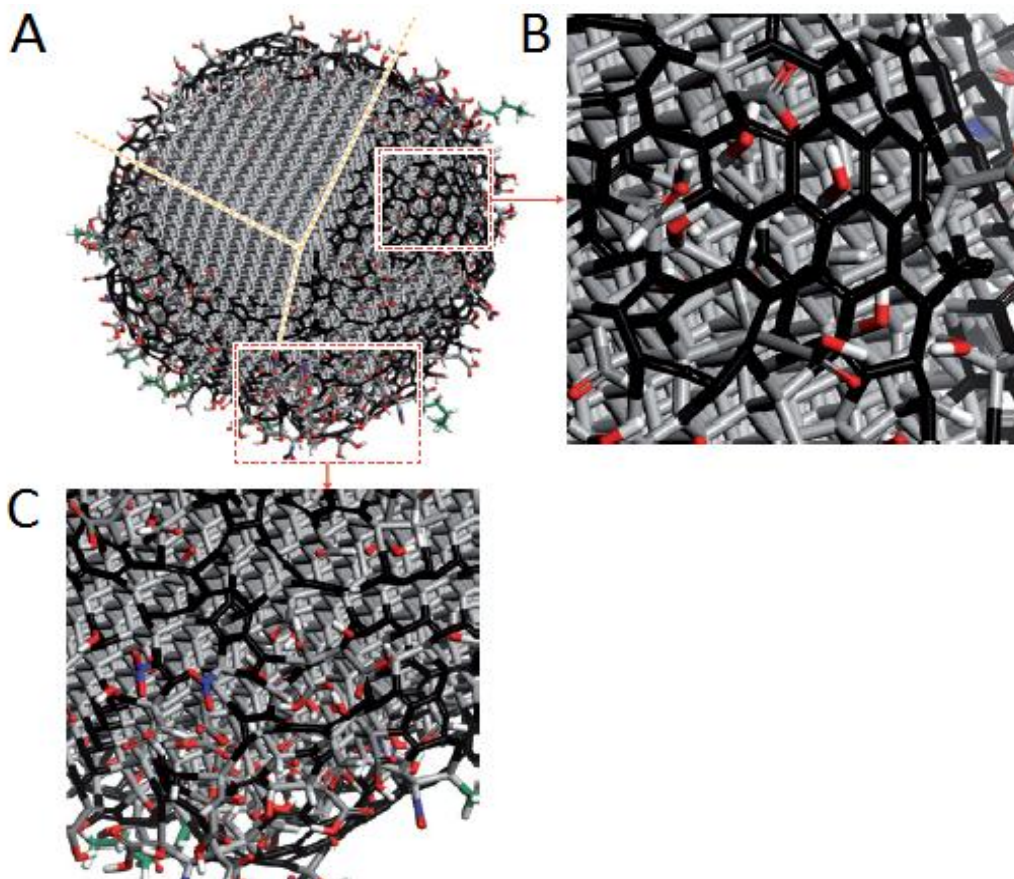


Figure 8: (A) Schematic representation of a 5 nm nanodiamond particle following oxidative treatment. The surface is widely covered with functional groups which aim to stabilise dangling bonds. The upper left corner of the nanoparticle has been cut away to reveal the diamond core. (B & C) Higher magnification regions of the nanoparticle illustrating the widespread oxygenation of the purified particle illustrating the presence of oxygen atoms (red), nitrogen atoms (blue), hydrocarbon chains (green) and hydrogen terminations (white) [115].

1.4.1 Nanodiamond Functionalisation Routes

Examples of functional routes for purified nanodiamond depend upon the initial termination of the ND surface. Hydroxyl terminations can undergo esterification using acyl-chlorides to create nanodiamond particles which are coated with long alkyl chains [118]. Diazonium chemistry can also be used with hydrogen-terminated nanodiamond and graphitic nanodiamond to form a C-C bond between the ND particle and the attached functional group [41]. On the other hand, carboxyl terminated ND can undergo high temperature gas treatments with chlorine to form acylchlorides, whilst treatment with fluorine gas produces C-F bonds. Ambient temperature wet chemistry routes are also available as illustrated in figure 9 [37, 119, 120].

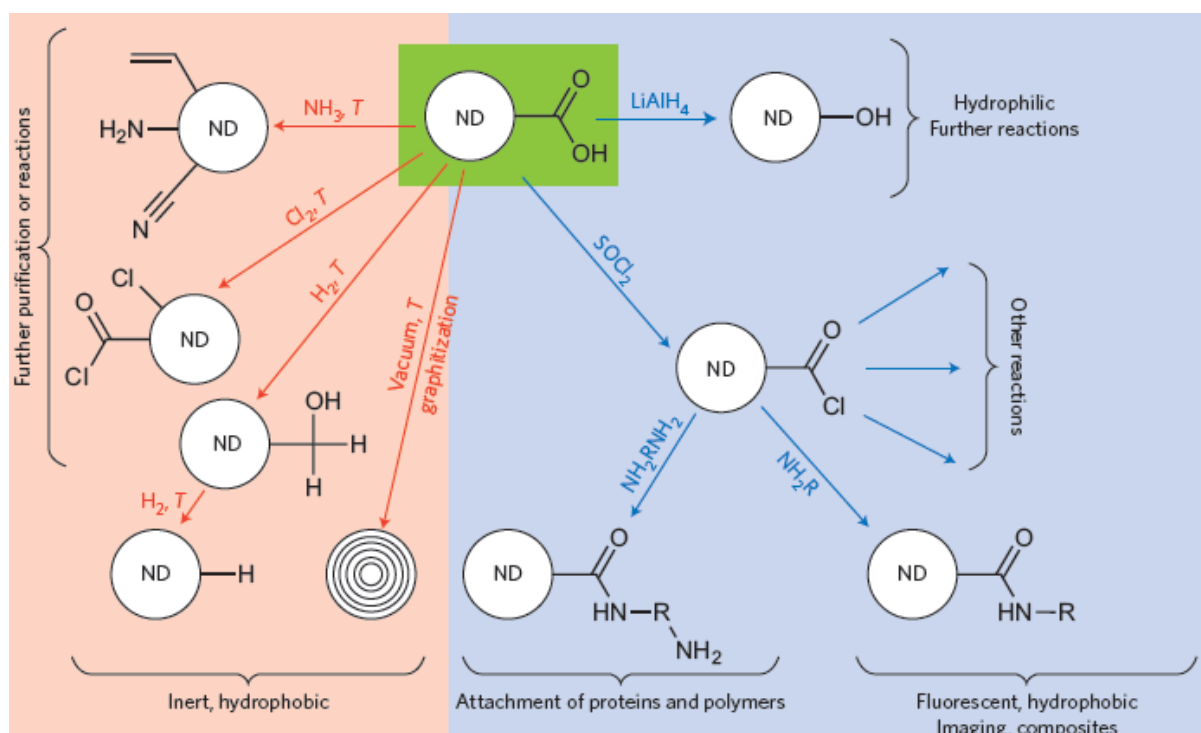


Figure 9: Functionalisation of Purified Nanodiamond. Nanodiamond which has been carboxylated (green) can easily be functionalised by a variety of high temperature gas treatments (red) or ambient wet chemistry routes (blue) [115].

1.4.2 Biocompatibility of Nanodiamond

The numerous mentioned chemical modification pathways indicate the versatility of nanodiamond functionalisation routes. Although diamond and its related forms are known to be non-toxic, the various purification and functionalisation procedures involved in nanodiamond production mean the same knowledge cannot automatically be assumed ND particles [121].

Various *in vitro* and *in vivo* research studies have been conducted to assess the effect of ND particles upon cell viability, gene programme activity and physiological processes [6, 121-125]. It has been reported that nanodiamonds instilled within murine trachea exhibit low toxicity, with ND concentrations within the alveolar region decreasing over time [123]. Additionally, ND complexes intravenously administered in mice have not been shown to trigger any systemic indicators of toxicity [125].

Nanodiamond aggregates (approximate diameter: 120 nm) conjugated with green fluorescent protein (GFP) have also been microinjected into translucent worms and tracked for several days [124]. It was discovered that GFP bearing aggregates were not toxic to the worms and could be easily visualised. Bare NDs were also injected, most of which resided within the worm's lumen, whilst BSA conjugated NDs were absorbed into the intestine [124]. This suggests that it is possible to target ND particles to a specific location of the body based on their surface chemistry. These beneficial properties of nanodiamond have helped develop numerous uses for the material within biological research as elaborated in section 1.4.3.

1.4.3 Applications of Nanodiamond Particles

Nanodiamonds are currently employed in several engineering applications, the most widespread of which is their use within cutting tools and drill bits to create cutting edges that are smooth yet extremely hard wearing. The addition of a nanodiamond coating to such cutting appliances potentially increases their lifetime up to 100-fold [126]. More recently they have also found uses within magnetic resonance imaging (MRI) [127], chemical vapour deposition (CVD) [128], chromatography [129] and mass spectrometry [130]. Boron doped nanodiamonds, meanwhile, have shown promise as electrochemical capacitors and batteries, due to their conducting properties [131]. Great interest has also been devoted to the advantages of utilising nanodiamond within biomedicine and nanocomposites as outlined below.

1.4.3.1 Nanocomposites

Nanodiamond's superior mechanical properties with its tuneable surface properties and nanoscale dimensions render it an ideal choice as a 'filler' for composites [115]. It was discovered that the supplementation of ND within polymeric materials results in significant improvements to the wear resistance [132], mechanical strength [6, 133-137], adhesion [138], electromagnetic shielding [139] and thermal conductivity of the bulk polymer [135, 140]. Conversely, however, degradation of the bulk properties was noted with the addition of raw and/or aggregated ND [115], thus illustrating the requirement for purification and deaggregation when using ND as a composite material.

To elaborate, the addition of small quantities of nanodiamond to poly(vinyl alcohol) nanocomposites has been documented as greatly improving the material's mechanical properties [55]. The dispersion of nanodiamond within the matrix, and their interactions at

the diamond:matrix interface, can be manipulated through tuning of the ND surface chemistry. Generally, most composite properties can be greatly improved by the addition of a form of nanodiamond that creates a strong covalent bond within a metal, ceramic or polymer matrix [134, 141, 142].

Furthermore, a nanodiamond enriched poly-L-lactic acid (PLLA) scaffold has been produced for bone tissue engineering [6]. The nanodiamond particles, functionalised with octadecylamine, resulted in a 200% increase in the polymer's Young's modulus and 800% increase in hardness. At these levels the polymer's properties approached that of human cortical bone. Furthermore the incubation of murine osteoblast cells within the polymer matrix over a one week period progressed without any noticeable toxicity or effect upon cellular proliferation. What is particularly interesting is the multifunctional potential of octadecylamine-bound ND, since it can be further functionalised to perform as a drug delivery vehicle or as a fluorescent marker. Indeed, in this particular case the polymer matrix exhibited intense fluorescence allowing for the progress of *in vivo* bone re-growth into the implant to be monitored easily in the future [6].

1.4.3.2 Protein Replicas

The small size of nanodiamonds, in addition to their biocompatibility, stability and extensive surface chemistry may make them suited as replicating some of the roles of globular proteins *in vivo* [54]. It has been suggested that functionalised ND could be utilised to transport genetic material across cellular membranes, including the blood-brain barrier.

Artificial nucleosomes may also be created, whereby alkaline-ND (made possible by the attachment of amino acid groups [134]), acting as a histone, could be surrounded with nucleic acids, helping to effectively and precisely fold and unravel DNA on demand.

1.4.3.3 Biolabelling

The ability with which biological systems function at the local level can be readily monitored through biolabelling and biomolecular probes, their interactions being observed *in vivo*. Laser-induced fluorescence is often selected for this procedure due to its inherent sensitivity and flexibility in coping with simultaneous probe detection [44]. To avoid interference with endogenous cellular components, it is beneficial for biological probes to absorb radiation at a wavelength greater than 500 nm whilst fluorescing above 600 nm. Although organic dyes and fluorescent proteins can fulfil these obligations, inherent disadvantages, such as photobleaching, limit their potential uses for long term or prolonged *in vivo* research [44].

Fluorescent nanodiamonds are able to combine the beneficial properties associated with quantum dots (namely photostability, bright multicolour fluorescence and nanoscale dimensions) whilst also being biocompatible, easy to synthesise and possessing a rich surface chemistry [115]. These properties may help nanodiamond to revolutionise future applications within the *in vivo* bioimaging sector [105, 143, 144].

In contrast, certain imperfections within nanodiamond known as nitrogen-vacancy (NV) centres provide useful fluorescent properties [115]. They are characterised as being located adjacent to nitrogen atoms within the particle's structure and emit fluorescence at approximately 700 nm, whilst absorbing strongly in the region of 560 nm [105, 145]. The irradiation of ND with high energy electrons or protons, and vacuum annealing at 600-800 °C usually creates fixed nitrogen vacancy centres which remain permanent features.

Most fluorescent NDs (FNDs) have been produced from starting materials created by a high temperature, high pressure synthesis route [105, 146]. These forms of diamond have greater amounts of indigenous nitrogen which are vital for the inclusion of NV centres. Detonation

based ND particles produced from TNT and hexogen precursors generally include lower concentrations of NV centres, but nevertheless have been shown to luminesce [147].

Greater levels of fluorescence may be observed through the conjugation of fluorophores upon the detonation ND surface [59, 112, 148]. These ND particles have the ability to travel unrestricted through various cellular organelles without any long-term negative impact upon the fluorophore structure or cellular viability [149]. Intense blue fluorescence has been recorded from NDs covalently linked with octadecylamine [106].

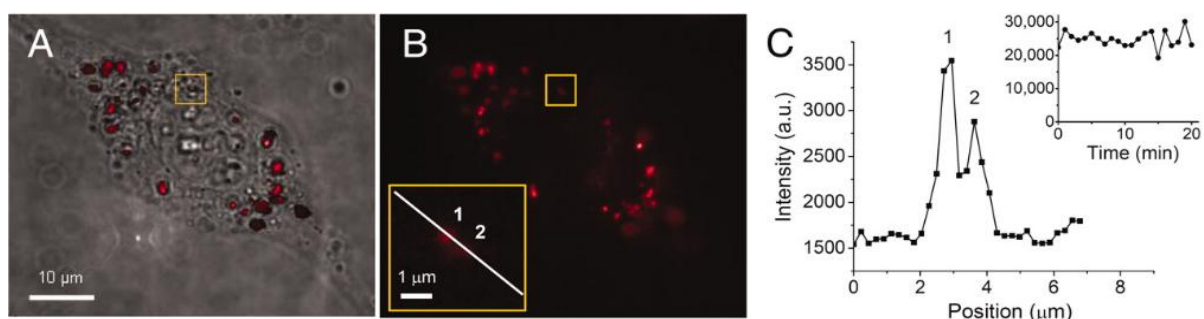


Figure 10: (A) Brightfield and (B) epifluorescence images of single fluorescent nanodiamonds (FNDs) in a HeLa cell. Enlarged view of Two FNDs shown inset. (C) The fluorescence intensity profile of the line drawn in image B between FND 1 and 2 is also shown. Smaller graph illustrates fluorescence intensity from the sample after continuous excitation over a 20 minute period, showing no sign of photobleaching [44].

These important properties may mean that FNDs could be suited for long term observation in biological cells as single biomarkers, being taken up through endocytosis [150]. This was proven by Fu *et al* [44], who demonstrated it was possible to track a single FND in a HeLa cell (figure 10). More recent work has focused on conjugated FNDs for the uses of homogeneous labelling and superresolution imaging [36]. Albumin conjugated FNDs can readily couple with biotin, forming a biotin-albumin complex which can be further

conjugated with avidin or streptavidin. Subsequently, such superconjugates can bind with biotinylated antibodies for highly specific binding and imaging purposes [36].

Additionally, it has been demonstrated that surface-carboxylated nanodiamond particles have been successfully used as *in vitro* probes in human lung cells (A549 lung epithelial and HFL-1 lung fibroblast cells), exhibiting natural green fluorescence by laser excitation, detected either via confocal microscopy or flow cytometry [17]. Industrially supplied particles of either 5 nm or 100 nm diameter have been shown to be fluorescently active, with further research indicating that no discernible photobleaching occurs during analysis [150]. Additionally, the treatment of the lung cells with carboxylated nanodiamond particles did not induce significant cell death, apoptosis or altered protein expression [17]. Separate studies have also confirmed that nanodiamond particles were non-toxic to human kidney cells [150] and neuroblastoma cells [122], further exemplifying the notion that diamond-based nanoparticles are biocompatible and suitable for future biomedical applications.

1.4.3.4 Drug Delivery

In order to perform effectively as a drug delivery vehicle a material needs to be biocompatible, dispersible in aqueous solutions, scaleable and have the ability to bind with a range of therapeutic molecules. Nanodiamond has been shown to competently meet all of these requirements (figure 11) [2, 111, 151-153].

Recently published data has raised the possibility of using nanodiamond particles as delivery vehicles for cancer drugs [3]. The incidence of chemoresistant growths such as recurring mammary tumours and liver cancer have exemplified the need for an alternative, yet effective method of controlling this disease. One possible solution may be the administration of doxorubicin, an anthracycline antibiotic, bound to nanodiamond particles [3]. These were

tested in murine models of liver and mammary cancer. Results indicated significantly increased apoptosis and tumour growth inhibition in the nanodiamond bound drug study in comparison to conventional doxorubicin treatment, by intravenous injection. Furthermore the *in vivo* ND-administration of the drug decreased its toxicity compared to the conventional delivery method. It is therefore apparent that the nanodiamond bound drug conjugate could have increased efficacy whilst decreasing the severe side effects of the drug, the most serious of which are heart attacks. Earlier research has also confirmed these findings [22].

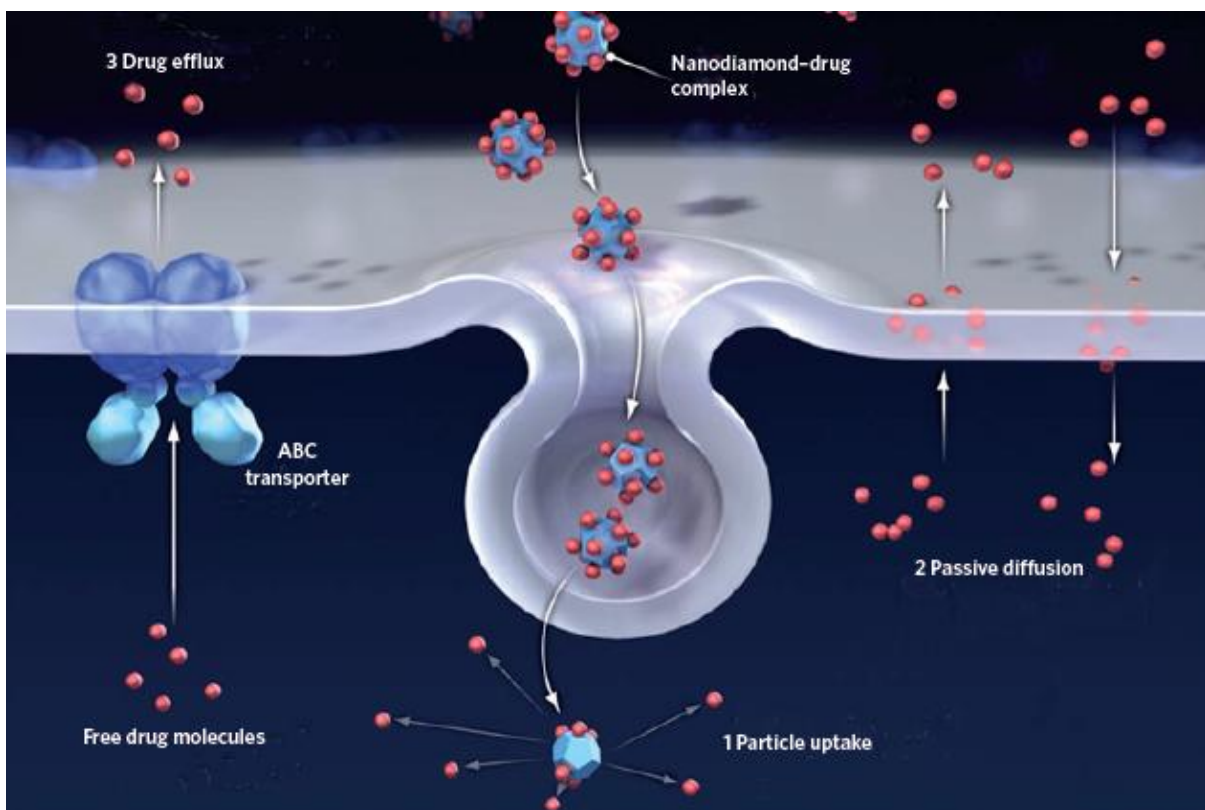


Figure 11: Proposed mechanism of ND-Drug complexes. (1) Endocytosis of ND-drug complex. (2) Diffusion of drug molecules across the cell membrane. (3) As required, excess free drug molecules are allowed to diffuse out of the cell via ABC transporter proteins, whereas ND-drug complexes remain within the cell to deliver a steady therapeutic dose of the drug [24].

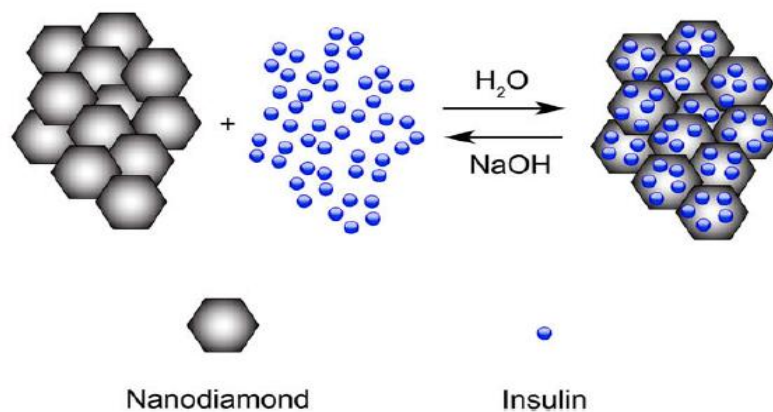


Figure 12: Schematic illustration depicting insulin adsorption to ND particles in water and desorption in the presence of sodium hydroxide. Alkaline conditions alter the insulin surface charge characteristics, releasing them from the ND surface [2].

Nanodiamonds surface coated with polyethylenimine 800 (PEI 800) were also studied for the transport of nucleic acids. Plasmid transfection efficiency was shown to increase 70-fold using ND-PEI800 compared to PEI800 alone [152]. This conjugated ND was also more effective at delivering siRNA to silence gene expression than lipofectamine, which is a conventional delivery molecule. Furthermore, ND has been effective at delivering siRNA targeting cancers [111] and transporting molecules within acidic environments; commonly experienced within tumour growths [110].

Additionally, bovine insulin has been successfully bound, non-covalently, to diamond nanoparticles via electrostatic interactions (figure 12) [2]. This was confirmed by fourier transform infrared (FTIR) spectroscopy and zeta potential measurements. The conjugated nanodiamonds exhibited pH-dependent release of insulin in sodium hydroxide solution. Adsorption and desorption could also be imaged by transmission electron microscopy (TEM) and quantified by the degree of protein functionality (demonstrated by MTT and RT-PCR). Additional RT-PCR measurements indicated that the insulin remained inactive whilst bound

to the nanodiamond particles and its biological activity had been preserved following desorption, illustrating the viability of the technique [2].

1.4.3.5 Gene Delivery

The inherent lack of cytotoxicity of diamond nanoparticles, their robust physical properties, drug carrying capabilities [2] and potential to migrate across cell membranes [13, 14] enable them to be ideally suited as carrier vehicles. Although there are already a number of different methods which exist for the facilitation of nucleic material into nuclei (viruses, charged lipids and cationic materials) the extremely low cytotoxicity of diamond nanoparticles is an essential property to justify future *in vivo* research. The lack of patient confidence in virus-mediated gene therapy and possible related toxicity, immune and inflammatory issues [154] illustrates the excellent potential diamond nanoparticles could play in gene therapy.

It has been reported [13] that fenton-treated diamond nanoparticles could be successfully functionalised with thionine and used to treat HeLa cells within the culture medium. Thionine emits red fluorescence upon excitation at 598 nm, a unique characteristic which can be utilised to locate the position of thionine-bound objects. After 24 hours incubation in the nanoparticle enriched media, fluorescence microscopy illustrated the presence of the functionalised nanodiamond within the cell nuclei. Quantitative flow cytometry analysis indicated that cellular toxicity did not deviate from the control during incubation, confirming nanodiamond biocompatibility *in vivo*. Cell nuclei also demonstrated normal morphology, showing no signs of apoptosis.

Additional findings demonstrating the migration of plasmid-bound diamond nanoparticles into nuclei has also been mentioned [13]. The oxidised nanodiamond particles were functionalised with a triethylammonium salt onto which a plasmid incorporating GFP was

bound. It was demonstrated that the plasmid alone could not enter the cell or nucleus of its own accord. Upon migration into the cell nucleus the GFP gene was expressed and transcribed, proven by fluorescence microscopy (excitation at 488 nm) and Western blotting.

1.4.3.6 Intracellular Antioxidant System

Fenton treated detonation diamond displays large surface concentrations of hydroxyl groups which are able to support gold and platinum nanoparticles (diameter: 2 nm). Gold and platinum can trap organic radicals whilst possessing high peroxide catalytic activity, enabling them to act as antioxidants. The ability of diamond nanoparticles to cross the cellular membrane enables them to act as reactive oxygen species (ROS) quenchers when coupled with gold or platinum particles, thus reducing cellular oxidative stress. This was confirmed by a different study whereby levels of ROS were significantly reduced following administration of rotenone, a mitochondrial inhibitor, to Hep3B cells [14]. Interestingly, the degree of ROS decomposition was greater than that of the conventional antioxidant glutathione, with the most beneficial results being obtained from gold nanoparticles [14].

1.4.3.7 Influence upon cell attachment

The effect of ND substrates on the attachment and proliferation of primary murine neuronal cultures has also been studied [8]. It was established that that the addition of ND particles on glass, mechanically polished polycrystalline diamond (PCD), nanocrystalline diamond (NCD) and silicon (Si) promoted the attachment of primary murine neurons. Neuronal attachment was minimal on these same substrates if they were not coated with ND. Furthermore, ND-coated materials exhibited similar neural attachment and outgrowth as displayed on more conventional ECM-derived substrates such as laminin, and were capable

of supporting both neuron and glial cells. This suggests that ND based substrates may have future applications in the development of specialised neuronal growth surfaces.

To conclude, research conducted to date has shown the wide range of applications for which diamond nanoparticles appear to be suited. Its lack of toxicity enables it to be extremely suitable for biological research, having applications such as fluorescent labelling; vehicles for genes, drugs and antibodies; and adsorptive separation, purification and analysis of proteins [32]. The ability to graft functional molecules including enzymes and DNA onto nanodiamond surfaces also is particularly useful and is partly the reason why it is anticipated that nanodiamond will play an increasingly important role in future biological research.

1.5 Diamond-Like Carbon (DLC) as Biocoatings

Diamond-like carbon (DLC) is an amorphous form of carbon which is composed of a network of sp^3 and sp^2 hybridised carbon atoms. The ratio of these atoms within DLC is partly responsible for the properties of the deposited film. However, the concentration of hydrogen within DLC also influences its properties; the greater the concentration of hydrogen, the more ductile, or polymeric, the DLC becomes. It is these properties which can have an influence upon which type of DLC is required for a specific biological application and determines the different forms of DLC which are available (figure 13).

1.5.1 Different Forms of DLC

Many different categories of DLC have been reported. Any such film which has been produced can be grouped into one of three categories, dependent upon their hydrogen content and the percentage of sp^3 carbon.

1.5.1.1 Polymeric (Highly Hydrogenated) Amorphous Carbon (a-C:H)

DLCs (type a-C:H) which have a composition greater than 40 at% hydrogen are termed polymeric amorphous carbon. They have comparatively low hardness compared to the other forms of DLC listed below and are ductile. Both of these properties can be explained by the large quantity of randomly distributed hydrogen held in the DLC structure and the associated van der Waals forces which have a low binding energy [155].

1.5.1.2 Soft [(Hydrogenated a-C:H) and (Non-Hydrogenated a-C)] Amorphous Carbon

These amorphous carbon films have properties similar to that of graphite, with most (exceeding 90 at%) carbon atoms bound in sp^2 sites. The hardness of these DLCs can be less than 10 GPa. Such graphitic amorphous carbon coatings can be obtained through a variety of routes. These include carbon evaporation, low plasma density sputtering, plasma-assisted chemical vapour deposition (PACVD) at low plasma density or by the thermal decomposition of other forms of amorphous carbon [18, 156].

1.5.1.3 Hard (Hydrogenated a-C:H) Amorphous Carbon and Tetrahedral (ta-C) Carbon

When hydrogenated amorphous carbon (a-C:H) has a hydrogen content lower than 20 at% combined with a high sp^3/sp^2 ratio the hardness of the material can approach 50 GPa [155, 157]. Being produced by PACVD using hydrogen precursors, the manufactured films have a low friction coefficient.

Tetrahedral amorphous carbon (ta-C) films are mostly composed of sp^3 carbon sites, the proportion varying from 50% to 100%. These forms of DLC demonstrate the best tribological and mechanical properties of any DLC films [18]. Consequently, the hardness of ta-C is the

highest detected of any DLC; usually in the region of between 70-100 GPa which approaches that of diamond. Since ta-C is deposited as an amorphous carbon film, the surface is far smoother than coatings formed from polycrystalline diamond coatings. The interatomic bond energies are similar to those of bulk diamond, being higher than those in other DLC films.

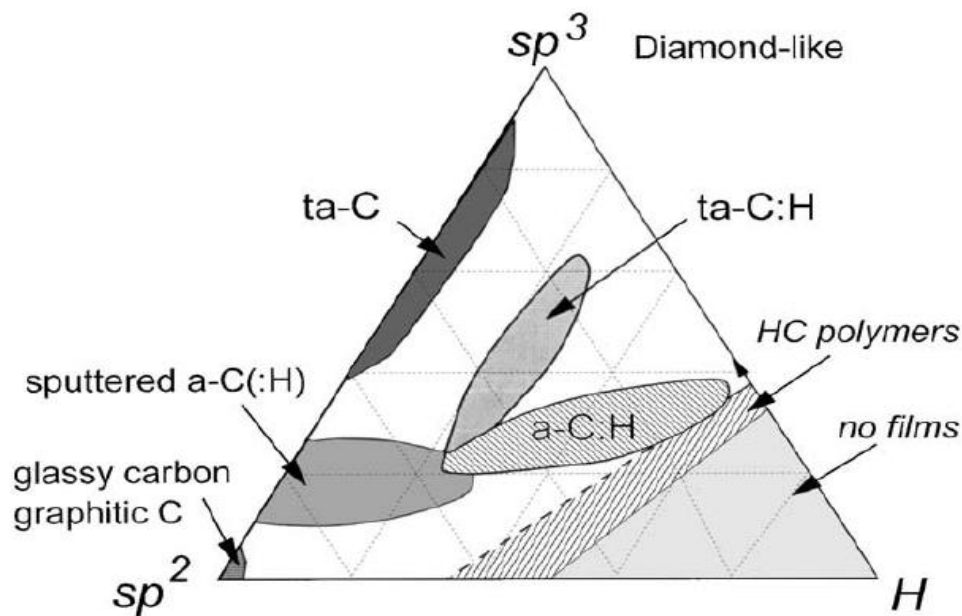


Figure 13: Phase diagram of diamond-like carbon materials [158].

This explains the material's high hardness and atomic packing density and the relative ease to which they can be doped [18]. It can therefore be seen that the concentration of hydrogen and the ratio of sp^3/sp^2 carbon atoms within the specific form of DLC reflects the properties of the material; those forms having a higher $sp^3:sp^2$ ratio (e.g. ta-C) demonstrating more diamond-like character. In contrast, DLC films which are mostly composed of sp^2 carbon atoms (e.g. hydrogenated a:C-H) display more graphitic character [51].

1.5.2 DLC Coating Methods

Numerous coating methods have been used for the growth of DLC films. These include cathodic arc spray, PLD, argon ion sputtering, ion beam deposition and PACVD. The production of DLC films by ion sputtering in a vacuum has been shown to promote a more

concentrated sp^3 carbon network, enhancing the diamond-like properties. The technique is also suitable for the coating of large surface areas [159]. However, the use of a vacuum can be prohibitive because of the expensive set-up costs involved and restrictions upon the shape or size of an object which can be treated. Therefore, various methods have been explored to perform DLC coating at atmospheric pressure to reduce the cost of producing effective coatings. One such technique involves electrochemical deposition using chemicals such as methanol and acetylene dissolved in ammonia. Naturally, this would involve the substrate being submerged in liquid which may not be preferable due to higher processing times associated with drying the finished products [160, 161].

However, PACVD is capable of producing a-C:H DLC films using a downstream acetylene, hydrogen and helium plasma. DLC produced via this method possesses an sp^3 carbon content of approximately 57 % [159]. PACVD is beneficial since it requires a processing temperature of only 200 °C and the procedure can be carried out at atmospheric pressure. This compares with typical diamond-coating temperatures of between 700 and 1000 °C, illustrating DLC deposited in this manner could be used as a coating on a far greater range of substrates [18].

Further developments have seen it possible to deposit tetrahedral amorphous carbon films at room temperature using either infrared ($\lambda = 1064$ nm) [162], or ultraviolet ($\lambda = 254$ nm) pulsed laser deposition [163], ion beam deposition [164] or magnetron sputtering [165]. The properties and structure of films manufactured by high ion energy deposition techniques (UV-PLD and ion beam deposition) can be controlled by the kinetic energy of the carbon species [18]. Furthermore, it has been shown in ion beam deposition that the incident angle of the kinetic carbon species plays an important role in the properties and structure of the DLC film produced. If the ion beam makes contact with the surface at an acute angle, the actual ion energy present on the developing film significantly decreases, favouring the development

of films with a higher sp^3 carbon content. Unfortunately this presents difficulties with the coating of three-dimensional products, where the incident angle of kinetic species will vary across the different faces of the specimen. Furthermore, elevating the discharge voltage in ion beam deposited DLC films has been shown to increase the nanohardness whilst reducing the elastic modulus, in line with increasing sp^3 content.

The deposition of DLC films by low ion energy deposition methods (IR-PLD) at room temperature in a reactive gas flow reactor was shown to be influenced by the reactive gas flow concentration (acetylene, C_2H_2 or nitrogen, N_2). The presence of nitrogen in the gas flow caused graphitisation to occur, whereas high concentrations of C_2H_2 favoured the production of a-C:H films; a more desirable outcome [166-169].

These low temperature routes for the deposition of DLC have been cited as a more amenable method for the chemical stabilisation or functionalisation-preparation of delicate materials for applications such as biosensing and microelectromechanical systems (MEMS) [65]. These applications will be covered in greater detail within sections 1.5.4.4. and 1.5.4.5 respectively.

1.5.3 Properties of DLC

The desirable properties associated with DLC films have ensured its popularity as a biological coating. DLC possesses exceptional hardness, chemical inertness and high dielectric strength. Additional important properties also include its biocompatibility, both *in vitro* and *in vivo*, low surface roughness, infrared transparency and high electrical resistivity and refractive index [51, 159, 170, 171].

Additional useful properties of DLC which have been widely exploited are its low friction coefficient and excellent wear and abrasion resistance [16]. These characteristics can be

explained by the production of a friction-induced interfacial transfer layer when the film is stressed. Formed in the uppermost region of a DLC coating, this layer possesses a much lower shear strength than the remaining DLC and exhibits the low friction and high wear resistance for which DLC is renowned. It is thought that friction-induced annealing, caused by the strain and thermal energy generated during sliding, is responsible for the transfer layer's existence [172, 173].

1.5.4 DLC Applications and its use as a Biocoating

DLC enjoys widespread and varied applications throughout industry, being integrated into everyday objects to enhance their usability and properties. However, it was not until the mid to late 1990s that industrial applications for the use of DLC started to accelerate. At first used in magnetic storage media, films were also applied to laser barcode scanners and eyeglasses to improve abrasion resistance [174]. In 1998 Gillette developed Mach 3 razor blades, which were manufactured with a DLC coating to improve the blade's quality and performance [16].

Additionally, DLC has also been utilised as an internal coating in polyethylene terephthalate (PET) bottles used in the drinks industry [175, 176]. The plastic has been used as an alternative to glass and metal beverage containers since 1976 due it being lightweight, less fragile, transparent and resealable. Unfortunately, however, PET is slightly permeable to gases, which transpires to any contents slowly oxidising as time progresses. At the same time, carbon dioxide can escape, leading to any carbonated drinks losing their fizz. These problems can be remedied through the application of a 50 nm DLC coating to the interior of any PET bottle preventing gaseous exchange. The technology, developed in Japan by Kirin in association with Mitsubishi Heavy Industries, is capable of coating up to 18,000 PET containers every hour, equating to 5 bottles per second. Such a rapid coating procedure is made possible through atmospheric plasma deposition. A colourless coating is deposited by

increasing the band gap of the DLC to above 2.5 eV from the conventional value of 1.5 eV, which is aesthetically more desirable for the drinks industry. It was found that oxygen permeability could be reduced by a 23-fold magnitude in 1.5 litre bottles [177]. As such, these coatings are currently applied to PET bottles in Japan containing beverages with a relatively short shelf-life, such as tea, increasing their longevity.

DLC has also been applied as a biocoating in a variety of circumstances as illustrated by the following examples.

1.5.4.1 Orthodontic Wires

Orthodontic wires are used in dentistry for the correction of dental abnormalities, and are held in place by brackets. They are primarily used to close gaps between a patient's adjacent teeth and are normally manufactured from stainless steel or nickel-titanium alloys [12]. It has been suggested that a decreased level of friction between the bracket and wire might reduce the treatment period and further improve their anchorage control [178]. The use of plasma immersion ion implantation techniques has been used before in an effort to improve the mechanical properties and friction characteristics of orthodontic wires [179], but clinical trials have shown the technique offers no discernible difference over untreated wires [180]. In contrast, DLC-coated (film thickness: 0.5 μm) orthodontic wires and brackets have been shown to reduce frictional resistance compared to those with untreated surfaces [12]. In a separate study DLC was also shown to protect against the breakdown of nickel in corrosive environments, which could prove useful for patients who suffer from nickel allergies [181]. Nanoindentation tests also confirmed that DLC-coated wires have a lower elastic modulus than as-received wires, providing greater flexibility [12].

1.5.4.2 Vascular Stents

Patients suffering from arterial lesions or occlusions are recommended, in severe cases, to undergo endovascular surgical treatment. This minimally invasive technique involves the widening of the affected vessel, which is usually achieved by the placement of a stent. Nitinol (nickel-titanium alloy) stents having properties such as high elasticity, biocompatibility, high radial strength and ‘shape-memory’ have become the clinical option for the treatment of arterial occlusive disease [182-184].

However, in-stent restenosis caused by neointimal hyperplasia, remains problematic [183]. Within 6 months of the operation occurring the incidence rate of restenosis varies between 20 – 40% for patients fitted with nitinol stents, illustrating the need for alternative materials possessing greater biocompatibility. Enhanced proliferative tissue response may be due to a contact allergy with nickel or the release of metallic ions from the stents. Subsequent *in vivo* studies of DLC-coated nitinol stents implanted into canine iliac arteries demonstrated a significant reduction in neointimal hyperplasia compared to the untreated stent [48]. In contrast, when polyethylene-glycol (PEG) was grafted on to the DLC-coated stent surface a significant increase in hyperplasia was observed due to greater fibroblast proliferation. This contrasts with a previous *in vitro* study which concluded that the addition of PEG enhanced uncoated, and DLC coated, nitinol stents [11]. These results illustrate that the use of DLC, however, is a useful addition when applied as a coating for stents, contributing to the structure’s biocompatibility.

1.5.4.3 Artificial Joint Implants

Patients requiring a total hip replacement are usually fitted with an artificial joint, the shaft of which is constructed from either metallic alloys or ceramics whilst the acetabular cup is

manufactured from ultra high molecular weight polyethylene (UHMEPE) [27]. Its use for conventional joint replacements has been widespread due to its chemical properties, price and biocompatibility [49].

However, UHMWPE does not exhibit long-term *in vivo* wear resistance, limiting the longevity of hip arthroplasties [49]. On average the UHMWPE component wears at an approximate rate of 0.1 mm per year, ejecting 100 million wear particles into the joint space every day [185]. These particulates have been shown to initiate a cascade of adverse tissue responses ultimately cumulating in osteolysis and possible component-loosening [185]. Alternative polymers, such as highly crosslinked polyethylene (HXLPE) have also been suggested [186, 187]. Although the volume of wear particles would be greatly reduced if a hip implant was produced from such a material, the size of the debris would also be smaller, which may have the potential to stimulate biological activity and lead to increased osteolytic reactions. Research has therefore focused on the application of a corrosion and wear resistant layer, such as DLC, to artificial implants to prolong their life [27, 49]. Depositing a 700 nm hydrogenated DLC film by PACVD was found to be effective in significantly increasing the wear resistance of UHMWPE [49]. Similarly, if the metallic femoral head is coated with DLC, the wear rate of uncoated UHMWPE was also found to greatly decrease. This can be attributed to the lower friction experienced between DLC and UHMWPE, compared to a metallic-UHMWPE interface. The fact that DLC prevents the metallic surface undergoing oxidation, further reducing the friction coefficient, is also noteworthy [27].

On a separate note, DLC coatings, especially when doped with phosphorous or silicon [188, 189], can improve the haemocompatibility of implanted devices. This is thought to occur through the reduced incidence of inflammatory cytokines which would normally accompany the release of metal ions or wear particles [190]. This haemocompatibility could also be

explained by the decrease in contact angle measurement between normal DLC (approximately 63°) compared to 5 at% phosphorous doped DLC (P:DLC) (approximately 17°). The lower the contact angle is, the lower the interfacial surface tension which could induce fewer conformational changes in any adsorbed plasma proteins [188].

1.5.4.4 Biosensors and Bioarrays

The chemical functionalisation of diamond and diamond-like carbon, which has been discussed previously (section 1.1), yields some interesting opportunities with respect to the creation of biosensors and bioarrays. These applications require materials that are robust and stable with DLC being shown to be most suitable. DLC is known to surpass the usability of alternative materials for these purposes, such as glass, silicon and gold. The signal to noise ratio is 40 % higher on oligonucleotide arrays prepared on DLC compared to gold, due to the lower background fluorescence of amorphous carbon and a greater number of hybridisation sites [50].

Numerous alkene-containing molecules have been grafted via UV irradiation to amorphous carbon substrates to provide a number of different chemical surface functionalities including 1-dodecene, trifluoroacetic acid protected 10-aminodec-1-ene (TFAAD), 10-N-Boc-amido--dec-1-ene and 9-decene-1-ol [32, 50, 63-65, 98, 191-193]. Of these, TFAAD has seen the most widespread use in research for the manufacture of biosensors upon carbon substrates.

Once the TFAAD molecule has been deprotected it produces a free amine group onto which biomolecules can be attached (figure 14). Amine groups are preferable for bioconjugation since they do not readily oxidise, negating the requirement for any immediate preparation and purification or unnecessary wastage [50]. It has also been shown that DLC substrates can withstand the conditions necessary for *in situ* oligonucleotide synthesis. They are also able to

better withstand high temperatures, basic conditions or repeated hybridisation cycles compared to arrays produced on glass [194]. It has been further demonstrated that oligonucleotide arrays produced on DLC are just as stable as those manufactured on diamond thin films [50, 65].

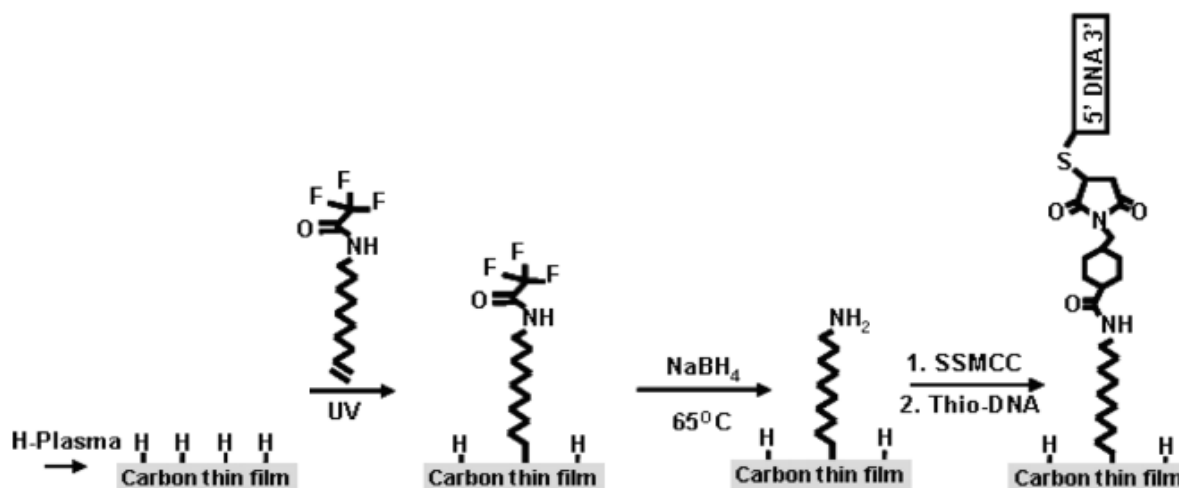


Figure 14: Functionalisation of amorphous carbon to produce a TFAAD-modified surface. Subsequent deprotection yields an amine-modified surface which is reacted with a sulfo-(succinimidyl 4-[N-maleimidomethyl]cyclohexane-1-carboxylate) [SSMCC] linker and thio-DNA to produce a covalently bonded DNA adduct on the amorphous carbon surface [65].

1.5.4.5 Cell Growth Patterning

Cell types including fibroblasts, osteoblasts, retinal pericytes, endothelial cells and glial-like cell lines have been successfully cultured on DLC *in vitro* [9, 10, 101, 188, 195, 196]. Emerging research has illustrated that the characteristics of DLC may be altered to either favour or deter the attachment and proliferation of certain cell types. This alteration, usually through the doping of elements, demonstrates the varying degree to which different cells can be bound to its surface. Rat primary cortical neurones display poor adhesion on pure DLC, instead preferring to form free-floating neurospheres [170]. In contrast, the doping of DLC with between 5 - 20 % phosphorous (P:DLC) causes the surface to be highly hydrophilic,

encouraging the adsorption of poly-L-lysine, a typical coating for neuronal cultures [51]. Consequently, neurones cultured on P:DLC form a coherent monolayer [170]. The production of a patterned grid of P:DLC upon a DLC substrate favoured the growth of the cells solely along the phosphate-doped lines (figure 15) [51].

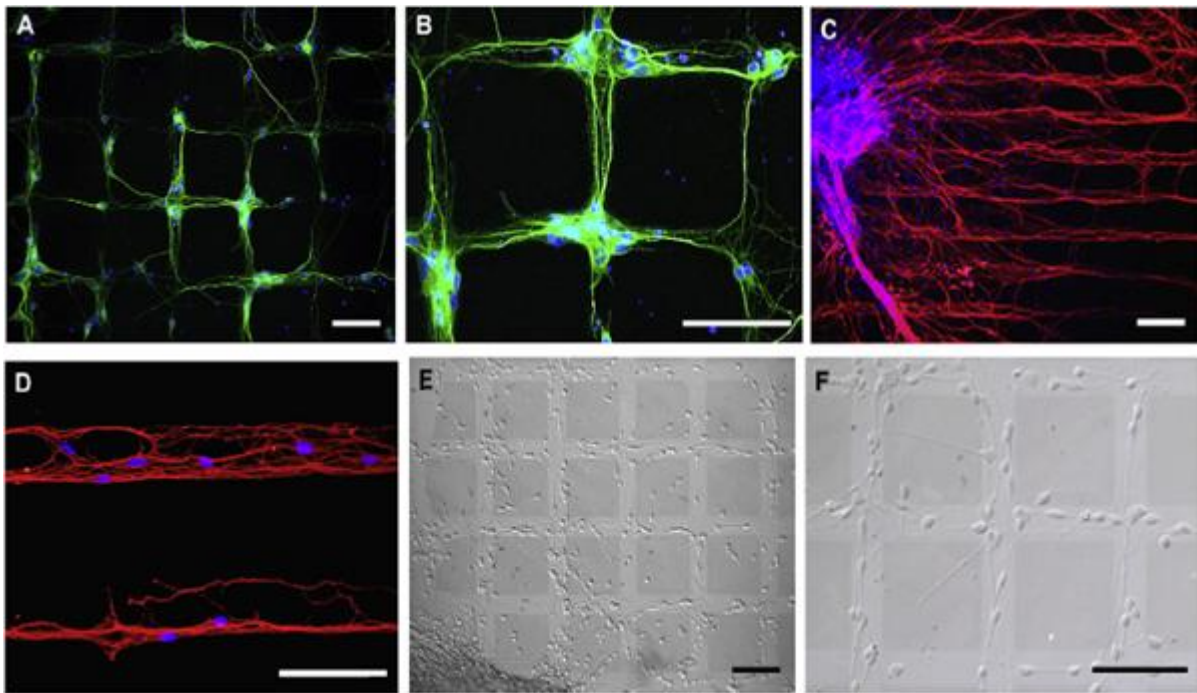


Figure 15: Preferential patterning of cortical neurons (A,B: Green=MAP2 Stain, Blue=DAPI), dorsal root ganglion cells (C,D: Red = β -III tubulin, Blue=DAPI) and human neural progenitors (E,F) cultured along P:DLC tracks. Scale bar: 90 μ m [51].

It has been mentioned that the doping of phosphorous on DLC improves its haemocompatibility, possibly due to a reduction in the surface contact angle. Experimentation has shown that DLC possesses a contact angle of between 60 - 70°, whilst that of P:DLC has been recorded between 16 - 33°, the value depending on the production process and the doping level [170, 188]. The decreased contact angle produces a film with a lower interfacial surface tension, which leads to any absorbed plasma proteins undergoing

fewer conformational changes and less denaturing [197]. With respect to neuronal cell cultures, poly-L-lysine has been observed to have greater adsorption on P:DLC and O:DLC compared to DLC, enhancing neuron attachment and growth [170]. Such findings are of interest to the future development of MEM systems.

Microcontact printing has also proved effective in directing the growth of neuronal cells on DLC [101]. Polydimethylsiloxane stamps were coated with protein solutions of laminin, an extracellular matrix protein which enhances the attachment and proliferation of neurons. These proteins were applied to diamond surfaces upon which murine cortical neurons were cultured for up to 8 days. Neuronal outgrowth occurred primarily along the laminin lines deposited by the stamps with cells failing to attach to any other untreated areas of the diamond surface. No degradation of the pattern occurred over the length of the experiment illustrating that the stamping technique is a relatively simple yet effective method of controlling directional cell growth.

Further work has analysed the possibility that patterned DLC surfaces could stimulate the differentiation of stem cells [198]. Surface topographical cues were found to encourage the production of neuronal-like cells from human bone marrow derived mesenchymal stem cells (hBM-MSCs) *in vitro* [198]. The deposition of DLC ridges of width 40 μm were shown to enhance the production of brain-derived nerve factor (BDNF). This factor in turn stimulated the production of nitric oxide (NO) which modulates neuronal function and controls neural differentiation. These mechanically stimulated elongated cells displayed long neurite-like protrusions and increased levels of NO comparable to differentiating neuronal cells. They also tested positive for the neuronal cell marker TUJ1 through immunofluorescence. Similarly, nanocrystalline diamond films (section 1.3) exert a similar neuronal differentiating effect upon stem cells [53, 81].

To conclude, over the past couple of decades, the use and application of DLC in biological research has continued to expand. Its recognition as a non-toxic material, which can be deposited at room temperature on to a wide variety of substrates to confer its desirable tribological properties, has seen use in numerous situations. The ability to graft functional groups and molecules on to its surface is of great importance for the production of biosensors, a field which will undoubtedly become of much greater importance in the years to come as technology advances. Meanwhile, DLC's advantageous properties remain desirable to the production of neurological-related devices also, ranging from nerve guidance conduits (NGCs) to brain computer interfaces (BCIs) and neuronal growth surfaces.

1.6 Carbon Nanoparticles

Carbon nanodots (C-dots) (figure 17) form a recently discovered group of nanocarbons which are composed of quasispherical nanoparticles of diameters less than 10 nm [199]. They were first discovered, accidentally, through the purification of single-walled carbon nanotubes (SWCNTs) and have attracted widespread research appeal due to their beneficial properties [200]. Importantly, C-dots are naturally carboxylated when produced by arc-discharge methods, enabling them to be water soluble and also capable of undergoing functionalisation with numerous organic/biological species. Their well-defined morphology, nanoscale dimensions, ability for chemical functionalisation and a variety of inexpensive and simple production routes provides a promising platform from which C-dots can hope to compete with other carbon forms to contribute to future biological research. Of notable interest is the possible replacement of quantum dots (QDs) with C-dots. QDs are metal-based nanometre sized particles which are frequently used as fluorescent probes for *in vitro* imaging. However, QDs are often produced from inherently toxic compounds (e.g. cadmium and selenium) which makes their translation to *in vivo* and clinical use rather problematic. Given this

disadvantage, important research has been directed into more biocompatible alternatives such as nanodiamond and carbon nanoparticles.

Synthesis of C-dots can occur through either top-down or bottom-up production methods [199]. In top-down procedures, such as arc discharge [200], laser ablation [201] and electrochemical oxidation [202], C-dots are formed from the disintegration of a larger carbon structure. Meanwhile, bottom-up methods, consisting of thermal [203], microwave [204] or supported synthetic [203, 205] approaches, produce C-dots from molecular precursors such as citric acid [206] and glucose [207] the structures of which are displayed in figure 16.

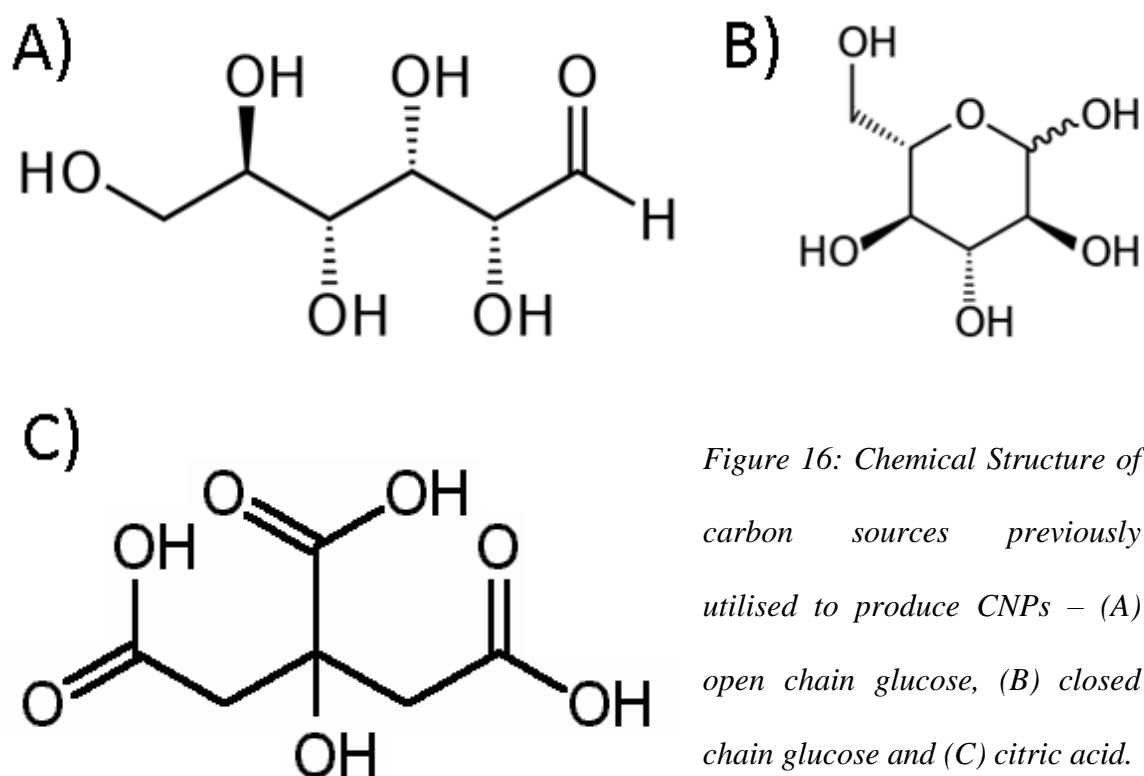


Figure 16: Chemical Structure of carbon sources previously utilised to produce CNPs – (A) open chain glucose, (B) closed chain glucose and (C) citric acid.

Once C-dots have been isolated they are normally oxidised using nitric acid and then purified further through the use of a separation technique, namely centrifugation or electrophoresis [199]. Further details on the production methods of C-dots have been published by Baker *et al* [199].

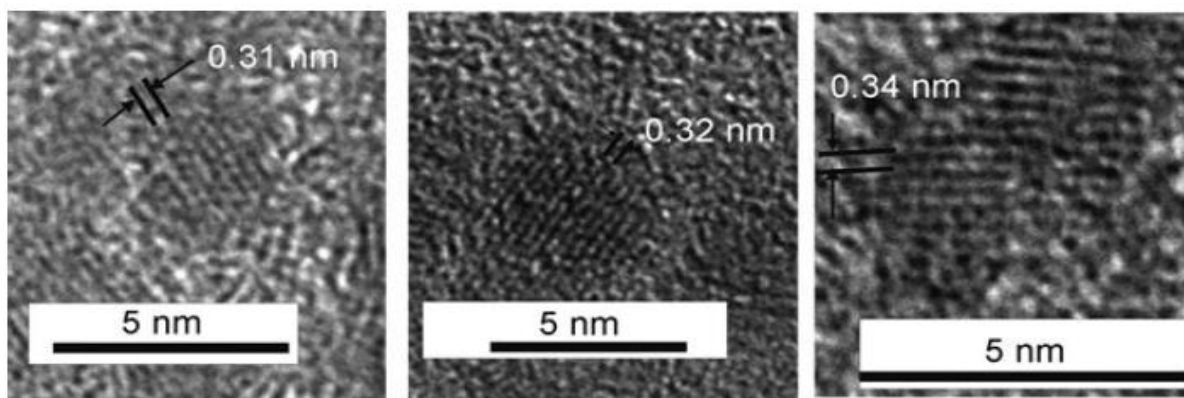


Figure 17: High-resolution transmission electron microscope (HRTEM) images of C-Dots [208].

In contrast to nanodiamond particles, C-dots exhibit more graphitic character, due to the greater abundance of sp^2 hybridised carbon atoms in their structure. They have a relatively high oxygen content, earning them the alternative name of carbogenic nanodots [199]. It is interesting to note that the production method used to synthesise C-dots can determine the particle's physical and chemical properties. Manufacture of C-dots through thermal reactions of citrate salts produces particles of approximately 7 nm diameter, with X-ray diffraction (XRD) analysis illustrating a disordered carbon structure [203], whereas C-dots synthesised by the electrochemical oxidation of multi-walled carbon nanotubes (MWCNTs) were largely graphitic, having sp^2 and disordered carbon structures [208].

1.6.1 Applications of Carbon Nanoparticles

One of the main research areas of C-dots focuses on understanding and taking advantage of their innate photoluminescence abilities. C-dots generally absorb radiation in the UV spectrum, possessing excitation edges at between 270-280 nm [208, 209]. Moreover, the precise emission wavelength is known to depend upon the intensity and wavelength of the excitation source. At present it is unclear how this phenomenon occurs but it may be due to

the different emissive ‘traps’ on the surface of the C-dots [199]. However, it is these photoluminescence properties which make C-dots such an interesting proposition for future biological applications, as mentioned below:

1.6.1.1 *In Vitro* Bioimaging

C-dots have become an attractive alternative to biologically hazardous quantum dots such as cadmium selenide (CdSe) for bioimaging purposes. Dependent upon the fabrication method used to produce the C-dots, surface passivation may be required to produce luminescence [199]. This is true in the case of laser-ablation synthesised C-dots, where it is speculated that surface energy traps present on the C-dots emit photon energy following passivation. This passivation occurs through the adsorption of an organic moiety such as 4,7,10-trioxa-1,13-tridecanediamine (TTDDA) or poly-ethylene glycol (PEG) [210, 211] which serves to increase C-dot absorbance/fluorescence in between 350 – 550 nm.

Initial biological experiments on the use of C-dots focused on the imaging of cancer cells. C-dots which have been passivated using poly(propionyl-ethylenimine-*co*-ethylenimine) [PPEI-EI] have been used to successfully image human breast cancer MCF-7 cells using two-photon luminescence microscopy [201]. After incubation with the C-dots in media for 2 hours at 37°C, and subsequent washing, it was discovered the cell membrane and cytoplasm exhibited vivid green luminescence, although the C-dots failed to migrate into the nuclei. It is assumed that the particles were taken up by the cells through endocytosis, although at cooler temperatures (4°C) uptake of the nanodots did not occur.

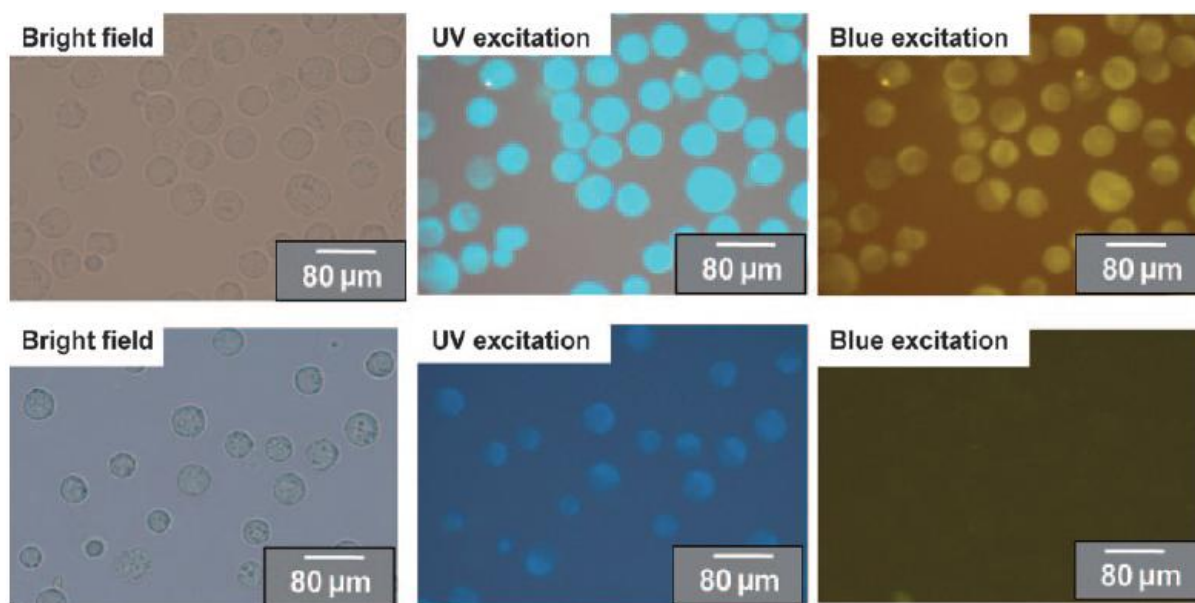


Figure 18: C-Dot labelling of EAC cells. The bottom row depicts control images where no C-dots were used. Cells were washed and observed under bright field, UV and blue light excitations [56].

Cellular imaging using C-dots produced from candle soot has also been achieved using Ehrlich ascites carcinoma cells (EACs) (figure 18) [56]. The C-dots were produced from the chemically homogenised soot of a burnt candle, producing 2 – 6 nm particles. These C-dots were incubated with the cells for 30 minutes, after which the remaining C-dots were separated from the solution by centrifugation, and subsequently imaged without the need for surface passivation to occur. The imaging of cells as diverse as *E. Coli* bacteria and murine progenitor cells has been achieved in a similar fashion [205]. All these samples exhibited fluorescence which was photostable and not affected by photobleaching. It is further anticipated in the future that C-dots could pass through the nuclear membrane of cells through their attachment to facilitator proteins or peptides, allowing for the effect of C-dots on nuclei to be effectively researched [199].

1.6.1.2 *In Vivo* Biolabelling

In order for a biological label to be suitable for *in vivo* use, it should be non-toxic, biocompatible, photostable and sufficiently intense so to be easily detected. Murine models have been procured to test the *in vivo* efficacy and efficiency of C-dots and zinc sulphide (ZnS) doped C-dots passivated with PEG [212]. The particles were injected subcutaneously, intravenously and intradermally into female DBA/1 mice (figure 19) and excited through light of wavelengths 470 nm and 545 nm. Following intradermal delivery, both forms of C-dots were found to migrate to the axillary lymph nodes, although the doped C-dots travelled at a slower rate, possibly as a result of PEG functionalisation restricting interaction with the murine lymph cells. After intravenous application the C-dots were seen to migrate around the body of the mice via the bloodstream. Photoluminescence was detected from the bladder with C-dot emission from the urine being recorded 3 hours post injection. After four hours the organs were harvested, with the C-dots having accumulated in the kidney, with significantly fewer present in the liver of the mice. Although this route followed the standard urine pathway it was expected that greater numbers of nanoparticles would be located in the liver, in accordance with previous studies on *in vivo* nanoparticle behaviour [213]. However, this discrepancy may have been the result of the PEG functionalisation, which decreased the protein affinity of the C-dots, causing them to pass relatively quickly to the kidney for excretion.

It is therefore possible to conclude that C-dots hold a great deal of promise for biological research. The wide availability of inexpensive renewable resources for their production (lignocellulosic biomass wastes being one example [199]) and a number of synthetic manufacturing methods enables them to be produced with relative ease. The advantages attributed to C-dots including their biocompatibility, colloidal stability, chemical stability and

photobleaching resistance illustrates their potential in future optical imaging applications. As research in the field continues to progress and mature the importance and influence attributed to C-dots will undoubtedly increase. Although numerous studies have been conducted in the area of C-dots there are many carbon sources that have yet to be analysed for their effectiveness as luminescent *in vitro* and *in vivo* labels.

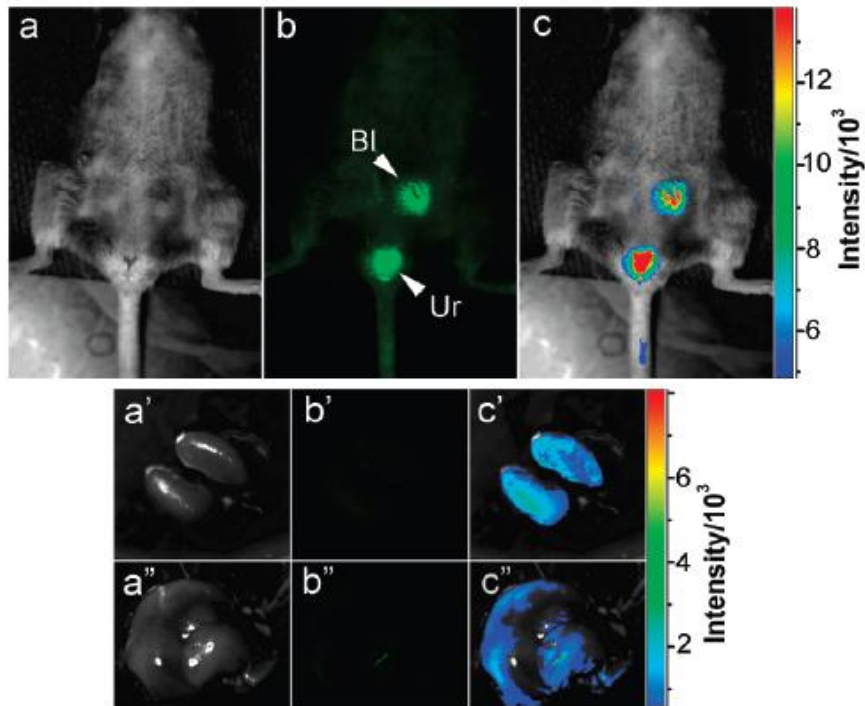


Figure 19: Intravenous injection of C-Dots: (A) bright field, (B) as-detected fluorescence (Bl = bladder; Ur = urine), and (C) colour-coded images. The same order is used for the images of the dissected kidneys (A' – C') and the liver (A'' – C'') [57].

1.7 Conclusion

This chapter has reviewed that diamond and its related materials are particularly well suited to be used in biological research. The ability of such materials to be deposited as thin films (DLC, UNCD) enables them to be utilised as surface coatings, either in their pure, original

form (DLC and ND coatings on artificial prostheses to enhance biocompatibility and reduce wear) or functionalised using a range of different chemical and biological moieties to give rise to biosensors and MEMs.

The existence of diamond materials in a nanoparticulate form allows for greater applications, particularly in the field of bioimaging where fluorescent NDs and C-dots hold particular advantages (lack of cytotoxicity and photobleaching) over existing conventional imaging alternatives. Furthermore, the possible use of diamond and carbon nanoparticles as drug and gene carriers can hold particular significance for the future of drug administration, allowing for less invasive, more effective therapies. The benefits associated with neural cell culture and neurological devices which could be constructed using DLC or ND related materials is also of importance due to the relatively minor amount of research conducted in the area to date.

In conclusion, the different forms of diamond discussed each possess unique advantages which are currently opening the door to a range of intriguing possibilities in biomedical research. In the future it is anticipated that the role which diamond has secured as a biomaterial will only increase in importance as the wide range of applications for which it is suited become more recognised.

1.8 Thesis Aims and Objectives

The literature review has illustrated the versatility of diamond and nanodiamond coatings and the numerous applications for which they are suited. It is envisaged that due to the beneficial properties of diamond-like carbon and nanodiamond they would provide an ideal basis for the creation of a neurocompatible culture substrate. Additionally, although extensive research has already been undertaken within the bioimaging field with respect to carbon nanoparticles

certain carbon sources, such as alginate, have yet to be tested for their suitability. Furthermore, the creation of CNPs from multiple carbon sources has yet to be tested. To overcome these issues, the aims of the thesis were as follows:

- 1) The production of separate amine-functionalised diamond-like carbon and amine-nanodiamond substrates that are resistant to degradation within liquid environments.
- 2) Analysis of the culture of neuronal cell lines and primary neural cells upon the diamond-based substrates and assess the substrate cytotoxicity and ability to act as a neural growth surface.
- 3) Microwave synthesis of carbon nanoparticles from various carbohydrate sources, including alginate, and the creation of nanoparticles sourced from multiple saccharides (i.e. glucose & sucrose).
- 4) Analysis of the fluorescent capabilities of the synthesised carbon nanoparticles and their effectiveness for bioimaging applications.

Chapter Two: Materials and Methods

2.1 Diamond-Like Carbon (DLC) Study Methods

The methods listed within this section concern the studies conducted upon diamond-like carbon (DLC) surfaces, where all materials were sourced from Sigma-Aldrich unless otherwise stated.

2.1.1 Preparation of Diamond-Like Carbon Substrates - Pulsed Laser Deposition of DLC

In order to coat glass cover slips and silicon wafers with a thin coating of diamond like carbon a pulsed laser deposition (PLD) method was utilised. The output of an argon fluoride (ArF) excimer laser (Lambda Physik, Compex 201) with a laser wavelength of 193 nm was focused (lens focal length: 20 cm, angle of incidence: 45°) on a graphite disc target (Poco Graphite Inc, DFP-3-2 grade) in a stainless steel chamber maintained at a pressure of approximately 10^{-6} Torr. The graphite was ablated using a laser fluence of 12 J / cm². A thin film of DLC of approximate 20 nm thickness was achieved with 1200 laser shots at a target-substrate distance of 5 cm at 20°C. The DLC-treated cover slips were then sonicated in methanol for 15 minutes and then washed in distilled water overnight. Once complete, the cover slips were allowed to air-dry before being stored in an air tight container in preparation for use.

2.1.2 SEM Electron Beam Deposition of DLC

Silicon wafers were cleaned in methanol before being cut into approximately 1 cm² pieces. These were then attached to SEM sample aluminium stubs (Agar, Stansted, UK) using

adhesive carbon discs and were loaded within the sample chamber of an Inspect F scanning electron microscope (SEM). The wafers were then bombarded with the electron beam of the SEM which used an accelerating voltage of 10 V and a spot size of 3 for approximately 80 minutes per piece of silicon wafer.

2.1.3 Synthesis of Trifluoroacetic acid protected-10-Aminodec-1-ene (TFAAD)

In a method previously published by Sun *et al* [65] TFAAD was synthesised by first adding 50.0 g of 10-undecenoyl chloride (97 % purity, 0.25 mol) to a sufficient quantity of tetrahexylammonium bromide (99 % purity, Acros, 0.6 mmol) in an ice bath. A solution of sodium azide (99.5 % purity) (16.6 g in 50 ml of distilled water) was then gradually added to the mixture within the ice bath and agitated using a magnetic stirrer. Once the reaction was complete, the organic fraction was separated, washed twice with an excess of distilled water, dried over MgSO₄ for 24 hours and filtered. Afterwards an excess of trifluoroacetic acid was added to the acyl azide, allowing for the reflux reaction to take place under nitrogen for 6 hours. The organic mixture was washed afterwards with a saturated solution of sodium bicarbonate, collected and subsequently dried using magnesium sulphate over 24 hours. TFAAD was finally acquired through purification by vacuum distillation with the product being stored at 4°C.

2.1.4 Determination of optimal UV radiation exposure for TFAAD grafting

DLC-coated glass cover slips were placed on top of a quartz slide and several drops of liquid TFAAD polymer were applied to the surface. A further quartz slide was then positioned on top to seal the cover slips within. Optimal UV irradiation time was then determined using a 6W shortwave (254 nm) UV fluorescent lamp (model UVG-54, UVP, Upland, Ca., USA) which was positioned 7.5 cm above the quartz slides. The samples were exposed to radiation

for varying time points up to 120 hours with the extent of surface functionalisation being analysed by x-ray photoelectron spectroscopy (XPS).

2.1.5 Preparation of 10-amino-dec-1-ene Functionalised DLC

The DLC coated glass cover slips were placed on top of a quartz slide, upon which a sufficient volume of liquid TFAAD polymer was applied to cover the samples. A further quartz slide was placed on top to seal the DLC samples and were exposed to UV radiation ($\lambda = 254$ nm) emitted by a 500 W continuous mode E10180 Hamamatsu Super Quiet Xenon Lamp (Hamamatsu, Japan) for periods of between 5 minutes and 4 hours to allow photochemical attachment to occur. Any excess TFAAD was removed and the protected amine bound DLC was deprotected in acidified methanol (0.36 M HCl in methanol) at 65°C over 24 hours. The samples were cleaned in pure methanol, dried with a nitrogen gas supply, and stored in sterile containers until required.

2.1.6 Preparation of 2-(10-Undecen-1-yl)-1,3-dioxolane

The protected aldehyde molecule was prepared using a similar method publicised by Lockett *et al* [50]. Briefly, 1.0 g of 10-undecenal (5.9 mmol, 95% purity) was dissolved in 10.0 ml of anhydrous toluene, before a catalytic volume of p-toluenesulphonic acid (95 mg, 0.5 mmol, 98.5% purity) was dissolved in 1.0 ml of anhydrous toluene and added to the 10-undecenal mixture. Additionally, 1.2 mol equivalent of anhydrous ethylene glycol (0.4 ml, 99.8% purity) was added and the reaction allowed to reflux for 1 hour. The resulting product was then purified by vacuum distillation, producing 0.82 g of protected aldehyde (3.9 mmol, 82% yield).

2.1.7 Preparation of 10-undecenal Functionalised DLC

The DLC coated glass cover slips were placed on top of a quartz slide, upon which several drops of 2-(10-Undecen-1-yl)-1,3-dioxolane were applied to cover the samples. A further quartz slide was placed on top to seal the DLC coated glass cover slips and were exposed to UV radiation ($\lambda = 254$ nm) emitted by a 500 W continuous mode E10180 Hamamatsu Super Quiet Xenon Lamp (Hamamatsu, Japan) for periods of between 5 – 20 minutes to allow photochemical attachment to occur. Any excess 2-(10-Undecen-1-yl)-1,3-dioxolane was removed and the samples cleaned in pure methanol. Finally, the functionalised cover slips were deprotected overnight (24 hours) within 1.5 M hydrochloric acid solution at 60°C to produce 10-undecenal terminated surfaces. They were then dried with a nitrogen gas supply, and stored in sterile containers until required for cell culture.

2.1.8 NG108-15 Cell Culture Medium

In order to prepare a suitable medium, firstly 61.25 ml of media was removed from a 500 ml flask of high glucose DMEM (Biosera, Boussens, France). The remaining DMEM was then supplemented with 50 ml foetal calf serum (FCS), 5 ml L-Glutamine (100×), 5 ml penicillin-streptomycin (10,000 $\mu\text{g} / \text{ml}$, 10,000 $\mu\text{g} / \text{ml}$) and 1.25 ml amphotericin (Fungizone™). This provided 500 ml of cDMEM. Sterility of the media was monitored by transferring 3 ml of the cDMEM to a universal which was stored in an incubator at 37°C and 5 % CO₂ for 72 hours. The media was examined under an optical microscope for signs of infection. The remaining medium was stored at 4°C and replaced at least every 6 weeks.

2.1.9 NG108-15 Neuroblastoma Cell Culture

NG108-15 cells were selected due to being a readily available neuronal based cell line originally produced from a hybrid of mouse neuroblastoma and rat glioma cells. They were

supplied by the American Type Culture Collection (ATCC) and were cultured in completed 10 % FCS high glucose Dulbecco's Modified Eagle's Medium (DMEM), which was produced as detailed within section 2.1.8. Cells were resurrected at passage 9 and cultured until at least passage 11 before being used for experimental work. All cells were discarded upon reaching passage 20.

The NG108-15s were seeded upon either glass, diamond-like carbon (DLC), 10-amino-dec-1-ene functionalised diamond-like carbon (DLC-Amine), 10-undecenal functionalised DLC (DLC-aldehyde) and poly-L-lysine coated tissue culture plastic (PL) at a density of 1×10^5 cells / ml within completed (serum-free) high glucose Dulbecco's Modified Eagle's Medium (DMEM). Serum starvation encourages the neuronal differentiation of the cells thus increasing neuritic outgrowth. The presence of serum within DMEM causes the prominence of neurites to be greatly reduced, yet cell growth and proliferation significantly accelerates. Alternative cell growth substrates were utilised within the nanodiamond experiments (section 2.2.8). The cells were cultured for either 1, 2, 5 or 7 days at 37°C and 5% CO₂ after which they were analysed by phalloidin-FITC & DAPI staining and 3-(4,5-dimethylthiazol-2-yl)-2,5-diphenyltetrazolium bromide (MTT) cell viability assay.

2.1.10 NG108-15 Cell Passaging

NG108-15 cells were cultured within T75 flasks until they were 75 % confluent, at which point they were passaged. In order to dislodge the cells, the flask was tapped sharply several times without the addition of trypsin. The flask was then checked under a light microscope to ensure the cells had separated. Afterwards the DMEM was removed and centrifuged within a universal tube at 1000 rpm for 5 minutes to form a cell pellet. The supernatant was then discarded and new DMEM was added to re-suspend the cells, which were plated in new T75 flasks at a concentration of 5000 cells / ml, with the media being replaced every 2 - 3 days.

2.1.11 Resurrecting Cells

Until required, cells were frozen down and stored in liquid nitrogen. Approximately 100,000 cells were stored within each 3 ml vial, which also contained dimethyl sulphoxide (DMSO). Vials were defrosted in a water bath over a period of several minutes at 37°C. Upon thawing, the contents of the vial were deposited in a 25 ml universal tube, additionally supplemented with 10 ml of cDMEM and centrifuged at 1000 rpm for 5 minutes. Once a cell pellet had formed the supernatant was disposed of and the pellet was resuspended in 20 ml of fresh cDMEM. The resulting cell suspension was then split between two T75 flasks (Costar, High Wycombe, UK). Cells were passaged two further times before being utilised for experimental procedures.

2.1.12 Primary Schwann Cell Isolation and Culture

The isolation was performed as previously reported by Kaewkhaw *et al* [214]. Animals were sacrificed in compliance with the Animals (Scientific Procedures) Act 1986. Briefly, sciatic nerves were removed from male Wistar rats (2 - 3 months) and the connective tissue was subsequently discarded. These nerves were teased and cut into 2 - 3 mm segments and incubated with 0.05 % (w/v) collagenase at 37°C for 1 hour. This cell suspension was then filtered through a 40 µm Falcon filter (Becton Dickinson, USA) and centrifuged at 400 g for 5 minutes. The resultant cell pellet was washed with DMEM (10 % (v/v) FCS) and resuspended in Schwann-cell growth medium containing DMEM D-valine (PAA, UK), 2 mM glutamine, 10 % (v/v) FCS, 1 % (v/v) N2 supplement (Gibco BRL, UK), 20 µg / ml bovine pituitary extract, 5 µM forskolin, 100 U / ml penicillin, 100 µg / ml streptomycin and 0.25 µg / ml amphotericin B. The Schwann cell suspension was plated within 35 mm Petri dishes which had been previously coated with 0.5 mg poly-L-lysine / 7 µg laminin. The

cultures were maintained at 37°C with 5 % CO₂. Cells were cultured until passage 2 before being used in experimental work and were discarded once reaching passage 6.

Primary Schwann cells were cultured on glass, diamond-like carbon (DLC), 10-amino-dec-1-ene functionalised diamond-like carbon (DLC-Amine) and poly-L-lysine treated tissue culture plastic (PL). To create a PL surface, a sufficient volume of poly-L-lysine solution (0.1% w/v) was deposited within one of the wells on a 6 well plate to wet the surface. The well was allowed to air dry and was washed 3 times with phosphate buffered saline (PBS). Cells were then deposited on the surfaces for 21 days at an initial seeding density of 10,000 cells / ml, with media being changed every 3 – 4 days. Once three weeks had elapsed the media was removed and the cells were washed twice with PBS. Cells were then fixed for 15 minutes with sufficient pre-warmed formaldehyde solution (3.7 % v/v) to submerge them. The formaldehyde was finally removed, the samples washed 3 times with PBS and stored at 4°C in PBS until required for immunostaining.

2.1.13 Fluorescence Cell Staining

After each time point the DMEM was removed from the NG108-15 cells, which were then washed once with PBS. To each well 500 µl of formalin (3.7 % v/v in PBS) was then applied for 15 minutes after which the cells were washed twice more with PBS. Cells were then permeabilised with Triton™ X-100 (0.1 % v/v in PBS) for 5 minutes, before being washed two further times with PBS. A stock solution of phalloidin-FITC was produced at a concentration of 0.5 mg / ml in dimethyl sulphoxide (DMSO). Staining was performed using this stock solution (1 % v/v in PBS) and DAPI (0.1 % v/v in PBS) for 1 hour at room temperature before the cells were rinsed three more times with PBS and were then visualised using an epifluorescence microscope (Axon ImageXpress, Molecular Devices, USA).

Phalloidin-FITC images, which stained the actin, were taken at $\lambda_{\text{ex}} = 490 \text{ nm} / \lambda_{\text{em}} = 525 \text{ nm}$, whilst DAPI images, which stained the nuclei, were taken at $\lambda_{\text{ex}} = 358 \text{ nm} / \lambda_{\text{em}} = 461 \text{ nm}$.

2.1.14 3-(4,5-dimethylthiazol-2-yl)-2,5-diphenyltetrazolium bromide (MTT) Cell Viability Assay

Cellular growth and proliferation from a fixed cell seeding density can be indirectly assessed by the MTT assay. This yellow, water-soluble tetrazolium dye can be reduced by mitochondria (figure 20) within viable cells to create a purple formazan product that is insoluble in aqueous solutions. The quantity of product formed can then be determined by spectrophotometry once it has been dissolved in a solvent such as acidified isopropanol [215].

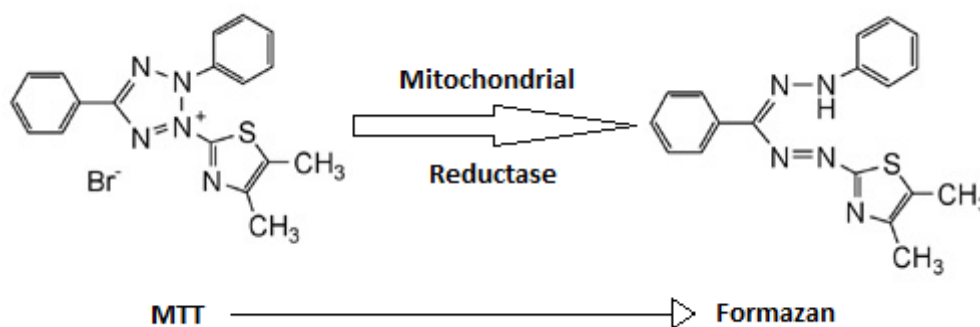


Figure 20: The conversion of MTT to formazan in live cells by mitochondrial reductase.

Cells were cultured at a density of 10,000 cells / ml within 24 well plates (Costar) over periods of 1, 2, 5 and 7 days. At each time point the DMEM was removed from the wells which were to be analysed, and the cells were washed once with PBS. MTT solution (thiazolyl blue tetrazolium bromide [98 % purity] was dissolved in PBS to produce a concentration of 0.5 mg / ml) was then added to each well of cells, and incubated at 37°C and 5 % CO₂ for 45 minutes. The MTT solution was then removed after which 300 μ l acidified isopropanol (125 μ l hydrochloric acid (10 M) added to 100 ml isopropanol) was added to

each well and allowed to stand for 2 minutes. The resulting solution was then transferred in triplicate 100 μ l volumes to a 96 well plate where the optical density was measured using a plate reader set at a wavelength of 540 nm, referenced at 630 nm.

2.1.15 Contact Angle Measurements

The contact angle of a surface describes its wettability, which indicates the degree of wetting between a solid and liquid interface. Smaller contact angles, namely those below 90° characterise hydrophilic surfaces which are highly wettable, whereas large contact angles above 90° correspond to hydrophobic surfaces which have restricted wettability. Although not true in every case, hydrophilic surfaces are generally more amenable to cell culture than hydrophobic ones.

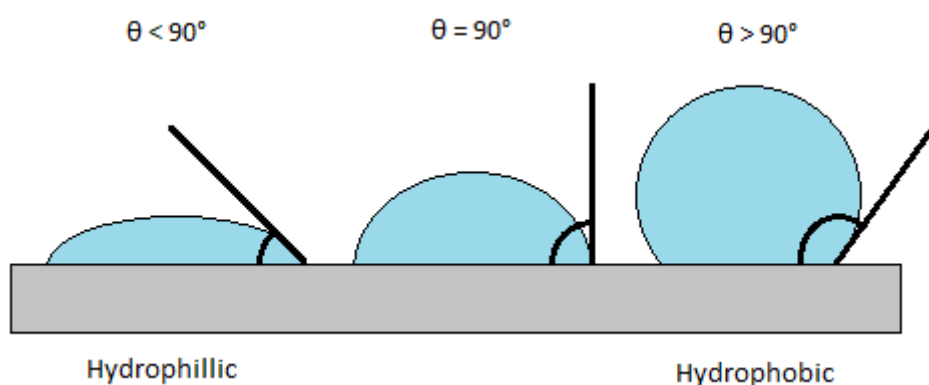


Figure 21: Illustration of the different contact angles (θ) that may form from sessile water droplets on smooth homogeneous surfaces that may be either hydrophilic or hydrophobic.

To ascertain the water contact angle of DLC, glass, DLC-Amine and DLC-Aldehyde one drop of distilled water (approximately 10 μ l) was deposited on the surfaces (figure 21). The contact angle was measured by the angle formed by the baseline and the tangent to the drop profile at the three-phase point (solid surface: water droplet: air) using a Rame-Hart contact

angle goniometer at a temperature of 21°C. A mean value was attained from twenty measurements for each sample surface [216].

2.1.16 X-Ray Photoelectron Spectroscopy (XPS)

In order to characterise the nanodiamond-derived and pure acrylic acid surfaces, x-ray photoelectron spectroscopy and water contact angle measurements were performed. First utilised in the 1950's by Kai Siegbahn [217] and further developed in the 1960's by his research group [218], XPS is recognised as one of the foremost surface characterisation techniques which can provide precise quantitative surface chemical compositions [219].

During XPS experimentation the sample surface is irradiated by an x-ray source which causes the ejection of core and valence electrons, also known as photoelectrons from the uppermost 10 nm of the surface. These photoelectrons have energies that are unique to each element and sensitive to the chemical state of the element concerned. The intensities of the photoelectrons detected are also proportional to the elemental composition of the surface from which they originated, allowing for a precise and detailed chemical composition to be ascertained [219].

Glass, DLC, DLC-Aldehyde and DLC-Amine samples were analysed by a Kratos AXIS Ultra DLD instrument. Spectra were collated utilising a monochromatised Al K α X-ray source (1486.6 eV) which operated at a power of 150 W, whilst charging of the sample during irradiation was reduced by an internal flood gun. Each sample was analysed using an emission angle which was normal to the sample surface. Survey spectra were collated at a pass energy of 160 eV with a 1 eV step width, whilst high resolution C (1s) core level spectra were collected at 20 eV pass energy using a 0.1 eV step width.

Atomic concentrations of each element were deduced by calculating the relevant integral peak intensities whilst applying the sensitivity factors supplied by Kratos (the XPS

instrument manufacturer). In all spectra a linear background was used. Whilst random error associated with elemental quantification approximated 1 - 2% of the absolute atomic percentage values [220], the systematic error was estimated to be in the region of 5 – 10 % [221].

Data processing, analysis and charge correction was carried out using CasaXPS (ver.2.3.12 Casa Software Ltd.) whereby the C (1s) component of the aliphatic hydrocarbon was set to 285.0 eV as an energy reference.

2.1.17 Scanning Electron Microscopy (SEM)

The amine functionalised DLC samples were first sputter coated with gold, using an Emscope SC500 sputter coater, prior to SEM analysis to form a conductive surface. The samples were imaged using an Inspect F scanning electron microscope (SEM). An accelerating voltage of 10 V and a spot size of 3 were utilised.

2.2 Nanodiamond (ND) Study Methods

The methods listed within this section concern the studies conducted upon nanodiamond (ND) surfaces, where all materials were sourced from Sigma-Aldrich unless otherwise stated.

2.2.1 Fenton Treated Nanodiamond Synthesis

It is possible to carboxylate detonation nanodiamond, therefore leading to functional homogeneity of the surface, without the use of high temperatures. The first method involves adding 1 g of detonation nanodiamond to 50 ml of distilled water (dH₂O). The next step involves adding 20 g of ferrous salt, such as iron sulphate (FeSO₄.7H₂O) until dissolution within the slurry, to act as a source of Fe²⁺ ions. Approximately 30 ml of concentrated

sulphuric acid (H_2SO_4) was then added, alongside 30 ml of hydrogen peroxide (H_2O_2), added dropwise, whilst noting the evolution of carbon dioxide to signify the beginning of the Fenton reaction. This step was performed in a fume hood. Due to the highly exothermic nature of the reaction the mixture was sonicated in an ice bath at 1 - 5°C for 5 hours. After one and two hours had passed, additional quantities of H_2SO_4 and H_2O_2 were added as the suspension first turned green and later to yellow as the reaction progressed. Once complete, the slurry was allowed to cool and the nanodiamond was purified and extracted through five centrifugation cycles with distilled water to remove the excess acid. The treated nanodiamonds were stored in distilled water until required.

2.2.2 Non-Fenton Treated Nanodiamond Synthesis

In the second method of carboxylation, approximately 0.5 g of detonation nanodiamond was deposited in a 9:1 (v/v) mixture of concentrated sulphuric acid (H_2SO_4) and nitric acid (HNO_3). This was heated to 75°C for 3 days, after which the nanodiamond was filtered out and treated within a 0.1M aqueous solution of sodium hydroxide (NaOH) at 90°C for 2 hours. Finally the nanodiamond was filtered again before being deposited in a 0.1M aqueous solution of hydrochloric acid (HCl) for 2 hours. The carboxylated nanodiamonds were then filtered and rinsed thoroughly with distilled water, and centrifuged 5 times at 6000 rpm to remove any residual chemicals. The nanodiamonds were stored in distilled water until required.

2.2.3 Synthesis of Trifluoroacetic acid protected-10-Aminodec-1-ene (TFAAD)

Please see section 2.1.3 for details.

2.2.4 Preparation of 10-Amino dec-1-ene functionalised Nanodiamond

Nanodiamond particles were hydrogenated by exposure to a hydrogen plasma flow for a total duration of ten minutes (2 cycles of 5 minutes, followed by 2 minutes in cold H₂ flow under a pressure of 100 Torr, power: 0.8 MW power and 500 sccm H₂ total gas flow). The hydrogenated nanodiamond was then spread across a quartz slide, on top of which several drops of TFAAD were applied. A further quartz slide was then positioned on top and exposed to UV radiation ($\lambda = 254$ nm) under a UV lamp (500 W continuous mode E10180 Hamamatsu Super Quiet Xenon Lamp (Hamamatsu, Japan)) for 4 hours to allow photochemical attachment to occur. The slide was then inverted and placed under the UV lamp a second time to functionalise the underside of the particles which had previously been in the shadow of UV radiation. Once complete, the excess TFAAD was then removed and the protected amine bound nanodiamond was deprotected in acidified methanol (0.36 M HCl in methanol) at 65°C over a period of 24 hours. The treated nanodiamond was then purified by 5 centrifugation cycles at 6000 rpm in distilled water. The treated nanodiamonds were stored in distilled water until required.

2.2.5 Plasma Polymerisation of Acrylic Acid

Plasma polymerisation involves the formation of a polymeric film from a vaporised monomer under the influence of a plasma. Due to the presence of an electric field, the monomer undergoes ionisation once introduced into an evacuated reaction chamber, causing the generation of free radicals, photons, electrons and ions in both elevated and ground states. Additionally, excitation of the monomer creates reactive sites on the surface which act as future positions for the covalent attachment of additional species, thus furthering the process and ensuring the film gradually grows in thickness with time.

The plasma polymerisation apparatus (figure 22) consisted of similar equipment utilised by Beck *et al* [222]. Briefly, a glass reactor (50 cm length) which had stainless steel flanges was surrounded by an external copper coil electrode. This electrode coupled the 13.56 MHz radiofrequency generator, used in continuous wave mode, to the plasma. Once a sample was loaded within the glass reactor to be coated, the reactor interior was evacuated with a rotary vacuum pump, utilising a liquid nitrogen cold trap, to achieve a base pressure which approximated 10^{-3} mbar. A monomeric pressure of approximately 2×10^{-2} mbar was achieved through manipulation of the monomer needle valve. The deposition of acrylic acid occurred for 10 minutes using a power of 10 W, with samples immediately transferred for cell culture or nanodiamond attachment afterwards.

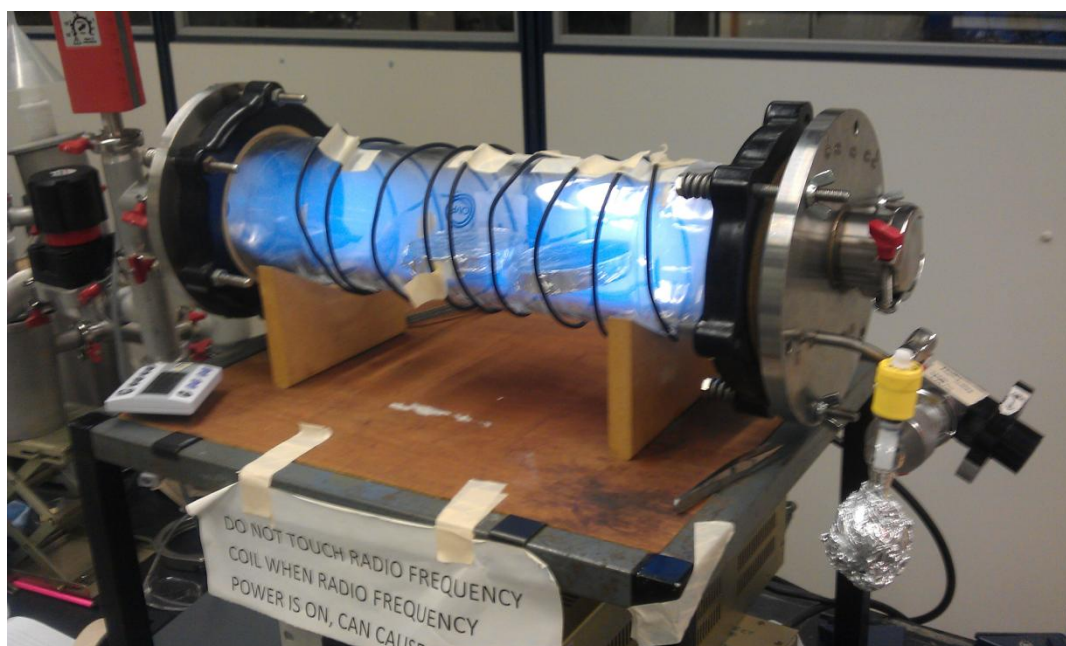


Figure 22: Glass cover slips being coated with ppAA within the glass vacuum vessel.

2.2.6 Production of AAND Substrates

Glass cover slips which had previously been coated with ppAA were placed within a plastic bijou container, ppAA side facing upwards. The amine-functionalised ND, suspended in

distilled water to form a slurry (5 mg / ml), was added dropwise to the cover slips until all were submerged. The samples were then ultrasonicated for 15 minutes, after which the cover slips were dipped in distilled water to remove any excess ND particles and allowed to air dry. AAND substrates were placed within 24 well plates and washed two times with PBS before being utilised for cell culture.

2.2.7 NG108-15 Cell Culture Medium

Please see section 2.1.8 for details.

2.2.8 NG108-15 Neuroblastoma Cell Culture

Please see section 2.1.9 for further details.

The NG108-15s were seeded upon either glass, acrylic acid coated glass (ppAA), 10-amino-dec-1-ene functionalised nanodiamond treated glass (Glass-ND), 10-amino-dec-1-ene functionalised nanodiamond treated acrylic acid coated glass (AAND), acrylic acid plasma polymer coated glass treated with hydrogenated nanodiamond (AAND-H) or poly-L-lysine coated tissue culture plastic (PL) at a density of 1×10^5 cells / ml within completed (serum-free) high glucose Dulbecco's Modified Eagle's Medium (DMEM). Further experiments utilising NG108-15 cells were conducted upon diamond-like carbon substrates (section 2.1.9).

2.2.9 Primary Schwann Cell Isolation and Culture

Please see section 2.1.12 for further details.

The primary Schwann cells were seeded upon either glass, acrylic acid coated glass (ppAA), 10-amino-dec-1-ene functionalised nanodiamond treated glass (Glass-ND), 10-amino-dec-1-ene functionalised nanodiamond treated acrylic acid coated glass (AAND), acrylic acid

plasma polymer coated glass treated with hydrogenated nanodiamond (AAND-H) or poly-L-lysine coated tissue culture plastic (PL) at a density of 1×10^5 cells / ml within Schwann cell growth medium. Further experiments utilising NG108-15 cells were conducted upon diamond-like carbon substrates (section 2.1.12)

2.2.10 NG108-15 Neuroblastoma and Primary Schwann cell Co-Culture

Primary Schwann cells were first cultured upon glass, ppAA, AAND and PL surfaces for 17 days at an initial seeding density of 10,000 cells/ml in the presence of Schwann cell growth medium. By day 17 additional NG108-15 cells were applied to each surface at a concentration of 5000 cells/ml and allowed to grow for a further 4 days in the presence of serum-free cDMEM. Twenty-one days post primary Schwann cell seeding all cells were fixed in formalin and visualised by immunofluorescence for the presence of β -tubulin III (staining NG108-15 cells) or S100- β (staining Schwann cells).

2.2.11 Primary Dorsal Root Ganglion (DRG) isolation and dissociation

The spinal column was removed from 2 - 3 months old male Wistar rats (figure 23) and divided along the sagittal plane exposing the dorsal root ganglia (DRGs). These DRGs were removed, trimmed and incubated (37 °C) within 2 ml F12 media (Biosera) (10 % (v/v) collagenase IV) for 1 hour. The medium was removed and a further 2ml F12 media (10 % (v/v) collagenase IV) was added for 45 minutes. This was also removed and the DRGs washed with fresh F12 media. The DRGs were then incubated (37 °C) within 2 ml F12 (Biosera) (10 % (v/v) trypsin) for 30 minutes, after which 1 ml F12 (Biosera) (50 % (v/v) FCS) was added to arrest digestion. This solution was then removed and the DRGs were washed several times with F12 medium. The DRGs then underwent mechanical dissociation with the cell suspension being passed through a 70 μ m filter. This suspension was centrifuged at 300 g for 5 minutes, after which all but 500 μ l was removed; the remainder being used to

resuspend the cell pellet, which was centrifuged at 500 g for 10 minutes. All unwanted cell debris was discarded with the neurons being resuspended in modified Bottenstein and Sato (BS) medium (50 ml medium: 0.005 g bovine serum albumin (BSA)(Sigma) and 500 µl N2 supplement (Invitrogen) added to 49.5 ml F12 medium). Neurons were cultured upon AAND, glass and PL surfaces, at first being allowed to adhere for 2 hours before additional volumes of BS medium were added, supplemented with 77 ng / ml neuronal growth factor (NGF). Neurons were cultured for three weeks before being visualised by immunofluorescence.

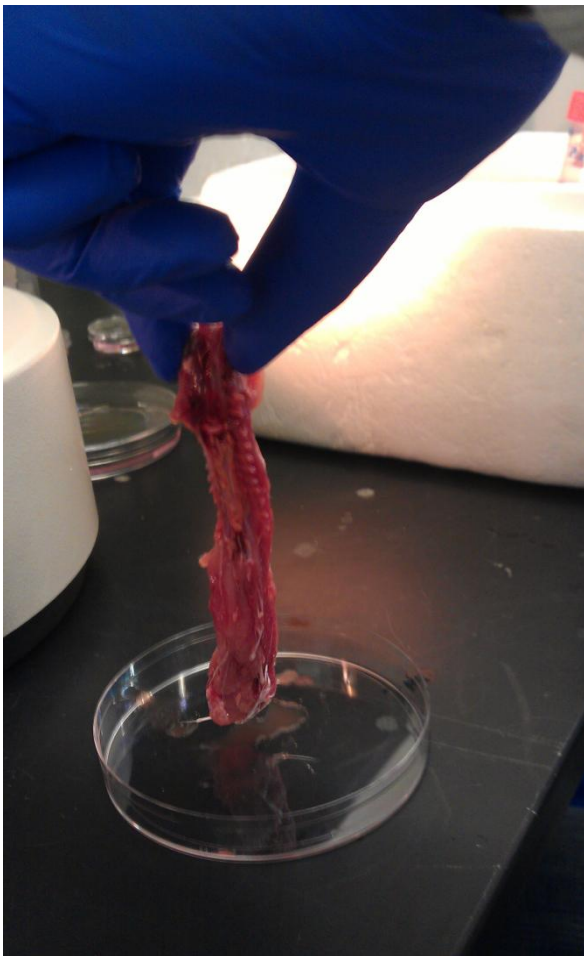


Figure 23: Rat spine taken from a male Wistar rat from which dorsal root ganglions (DRGs) were isolated.

2.2.12 Fluorescence Cell Staining

Please see section 2.1.3 for details.

2.2.13 Dissociated DRG (dDRG) Immunofluorescence Cell Staining

After 21 days culture the BS media was removed from the dissociated DRGs (dDRGs) which were then washed once with PBS. The cells were then fixed with formalin (3.7 % v/v) for 15 minutes, washed with PBS, and permeabilised with 0.1 % Triton™ X-100 for 20 minutes at 4°C. Cells were washed again with PBS and then blocked with 3 % (w/v) BSA for 60 minutes at 4°C. This was followed by incubation with polyclonal rabbit anti-S100 β (1:250) (Dako) and monoclonal mouse anti-GFAP (1:250) (Lab Vision, UK) diluted in 1 % (w/v) BSA overnight at 4°C. Once complete, the cells were washed twice with PBS to remove non-specific binding and incubated with Texas Red/FITC conjugated secondary anti-mouse/rabbit IgG antibody (1:100 in 1 % (w/v) BSA) (Vector Labs, USA) for 90 minutes at room temperature. This was then removed and the samples were washed a further 2 times with PBS before being further stained with DAPI (1:1000 in PBS) for ten minutes at room temperature. The samples were washed two final times with PBS before being imaged using an epifluorescence microscope (Axon ImageXpress, Molecular Devices, USA). S100 β -FITC images, which stained the cytoplasm of the dDRGs, were taken at $\lambda_{\text{ex}} = 490 \text{ nm} / \lambda_{\text{em}} = 525 \text{ nm}$, whilst GFAP-Texas Red images, which stained the cell cytoskeleton of the dDRGs, were taken at $\lambda_{\text{ex}} = 596 \text{ nm} / \lambda_{\text{em}} = 615 \text{ nm}$, whilst DAPI images, which stained the nuclei, were taken at $\lambda_{\text{ex}} = 358 \text{ nm} / \lambda_{\text{em}} = 461 \text{ nm}$.

2.2.14 Transmission Electron Microscopy (TEM)

TEM is an imaging technique where electrons are transmitted directly through an ultrathin specimen of approximate thickness of 100 nm or less. It is the interaction of these electrons with the specimen, mounted on a metal grid, which, when focused, forms a black and white two-dimensional image. Typically magnifications of between 500 to 500,000 times can be attained [223]. The nanodiamond samples were suspended in distilled water and agitated to

form a slurry. One drop from each sample was deposited upon a separate copper TEM grid (diameter 3.05 mm) (Agar, UK) and allowed to air dry. This step was repeated two further times to deposit sufficient diamond nanoparticles upon the grids. Samples were analysed with an accelerating voltage of 120 kV using an FEI Tecnai G2 Spirit and FEI Tecnai TF20 FEGTEM.

2.2.15 Atomic Force Microscopy (AFM)

Atomic force microscopy, developed by Binnig *et al* in 1986 [224], can produce high resolution images of surface topography. The imaging technique utilises the interaction of attractive and repulsive forces between a cantilever and a sample to probe the chemical and physical characteristics of surfaces. Variations in friction, composition, adhesion and viscoelastic properties of a surface can all be differentiated with nanoscale resolution. Furthermore, detailed 3-dimensional images of a surface can be attained to precisely illustrate surface topography [225].

In this study, ppAA and AAND samples were analysed by a Veeco Instruments Nanoscope IV multimode AFM in tapping mode with images being analysed by WsXM software (ver 3.1, Nanotec Electronica S.L.)

2.2.16 Contact Angle Measurements

Please see section 2.1.15 for details.

2.2.17 X-Ray Photoelectron Spectroscopy (XPS)

Please see section 2.1.16 for further details

Nanodiamond samples which had been previously stored, as a slurry, in distilled water were agitated, before one drop from each sample was deposited on separate glass cover slips (13

mm diameter). The water from each droplet was allowed to air-dry, leaving a dried layer of ND powder upon each cover slip. This process was repeated 4 more times to build up a ND layer of appropriate thickness for XPS analysis.

2.3 Carbon Nanoparticles Methods

The methods listed within this section concern the studies conducted with carbon nanoparticles (CNPs), where all materials were sourced from Sigma-Aldrich unless otherwise stated.

2.3.1 Carbon Nanoparticle (CNP) Production

In order to produce CNPs the following list of carbon sources were added to glycerol and several drops of distilled water and magnetically stirred until dissolution, forming the following molar solutions:

- 1M and 2.5M glucose
- 1M alginate
- 0.5M sucrose
- 1M glucose & 0.5M alginate
- 0.5M sucrose & 0.5M alginate

Each sample was separately heated in a conventional microwave oven at 800 W for 5 minutes. The appearance of the solution was observed to change as microwave pyrolysis progressed. The colourless solution first began to change to yellow, with the solution becoming darker and more viscous to form a brown hue before finally turning black. This highly viscous product was allowed to stand at room temperature to cool, before 40 ml of distilled water was added and stirred to form a CNP solution. Each solution was centrifuged 5

times at 4000 rpm to purify the CNPs produced which were then dispersed in distilled water (pH = 7) until ready for use.

2.3.2 Primary Human Dermal Fibroblast Isolation

Human dermal fibroblasts were isolated from split thickness skin grafts (STSGs) which were obtained following abdominoplasties and breast reduction surgeries with the informed consent of the patients involved. The skin was accepted for research use by a protocol approved by the Ethical Committee of the Northern General Hospital Trust, Sheffield, UK. Briefly, using previously published methods [226, 227], STSGs were cut into 0.5 cm² pieces and incubated for 24 hours in 0.1 % (v/v) trypsin. The dermal layer was separated using a pair of forceps. Any keratinocytes on the papillary surface of the dermis were scraped away using a scalpel blade. The dermis was then washed in PBS and finely minced with a scalpel blade before being incubated overnight in 0.5 % collagenase A at 37°C. The next day the solution was centrifuged at 1000 rpm for 5 minutes and the supernatant was discarded, with the cell pellet resuspended in 4 ml of cDMEM. These fibroblasts were firstly cultured in a T25 flask (Costar, High Wycombe, UK) with subsequent passages cultured in T75 flasks and utilised between passages 4 and 12.

2.3.3 Cell Passaging

To passage cells, firstly the culture medium was removed from the T75 flask and the cells washed twice with PBS to remove any residual media proteins which would otherwise inhibit the action of trypsin. Afterwards, 1.5 ml of trypsin was added and the flask was incubated at 37°C for 5 minutes. Following this, the flask was gently tapped several times to aid in the detachment of the cells, the progress of which was checked using a light microscope. Once successful, 10 ml of cDMEM was added to arrest the trypsin, with the contents of the flask transferred to a universal tube and centrifuged at 1000 rpm for 5 minutes. The supernatant

was then discarded and the cell pellet which formed was resuspended in 10 ml of fresh, pre-warmed (37°C) cDMEM. A cell count was then carried out and the corresponding volume of medium containing 250,000 cells was added to a new T75 flask containing 15 ml of cDMEM. The flask was gently swirled to evenly circulate the cells throughout the medium, with new passages occurring as cells reached 75 % confluence. The media was changed every 3 - 4 days.

2.3.4 RN22 Cell Culture

RN22 cells are a Schwannoma cell line derived from rats which were sourced from the European Collection of Cell Cultures (ECACC). They are an easily obtainable source of Schwann cell like cells for *in vitro* experiments and were used between passage 9 and 20. The cells were cultured in cDMEM which contained foetal calf serum, Fungizone™ (amphotericin B), L-Glutamine and penicillin/ streptomycin.

The culture of RN22 cells broadly follows that of human dermal fibroblasts. Briefly, upon reaching confluence, cells are washed twice with PBS and 1.5 ml of trypsin is added to the T75 flask. The flask was incubated for 5 minutes at 37°C and then gently tapped to dislodge the cells. The cells and media were then centrifuged at 1000 rpm for 5 minutes with the resulting supernatant discarded. The cell pellet was then resuspended in 10 ml of fresh DMEM with 100,000 cells from this solution being deposited in a new T75 flask containing 15 ml of fresh, pre-warmed cDMEM. Cells were passaged upon reaching 75 % confluence and the media was changed every 3 days.

2.3.5 NG108-15 Cell Culture Medium

Please see section 2.1.8 for details.

2.3.6 NG108-15 Neuroblastoma Cell Culture

Please see section 2.1.9 for details.

2.3.7 Primary Schwann Cell Isolation and Culture

Please see section 2.1.12 for details.

2.3.8 Analysis of CNP Autofluorescence Within Cells

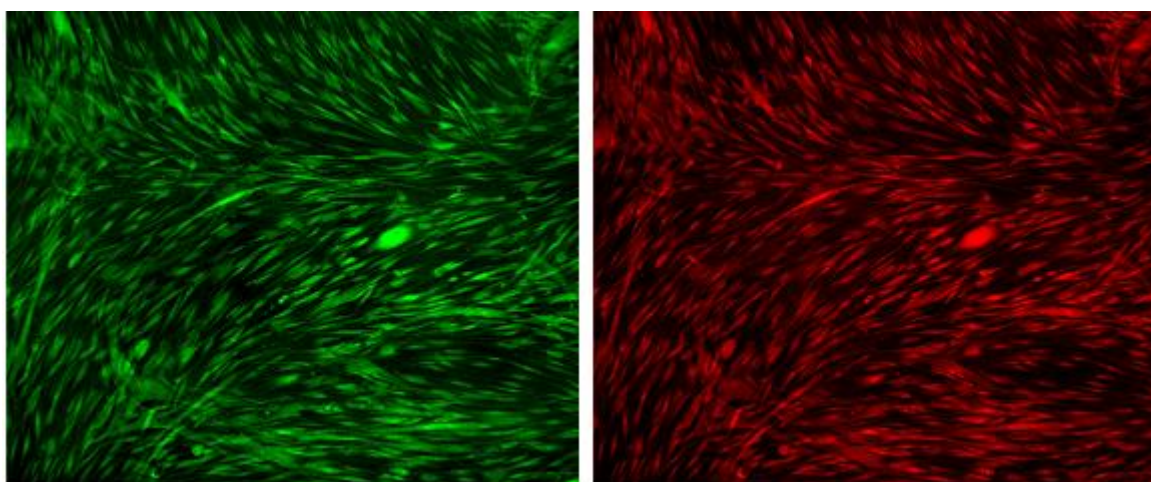


Figure 24: Autofluorescence of primary human fibroblasts incubated with alginate CNPs.

To analyse the uptake of CNPs and the degree of autofluorescence, cells (NG108-15, RN22, human fibroblast and rat Schwann cells) were cultured within the individual wells of a 24 well plate until surpassing 75 % confluency. Various CNP solutions then supplemented the growth media (either 20 or 200 μ l within 1 ml of cDMEM) allowing the cells to uptake the CNPs for periods of either 2 hours or 2 days. Once this time period had elapsed the media and CNPs were removed with the cells being washed repeatedly with PBS until all excess CNPs had been removed. Cells were then analysed using an epifluorescence microscope (Axon ImageXpress, Molecular Devices, USA) with uptaken CNPs excited at light

wavelengths of 358 nm (blue), 490 nm (red) and 532 nm (green) to analyse autofluorescence (figure 24).

2.3.9 3-(4,5-dimethylthiazol-2-yl)-2,5-diphenyltetrazolium bromide (MTT) Assay

Please see section 2.1.14 for details.

2.3.10 Live-Dead Assay

The proportion of living to dead fibroblast cells cultured in the CNP enriched media was examined using the live-dead assay to ascertain CNP cytotoxicity. After the cells were incubated for the specified amount of time with the CNPs, the medium was discarded, and the cells washed repeatedly with PBS until all excess CNPs were removed. The cells were then incubated with a solution which allowed for living and dead cells to be differentiated according to the dye uptaken by the cells and ultimately the colour of the fluorescent dye emitted. Syto-9 (1 μ M in PBS) ($\lambda_{\text{ex}} = 488$ nm, $\lambda_{\text{em}} = 518$ nm) is a cell permeable dye which fluoresces green and only stains live cells, whereas propidium iodide (0.5 mg / ml in PBS with 0.1 % sodium azide) only stains non-viable cells and fluoresces red ($\lambda_{\text{ex}} = 488$ nm, $\lambda_{\text{em}} = 615$ nm). Stained cells were analysed by fluorescence microscopy, where random areas of each sample were imaged and the numbers of live and dead cells, if any, noted.

2.3.11 Dynamic Light Scattering (DLS)

Dynamic light scattering determines the size distribution of particles within a solution. The requirement for only a dilute solution of particles to be present, and the ease of the technique and speed at which a result can be attained make it a popular choice for determining the size of nanoparticles [228].

The technique focuses on the notion that as light, such as a laser, passes through a solution containing particles the rays are scattered. The Brownian motion of the particles within the solution causes fluctuations in the scattering intensity. All the statistical data associated with the scattering signal is then analysed with a correlator, producing a correlation function. Inverting this function then produces a size distribution of the particles, from which an average particle size can be determined [228].

Studies on CNP size were conducted using a Malvern Zetasizer Nano ZS instrument which was incorporated with a 4 mW He-Ne solid-state laser which operated at 632.8 nm. Back-scattered light was detected at 173° and the mean particle diameter was ascertained over thirty cycles of ten seconds duration from the quadratic fitting of the correlation function using the Stokes-Einstein equation. All the CNPs were dispersed in aqueous solutions (the original solutions being diluted ten-fold in distilled water) with all measurements taken at 25°C in triplicate.

2.3.12 Sodium Dodecyl Sulphate Polyacrylamide Gel Electrophoresis (SDS-PAGE) of CNP Solutions

The gel electrophoresis apparatus was set up according to the manufacturer's instructions (Biorad). The 10 % resolving gel was firstly made up by combining 3.2 ml of 30 % acrylamide (Biorad), 2.5 ml Tris pH 8.8 (Biorad, Hemel Hempstead, UK), 4.02 ml distilled water, 0.2 ml sodium dodecyl sulphate (SDS) (10 % w/v), 10 µl tetramethylethylenediamine (TEMED) and 67 µl ammonium persulphate (APS) (10 % w/v) in a universal tube. This provided a total volume of 10 ml which was sufficient to cast two resolving gels. The solution was pipetted into the space between the glass plates allowing sufficient space for the future casting of the stacking gel. A small volume of water was applied at the gel:air interface to prevent deformation of the gel whilst setting. Once set (after a period of 30 – 60 minutes,

dependent upon room temperature) the water was removed and the stacking gel component was pipetted on top of the set resolving gel. The stacking gel consisted of 0.76 ml 30% acrylamide gel, 0.5 ml Tris pH 6.8 (Biorad), 3.61 ml distilled water, 0.1 ml SDS (10 % w/v), 5 μ l TEMED and 50 μ l APS (10 % w/v). This was sufficient to create two stacking gels. The resulting solution was pipetted on top of the set resolving gel and a well comb positioned within the stacking solution as it set, to create 10 wells for the deposition of the CNP solutions. Once set, the comb was removed, and sufficient running buffer (28.8 g glycine, 6.04 g Tris base, 2 g SDS and 1.8 litres distilled water, adequately mixed and additional distilled water added as required to produce a total volume of 2 litres) was added to the apparatus. Approximately 20 μ l of CNP solution was added to each well in the stacking gel which then migrated through the resolving gel as a power of 180 Volts was applied for 45 minutes. The gels were then removed and illuminated under a UV lamp ($\lambda = 254$ nm) to display CNP autofluorescence.

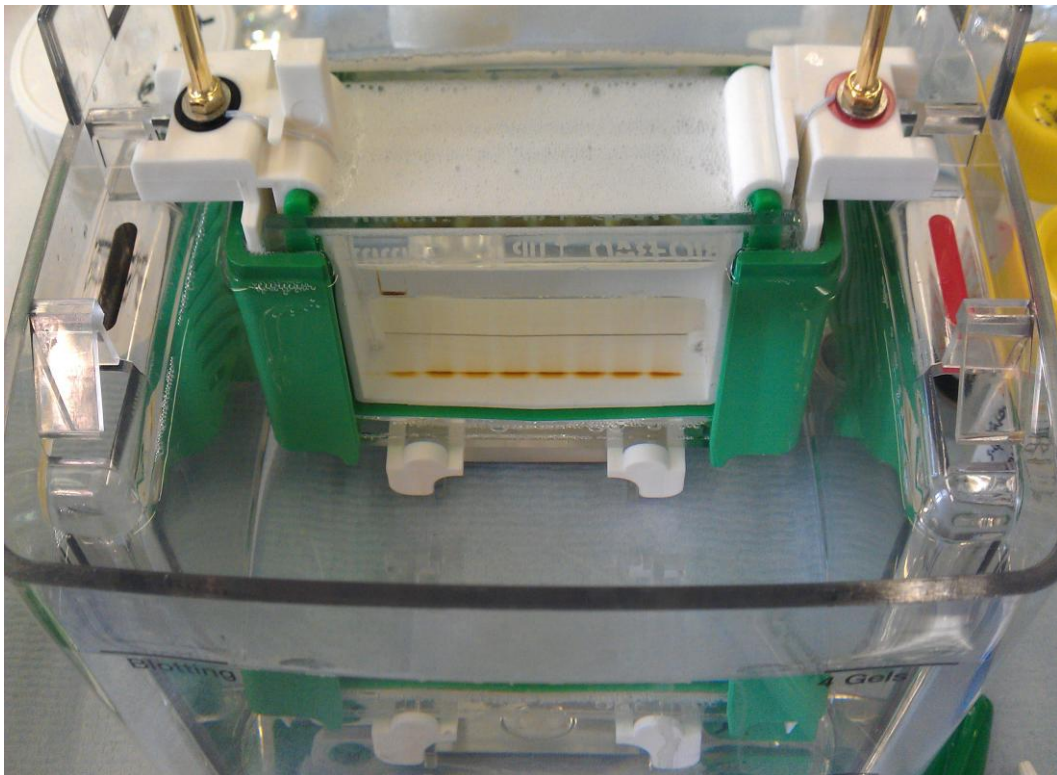


Figure 25: Completed SDS-PAGE of CNPs within the electrophoresis chamber.

2.3.13 Fluorescence Spectroscopy

Prior to analysis a small aliquot of each CNP sample was taken and diluted by a factor of ten in distilled water. Fluorescence emission was detected using a FluroMax-4 spectrofluorometer. All samples were excited at wavelengths of 420 nm, 450 nm and 470 nm.

2.3.14 Ultraviolet/Visible (UV/Vis) Spectroscopy

CNP solutions were diluted ten-fold in distilled water, transferred to UV-transparent cuvettes and analysed using a Varian Cary 50b spectrofluorimeter. Samples analysed over a spectral range between 200 and 800 nm.

2.3.15 X-Ray Photoelectron Spectroscopy (XPS)

Please see section 2.1.16 for details.

Chapter Three: Diamond-Like Carbon (DLC) Study Results

3.1 Introduction

Diamond possesses a range of valuable mechanical and tribological properties which offer interesting opportunities towards the development of future applications. One such advantage that diamond possesses which is useful within biological research is the ease with which it can be doped or functionalised whilst retaining its stability and biocompatibility. The material's mechanical strength and hardness are also particularly desirable especially where device longevity is a major consideration. However, the harsh synthesis route required for conventional diamond, usually requiring high temperatures and pressures normally prohibits its deposition upon biological substrates such as plastics, glass or silicon. In these circumstances an alternative structural form of carbon, known as diamond-like carbon (DLC), can be utilised since it is synthesised directly upon substrates under relatively mild deposition conditions (ambient temperature and pressure).

DLC films can be produced by a variety of methods including argon ion sputtering and cathodic arc spray although the DLC produced for this thesis was created by pulsed laser deposition (PLD). The diamond-like character of the DLC produced is dependent upon the ratio of sp^2 and sp^3 carbon, with greater diamond-like properties resulting from a higher sp^3 content.

Importantly, DLC can also be readily photofunctionalised with the aid of UV radiation allowing the attachment, for example, of functionalities that confer neurocompatible properties. Polylysine's (PL) neuroadhesive properties are thought to originate from the

amine groups within its structure, creating a highly polar molecule which assists in cell adhesion. Other amine-containing molecules, such as trifluoroacetic acid protected 10-amino-dec-1-ene (TFAAD), are known to exert a similar effect and can be easily UV-attached to DLC. Such a method has been utilised within the experiments conducted for this thesis to create a neurocompatible substrate which possesses all the positive attributes of conventional neuroadhesive surface treatments such as polylysine. It is envisaged these diamond-based substrates however will have lower cytotoxicity issues and greater stability in comparison to polylysine, thus being better served to be utilised within future neural *in vivo* applications such as neural prostheses and brain computer interfaces (BCIs).

Thus, this thesis chapter is concerned with the photofunctionalisation of DLC with deprotected TFAAD (10-amino-dec-1-ene) and its amenability to act as a neurocompatible substrate for the growth of neural cell lines and primary Schwann cells. The success of functionalisation was assessed by XPS measurements and *in vitro* cell responses to the amine-functionalised DLC substrate (cell morphology, dendrite length analysis and MTT cytotoxicity assay). Where appropriate, all data from the following chapter will be quoted to three significant figures (3 s.f.).

3.2 Surface Characterisation of DLC Coatings

DLC was applied to the surface of glass cover slips either via pulsed-laser deposition or SEM electron beam induced deposition methods (see section 1.1.2 within the appendix). Once complete, the DLC-coated glass was subject to UV-induced photografting with TFAAD or 2-(10-undecen-1-yl)-1,3-dioxolane to eventually yield either amine (DLC-Amine) or aldehyde (DLC-Aldehyde) functionalised substrates. Prior to this, several DLC/TFAAD functionalisation studies were completed to determine the optimal irradiation time to ensure maximum surface-functionalisation (section 3.2.1).

To determine the success of the amine and aldehyde grafting processes water contact angle measurements and XPS scans were undertaken of the functionalised and control samples. Additionally, an SEM image was recorded of the 10-amino-dec-1-ene-bound surface to determine morphology differences which had occurred post-functionalisation.

The results indicated that alkenes containing aldehyde or amine groups could be effectively bound to DLC by irradiation with UV light. With increased exposure time to UV light greater numbers of atoms, which were indicative of amine or aldehyde functional groups, were detected upon the substrate by XPS. Additionally, water contact angle measurements illustrated the greater hydrophilicity of the functionalised substrates in comparison to bare PLD-DLC.

3.2.1 Determination of Optimal Irradiation Time for TFAAD Grafting

In order to determine the optimum irradiation time to graft TFAAD to the DLC surface a series of amine adsorption experiments were conducted to test the functionalisation rate as a function of time. Although the proportion of bound nitrogen to the surface during amine functionalisation gives a broad indication of the grafting rate it could not be verified whether all of this detected nitrogen originated from the adsorption of 10-amino-dec-1-ene. Therefore to quantify the degree of functionalisation as a function of irradiation time the peak area of the F(1s) curve relative to the peak area of the C(1s) curve was plotted since it could be ascertained that any fluorine bound to carbon could only originate from TFAAD adsorption (figure 26).

Prior to deprotection, as irradiation time increased the fluorine content of the DLC was also seen to increase, but as the experiment progressed it was discovered that the functionalisation rate also eventually decreased, appearing to stagnate as irradiation time approached 120

hours. This was to be expected as available carbon sites for grafting gradually deplete as the reaction progresses.

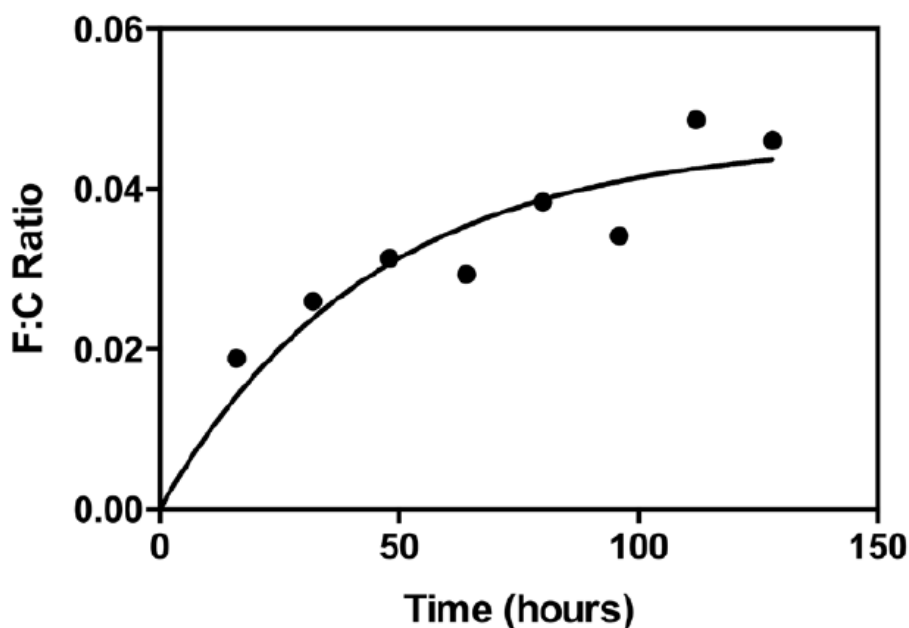


Figure 26: Plot displaying the ratios of the integrated peak areas of the fluorine 1s and carbon 1s curves as a function of UV irradiation time. The curve illustrates a logarithmic decay as a guide to the eye.

The radiance of the 6.00 W lamp at a distance of 7.50 cm was calculated to be 2.25 mW/cm², whilst the radiance of the 500 W lamp at a wavelength of 250 nm at a distance of 20.0 cm was approximately 78.0 mW/cm². Therefore, the effective exposure from the more powerful 500 W lamp over a 4 hour period was approximately equal to 140 hours exposure from the lower power 6 W lamp. Figure 26 illustrates that after this length of UV-exposure the F:C ratio stagnates, indicating near completeness of the photochemical reaction.

3.2.2 Scanning Electron Microscopy of DLC-Amine Surface

To compare the amine-DLC surface at the microscale, part of the original DLC surface was preserved during photochemical functionalisation (figure 26) through the use of a mask

provided by a copper TEM grid. This section was then highly magnified using a scanning electron microscope to highlight the surface topography prior and post amine attachment.

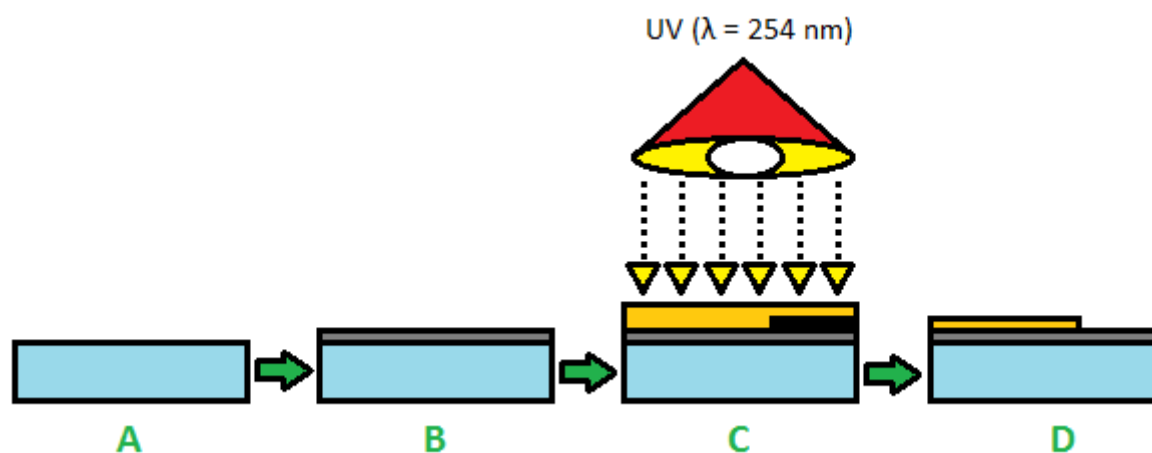


Figure 27: Production of amine functionalised DLC substrate as shown in figure 27. Glass cover slips (A) were coated with DLC by pulsed laser deposition (B). Liquid TFAAD polymer was applied to the DLC surface, with part of the DLC obscured by a mask, whilst the surface was irradiated with UV light for 4 hours (C). The excess TFAAD and mask was removed and the surface deprotected overnight to yield a partially functionalised amine-DLC substrate (D).

Magnification of the functionalised surface revealed significant differences between the functionalised and native DLC substrate (figure 28). Areas which had been exposed to TFAAD and UV light appeared to produce a surface resembling polymeric growth, an analogy often utilised to describe the photochemical attachment of alkenes. Regions where amine groups had attached to the surface appeared brighter than the adjacent native DLC substrate, illustrating that these functionalised areas reflected greater numbers of electrons to the detector. This was possibly due to the functionalised area having a slight raised topography in comparison to the underlying DLC, giving greater surface contrast. However usually the binding of TFAAD to DLC surfaces initially produces a monolayer coating; only

after prolonged UV irradiation does crosslinkage and the grafting of additional layers occurs [229].

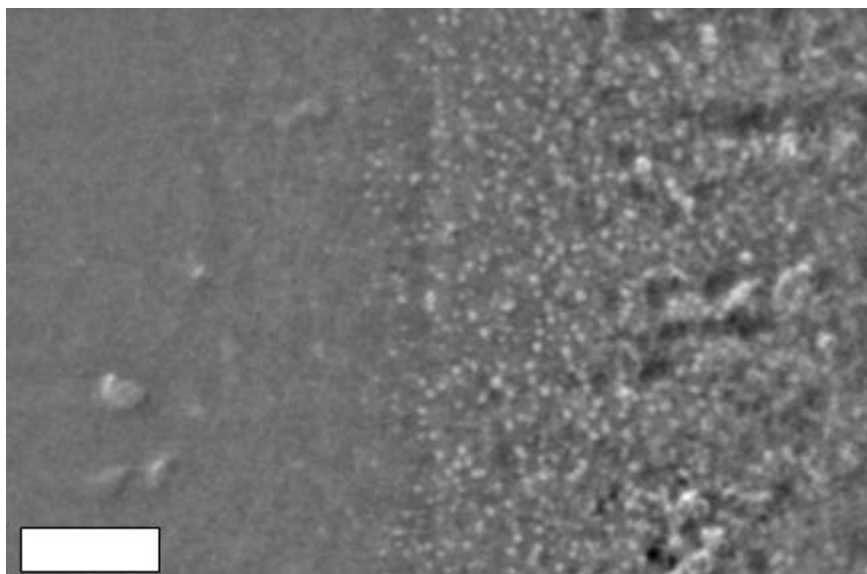


Figure 28: Scanning electron microscope (SEM) image illustrating the binding of 10-amino-dec-1-ene to DLC-coated glass (light grey speckled area to the right of the image). The slightly darker, featureless area to the left of the image reveals untreated DLC which was masked during UV irradiation to prevent functionalisation (Magnification: X3500. Scale Bar: 5 μm).

3.2.3 Substrate contact angle measurements

Contact angle measurements were all conducted at room temperature across five different specimens from each sample category, with each specimen being subject to four contact angle measurements. Therefore, in total, twenty readings were accumulated for each substrate. Although most readings were fairly similar, two sets of data did produce significant results. When comparing the contact angles (figure 28) measured from DLC ($64.3^\circ \pm 3.10^\circ$), significantly smaller angles were reported on average from DLC-aldehyde (DLC-10-undecenal) ($49.7^\circ \pm 2.90^\circ$) and DLC-amine [DLC-(10-amino-dec-1-ene)] ($48.4^\circ \pm 1.70^\circ$) indicating that functionalisation increased the hydrophilicity of the substrates. Indeed, DLC

was the least hydrophilic surface tested, although it would not actually be categorised as being hydrophobic due to possessing a contact angle less than 90.0°. Furthermore, the contact angle of glass ($52.1^\circ \pm 4.80^\circ$) was remarkably similar to those of the functionalised DLC samples, but this had little bearing on the ability of each substrate to support a healthy population of neuronal or glial cells.

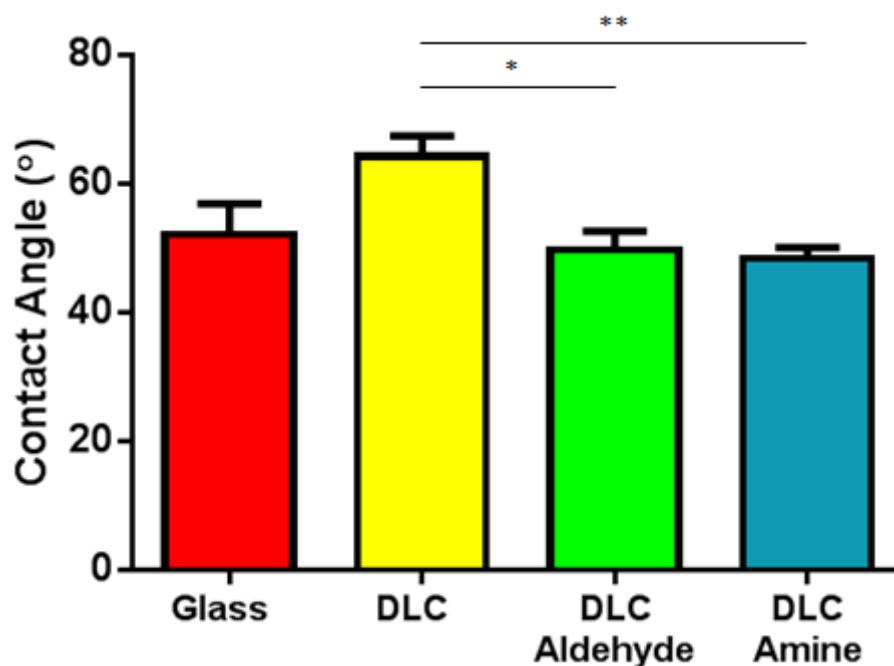


Figure 29: Mean water contact angle measurements of glass, DLC, DLC-Aldehyde and DLC-Amine taken at room temperature. Values were reported from the mean of twenty different readings \pm standard error. Significance was determined by one way anova utilising Tukey's multiple comparison test whereby; * $p < 0.05$ and ** $p < 0.01$.

3.2.4 X-ray Photoelectron Spectroscopy (XPS) Graphs

XPS data was collected from the DLC surfaces in order to corroborate their functionality. Both survey and high resolution C(1s) scans were collated from DLC and glass control surfaces, as well as DLC functionalised with TFAAD and 10-undecenal. XPS studies were

conducted using a Kratos AXIS Ultra DLD instrument, whilst data processing and charge correction were calculated using CasaXPS (ver.2.3.12 Casa Software Ltd.).

3.2.4.1 XPS: PLD-Derived Diamond-Like Carbon

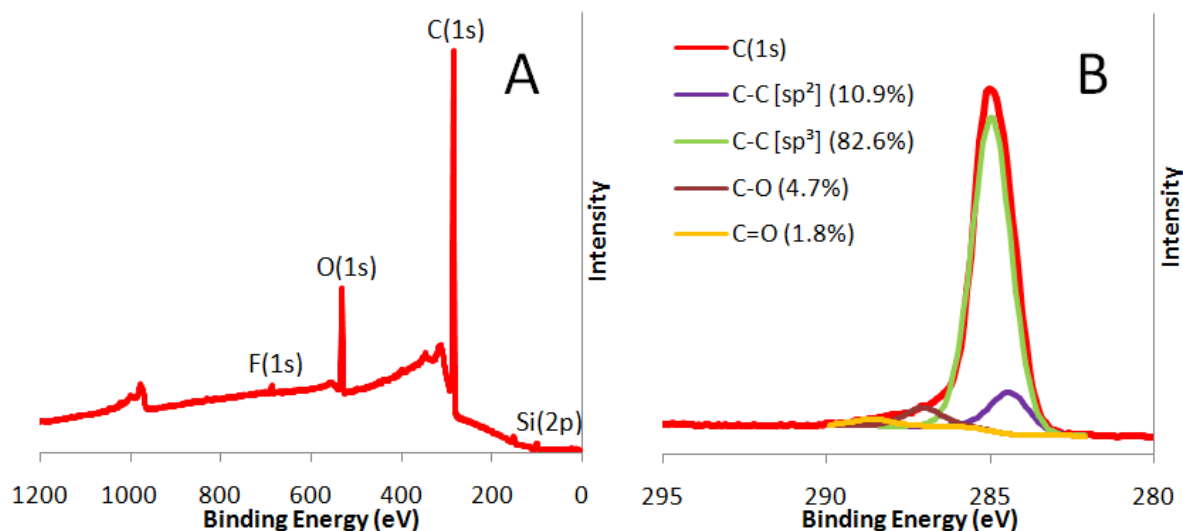


Figure 30: X-ray photoelectron spectra (XPS) depicting survey (A) and high resolution carbon (B) scans of PLD diamond-like-carbon (DLC) upon silicon wafer.

PLD-DLC displayed a survey XPS spectrum (figure 30A) free from impurities with the exception of a trace reading of fluorine (F 1s) (0.380%). This contrasted with the SEM-EBID DLC as depicted in the appendix (figure A-2). Furthermore, the absence of a silicon peak on the survey spectrum signified that the thickness of the DLC film created was greater than the attenuation depth of the XPS electron beam (approximately 10.0 nm). The low ratio of oxygenated carbon atoms which were present (Figure 30B: C-O bonds: 4.70%, C=O bonds: 1.80%) is typical of DLC, where the vast majority of carbon atoms are bound to other carbons producing either sp² (graphitic character) or sp³ (diamond character) carbon.

3.2.4.2 XPS: TFAAD bound to PLD-DLC (5-20 minutes)

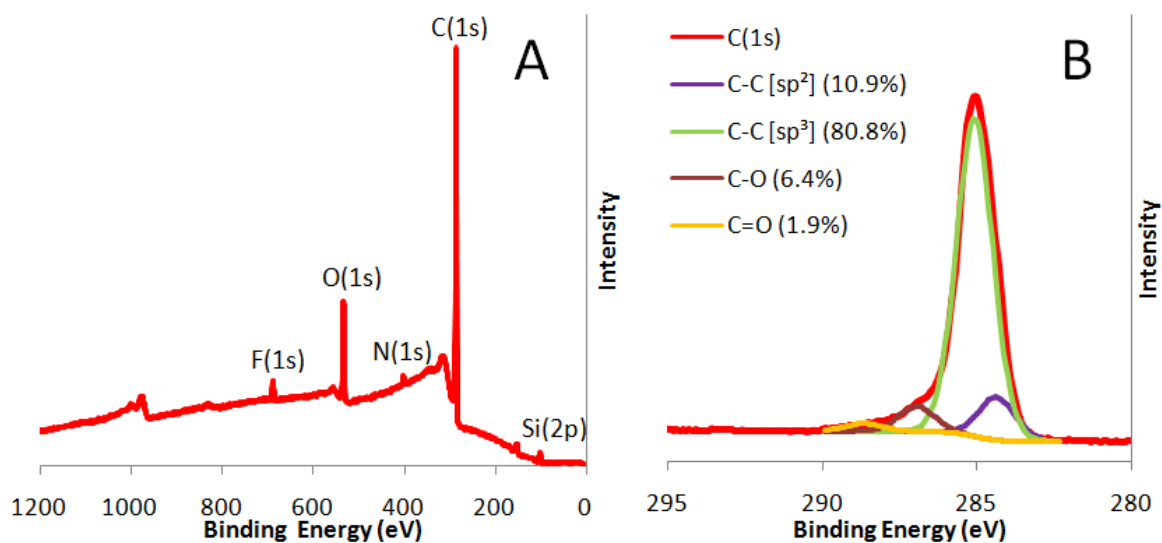


Figure 31: X-ray photoelectron spectra (XPS) depicting survey (A) and high resolution carbon (B) scans of TFAAD photochemically bound to PLD-DLC for 5 minutes.

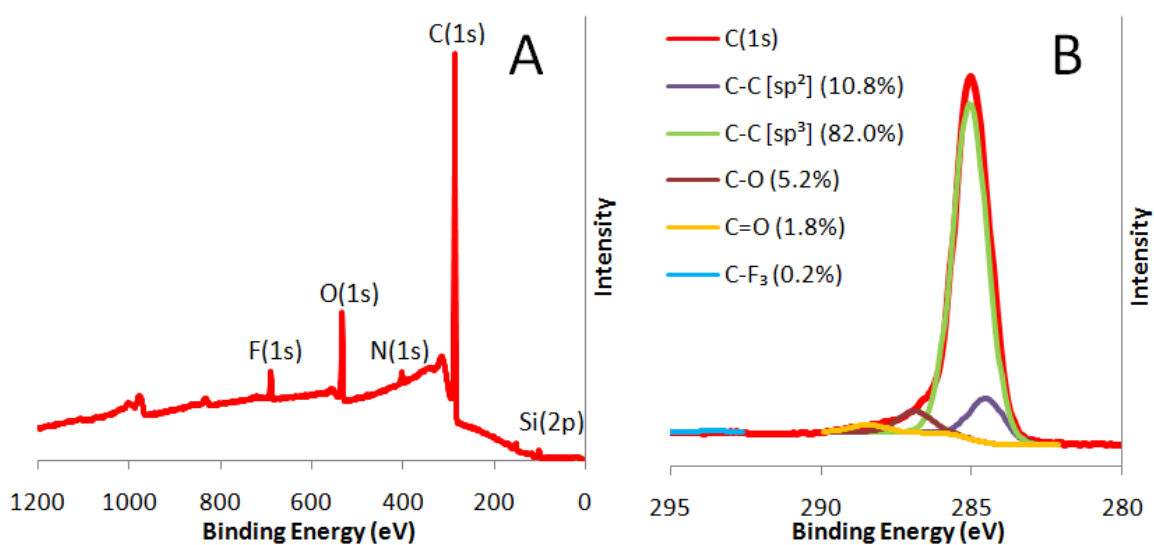


Figure 32: X-ray photoelectron spectra (XPS) depicting survey (A) and high resolution carbon (B) scans of TFAAD photochemically bound to PLD-DLC for 10 minutes.

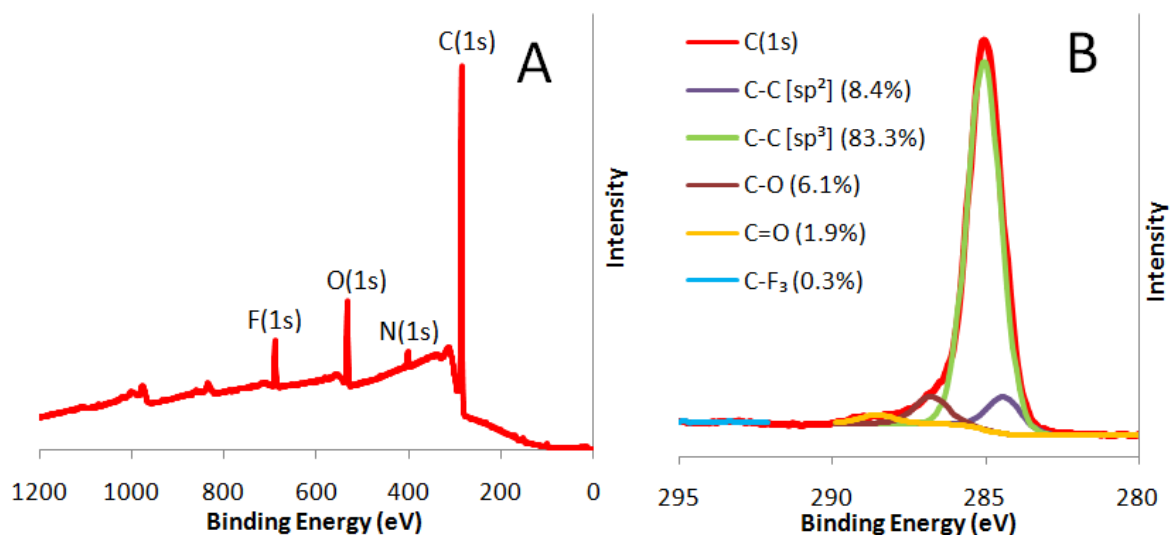


Figure 33: X-ray photoelectron spectra (XPS) depicting survey (A) and high resolution carbon (B) scans of TFAAD photochemically bound to PLD-DLC for 15 minutes.

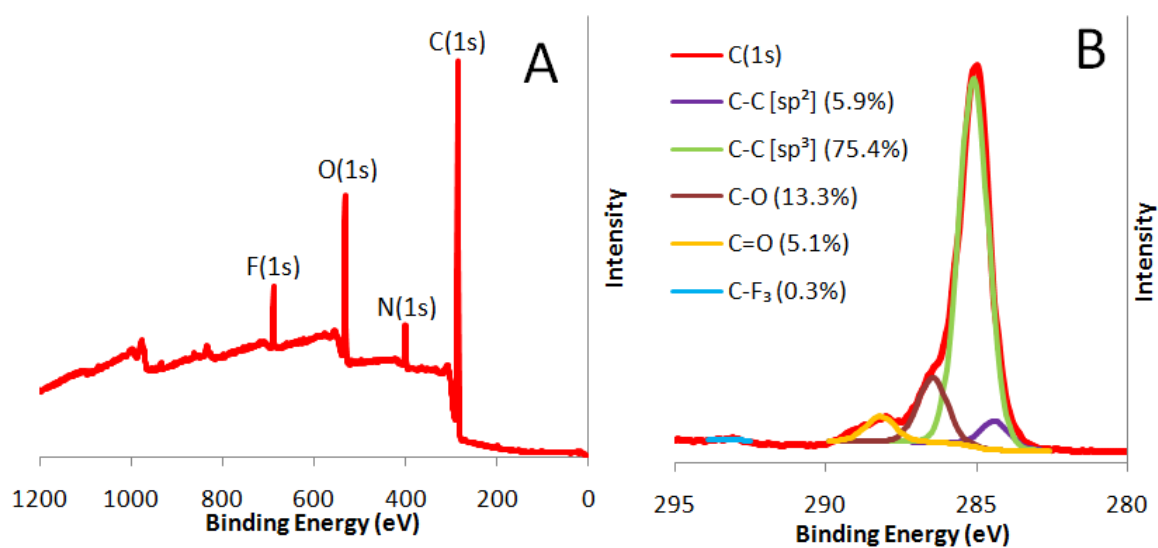


Figure 34: X-ray photoelectron spectra (XPS) depicting survey (A) and high resolution carbon (B) scans of TFAAD photochemically bound to PLD-DLC for 20 minutes.

The data collected to study the photochemical attachment of TFAAD over a short timescale of between 5 – 20 minutes UV exposure illustrated that longer irradiation times were necessary to adequately functionalise the DLC surface (figures 31 – 34). Nitrogen and

fluorine levels steadily increased across the samples as they were exposed to greater levels of radiation, recording readings of 2.00% and 2.30% respectively, once 15 minutes of attachment had elapsed (figure 33A).

No impurities were detected across the samples except for trace readings of sodium (0.0300%) and sulphur (0.580%) upon the sample irradiated for 15 minutes (figure 33A). After twenty minutes, significantly greater numbers of nitrogen atoms were detected (5.37 %) (figure 34A) whilst the proportion of carbon atoms bound to oxygen were seen to more than double from the figure reported at the 15 minute timepoint, from 8.00 % to 18.4 % (figure 34B), which may have indicated greater TFAAD attachment. However, the proportion of C-F₃ bonds being detected was seen to stagnate between the 15 and 20 minute timepoints (figures 33B and 34B).

In addition, the level of silicon detected was noted to decrease with greater irradiation time from 5 to 20 minutes. However, this may only be a result of the varying thickness of the DLC layer deposited by PLD and may not be attributed to TFAAD attachment. The silicon levels detected across samples irradiated for between 1 – 4 hours upon PLD-DLC were seen to randomly fluctuate between 0.360 % - 1.97 % seemingly as a result of DLC thickness (figures 40 – 43).

3.2.4.3 XPS: 10-undecenal bound to PLD-DLC (5-20 minutes)

Although amine groups have widely been acknowledged as assisting in cell attachment and growth to create effective cell culture substrates there are reports of further functionalities which may produce beneficial cell culture surfaces [230]. However, to attach such moieties to substrates such as DLC by photochemical grafting it is a necessity for the compound to be an alkene. It has previously been reported that substrates functionalised with aldehyde groups, deposited by plasma polymerisation, have supported the growth and attachment of cells

[230]. Nichols *et al* have also commented on the widespread functionalisation of hydrogenated and oxygenated DLC with various alkenes by UV irradiation, implying that the grafting of aldehyde-functionalised alkenes to DLC is a possibility [64]. A reaction scheme depicting alkene functionalisation of DLC is depicted in figure 35.

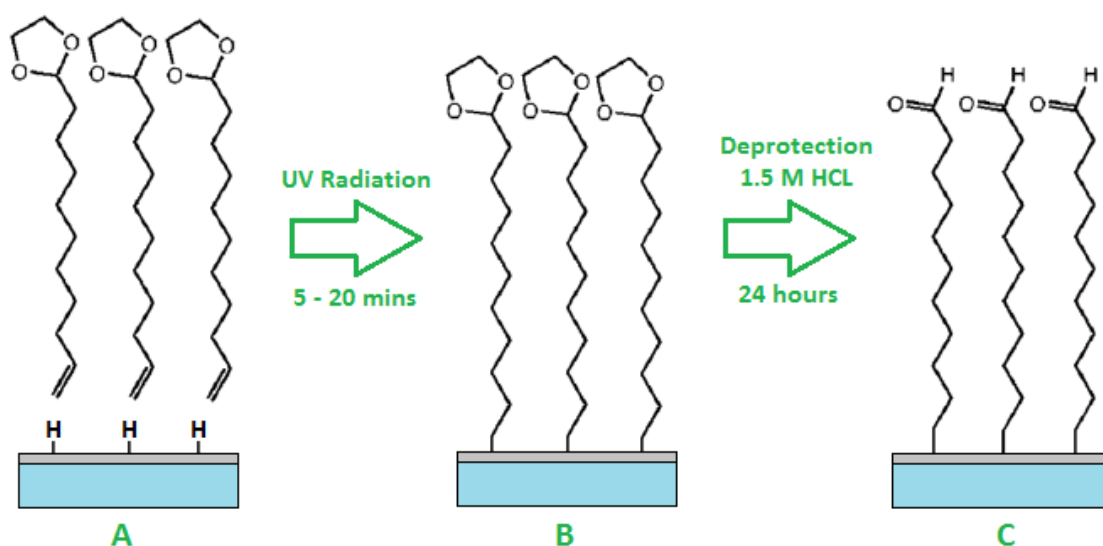


Figure 35: The production of aldehyde-terminated DLC substrates. (A) 2-(10-undecen-1-yl)-1,3-dioxolane was applied to the surface of DLC-coated glass cover slips which were then sandwiched between two quartz slides. (B) The substrates were then irradiated with UV light for between 5 – 20 minutes after which (C) the functional group was deprotected overnight within 1.50 M HCl to yield a surface grafted with 10-undecenal.

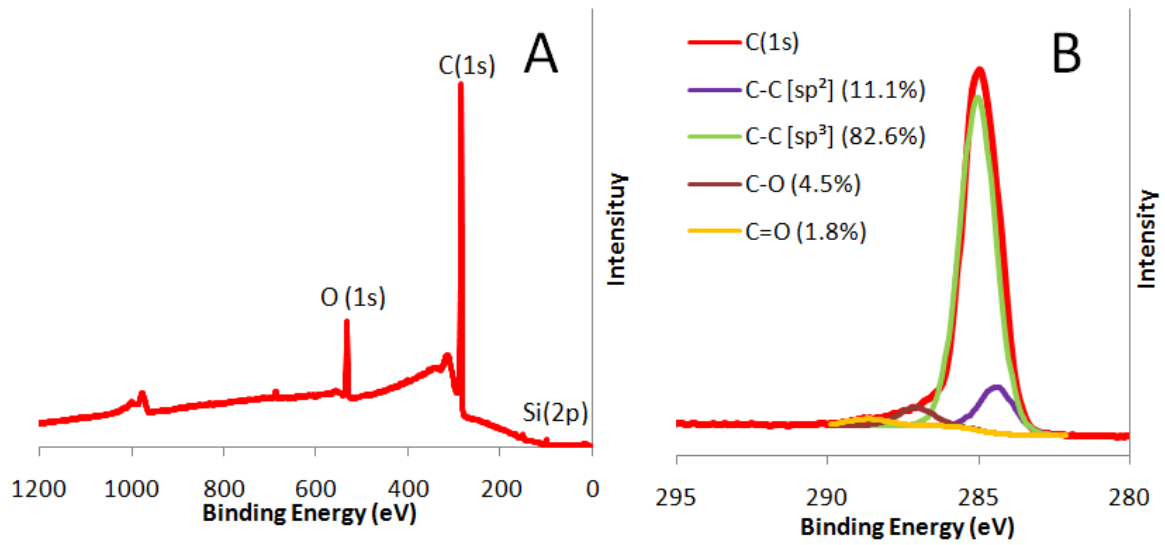


Figure 36: X-ray photoelectron spectra (XPS) depicting survey (A) and high resolution carbon (B) scans of 10-undecenal photochemically bound to DLC for 5 minutes.

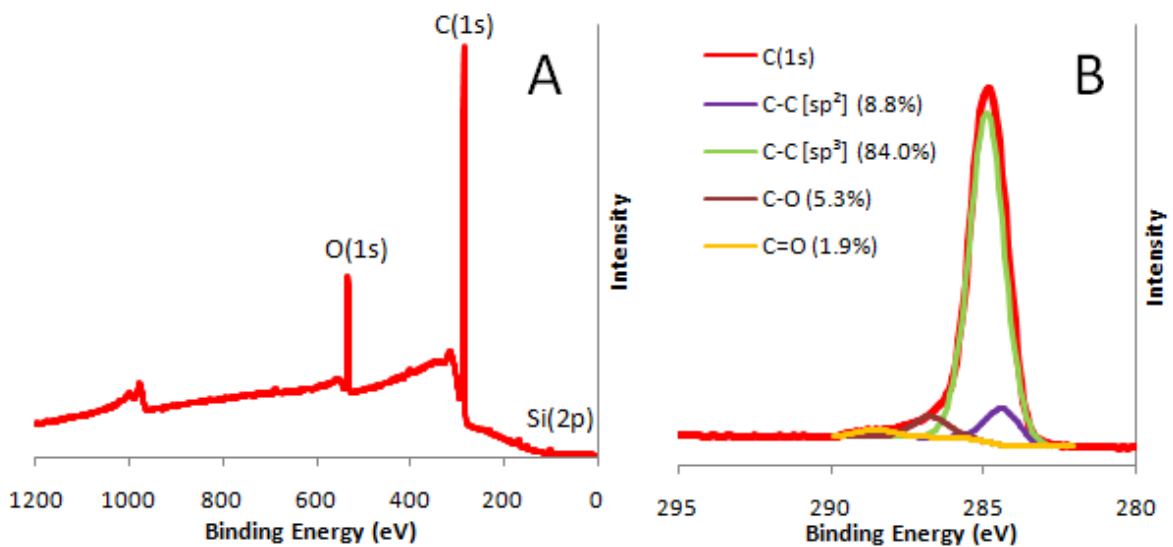


Figure 37: X-ray photoelectron spectra (XPS) depicting survey (A) and high resolution carbon (B) scans of 10-undecenal photochemically bound to DLC for 10 minutes.

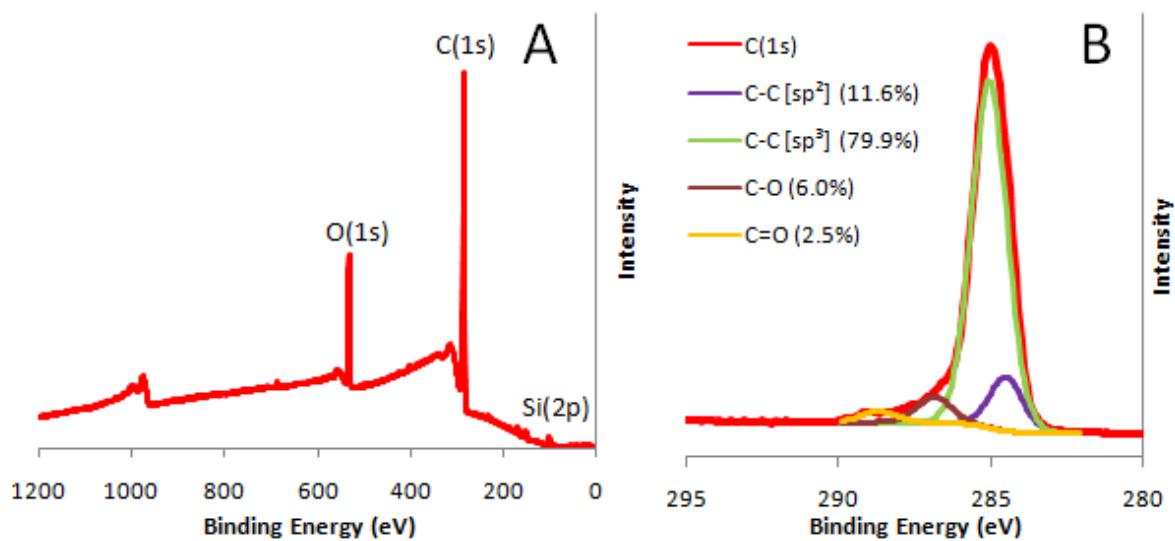


Figure 38: X-ray photoelectron spectra (XPS) depicting survey (A) and high resolution carbon (B) scans of 10-undecenal photochemically bound to DLC for 15 minutes.

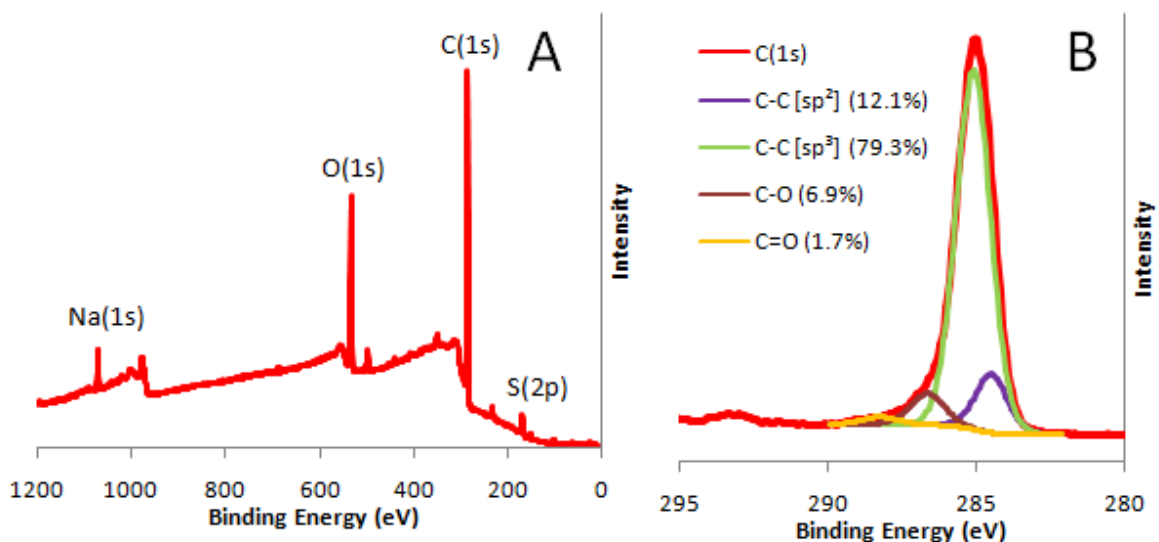


Figure 39: X-ray photoelectron spectra (XPS) depicting survey (A) and high resolution carbon (B) scans of 10-undecenal photochemically bound to DLC for 20 minutes.

To test the effectiveness of other alkenes photochemically binding to DLC it was decided to trial the reaction of 10-undecenal, testing the reaction progress after samples had been

exposed to 5, 10, 15 and 20 minutes of UV radiation (figures 36 - 39). The aldehyde-functionalised alkene was protected prior to photochemical grafting, producing 2-(10-undecen-1-yl)-1,3-dioxolane, before being deprotected overnight at 60.0°C in the presence of 1.50M hydrochloric acid. The procedure was carried out identically to that performed using TFAAD, whereby 2-(10-undecen-1-yl)-1,3-dioxolane was photoattached to PLD-DLC upon exposure to UV light and subsequently deprotected producing 10-undecenal.

Although a proportionate increase in the C=O signal was also detected on the carbon high resolution scan between samples irradiated for 10 – 15 minutes (from 1.90% to 2.50%), this proportion then decreased again to 1.70% following 20 minutes of UV exposure. This may not be a result of fewer aldehydes binding to the surface, but rather due to greater levels of contaminants, such as sulphur, calcium and sodium (figure 39A) being detected which may have diluted the C=O signal or the spectrum may have been erroneous.

The increased reaction rate of this aldehyde group is certainly of research interest and occurs far faster than the alternative functionalisation route demonstrated in this thesis with TFAAD. The reasons for these differences are not entirely clear, although it has been stated previously that similarly sized alkenes possessing different distal functional groups have varying reactivity rates [191, 231]. This issue which will be further elaborated upon in the discussion section (chapter 6).

3.2.4.4 XPS: TFAAD bound to PLD-DLC (1-4 hours)

Although slight progress was made with the photochemical attachment of TFAAD to SEM-EBID DLC (figures A-3 – A-6 listed in the appendix), figures 40 – 43 depict the greater effectiveness of using PLD-DLC as a substrate for carbon functionalisation. Not only did the survey spectra appear cleaner, with fewer contaminants reported, but also the nitrogen and

fluorine levels detected, which were indicative of TFAAD attachment, were far greater across all time points.

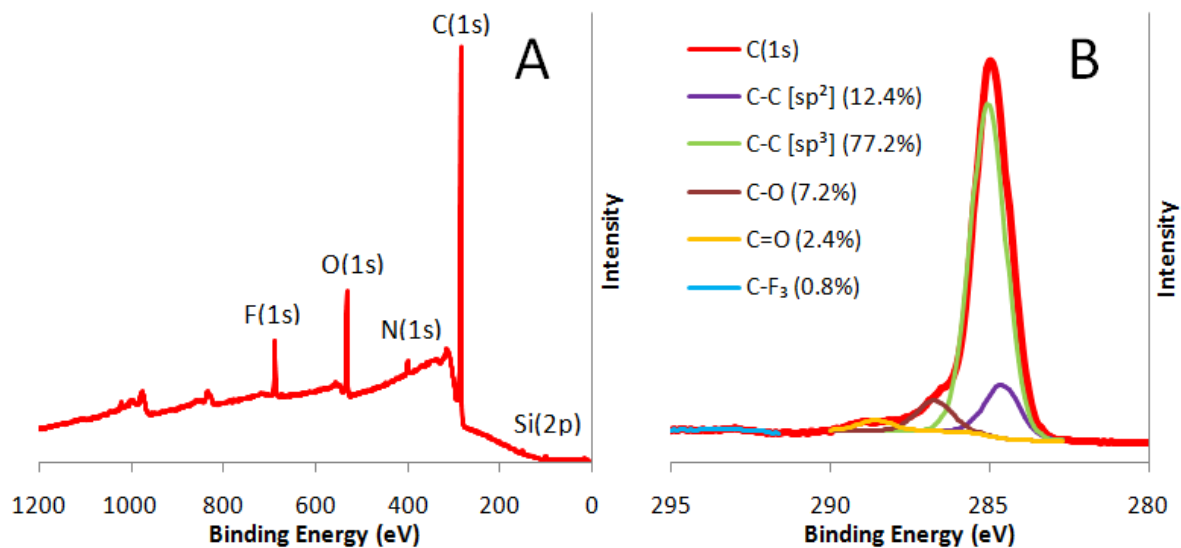


Figure 40: X-ray photoelectron spectra (XPS) depicting survey (A) and high resolution carbon (B) scans of TFAAD photochemically bound to PLD-DLC for 1 hour.

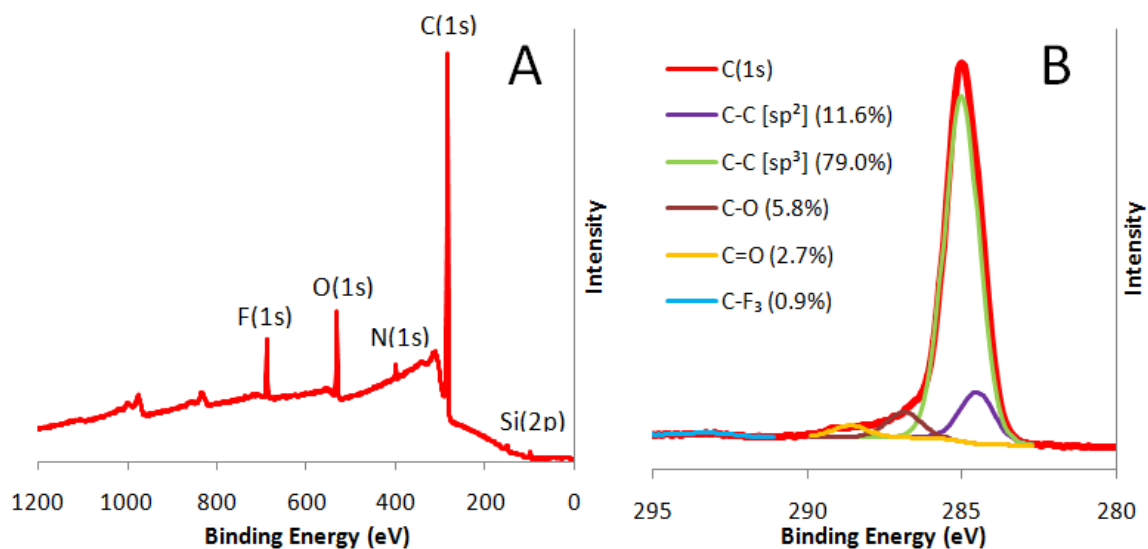


Figure 41: X-ray photoelectron spectra (XPS) depicting survey (A) and high resolution carbon (B) scans of TFAAD photochemically bound to PLD-DLC for 2 hours.

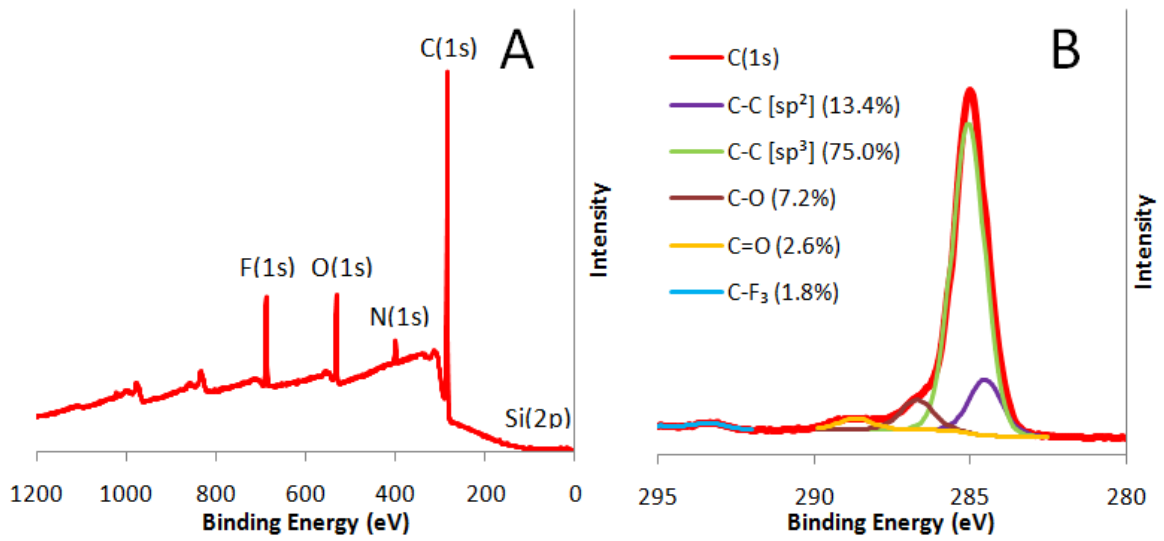


Figure 42: X-ray photoelectron spectra (XPS) depicting survey (A) and high resolution carbon (B) scans of TFAAD photochemically bound to PLD-DLC for 3 hours.

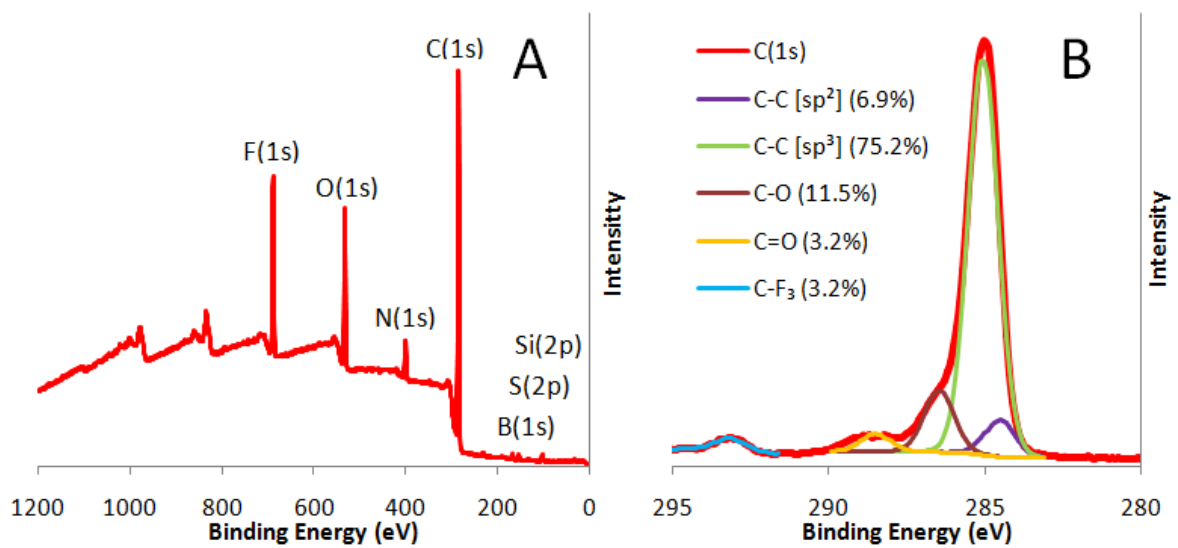


Figure 43: X-ray photoelectron spectra (XPS) depicting survey (A) and high resolution carbon (B) scans of TFAAD photochemically bound to PLD-DLC for 4 hours. For clarity, the B(1s), S(2p) and Si(2p) peaks are located at 190 eV, 167 eV and 101 eV respectively.

Element	Binding Energy (eV)	[Atomic Presence Within Each Sample (%)]				
		UV Irradiation Time (Hours)				
		0	1	2	3	4
O(1s)	533	8.20	8.20	7.00	7.50	11.8
C(1s)	285	88.5	87.5	86.2	83.2	73.0
N(1s)	400	0.400	1.30	1.90	3.20	4.60
F(1s)	686	0.400	2.70	3.40	5.50	8.40
S(2p)	167	-	-	-	-	0.600
B(1s)	190	-	-	-	-	0.400
Si(2p)	101	2.00	0.400	1.50	0.700	1.30

Table 2: Atomic presence (%) of each element detected by XPS (survey spectra) from PLD-DLC samples irradiated in the presence of TFAAD for 0, 1, 2, 3 or 4 hours.

As in the SEM-EBID DLC film, oxygen levels in the functionalised DLC films remained largely static between hours 1 – 4, only fluctuating slightly between 7 – 12 % (figures 40A – 43A). The proportion of nitrogen and fluorine detected between 1 and 2 hours of UV irradiation also appeared to change very little (figures 40A and 41A) however the general trend was for these levels to increase with greater exposure to UV radiation, so that once the samples had been irradiated for 4 hours, the level of fluorine detected was in excess of 8 % (figure 43A). This compared with a figure of less than 4 % for TFAAD bound under the same conditions upon SEM-EBID DLC (figure A-2 listed within the appendix). At this time point the C-F₃ peak detected within the XPS carbon spectrum (3.20% - figure 43B) was also more prominent than in the SEM-EBID DLC spectrum (1.80% - figure A-2 listed within the appendix) confirming greater TFAAD attachment.

With respect to the high resolution carbon spectra for both surfaces, it can be seen for the DLC-derived surfaces, that with increased TFAAD attachment, the level of sp³ carbon detected appeared to stay relatively constant (figures 40B – 43B) fluctuating from between

75.0% and 79.0%. However, in the SEM-EBID DLC samples under the same conditions, the level of sp³ carbon appeared to increase by hours 3 and 4, leading to moderately decreased proportions of sp² being detected (figures A-5 and A-6 respectively, listed within the appendix). However, for both SEM-EBID DLC and PLD-DLC, far lower proportions of sp² (graphitic) carbon were present across all timepoints. This is to be expected of carbon films which possess more diamond-like character such as DLC. Only low levels of the underlying silicon substrate were detected upon functionalised PLD-DLC surfaces with values typically reported at approximately 1 – 2 %, which compared favourably with the SEM-EBID DLC surface where the presumably incoherent coating sometimes resulted in silicon being the most widely detected surface element (41.0 % - figure A-2A listed within the appendix).

These XPS spectra have been valuable in assessing the functionalisation capability of DLC. It has been seen possible to functionalise SEM-EBID DLC with photografted TFAAD which has not been reported previously, albeit PLD-DLC was a more effective substrate for this purpose. Additionally, the grafting of aldehyde functionalised alkenes has been shown to occur much more readily than TFAAD. The ability to rapidly functionalise a surface with aldehyde groups may prove useful for future cell growth applications.

3.3 Cell Culture upon DLC surfaces

3.3.1 Determination of Correct Seeding Density of NG108-15 cells

In order to ascertain the most amenable NG108-15 seeding density upon control and DLC surfaces two different concentrations of cells (5000 cells/ml and 10000 cells/ml) were deposited within the wells of a tissue culture plastic (TCP) cell culture plate. These cells were cultured for 7 days in serum-free cDMEM, after which the degree of cell spreading was documented by epifluorescence microscopy (figure 44). It was important to select a cell

concentration that was sufficient to encourage the proliferation of cells and the establishment of a cell population, but not excessively high so that the number of cells dwarfed the substrate prior to the expected end time-point of the experiment and so restricting neurite outgrowth.

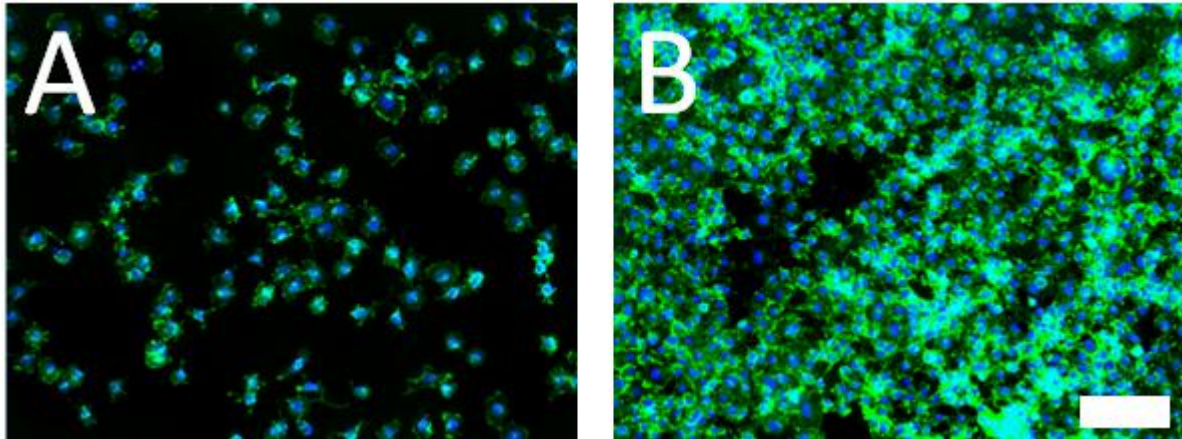


Figure 44: Fluorescence micrographs of NG108-15 cells cultured for 7 days upon TCP at a seeding density of (A) 5000 cells/ml and (B) 10000 cells/ml. Three separate triplicate repeat experiments (n=9) were conducted with each triplicate utilising a different batch of cells (N=3). Scale: 150 μ m.

The high level of cell surface coverage associated with a seeding density of 10000 cells/ml as indicated by figure 44B restricted neurite development, rendering the identification and measurement of any outgrowths difficult. However, the lower surface coverage as displayed by figure 44A illustrated that cells cultured at a seeding density of 5000 cells/ml upon TCP still had adequate space for the further development of neurites. Neurite outgrowth is a reliable indicator of neural cell development, a key area of investigation for this study. Serum starvation of NG108-15 cells has also been cited as a neural differentiation cue which further promotes neuritic outgrowth [232]. These findings therefore proved that the adaption of the comparatively low seeding density of 5000 cells/ml for neuroblastoma cell lines would be adequate to satisfy the aims and objectives of the thesis cell experiments.

3.3.2 NG108-15 MTT Cell Viability on Functionalised DLC Surfaces

To provide an indication of cell viability and cell density upon the functionalised surfaces an MTT assay was performed 7 days post cell-seeding on the glass, DLC, DLC-Amine, DLC-Aldehyde and poly-L-lysine surfaces (figure 45).

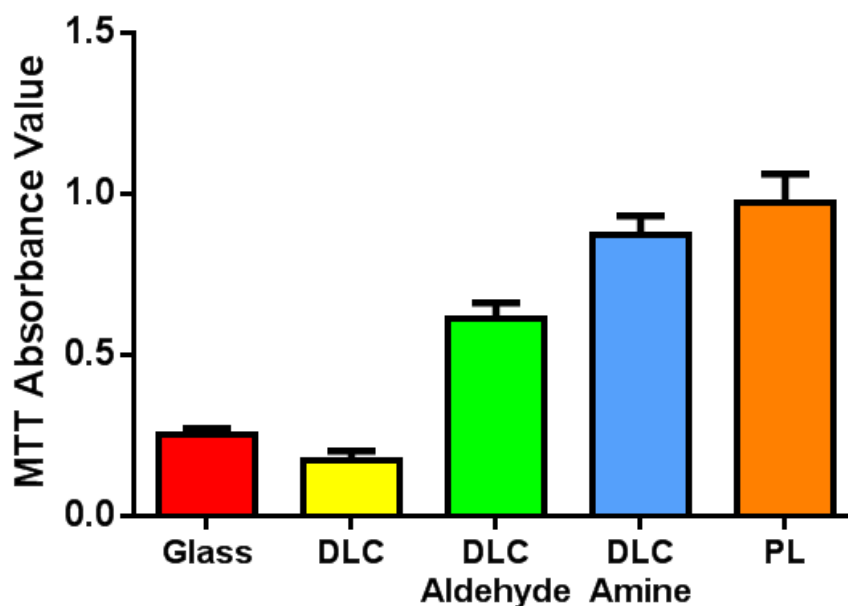


Figure 45: MTT assay absorbance values, measured at 570 nm and referenced at 630 nm, collated from NG108-15 cells cultured upon glass, DLC, DLC-Aldehyde, DLC-Amine and PL surfaces over a period of 7 days.. Three triplicate repeat experiments were conducted ($n = 9$) with each triplicate using a different batch of cells ($N=3$). Values are reported from the mean of three different repeats \pm standard error. Complete statistical analysis of the mean dendrite length data is provided in table 3 overleaf.

As evidenced by the cell fluorescence images (figure 46), the cell density of neuroblastoma cultured upon glass and DLC appeared far greater than those cultured upon functionalised DLC or PL surfaces. This was confirmed by the MTT results displaying significant differences between the negative controls and the test samples (figure 45); for example the

reading for DLC-Amine yielded an MTT result (0.870) over 4 times higher than the corresponding reading upon untreated DLC (0.170).

- Statistical Analysis Tables – MTT Data

	DLC	DLC-Aldehyde	DLC-Amine	PL
Glass	N/S	***	***	***
DLC		***	***	***
DLC-Aldehyde			*	***
DLC-Amine				N/S

*Table 3: Statistical significance data relating to figure 45 determined by Tukey’s multiple comparison test and one way-anova, whereby; * $p < 0.05$, ** $p < 0.01$, *** $p < 0.001$ and N/S = no significant difference.*

Although cells grown upon PL elicited a slightly higher average reading (0.970) than upon DLC-Amine, there were no significant differences between the two sets of data, highlighting the similar nature in which cells proliferate across both surfaces. Consequently, the relatively low MTT readings for the glass and DLC surfaces indicated low metabolic activity, due to the lower density of cells that were present.

3.3.3 Fluorescence Images of NG108-15 Cells Cultured upon DLC surfaces

NG108-15 neuroblastoma cells were cultured on the DLC surfaces within serum-free DMEM for 7 days before being fixed in formalin. They were then stained for phalloidin-FITC and DAPI and imaged using epifluorescence microscopy.

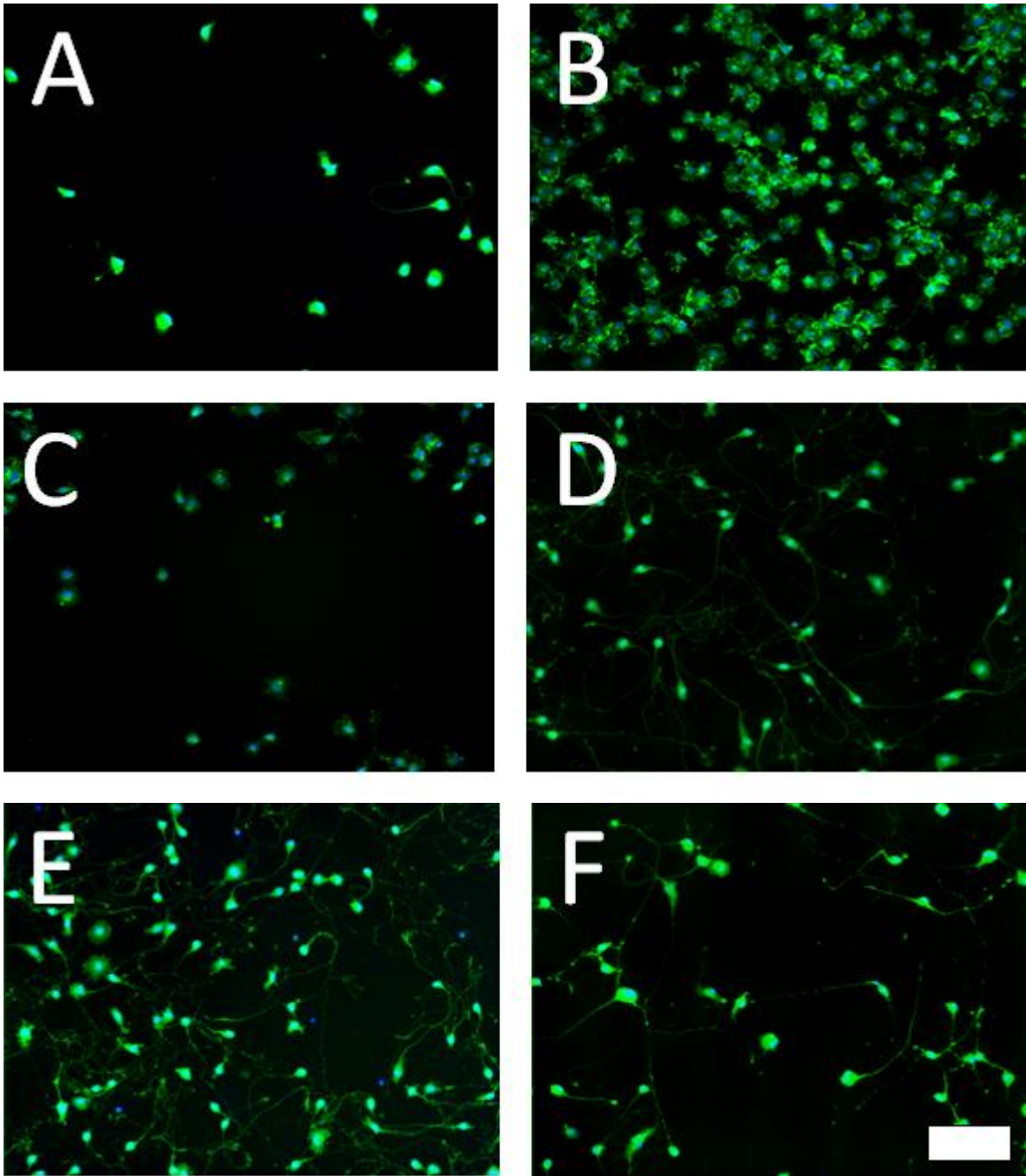


Figure 46: Fluorescence micrographs displaying the growth of NG108-15 cells cultured for 7 days upon (A) glass, (B) TCP, (C) DLC, (D) DLC-Amine, (E) PL and (F) DLC-Aldehyde. Cells were stained for phalloidin-FITC (green) and DAPI (blue). Three separate triplicate repeat experiments (n=9) were conducted with each triplicate utilising a different batch of cells (N=3). Scale: 150 μ m.

Although cells adhered to all the surfaces tested, comparatively few remained on glass (46A) or DLC (figure 46C). Cells on these surfaces displayed few neurites and any that had developed were considerably shorter than those recorded upon the other samples tested. The cells acquired a spherical morphology highlighting poor surface spreading and a minimal substrate contact area.

NG108-15 cells achieved greater confluence upon TCP (figure 46B) and PL (figure 46E), as well as upon the amine and aldehyde terminated DLC samples (figures 46D and 46F respectively). Despite all surfaces receiving an equal seeding density of cells, they proliferated at a higher rate upon these latter samples than upon the negative controls, with much longer neurites also being evident. However, cells did not proliferate at such a rate as to impede dendrite development. In addition, numerous cells displayed a bipolar or even tripolar phenotype, some possessing neurites whose lengths exceeded 300 μm , whereas upon the glass and untreated DLC surfaces most neuronal cells were neurite-free. Upon the DLC-Amine surface especially, cells appeared to develop similarly to those cultured upon PL resulting in an almost identical appearance.

3.3.4 Immunofluorescence Microscopy of Primary Schwann Cells Cultured upon DLC Surfaces

Primary Schwann cells were isolated from male Wistar rats using an established harvesting method [214] and cultured upon the glass, DLC, DLC-Amine and PL surfaces for 21 days in Schwann cell media. Cells were then washed, fixed in formalin and stained for the presence of S100 (a protein which acts as a glial marker due to it being present in neuronal crest isolates).

Clear differences in Schwann cell phenotype were observed across the different surfaces. Noticeably, a considerable number of Schwann cells attached to the glass substrate (figure

47A), which contrasted with NG108s that appeared to struggle and most of which detached by day 7 of cell culture on glass (figure 46A). However, the cell morphology of Schwann cells cultured upon glass differed from their conventional morphology which is evident in figures 47C and 47D. Upon glass the cells adapted a spindle like shape, exerting a slight preference to congregate together. Although most cells were bipolar, their neurites aligned randomly across the surface without any directional-preference with most cell bodies having an angular rather than an oval/spherical morphology.

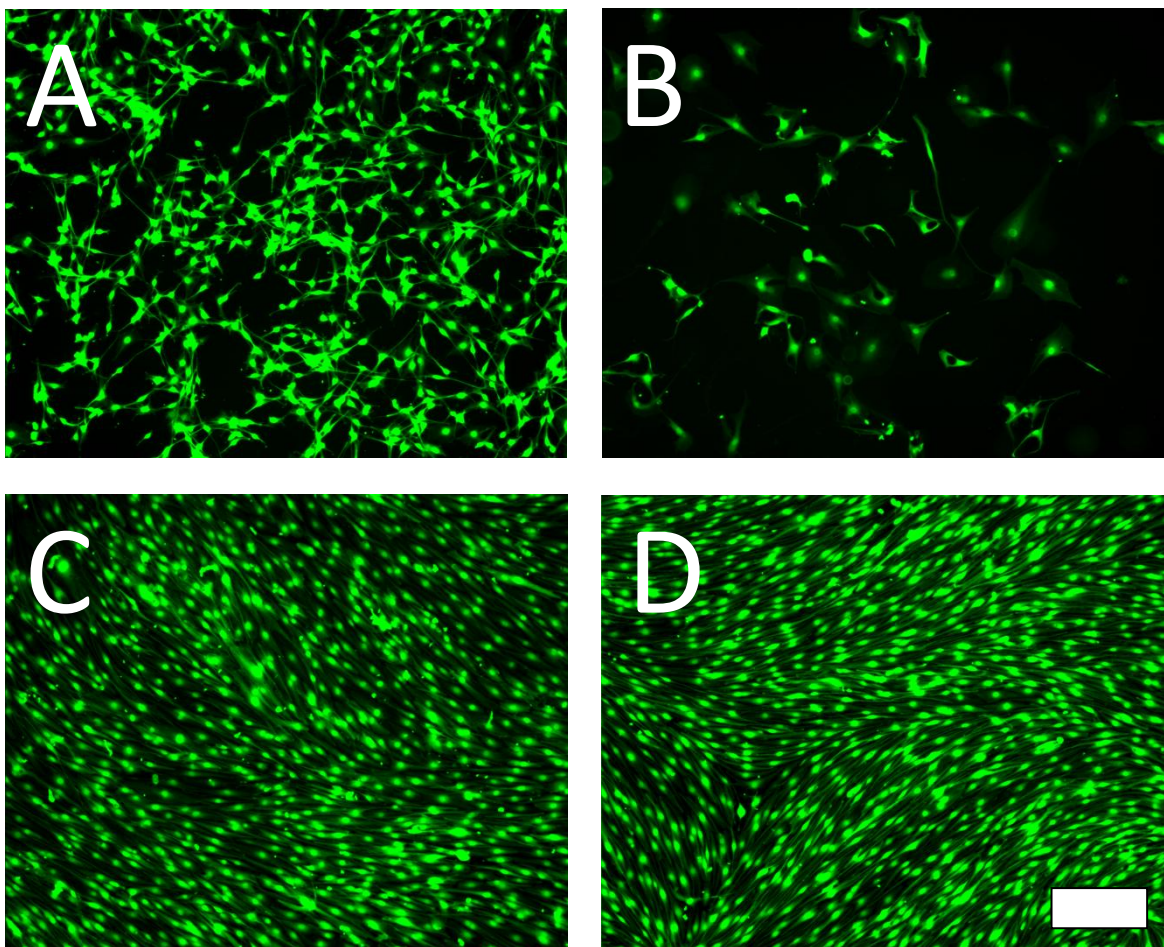


Figure 47: Fluorescence micrographs displaying the growth of primary rat Schwann cells cultured for 21 days upon (A) glass, (B) DLC, (C) DLC-Amine and (D) PL. Cells were stained for the presence of S100 (green). One triplicate experiment (n=3) was conducted which utilised a single batch of cells (N=1). Scale: 150 μ m.

Schwann cells did attach to DLC also, albeit sparingly, highlighting the relatively low proliferation rate upon pure carbon surfaces (figure 47B). Cells adopted a variety of morphologies upon this surface, some resembling a squamous phenotype typical of a fibroblast whilst others were more similar to the bipolar elongated phenotype associated with typical Schwann cells. Those cells that did exhibit neurites also alligned themselves randomly with respect to each other.

In contrast, Schwann cells cultured upon amine-functionalised DLC (figure 47C) and poly-L-lysine (figure 47D) exhibited similar morphologies. All Schwann cells which developed on these amine terminated surfaces adapted a bipolar, elongated phenotype with a smooth cell body. Nearly all neurites were alligned alongside adjacent cells, forming a confluent Schwann cell monolayer which was stable and showed no sign of delamination from the substrate.

3.3.5 NG108-15 Neurite Lengths Upon Control/DLC Substrates

Neurite lengths were measured from NG108-15 cells cultured on the control and DLC-derived surfaces using neurite tracer software (NIH, Image J). Certain trends were observed across the different samples as time progressed. Indeed, NG108-15 cells cultured on glass reported a decrease in average neurite length from measurements conducted on day 1 ($68.2 \mu\text{m} \pm 3.44 \mu\text{m}$) through to day 7 ($37.6 \mu\text{m} \pm 2.61 \mu\text{m}$) [figure 48]. This was to be expected, due to poor neuronal adhesion and gradual cell detachment from the surface. DLC surfaces, although having an average neurite length greater than glass across all assessed timepoints, only supported cells with a significantly greater neurite length than glass on day 2 (glass: $58.4 \mu\text{m} \pm 5.65 \mu\text{m}$) versus (DLC: $92.8 \mu\text{m} \pm 5.20 \mu\text{m}$), demonstrating the inappropriateness of untreated DLC for neuronal cell growth.

In contrast the treated DLC surfaces and PL-coated TCP encouraged greater neurite growth as the experiment progressed. Consecutive increases in the average neurite length were recorded, although the growth rate of neurites upon DLC-Aldehyde (52.8 %) was smaller than upon either PL (58.7 %) or DLC-Amine (90.2 %) when analysed over the course of the study. Although poly-L-lysine recorded consistently longer neurites, on average, the growth rate of neurites upon DLC-Amine was sufficiently great that the differences in neurite length between the two substrates was insignificant by day 7 of cell culture.

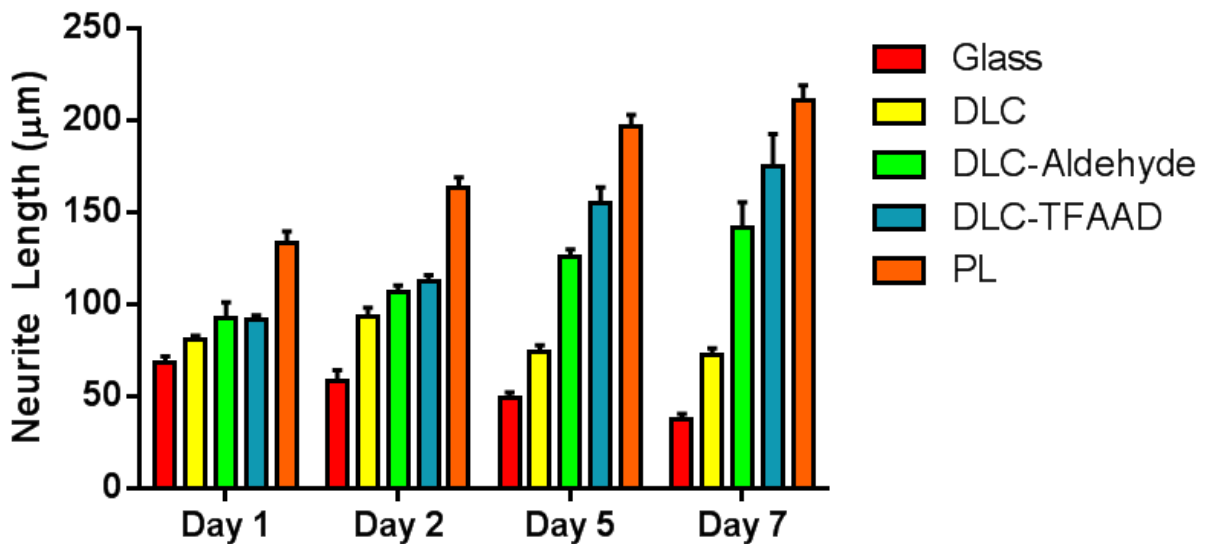


Figure 48: Mean neurite lengths (μm) of NG108-15 cells cultured upon glass, DLC, DLC-aldehyde, DLC-amine and PL surfaces over periods of either 1, 2, 5 or 7 days. Values are reported from the mean (\pm standard error) of three separate triplicate repeat experiments ($n = 9$) with each triplicate using a different batch of cells ($N=3$). Complete statistical analysis of the mean dendrite length data are provided overleaf in table 4.

- Statistical analysis tables - neurite length data

DAY 1	DLC	DLC-Aldehyde	DLC-Amine	PL
Glass	N/S	N/S	N/S	***
DLC		N/S	N/S	***
DLC-Aldehyde			N/S	***
DLC-Amine				***

DAY 2	DLC	DLC-Aldehyde	DLC-Amine	PL
Glass	**	***	***	***
DLC		N/S	N/S	***
DLC-Aldehyde			N/S	***
DLC-Amine				***

DAY 5	DLC	DLC-Aldehyde	DLC-Amine	PL
Glass	N/S	***	***	***
DLC		***	***	***
DLC-Aldehyde			N/S	***
DLC-Amine				***

DAY 7	DLC	DLC-Aldehyde	DLC-Amine	PL
Glass	N/S	***	***	***
DLC		***	***	***
DLC-Aldehyde			N/S	***
DLC-Amine				N/S

Table 4: Statistical significance data relating to figure 48 determined by Tukey's multiple comparison test and one way-anova, whereby; * $p < 0.05$, ** $p < 0.01$, *** $p < 0.001$ and N/S = no significant difference.

3.3.6 Mean Number of Neurites per NG108-15 Cell Across All Substrates

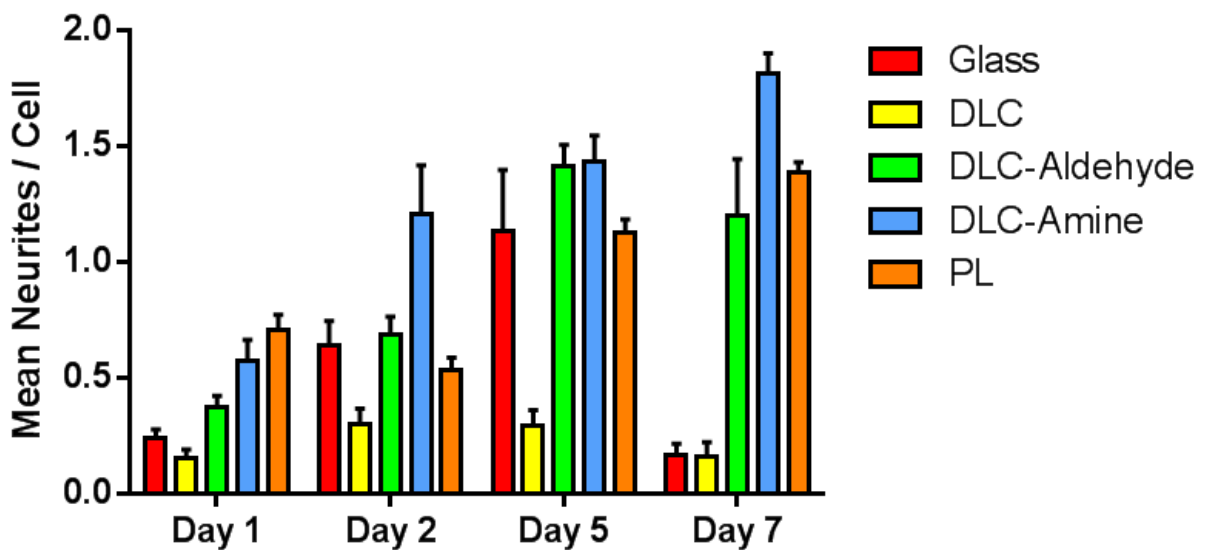


Figure 49: Mean number of neurites per NG108-15 cell cultured upon glass, DLC, DLC-Aldehyde, DLC-Amine and PL surfaces over periods of either 1, 2, 5 or 7 days. Values are reported from the mean (\pm standard error) of three separate triplicate repeat experiments ($n=9$) with each triplicate using a different batch of cells ($N=3$). Complete statistical analysis of the data is provided below and overleaf in table 5.

- Statistical analysis tables - mean number of neurites per cell

DAY 1	DLC	DLC-Aldehyde	DLC-Amine	PL
Glass	N/S	N/S	***	***
DLC		*	***	***
DLC-Aldehyde			N/S	***
DLC-Amine				N/S

DAY 2	DLC	DLC-Aldehyde	DLC-Amine	PL
Glass	N/S	N/S	**	N/S
DLC		N/S	***	N/S
DLC-Aldehyde			*	N/S
DLC-Amine				***

DAY 5	DLC	DLC-Aldehyde	DLC-Amine	PL
Glass	***	N/S	N/S	N/S
DLC		***	***	***
DLC-Aldehyde			N/S	N/S
DLC-Amine				N/S

DAY 7	DLC	DLC-Aldehyde	DLC-Amine	PL
Glass	N/S	***	***	***
DLC		***	***	***
DLC-Aldehyde			**	N/S
DLC-Amine				***

*Table 5: Statistical significance data relating to figure 49 determined by Tukey's multiple comparison test and one way-anova, whereby; * $p < 0.05$, ** $p < 0.01$, *** $p < 0.001$ and N/S = no significant difference.*

The mean number of neurites each neuronal cell was capable of nurturing upon each surface was also important to note so to determine the affinity of each substrate for supporting nerve cells. Greater neurite density may indicate a higher capacity of a substrate to encourage neural differentiation. As the experiment progressed up to day 5 there was a general trend for the mean number of neurites per cell to increase (figure 49), the exceptions being a slight decrease in this statistic for cells cultured upon poly-L-lysine between day 1 (0.708 ± 0.0627) and day 2 (0.533 ± 0.0524) and the start of a downward trend noted for DLC from day 2 (0.350 ± 0.109) to day 7 (0.0909 ± 0.0627). In comparison to other substrates, neurite formation upon DLC was heavily restricted and became increasingly sparse as time progressed.

Greater neuritic sprouting was particularly evident across neuronal cells cultured upon DLC-Amine, where by day 2 the number of neurites recorded already exceeded the number of cells present across the surface (1.21 ± 0.208). This pattern continued up to day 7, where the DLC-Amine substrates supported neuroblastoma cells which possessed significantly greater numbers of neurites per cell than any others surveyed in the study (1.81 ± 0.0855), including

those cultured upon poly-L-lysine (1.39 ± 0.0446) indicating the nature of the surface encouraged neuronal cellular development. Neuritic outgrowth appeared to increase in cells cultured on glass up to day 5 (1.14 ± 0.260), whereupon neurite formation appeared to collapse, decreasing by over 85% by day 7 just forty-eight hours later (0.165 ± 0.0501) thus giving an indication of the sustainability of NG108-15 upon glass and the rapid nature by which they detach.

DLC-Aldehyde also promoted neurite growth to a certain degree. Evidently, between days 2 and 5 the rate of outgrowth appeared to greatly increase with the number of neurites per cell accelerating from (0.688 ± 0.0746) to (1.41 ± 0.0958). However, by day 7 this figure started to decrease (1.20 ± 0.243) although the difference with poly-L-lysine at this stage was relatively small and not significant (1.39 ± 0.0446).

3.3.7 Neurite Plurality Across the Surfaces

Although analysing the same data presented within section 3.3.5, figure 50 displays the findings in a different manner as the proportion of cells exhibiting either 0, 1, 2, 3 or 4 neurites upon the control and DLC-related substrates. What was of particular interest was the large proportion of cells which bore two neurites (55.2 %) on DLC-Amine samples by day 7 (figure 50). These neuroblastoma resembled a bipolar morphology, one which is most often associated with glial cells and Schwannoma. In addition, although a small proportion of NG108's at this time point upon DLC-Amine failed to develop neurites (4.20%), an almost equal share of the neuroblastoma possessed four neurites (4.10%) the only sample where such cells were recorded. Furthermore, although all cells cultured on the PL surface by day 7 had developed neurites, a significant proportion (61.0%) had only developed one; this usually consisting of a lengthy outgrowth stretching up to 300 μm .

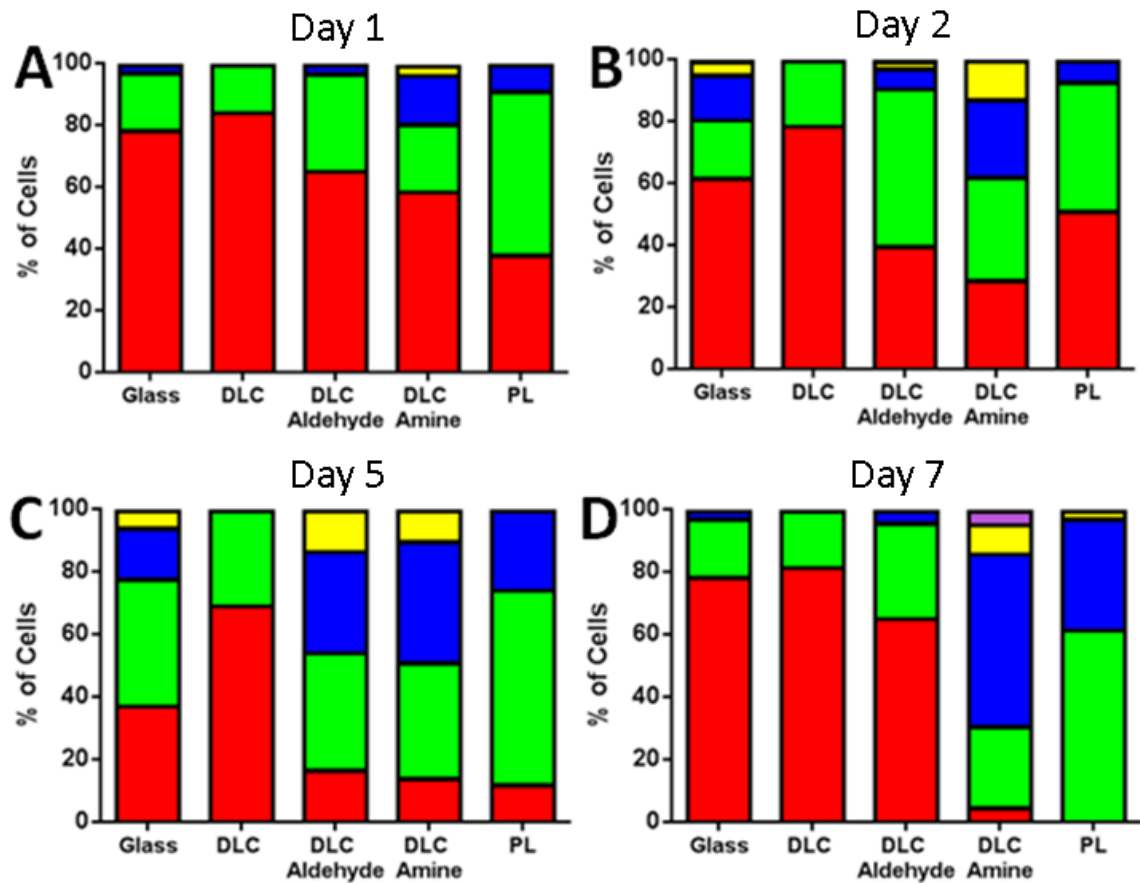


Figure 50: The percentage of NG108-15 cells producing 0, 1, 2, 3 or 4 neurites cultured upon glass, DLC, aldehyde functionalised DLC, amine functionalised DLC and poly-L-lysine. Neurite counting took place after Day 1 (A), Day 2 (B), Day 5 (C) and Day 7 (D) of serum-free culture. Three separate triplicate repeat experiments ($n=9$) were conducted with each triplicate utilising a different batch of cells ($N=3$).

Across all samples the proportion of neurite-free cells decreased from day 1 to day 5, with the exception of PL where the number of neurite-free cells was seen to increase between days 1 (37.5 %) and day 2 (50.5 %), before declining sharply by day 5 (11.6 %), and further by day 7 to zero. By day 7 however, the proportion of neurite-free cells upon the negative controls, glass and DLC, increased significantly to approximately 80 %, whilst DLC-Aldehyde also

appeared to discourage neurite formation, the proportion of neurite-free cells increased four-fold between samples surveyed at day 5 and day 7 of culture.

3.4 Conclusion

This chapter illustrated the successful photofunctionalisation of diamond-like carbon substrates with amine and aldehyde groups by UV radiation. Although SEM-EBID DLC was trialled as a possible source of amorphous carbon it was discovered that PLD-DLC was more amenable to functionalisation and therefore was selected as the primary method to create functionalised cover slips. *In vitro* cell culture revealed that neuronal cell lines and primary Schwann cells developed equally upon PL and DLC-Amine surfaces with neurite measurements confirming the continued development of the cells over experimental periods of between one day and three weeks duration. MTT assays also confirmed that the functionalised DLC substrates were not cytotoxic, although cells appeared to proliferate faster upon PL and DLC-Amine than upon DLC-Aldehyde substrates. The success of these experiments displayed the neurocompatibility of functionalised DLC surfaces and illustrated they may be possibly utilised for various *in vivo* neural-related applications in future, such as brain computer interfaces (BCI).

Chapter Four: Nanodiamond (ND)

Study Results

4.1 Introduction

The plentiful supply of nanodiamond from the detonation of explosives ensures that the synthesis process is inexpensive, ecological and fast. It therefore follows that industrial quantities of the material for biological purposes, such as the creation of a neuronal substrate, could be easily catered for. However, detonation nanodiamond particles are coated in a variety of functional groups and superfluous waste material upon creation, whose presence may be masked by functional homogenisation of the surface. Various methods of homogenisation were trialled during the course of experiments to complete this thesis. One method investigated was the Fenton treatment of the particles to fully hydroxylate the ND surface. However, it was deemed more effective and more time efficient to utilise plasma hydrogenation to achieve surface homogenisation, resulting in complete hydrogen termination. In order to mimic the functionality of polylysine, which aids neuroadhesion and growth when applied to a culture substrate, it was decided to attach an amine containing compound to the hydrogenated ND particles. This was achieved through the photochemical attachment of trifluoroacetic acid protected 10-amino-dec-1-ene (TFAAD), which upon deprotection yields exposed amine functionality.

In order to attach these positively charged particles to glass cover slips the best course of action was to first coat the glass with a negatively-charged surface layer to enhance electrostatic attachment of the ND. The surface layer chosen was acrylic acid, deposited by

plasma polymerisation due to speed, biocompatibility, convenience and stability. This ensured attachment of the ND remained steadfast.

The coating was assessed by its ability to sustain the attachment and growth of neuronal cell lines and primary rat neural cells for periods of up to 21 days. Cells were fluorescently stained at various time points and cytotoxicity analysis was undertaken by way of MTT assays. ND attachment was also verified by atomic force microscopy (AFM), with the particles themselves assessed by transmission electron microscopy (TEM). Lastly, surface functionality of the particles was also confirmed by X-ray photoelectron spectroscopy (XPS) which verified the UV photoattachment procedure of protected amines to hydrogenated ND surfaces was successful and viable. Where appropriate, all data in the following chapter will be quoted to three significant figures (3 s.f.).

4.2 Surface Characterisation of Nanodiamond Particles

4.2.1 Nanodiamond Functionalisation Routes

Detonation nanodiamond (ND), as received, contains a litany of functionalities upon the particle surface that initially renders photochemical grafting of desirable moieties difficult. Therefore to enable grafting of functional groups the surface of the particles first required homogenisation, either via hydrogenation or hydroxylation (figure 51). Hydroxylation, which coated the particle surface with hydroxyl groups, was performed either via a Fenton process (Fenton ND) or one which utilised nitric acid and sulphuric acid to achieve a similar outcome (non-Fenton ND). The hydrogenated particles, on the other hand, were further functionalised by photografting with TFAAD. Once deprotected, this molecule became 10-amino-dec-1-ene which exposed amine functional groups upon the ND surface.

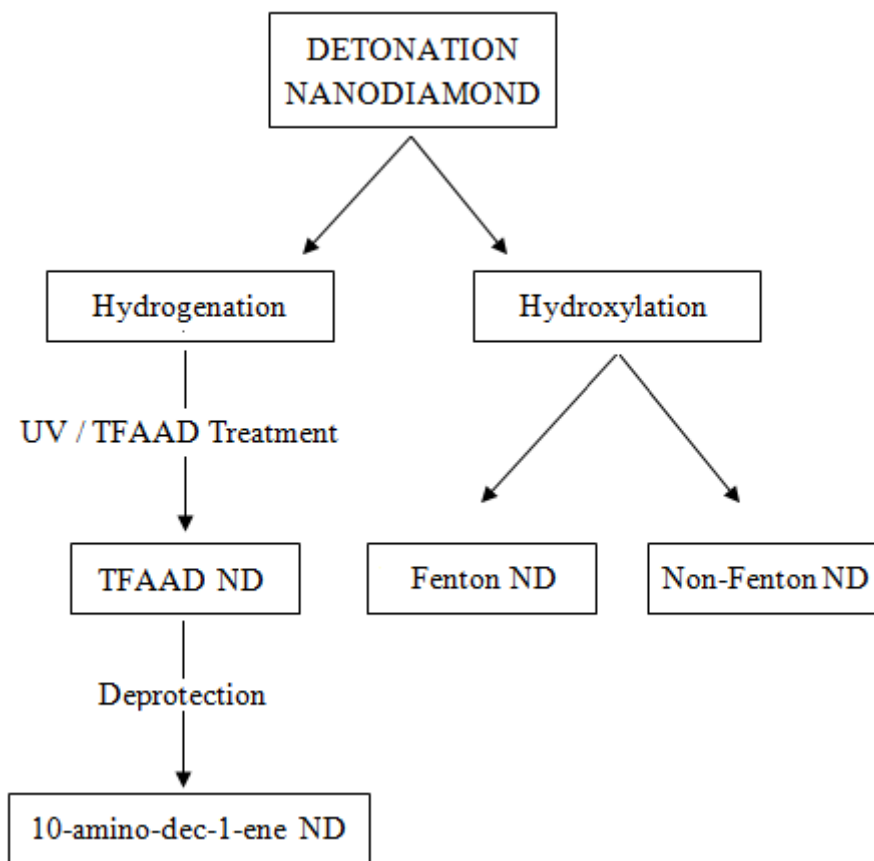


Figure 51: Homogenisation routes of detonation ND and subsequent functionalisation processes utilised

<u>Detonation Nanodiamond</u>		
Hydrogenated ND	Hydroxylated ND	
TFAAD-ND	Fenton ND	Non-Fenton ND
<i>10-amino-dec-1-ene ND</i>		

Table 6: Summary of detonation nanodiamond functionalisation routes

Although two functional-homogenisation routes were chosen to ameliorate the undesired moieties present upon the detonation-ND surface (table 6), hydrogenation was selected as the main method as the initial step in the functionalisation process. Both surface functionalities

(C-H and C-OH) could act as suitable substrates upon which TFAAD could be attached using UV radiation. However, XPS analysis of hydrogenated ND illustrated that a greater proportion of the surface was hydrogenated following surface treatment (approximately 57.0% - figure A-8 listed within the appendix) in comparison to the hydroxylated nanodiamond samples where comparatively fewer C-OH groups were detected (approximately 36.0% - figures A-9 and A-10 listed within the appendix). Additionally, ND-hydroxylation was a cumbersome and time-consuming procedure, whereas hydrogenation could be achieved relatively quickly using a hydrogen plasma.

4.2.2 X-ray Photoelectron Spectroscopy (XPS) Graphs

In order to characterise the nanodiamond-derived and pure acrylic acid surfaces, X-ray photoelectron spectroscopy was performed. Contact angle measurements complemented this data also and are listed under section 4.2.5 within this results chapter.

Survey and high resolution carbon (C(1s)) XPS spectra were collected for the nanodiamond derived surfaces, as well as from glass and ppAA, to allow for functionality comparison across the samples. The uppermost nanometres of the surface were analysed by a Kratos AXIS Ultra DLD instrument with data processing, analysis and charge correction completed by CasaXPS (ver.2.3.12 Casa Software Ltd.).

4.2.2.1 XPS - Plasma Polymerised Acrylic Acid (ppAA)

The acrylic acid polymer surface was created by plasma polymerisation upon glass cover slips using a custom-built glass reactor. Analysis of the plasma polymerised acrylic acid (ppAA) survey spectrum (figure 52A) illustrated that the percentage of carbon present ($78.6\% \pm 0.210\%$) was higher than that recorded in the monomer chemical structure (typically 60%) [233]. This was a result of bond breakage and fragment synthesis, followed

by recombination, all of which are typical events during the plasma polymerisation process [234]. Within the survey spectrum the presence of oxygen ($21.3\% \pm 0.130\%$) and carbon ($78.6\% \pm 0.210\%$) was recorded with trace amounts of nitrogen ($0.750\% \pm 0.120\%$) and sodium ($0.270\% \pm 0.130\%$) also being detected. No substrate silicon signal was detected, indicating that the acrylic acid substrate had a thickness of at least 10 nm.

The C(1s) peak was also deconvoluted illustrating the presence of five component peaks (Figure 52B), which comprised 56.0% aliphatic carbon (C-C) at 285 eV, 14.4% hydroxyl / ether (C-O) at 287 eV, 7.80% carboxyl / ester (COOH) at 289 eV and a 11.7% corresponding β shift (C-COOH) at 286 eV and 10.1% carbonyl (C=O / O-C-O) groups at 288 eV. This is in broad agreement with previous XPS studies on plasma polymerised acrylic acid surfaces [211, 222, 233, 235] and in stark contrast to the glass spectra listed in figure A-1 within the appendix.

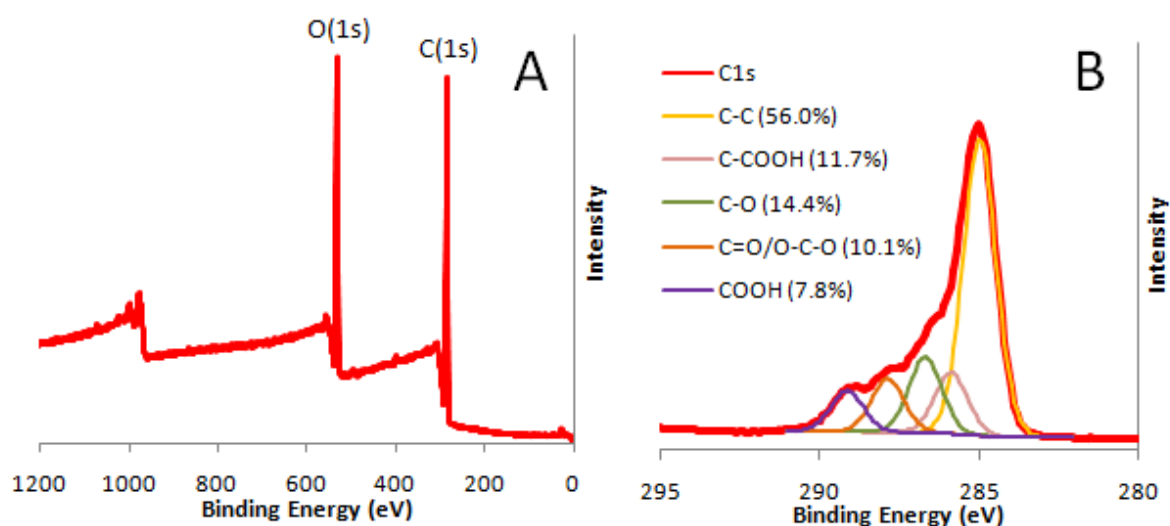


Figure 52: X-ray photoelectron spectroscopy spectra (XPS) depicting survey (A) and high resolution carbon (B) scans of plasma polymerised acrylic acid on glass (ppAA).

4.2.2.2 XPS - 10-amino-dec-1-ene functionalised Nanodiamond bound to plasma polymerised acrylic acid (AAND)

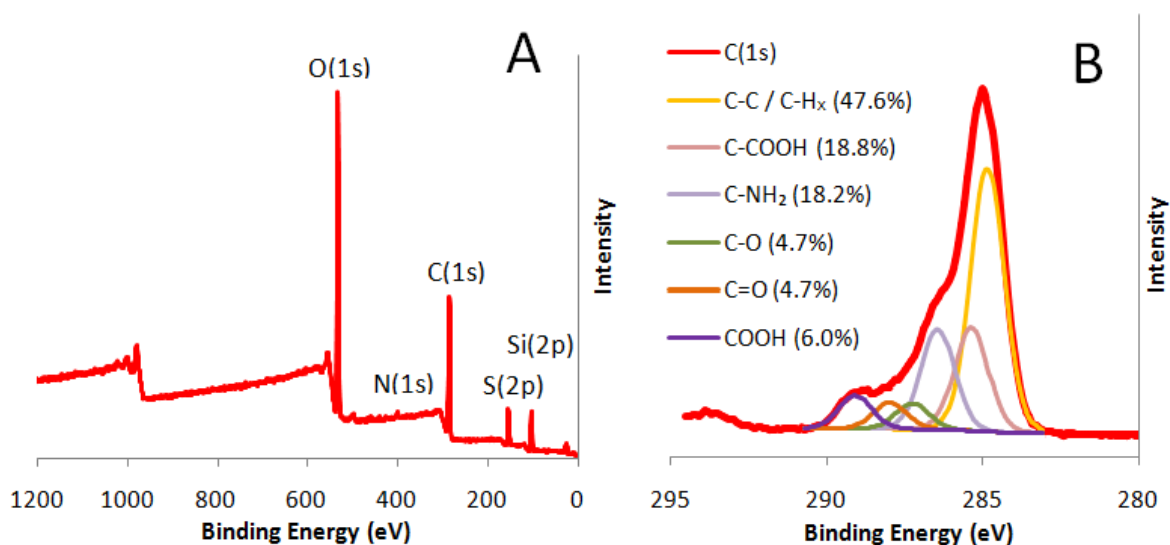


Figure 53: X-ray photoelectron spectroscopy spectra (XPS) depicting survey scan (A) and high resolution C(1s) scan (B) of hydrogenated nanodiamond functionalised with 10-amino-dec-1-ene electrostatically bound to ppAA (AAND). For clarity, the S(2p) and Si(2p) peaks are located at 167 eV and 101 eV respectively.

This particular sample (AAND) was created through the deprotection of the TFAAD group bound to the hydrogenated ND. The XPS survey spectrum (figure 53A) displayed several differences compared to the pure acrylic acid XPS data (figure 52). The presence of oxygen ($35.7\% \pm 1.40\%$) was higher, whilst the silicon content ($9.87\% \pm 2.04\%$) was significantly greater, which was probably due to the readings being taken from an area of the acrylic acid / nanodiamond layer that was thinner than 10 nm with the underlying glass character of the substrate being detected. This may have been due to a batch of ppAA glass cover slips being coated to a thinner thickness than usual. However, it was thought that the amine-functionalised ND attachment process, which occurred by sonication, did not affect the integrity of the ppAA layer since AFM analysis revealed an uninterrupted surface coating of

amine-NDs, which would only adhere if the underlying glass had been sufficiently coated with ppAA (figure 60).

The atomic percentage of nitrogen present was also more than double ($1.16\% \pm 0.280\%$) than that present in the acrylic acid sample, which again, was to be expected due to the attached amine-nanodiamond associated with the 10-amino-dec-1-ene functionalisation step. No other elements were detected in the survey scans confirming minimal contamination.

The C(1s) spectrum was shown to consist of six different carbon environments, reflecting the inclusion of the acrylic acid substrate and the amine functionalised nanodiamond. The removal of the highly electronegative trifluoroacetic acid, through deprotection, was verified due to no fluorine signal being detected within the XPS survey scan (figure 53A). The absence of the fluorine peak illustrated the variability of the deprotection process, since a small fluorine peak was detected in the survey spectrum analysing Am-ND (figure 54A). The carbon environments detected within the high resolution carbon scan of AAND are listed within figure 53B. Importantly, the proportion of amine groups present accounted for 18.2% of the total signal recorded and could be directly attributed to the binding of amine-functionalised ND to the ppAA surface.

It is significantly more difficult to hydrogenate the surface of a nanoparticle compared to a flat sample due to the need for two surface treatments and the requirement to rotate the particles after one treatment to hydrogenate the area that was previously in the shadow of the hydrogen plasma. Fortunately however it is anticipated this low level of oxidation had little impact on the binding of TFAAD to the hydrogenated ND surface. Assuming a smooth (100) oriented diamond surface there would be approximately $1.50 \times 10^{15} \text{ cm}^{-2}$ carbon bonds which could be hydrogen-terminated following surface treatment. The diameter of a 10-amino-dec-1-ene molecule is approximately 5.01 \AA [236]. However, this does not take into account the

trifluoroacetic acid group on the TFAAD molecule, which, due to it being situated perpendicular to the carbon backbone of the amine molecule, would give a diameter of 8.78 Å. In the case of a closely-packed 10-amino-dec-1-ene film, an upright standing molecule would require an area of approximately $2.00 \times 10^{-15} \text{ cm}^2$, assuming rotational symmetry. Each 10-amino-dec-1-ene molecule covers an area of 6 hydrogen atoms, of which only one needs to be cleaved for amine attachment to the ND surface. It therefore follows that even if the carbon surface is only 50% saturated with hydrogen this would still far exceed the concentration required for the development of a close-packed 10-amino-dec-1-ene film [236].

4.2.2.3 XPS - 10-amino-dec-1-ene functionalised ND (Am-ND)

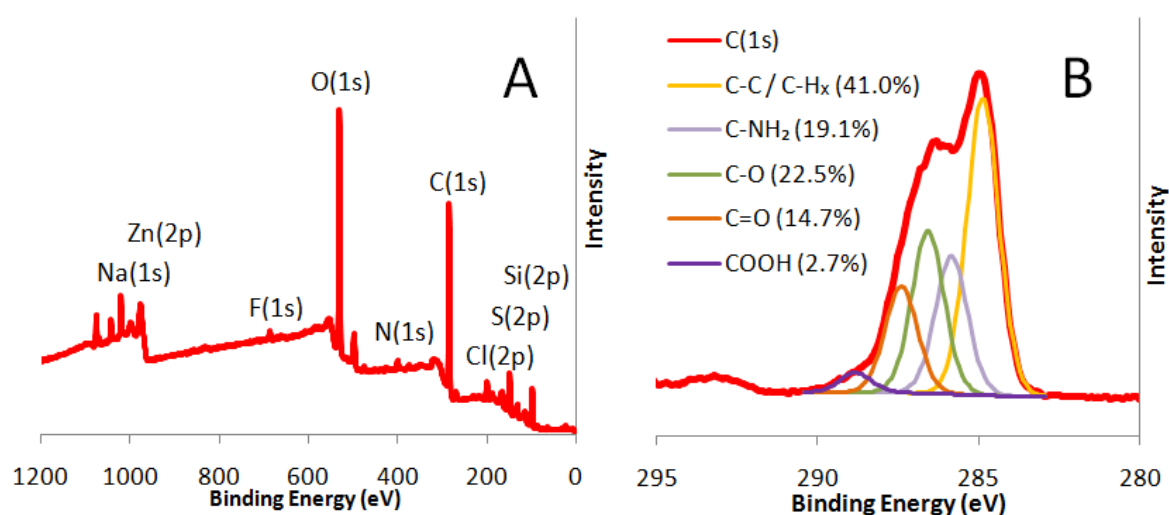


Figure 54: X-ray photoelectron spectroscopy spectra (XPS) depicting survey scan (A) and high resolution C(1s) scan (B) of 10-amino-dec-1-ene functionalised ND. For clarity, the Cl(2p), S(2p) and Si(2p) peaks are located at 200 eV, 167 eV and 101 eV respectively, whilst the Na(1s) and Zn(2p) peaks are located at 1072 eV and 1021 eV respectively.

Amine-terminated ND (ie TFAAD-ND which has been deprotected) was difficult to categorise due to the small quantity of sample available for analysis. Trace levels of contamination were present from sodium (1072 eV), chlorine (200 eV), zinc (1021 eV) and

sulphur (168 eV) as depicted on the survey spectrum (figure 54A). Carbon ($53.1\% \pm 0.530\%$) and oxygen ($19.2\% \pm 0.330\%$) were the two most prominent elements.

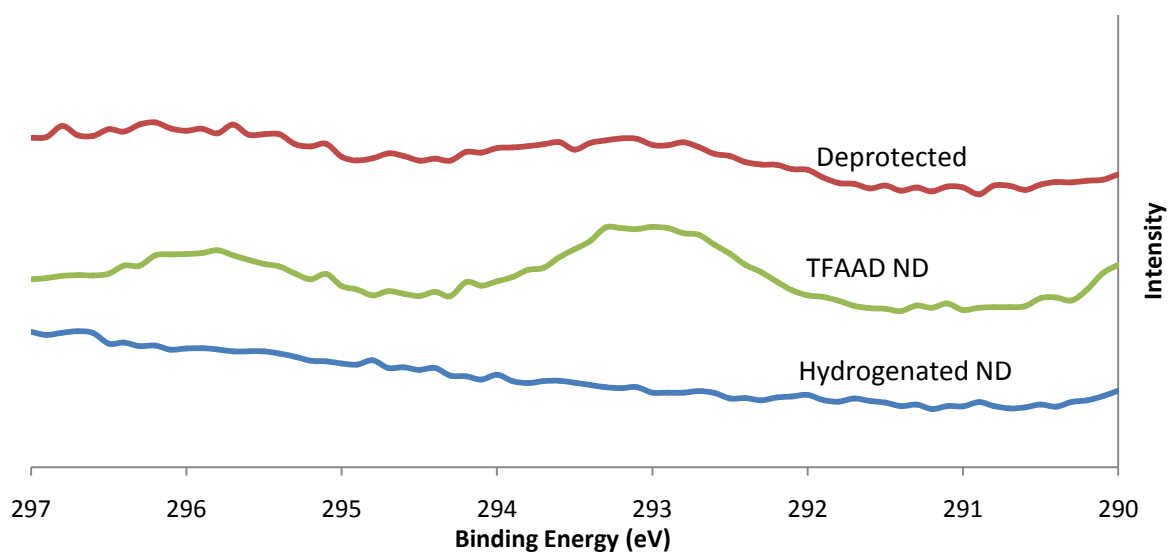


Figure 55: C(1s) XPS spectra of ND after hydrogenation in a hydrogen plasma (blue), after photografting of TFAAD (green) and following deprotection (red) to yield the primary amine functionality. The main C(1s) peak at 285.0eV is off-scale to enhance visibility of the peaks associated with the CF_3 group (295.8 eV) and the carbonyl group (292.9 eV) from the trifluoroacetamide molecule within TFAAD.

The C(1s) spectrum of Am-ND (figure 54B) at first appears similar to that of hydrogenated ND (appendix figure A-8), however deconvoluting the peak revealed a number of different carbon environments. Approximately 60% of the carbon bonds could be attributed to the C-C / C- H_x or amine functional groups. The remainder were oxygenated carbons which may have arisen due to contamination. The presence of a slight residual peak at 292.2 eV indicated the carbonyl group of the trifluoroacetic acid. This remained bound to a minority of 10-amino-dec-1-ene molecules following the deprotection process. This distinction is illustrated more clearly in figure 55. However, after deprotection had occurred the peaks at 292.9 eV and 295.8 eV (associated with the C- F_3 group) vastly reduced in size (figure 55 – red line) and the

fluorine peak at 689.8 eV (figure 54A) became approximately 40% of its original size. It therefore follows that around 60% of the $-CF_3$ groups were removed by deprotection. This figure has been corroborated from previous procedures where similar TFAAD deprotection rates were recorded [65, 237]. Although no high resolution N(1s) spectra were collected, previous studies [65] have stated that although the intensity of the N(1s) peak remains unchanged following deprotection, the peak is said to broaden slightly and shift to a lower binding energy of 401.1eV from 401.6 eV. This is due to the vastly reduced presence of the electron-withdrawing trifluoroacetic acid protecting group.

It has been stated that the deprotection efficiency of TFAAD can be increased further if the molecules are physically separated from one another [65]. This can be aided by the use of a diluent such as dodecene within the TFAAD monolayer. It is therefore probable that the success of TFAAD deprotection is limited by the density and close-packed nature of the monolayer. Cross-polymerised 3D functionalised TFAAD layers will naturally be more difficult to deprotect and have a lower rate of deprotection efficiency. It was therefore preferable not to overexpose the sample surface to excessive UV illumination to prevent cross-polymerisation of the TFAAD.

4.2.3 Nanodiamond Transmission Electron Micrographs (TEMs)

Diamond particles, either treated or in the raw form, were immersed in distilled water to form a slurry before being applied to carbon coated TEM grids. These were allowed to air dry and were then analysed by TEM to illustrate the shape and size of the nanodiamonds and the degree of aggregation within each sample.

The synthesis procedure utilised to produce synthetic nanodiamond resulted in the formation of large aggregates as illustrated in figure 56A. The darker shading on the image represents larger ND clusters, the majority of whose surface area was concealed within the aggregate. In

order to efficiently functionalise the surface of each ND particle it was essential to break-down the clusters as much as possible to create greater numbers of smaller aggregates and single particles. By doing so, this ensured that ND amine-functionalisation was optimal, allowing for the treated surface to interact and positively influence cultured neuronal cells. The creation of a minimal-aggregate ND slurry also assisted in the development of a cell-substrate devoid of significant peaks or troughs that could have restricted neuronal growth and attachment.

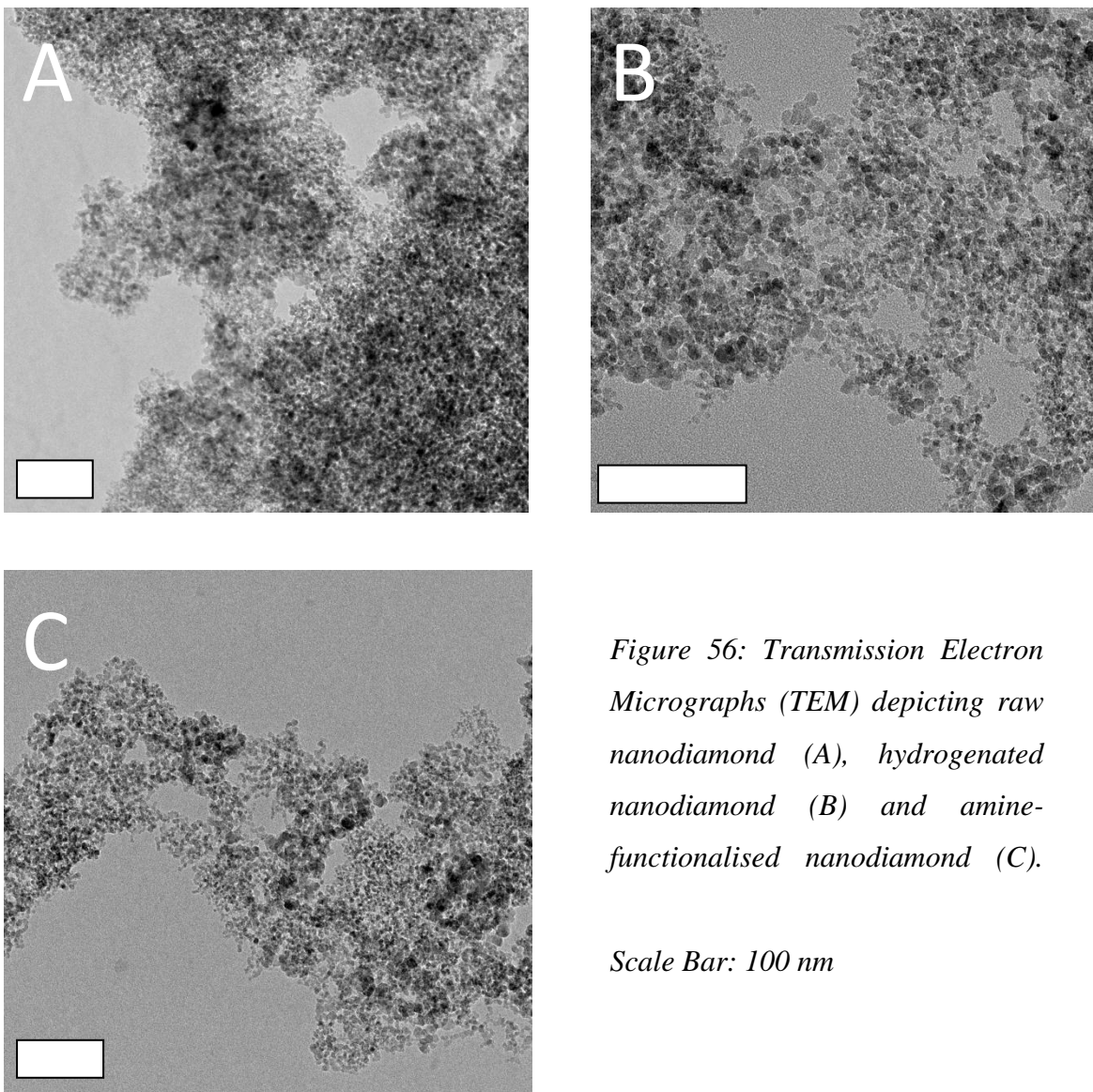


Figure 56: Transmission Electron Micrographs (TEM) depicting raw nanodiamond (A), hydrogenated nanodiamond (B) and amine-functionalised nanodiamond (C).

Scale Bar: 100 nm

Larger nano- and microscale ND clusters were heavily diminished in the ND-H and amine-functionalised ND samples (Figures 56B and 56C respectively), illustrating the effectiveness of hydrogenation in assisting deaggregation. However, due to the ND being stored as a slurry within distilled water, once this had been applied to a surface and had been allowed to air-dry, limited aggregation could reoccur due to capillary action and attractive van der Waals forces bringing individual particles together [115]. This process could be limited somewhat by slurry ultrasonication prior to ND-deposition, alleviating extreme surface roughness. The absence of significantly large peaks on the AFM image depicting AAND (figure 60) corroborated this, although several multi-particle sized clusters were present.

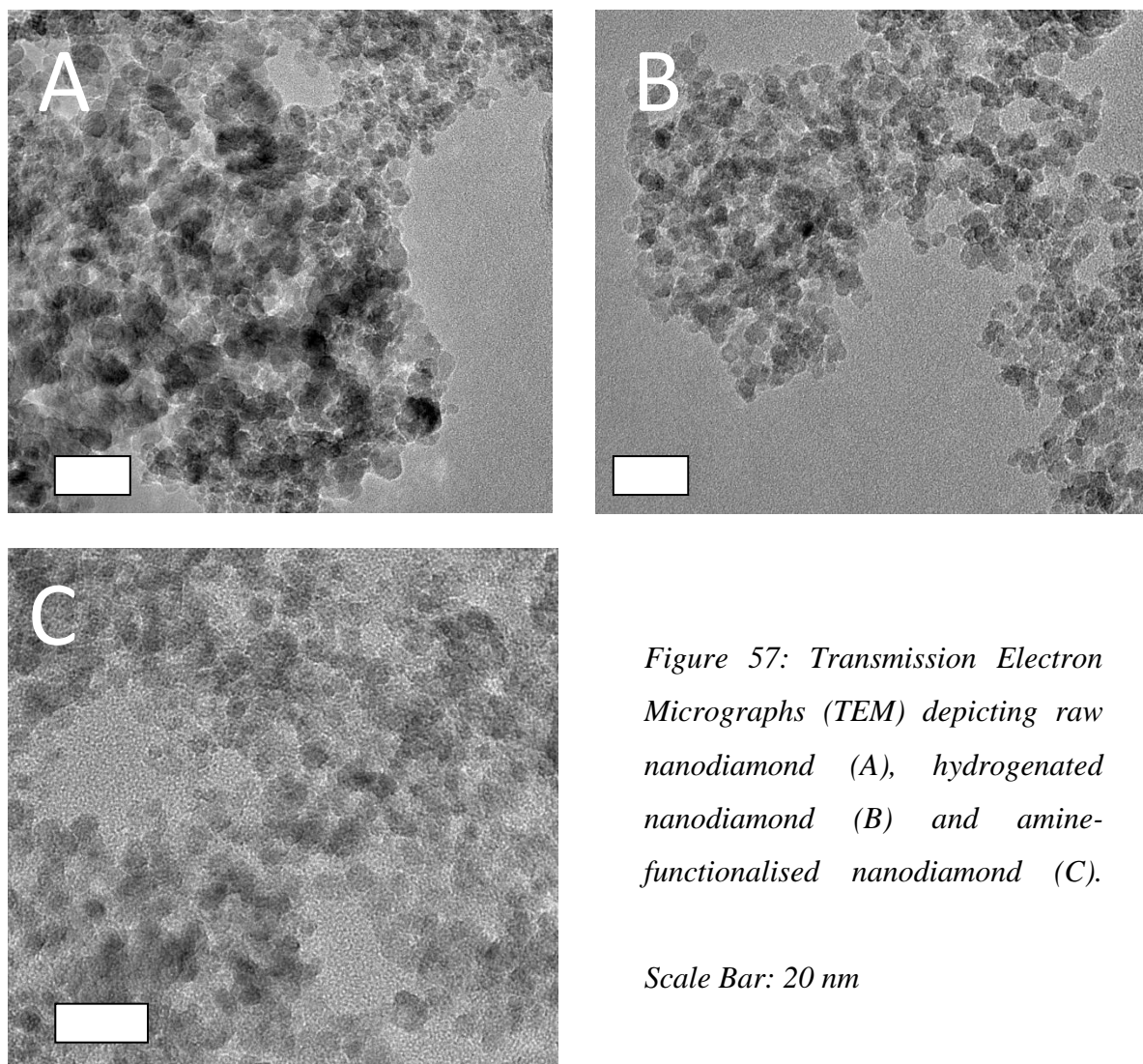


Figure 57: Transmission Electron Micrographs (TEM) depicting raw nanodiamond (A), hydrogenated nanodiamond (B) and amine-functionalised nanodiamond (C).

Scale Bar: 20 nm

Higher magnification images also depicted a lower degree of aggregation in the H-ND (Figure 57B) and amine-functionalised ND (Figure 57C) when compared to the raw ND image (Figure 57A). Individual particles could be easily identified, all of which had an approximate diameter of between 5 - 10 nm and a spherical appearance. Unfortunately it was not possible to analyse the surface coverage of AAND by TEM, although this was attained using a different analytical method (atomic force microscopy - figure 60). Despite the carbon coated TEM grid being successfully treated with ppAA, the carbon film was mostly destroyed following ultrasonication with the ND slurry (figure 58), highlighting that this coating technique may not be suitable for the most fragile of substrates. Importantly, however, AAND which was prepared on fairly fragile glass cover slips, reported no breakage or damage following plasma treatment or ultrasonication.

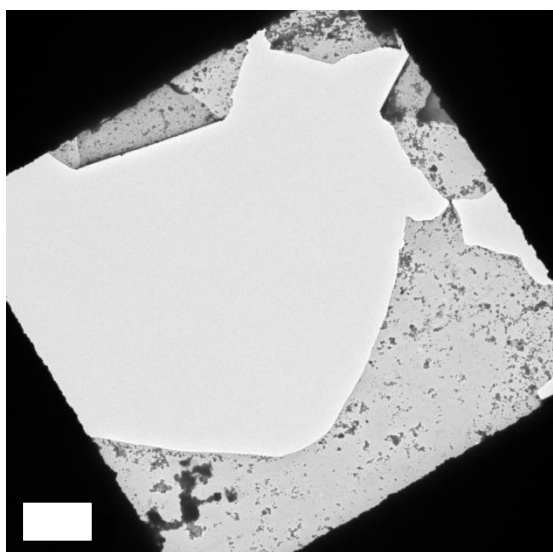


Figure 58: TEM Grid subject to coating with ppAA and attachment of amine-coated nanodiamond through ultrasonication. The process severely damaged the carbon film of the TEM grid and compromised the ND coating.

Scale bar: 5 μ m

4.2.4 Atomic Force Microscopy (AFM) Images of ppAA and AAND

Atomic force microscopy was performed on plasma polymerised acrylic acid (ppAA) and AAND surfaces to indicate their surface roughness and to provide illustrative proof of the binding of positively charged Am-ND to the negatively-charged acrylic acid coated substrate.

It was also useful to illustrate the effectiveness of the overall functionalisation process for ND deaggregation.

4.2.4.1 AFM Images - Plasma-Polymerised Acrylic Acid Coated Glass (ppAA)

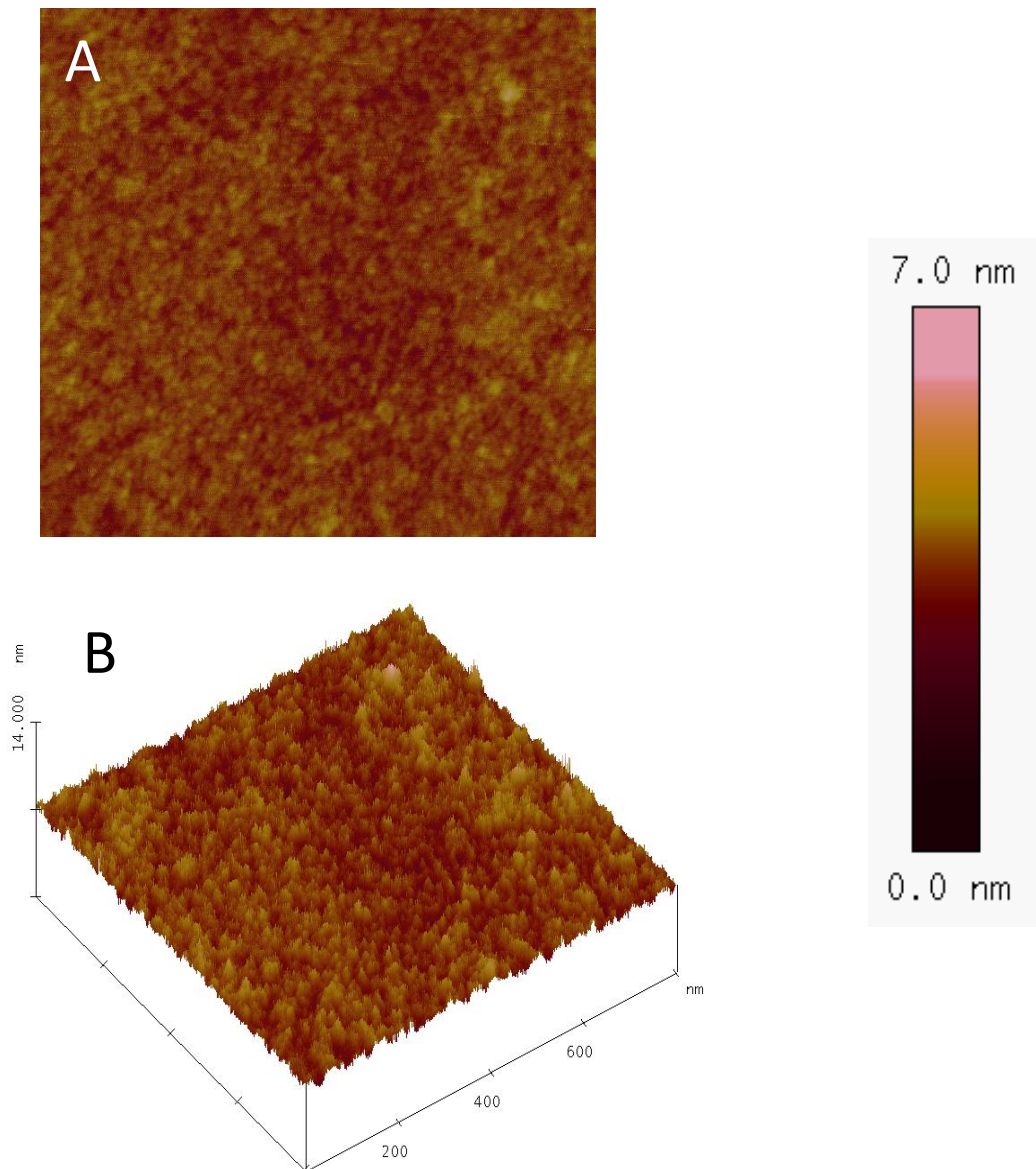


Figure 59: 2-D (A) and 3-D (B) atomic force microscopy (AFM) of plasma polymerised acrylic acid coated glass. Area Analysed: 800 nm².

The acrylic acid coated glass was cleaned in methanol prior to the AFM procedure and 800 nm² area was selected for analysis. The ppAA surface was remarkably devoid of any

significant surface features (figure 59). The polymer was coated to an approximate thickness of 10 nm to provide a smooth surface for the electrostatic attachment of amine functionalised nanodiamond. Any defects in the glass surface were concealed by the polymer film.

4.2.4.2 AFM Images - ppAA Coated with Amine Functionalised ND (AAND)

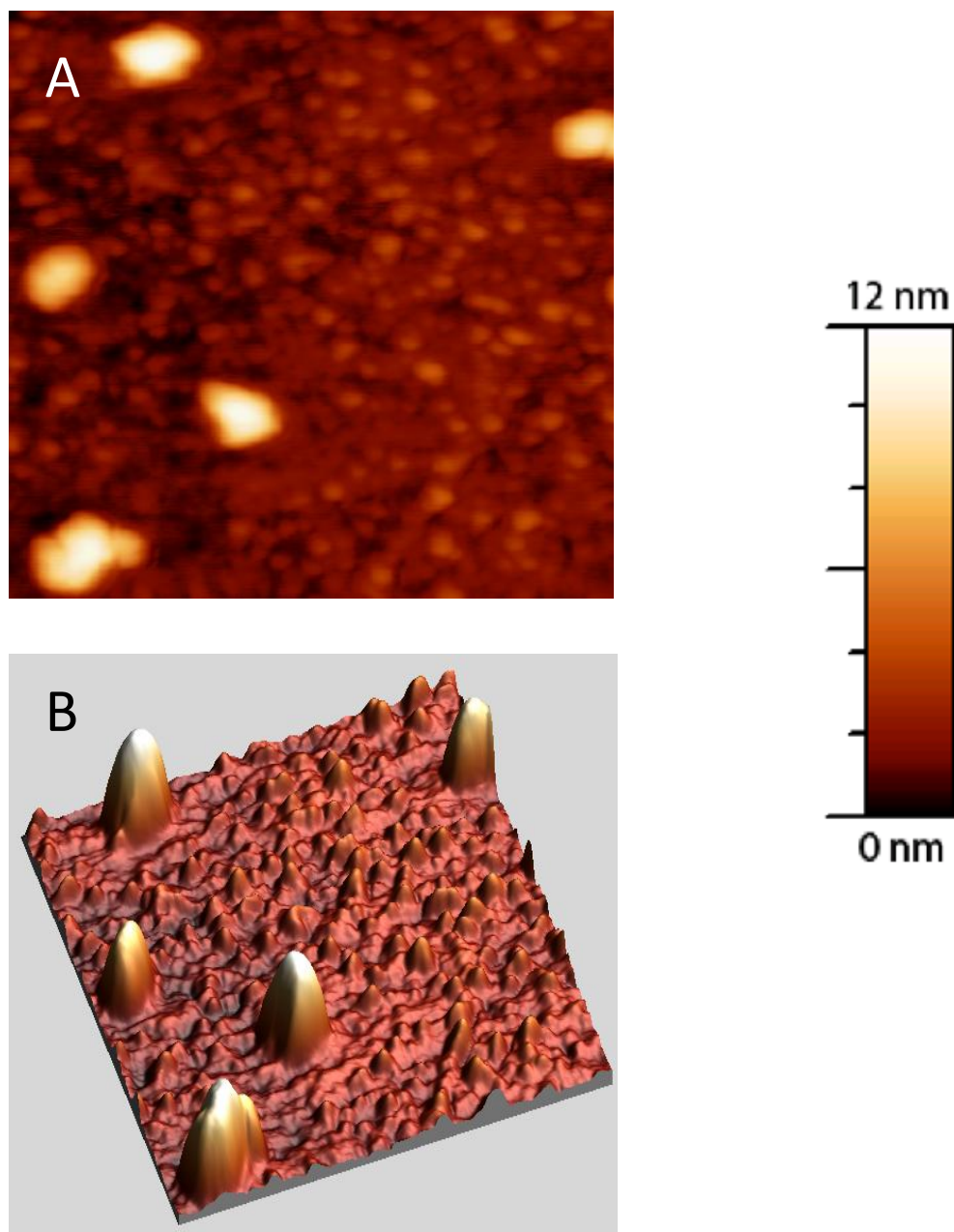


Figure 60: 2-D (A) and 3-D (B) atomic force microscopy (AFM) of AAND surface. Area Analysed: 250 nm².

Analysis of the AAND surface by AFM (figure 60) clearly depicted the uniform attachment of amine functionalised nanodiamond to the ppAA substrate. The ND clusters were mostly deaggregated following hydrogenation and sonication, however, some smaller clusters did remain, as depicted by the lighter coloured regions on the 2-D and 3-D micrographs.

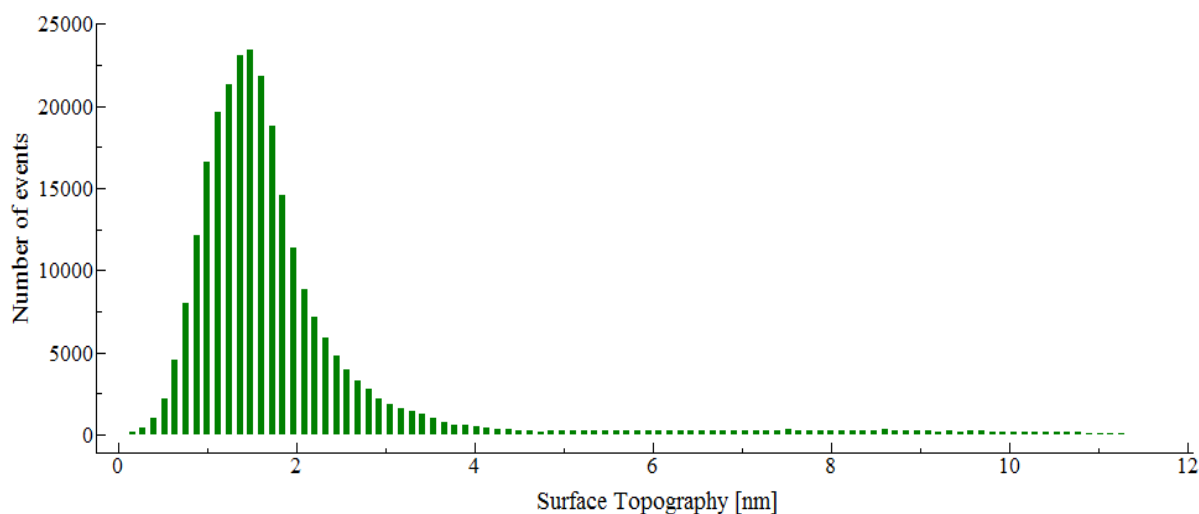


Figure 61: Surface height histogram representing the surface topography of AAND from figure 60.

The maximum height recorded from these clusters was approximately 12.0 nm, suggesting the clusters were only composed of three to four particles. This still compared very favourably to the aggregates which formed detonation ND which typically have a diameter between 50.0 – 500 nm [115]. The mean surface height of the sample approached 2.00 nm (figure 61), which is somewhat lower than the mean diameter of single ND particles at between 5.00-10.0 nm [115]. The root mean square roughness of the sample was 1.54 nm. It therefore follows that some of the ND particles embedded themselves in the ppAA film during sonication, this process being assisted by the coating's negative charge. Analysis of the 2-D AFM image clearly depicted at least two ND layers upon the surface, all of which were electrostatically attached within 10 minutes. It is not known whether the 'soft' nature of

the ppAA layer assisted in the binding of Am-ND, or whether it is the negative charge of the ppAA surface which is the more dominant factor.

4.2.5 Water contact angle measurements

The wettability of the surfaces was determined by contact angle measurement, which in itself provides an indication of surface-free energy. The water contact angles of glass, ppAA and AAND were measured ten times using a goniometer and an average was recorded. It can generally be said that surfaces which record a contact angle in excess of 90.0° can be regarded as being hydrophobic, being characterised by poorer wetting and lower surface energy. The lower the measured contact angle, the greater the hydrophilic character of the surface.

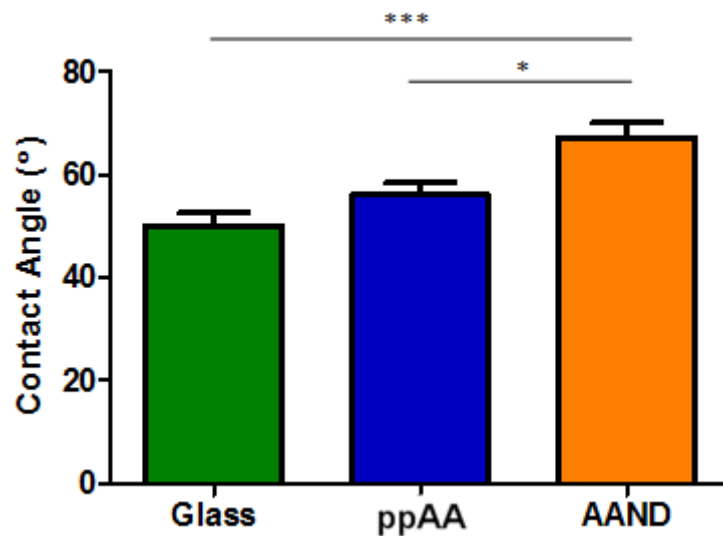


Figure 62: Mean water contact angle measurements of glass, ppAA and AAND taken at room temperature. Values were reported from the mean of twenty different readings \pm standard error. Significance was determined by one way anova utilising Tukey's multiple comparison test whereby; * $p < 0.05$, ** $p < 0.01$ and *** $p < 0.001$.

Although not a true indicator of the ability of a surface to sustain a population of cells, contact angle measurements can be useful in relation to other measures such as surface topography and chemistry in assessing cell culture suitability. Although all the surfaces were recognised as being hydrophilic (figure 62: Glass $49.9^{\circ} \pm 2.00$, ppAA $56.1^{\circ} \pm 1.90$, AAND $67.9^{\circ} \pm 2.3$) the lower contact angle recorded for glass illustrated its slightly greater wetting ability compared to either ppAA or AAND. However, this had little bearing on neuronal cell attachment capability, as the glass failed to support a healthy population of neuronal cells (figure 63A). Despite greater cell wettability generally supporting cell adhesion the apparent contradiction displayed in this data indicated that surface chemistry and topography can be greater determinatives to predict cell culture success [238].

4.3 Cell Culture upon ND Surfaces

4.3.1 Fluorescence Microscopy Images

Neuronal compatibility was assessed firstly by culturing NG108-15 neuroblastoma cells for 7 days upon the surfaces (ppAA, AAND, Glass, PL, Glass-ND and AAND-H) in serum free completed Dulbecco's modified eagle's medium (cDMEM). Once the cells had been fixed in formalin fluorescence microscopy allowed for the cells to be visualised using phalloidin-FITC and DAPI stains to assess phenotypical variations.

4.3.1.1 NG108-15 Cell Fluorescence Microscopy

Ideally, a surface for sustaining the growth and differentiation of neuronal cells should encourage cell adhesion and neurite outgrowth, whilst controlling proliferation at an acceptable rate so as not to impede neurite development.

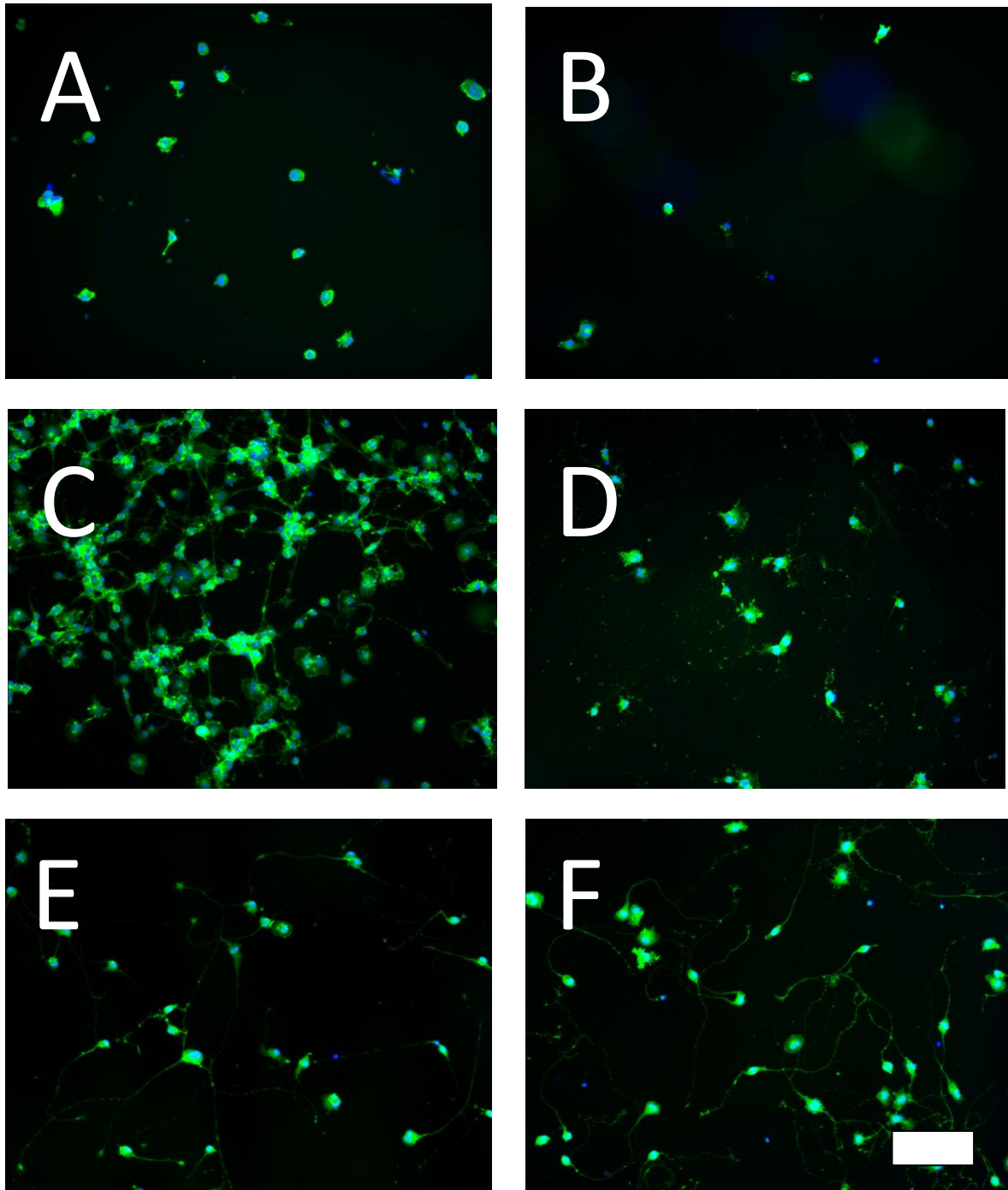


Figure 63: Fluorescence micrographs illustrating the growth of NG108-15 cells cultured for 7 days on (A) glass, (B) 10-amino-dec-1-ene functionalised nanodiamond treated glass (Glass-ND), (C) ppAA, (D) acrylic acid plasma polymer coated glass treated with hydrogenated nanodiamond (AAND-H), (E) AAND and (F) PL. Three separate triplicate repeat experiments ($n=9$) were conducted with each triplicate utilising a different batch of cells ($N=3$). Scale: $150\mu\text{m}$

After seven days cell culture it was seen that NG108-15 neuroblastoma adapted to each surface differently, all other factors being kept constant (temperature, media, initial cell seeding density). Upon glass, few neurites were apparent whilst cell growth and proliferation appeared to progress slowly. Indeed figure 63A depicts a circular cell phenotype normally associated with cells which experience weak surface binding.

Traditionally NG108-15 cells exhibit a phenotype which closely resembles that displayed on figures 63E and 63F. The poor surface growth on glass was expected of neuronal-type cells since a surface pre-treatment of adhesion molecules (typically polylysine or laminin) is normally required to aid adherence and differentiation to otherwise neutrally-charged or hydrophobic substrates. The gradual decrease in the mean NG108 neurite length recorded on glass between day 1 and day 7 from $68.2 \mu\text{m} \pm 3.30 \mu\text{m}$ to $37.6 \mu\text{m} \pm 2.70 \mu\text{m}$ further indicated the weak binding of the cells to the substrate as greater numbers of cells detached as the culture period progressed.

4.3.1.2 Dissociated Rat Dorsal Root Ganglia Immunofluorescence Microscopy

Dorsal root ganglia were isolated from the spines of euthanized rats and cultured on AAND, PL and glass surfaces for 21 days. After this period of time had elapsed the cells were fixed using formalin and analysed by immunofluorescence microscopy whereby Schwann cells and axons were visualised.

Dissociated dorsal root ganglia and Schwann cells were cultured successfully on AAND surfaces, forming a confluent layer of cells 21 days post-seeding. It was evident from figure 64A that three types of cells were isolated from the DRGs due to the differential staining observed. Axons positively stained red for the presence of β -tubulin III, which is a neuronal cell marker, whilst Schwann cells were stained green, signifying that they were S100 immunoreactive. However, a minority of cells only stained positive for DAPI, a nuclear

marker. It was deduced these cells were contaminating fibroblasts originating from the primary rat tissue. However, their presence was small, and had no adverse effect upon the viability of the neuronal or Schwann cells. Most fibroblasts had been removed during the isolation procedure. Further centrifugation of isolated DRGs prior to cell seeding may ensure future cultures are fibroblast-free.

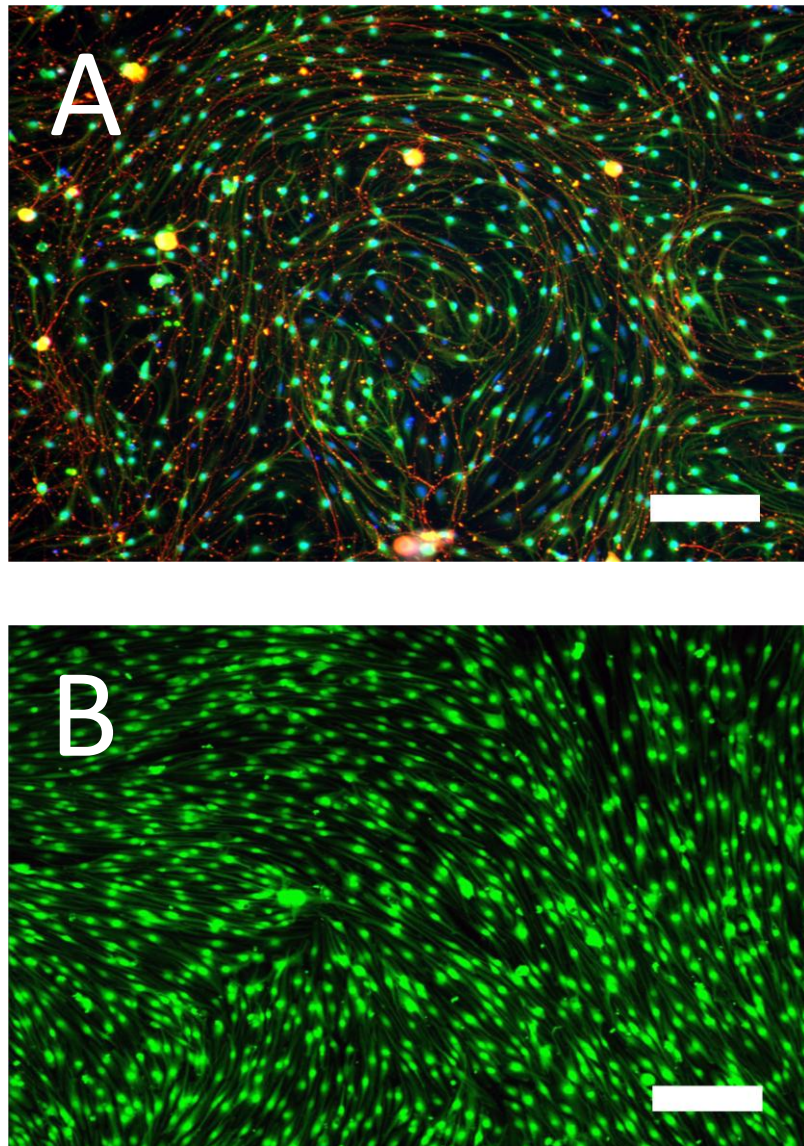


Figure 64: (A) Dissociated dorsal root ganglia (dDRGs) and (B) primary Schwann cells isolated from male Wistar rats cultured upon AAND surfaces for 3 weeks. Cells stained positive for β -tubulin III (red), S100 (green) and DAPI (blue). One triplicate experiment ($n=3$) was conducted which utilised a single batch of cells ($N=1$). Scale Bar: 150 μ m.

It was noted that the AAND surface was capable of supporting a healthy population of primary Schwann cells (figure 64B) signifying the terminal amine groups provided a preferential surface for cellular attachment, spreading and differentiation.

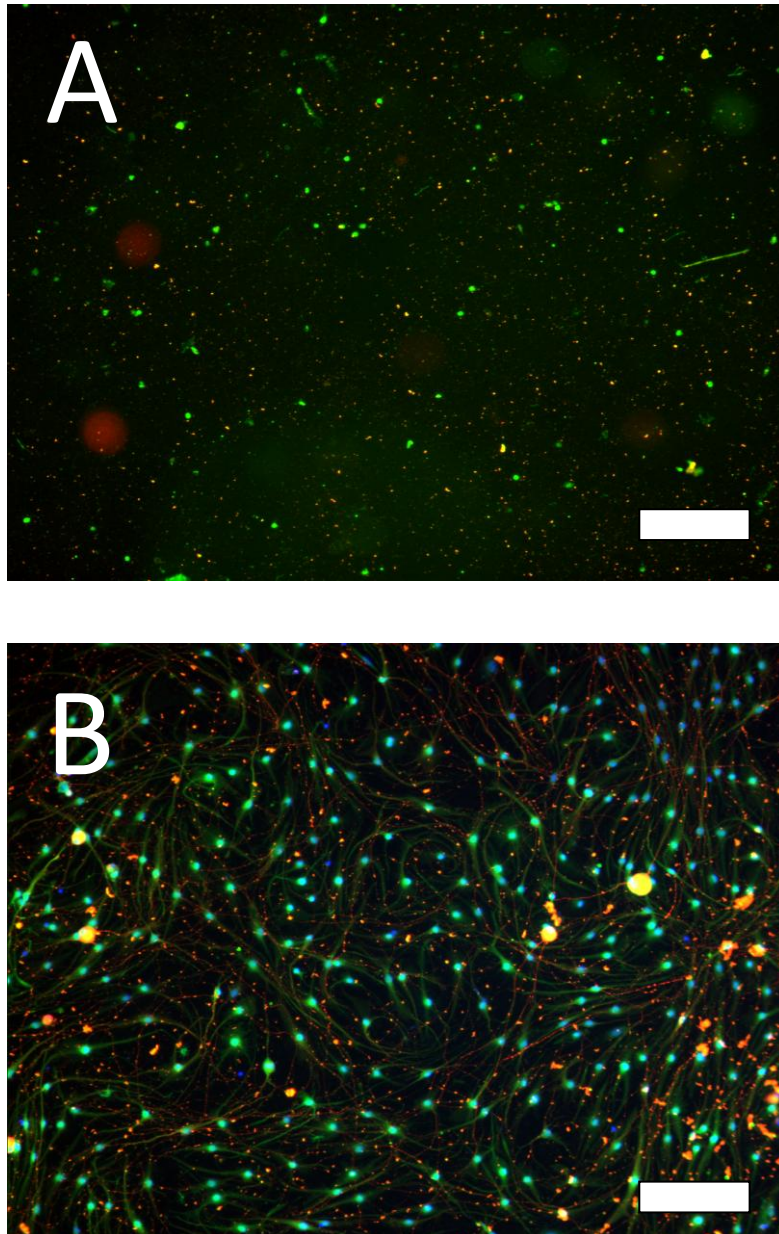


Figure 65: Dissociated dorsal root ganglions (dDRGs) isolated from male Wistar rats cultured upon (A) glass and (B) PL surfaces for 3 weeks. Red stain: β -tubulin III, Green stain: S100, Blue stain: DAPI. One triplicate experiment ($n=3$) was conducted which utilised a single batch of cells ($N=1$). Scale Bar: 150 μ m.

There appeared to be no morphological differences between the dissociated DRGs cultured on the positive control PL surface or the AAND surface. Both supported a confluent layer of cells with healthy sub-populations of neurons and Schwann cells. Cells on both surfaces appeared to grow at approximately the same rate; the seeding density being identical in both samples. What was also apparent was the lack of cell attachment on glass evidenced by figure 65A. Neither neuronal nor Schwann cells attached to the surface 21 days post seeding, with cell debris being the only visible feature on the micrograph. It was not clear whether cells were initially bound to the surface, only to later detach, or they never attached at all. The latter case is thought to be more likely, due to most neural cells negating to attach to a surface unless adhesion promoters such as polylysine are present to produce a surface more amenable to cell attachment. Although primary Schwann cells are known to attach to untreated glass the use of Bottenstein-Sato media may have disrupted their binding to glass in figure 65A, as Schwann cell growth medium was utilised for the culture of Schwann cells upon glass displayed in figure 66A.

4.3.1.3 Schwann Cell Immunofluorescence Microscopy

Schwann cells play a pivotal role in the process of peripheral nerve regeneration, assisting in axonal regrowth following neural transection. By creating a surface which is amenable to the adhesion, proliferation and culture of Schwann cells it would be appropriate to assume the possibility of utilising such a product within applications including brain computer interfaces (BCIs) where neuronal/axonal growth is of paramount importance.

Rat primary Schwann cells were isolated from the sural nerve and cultured on surfaces including AAND and PL for 21 days within Schwann cell media. Once this period had elapsed the cells were fixed in formalin and stained for the presence of the Schwann cell marker S100- β allowing for cell visualisation via immunofluorescence microscopy.

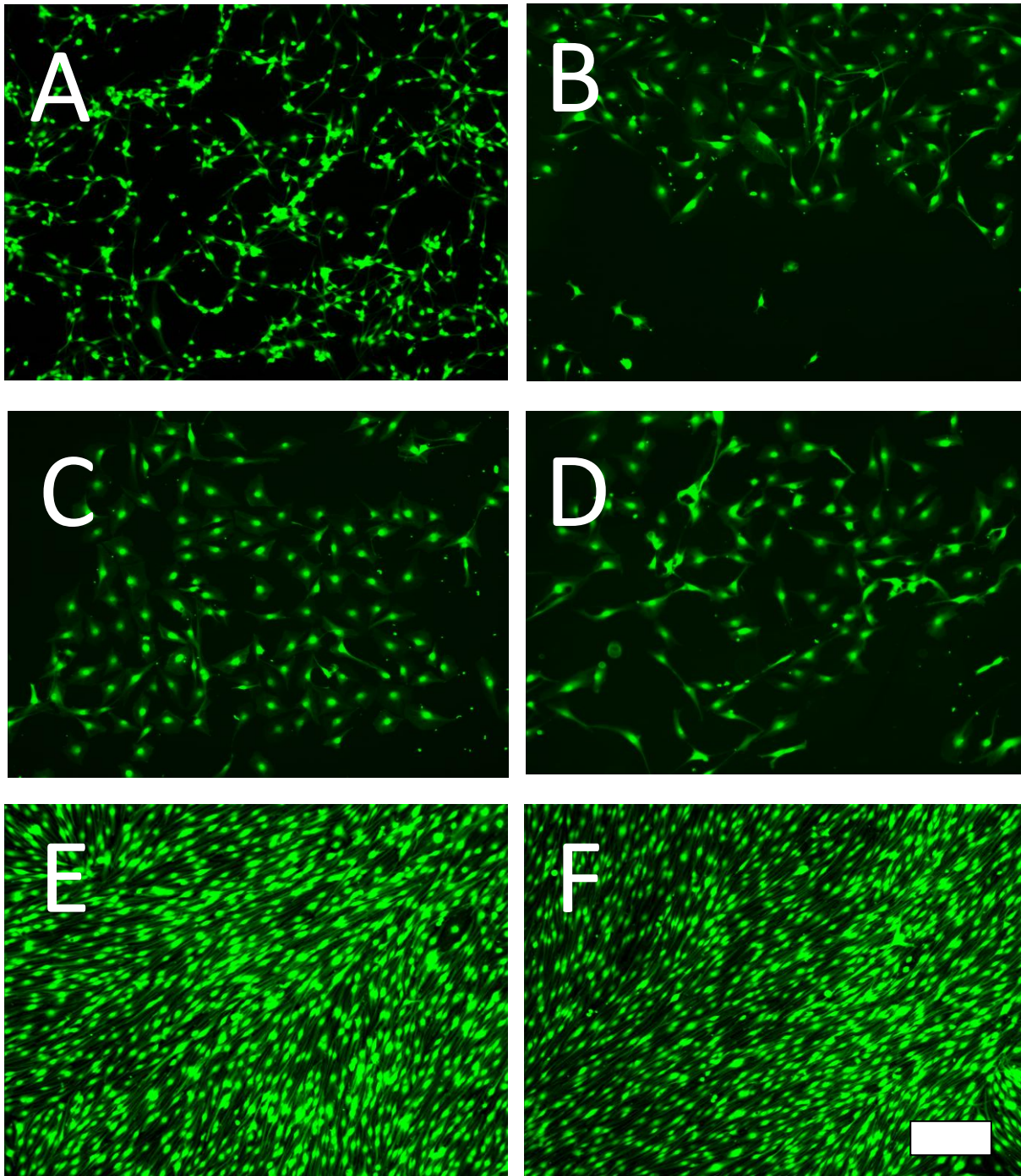


Figure 66: Fluorescence micrographs illustrating the growth of rat Schwann cells cultured for 21 days on (A) glass, (B) Glass-ND, (C) ppAA, (D) AAND-H, (E) AAND and (F) PL. Cells were stained for S100- β (green). One triplicate experiment ($n=3$) was conducted which utilised a single batch of cells ($N=1$). Scale: 150 μm .

Once 3 weeks had elapsed, it was important to note that all surfaces recorded attachment of primary Schwann cells, even those (glass – figure 66A and glass-ND – figure 66B) that were noticeably poor at sustaining neuroblastoma cells (figures 63A and 63B). Significant numbers of cells attached and appeared to replicate on the glass, albeit slowly.

However, the surface did not appear to provide any encouragement for the cells to proliferate in an ordered manner, as they appeared to align randomly. Cell spreading upon glass approximated 60-70% of the surface area three weeks post-seeding. This was opposed to the cells cultured on AAND and PL (Figures 66E and 66F) where a monolayer of 100% confluency was achieved, with dendrites mostly aligning parallel to each other and adopting a bipolar morphology. The aspect ratio (cell length/cell width) of cells cultured upon AAND and PL also appeared much greater due to the elongated cell morphology. Cells cultured on glass recorded shorter neurites due to the cells' slow rate of development.

On the other hand, Schwann cells cultured on glass-ND (figure 66B), ppAA (figure 66C) and AAND-H (figure 66D) all appeared comparable to each other where they adopted a phenotype not too dissimilar to those of fibroblasts. Relatively few cells possessed neurites, which reflected in cellular aspect ratios being far lower than those recorded upon PL or AAND. Glass-ND, ppAA and AAND-H also recorded lower cell densities than upon PL or AAND, however each cell covered a greater surface area on average. Indeed, despite all the surfaces tested being capable to supporting a population of Schwann cells, it appeared glass, ppAA, AAND and AAND-H would be poor choices of substrate due to poor cell morphological development despite cells being cultured in Schwann cell media.

4.3.1.4 Neuronal & Primary Schwann Cells Co-Culture upon AAND

It was beneficial to record the response of a neuronal and primary Schwann cell co-culture on the main surfaces tested in the study. Primary Schwann cells were first cultured upon glass,

ppAA, AAND and PL surfaces for 17 days in the presence of Schwann cell media. Once this time had elapsed NG108-15 neuroblastoma cells were applied to each surface and cultured with serum-free cDMEM and allowed to grow for four further days, so that by day 21 the cells on each substrate were fixed in formalin and visualised by immunofluorescence.

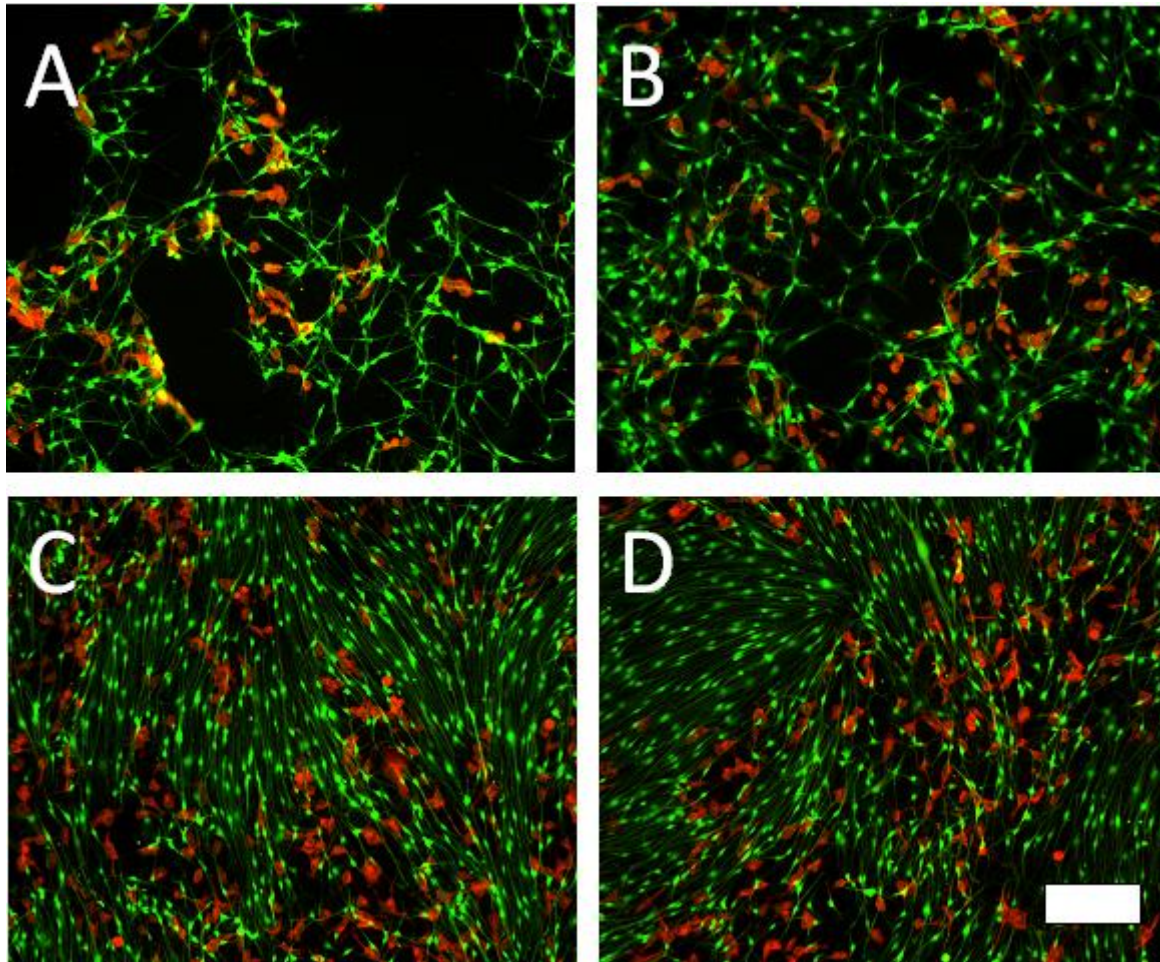


Figure 67: Neuronal (NG108-15) and primary Schwann cell co-cultures grown upon (A) glass, (B) ppAA, (C) AAND and (D) PL. Primary Schwann cells were cultured for 17 days on the substrates, after which NG108-15 cells were additionally applied and allowed to grow until day 21 when the cells were fixed. Cells were visualised by immunofluorescence for the presence of β -tubulin III (red) and S100- β (green). One triplicate experiment ($n=3$) was conducted which utilised a single batch of cells ($N=1$). Scale bar: 150 μ m.

Across glass, ppAA, AAND and PL Schwann cells and NG108-15 cells attached to create partial or full cellular monolayers of varying degrees of coverage. On glass (figure 67A), Schwann cells exhibited a spindle-like morphology and attached relatively sparingly, but at a greater density than the NG108-15's which were introduced at day 17. The NG108-15 cells appeared to adopt a spherical appearance and adhered to the surface in clusters with few neuritic processes apparent mirroring prior results and corroborating the poor performance of this cell type upon glass. The addition of the Schwann cells appeared to aid the adhesion of the NG108-15s possibly due to the integrins and cell adhesion molecules (CAMs) located upon Schwann cells, such as N-cadherin, since all NG108-15s were found in their immediate vicinity [239] [240]. This therefore suggests that NG108-15 cells may favour being cultured in the presence of Schwann cells rather than as a monoculture as seen in figure 63.

The co-cultures exhibited enhanced coverage on ppAA (figure 67B), being more evenly distributed with greater numbers of NG108-15 cells present, some of which displayed the onset of neurite formation. Schwann cells exhibited a more glial-type morphology upon ppAA than upon glass, with the cell nuclei being more apparent. Neurites upon both glass and ppAA surfaces however, appeared much shorter than those upon either AAND (figure 67C) or PL (figure 67D). Schwann cell development appeared to progress faster on AAND and PL with a complete surface monolayer of cells formed on both surfaces by day 21. Schwann cell neurites were mostly aligned parallel to each other on AAND and PL also, a trend which was not identified on either glass or ppAA. Additionally, NG108-15 cells also appeared fairly evenly distributed between the adhered Schwann cells, approximately half of which had developed neurites 72 hours following seeding.

4.3.2 Neurite Length Measurement Analysis – NG108-15 cells

The neurite lengths of cells cultured upon glass were seen to gradually decrease over the course of the study from an average of $68.2 \mu\text{m} \pm 3.30 \mu\text{m}$ at day 1 to $37.6 \mu\text{m} \pm 2.70 \mu\text{m}$ by day 7 (figure 68).

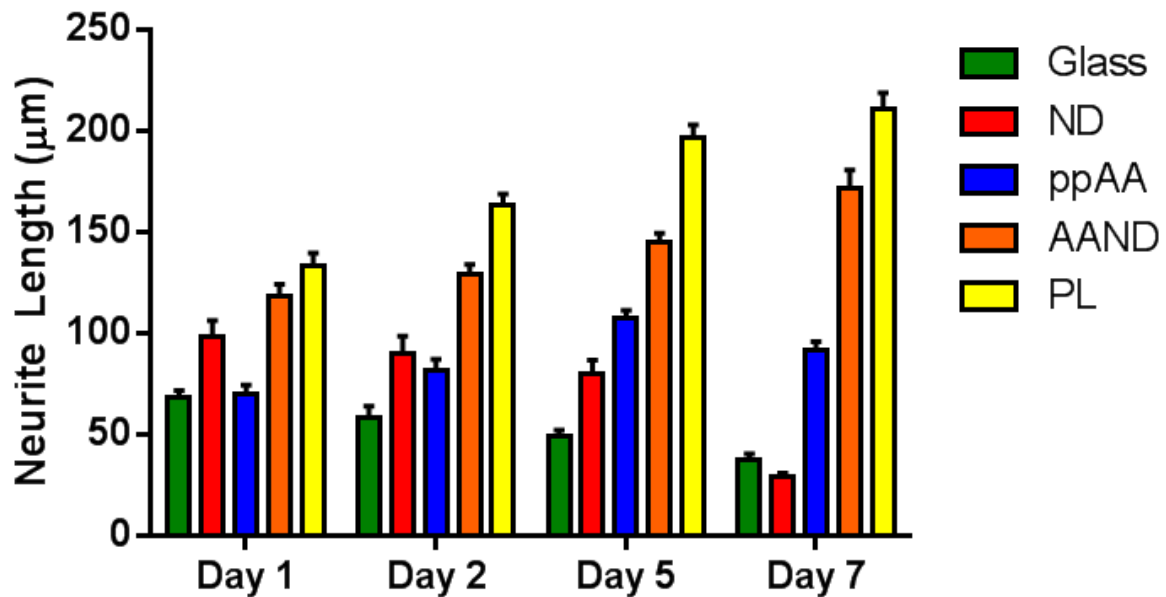


Figure 68: Mean neurite lengths (μm) of NG108-15 neuroblastoma cells cultured upon glass, glass-ND, ppAA, AAND and PL surfaces over periods of either 1, 2, 5 or 7 days. Values are reported from the mean (\pm standard error) of three separate triplicate repeat experiments ($n=9$) with each triplicate using a different batch of cells ($N=3$). Complete statistical analysis of the mean dendrite length data are provided overleaf in table 7.

- Statistical Analysis Tables – Neurite Length Data

DAY 1	Glass-ND	ppAA	AAND	PL
Glass	*	N/S	***	***
Glass-ND		**	*	***
ppAA			***	***
AAND				N/S

DAY 2	Glass-ND	ppAA	AAND	PL
Glass	*	N/S	***	***
Glass-ND		N/S	***	***
ppAA			***	***
AAND				***

DAY 5	Glass-ND	ppAA	AAND	PL
Glass	N/S	***	***	***
Glass-ND		N/S	***	***
ppAA			***	***
AAND				***

DAY 7	Glass-ND	ppAA	AAND	PL
Glass	N/S	***	***	***
Glass-ND		**	***	***
ppAA			***	***
AAND				**

*Table 7: Statistical significance data relating to figure 68 determined by Tukey's multiple comparison test and one way-anova, whereby; * $p < 0.05$, ** $p < 0.01$, *** $p < 0.001$ and N/S = no significant difference.*

Similarly glass-ND surfaces also reported a decrease in mean neurite length over the period of the experiment. However, the results recorded in the initial stages of cell culture (days 1 and 2) were encouraging with neurite lengths averaging close to 100 μm , which was significantly higher than those recorded on pure glass. The mean neurite length then decreased by day 5 ($79.6 \mu\text{m} \pm 6.90 \mu\text{m}$) and significantly so by day 7 ($28.8 \mu\text{m} \pm 1.80 \mu\text{m}$). This was most probably the result of a weakly-bound ND layer, which formed on the glass during sonication and gradually disintegrated after 5 days immersion in DMEM. Once the layer started to break-away from the surface this would also have encouraged cell detachment, thus leading to a decrease in the average neurite length. The proportion of cells which bore neurites (figure 69) tended to also decrease as time progressed, stagnating by days 5 – 7 at just 20 – 25%. This reflected the poor compatibility of such a surface for neuronal cell culture as ideally all viable NG108s should express neurites. Less than optimal neurite expression is normally an indication of weak cell adhesion to a substrate, as well as restricted cell mobility.

The hydrophilic ppAA substrate, despite being negatively-charged, encouraged cell proliferation and, to some extent, neuritic outgrowth. It has been previously reported that ppAA acts as a cell adhesive [241, 242] due to the presence of highly polar carboxylic groups [243]. Indeed, the hydrophilic nature of the coating encouraged proliferation to such an extent that expression of neuronal phenotype and differentiation appeared to suffer. Figure 63C, depicting NG108s which had been cultured on ppAA for one week, exhibited a higher cell density than on any of the other surfaces. However, the cells appeared to bunch together on the surface, restricting the ability of some neuronal bodies to bear neurites. This was evident from figure 69 which showed a marked decrease in the proportion of neurite-bearing cells present between day 5 ($43.3\% \pm 0.800\%$) and day 7 ($30.3\% \pm 1.00\%$) which contrasted with the consistent increases recorded from NG108-15s cultured on AAND and PL surfaces. Consequently, as the cells continued to proliferate and approach confluence, the mean neurite length began to decrease in the latter stages of the study upon ppAA, recording a value of $91.1 \mu\text{m} (\pm 4.60 \mu\text{m})$ by day 7, which had declined from a peak of $107 \mu\text{m} (\pm 3.70 \mu\text{m})$ by day 5 (figure 68). Similar findings were echoed by He *et al* [233] who discovered that endothelial cells cultured upon ppAA proliferated over 100% faster, produced greater quantities of extracellular matrix and acquired a different phenotype compared to those grown on control surfaces. Although no analysis of the ppAA film utilised in the thesis experiments was conducted post-cell culture, the growth of NG108s on the surface did not suggest any significant spallation or swelling had occurred by day 7, otherwise cell detachment would have been apparent.

Hydrogenated nanodiamond was also electrostatically attached to ppAA to test whether the ND nanostructured surface exerted an influence on the attachment, proliferation or phenotype of neuronal cells (figure 63D). This also permitted the influence of the 10-amino-dec-1-ene functional group on H-ND to be compared (figure 63E). Few cells were present on the

AAND-H surface, with a distinct lack of neurites. This meant measuring the length of any processes that were present originated from a sample size much smaller than from all other surfaces where at least fifty neurites were selected for measurement.

These results for the AAND-H surface contrast sharply with figure 63E and 63F displaying NG108-15 growth upon AAND and PL respectively. Over the week-long period of culture the growth of NG108-15s on AAND were comparable to those of PL, the positive control. Long neuritic processes, some in excess of 300 μm , were present on both AAND and PL, however NG108-15s cultured on AAND had shorter neurites on average over all the time points measured. Nevertheless, AAND still exhibited neurites which were far longer than those upon the other surfaces analysed, and between days 5 - 7, the growth of neurites appeared to accelerate (day 2 – 5 AAND growth rate: 12.0 %, day 5 – 7 AAND growth rate: 18.3 %) whilst those on PL showed signs of length stagnation (day 2 – 5 PL growth rate: 20.0%, day 5 – 7 PL growth rate: 7.50 %) which is apparent from figure 68. From these differences in growth rates it can be assumed that had the cell culture time-points been extended the mean neurite length of NG108-15s cultured upon AAND would have approached those cells which were measured upon PL. The decreasing neurite growth rate on PL could be attributed to increased levels of cell confluence, although it is important to also highlight the cytotoxicity associated with PL especially at concentrations exceeding 1 μM [244-246]. However, the surface coatings of PL utilised in those experiments were not thought to have a detrimental effect upon cell viability.

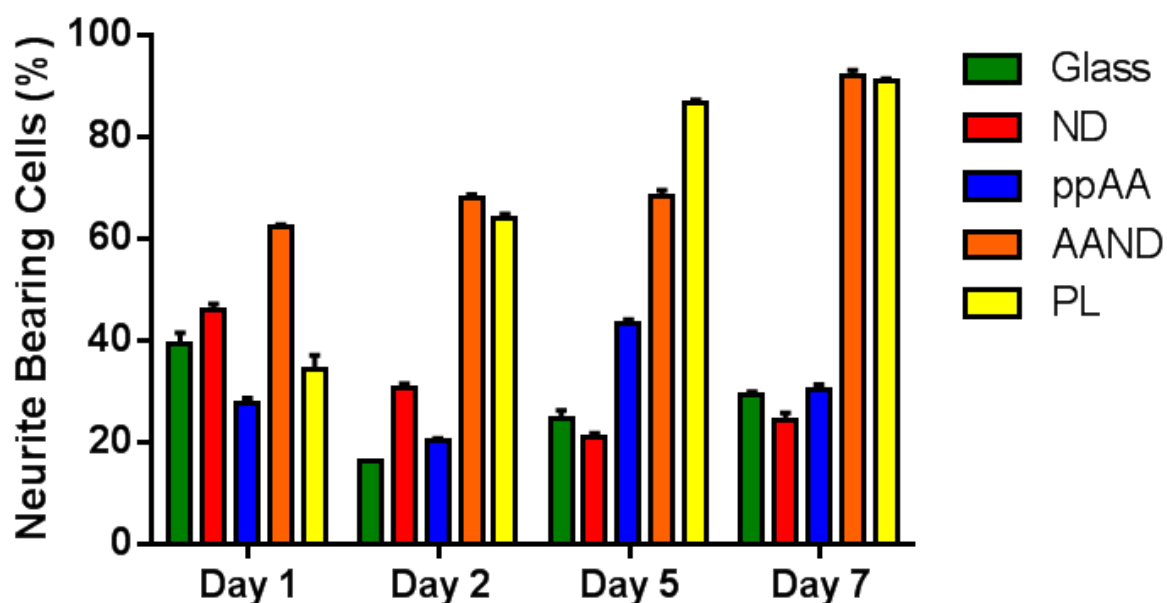


Figure 69: The proportion of NG108-15 cells bearing neurites (%) cultured upon glass, glass-ND, ppAA, AAND and PL surfaces over periods of either 1, 2, 5 or 7 days. Values are reported from the mean (\pm standard error) of three separate triplicate repeat experiments ($n=9$) with each triplicate utilising a different batch of cells ($N=3$). Complete statistical analysis of the mean dendrite length data is provided in table 8 below and overleaf.

- Statistical Analysis Tables – Neurite Bearing Cells data

DAY 1	Glass-ND	ppAA	AAND	PL
Glass	*	***	***	N/S
Glass-ND		***	***	***
ppAA			***	N/S
AAND				***

DAY 2	Glass-ND	ppAA	AAND	PL
Glass	***	**	***	***
Glass-ND		***	***	***
ppAA			***	***
AAND				**

DAY 5	Glass-ND	ppAA	AAND	PL
Glass	N/S	***	***	***
Glass-ND		***	***	***
ppAA			***	***
AAND				***

DAY 7	Glass-ND	ppAA	AAND	PL
Glass	**	N/S	***	***
Glass-ND		**	***	***
ppAA			***	***
AAND				N/S

*Table 8: Statistical significance data relating to figure 69 determined by Tukey's multiple comparison test and one way-anova, whereby; * $p < 0.05$, ** $p < 0.01$, *** $p < 0.001$ and N/S = no significant difference.*

Of further note was the lack of neurites present on the AAND-H surfaces which contrasted with the healthy appearance of NG108-15 cells cultured upon AAND and PL, despite all

surfaces being positively-charged. However, this is explained by the preference of neuronal cells to bind to highly polar substrates, including amine-terminated surfaces such as PL and AAND. The negative charges of the cell membrane are electrostatically attracted to the positive amine groups on the surface, promoting adhesion and cell-spreading [247]. This further accounted for the much longer dendrites present on AAND and PL.

Furthermore, a high proportion of neurite-bearing NG108-15 cells was recorded at day 1 on AAND surfaces, as seen on figure 69, ($62.2\% \pm 0.4\%$) which was significantly higher than the positive control PL ($34.3\% \pm 2.70\%$). By day 7 PL and AAND had approximately equal proportions of cells bearing neurites ($91.1\% \pm 0.300\%$ and $91.8\% \pm 1.20\%$ respectively).

4.3.3 3-(4,5-dimethylthiazol-2-yl)-2,5-diphenyltetrazolium Bromide (MTT) Assay

It was important to determine the growth of neuronal cells cultured upon the surfaces utilised in the study. This was ascertained by analysing the metabolic activity of each cell population cultured upon glass, glass-ND, ppAA, AAND and PL for 7 days (figure 70). Assuming the metabolic rate of each cell remained constant on each surface, a sample exhibiting a greater metabolic rate indicated a higher cell population thus providing an indication of the amenability of a particular surface to cell culture.

Each surface was cultured with an identical number of cells for 7 days, and so it would be expected any difference in metabolic activity would either be due to the surface encouraging a greater cell growth rate or enhanced cell adhesion. None of the surfaces tested were cytotoxic, all of which demonstrated some level of cell metabolism. The glass and glass-ND surfaces showed comparatively low activity which was indicative of few attached cells, as evidenced by the fluorescent micrographs in figure 63. Meanwhile, ppAA contrasted with this, showing metabolic activity almost 5 times the level of glass, due to the surface encouraging cell proliferation. This again was evidenced by figure 63, where bunching of

cells and a higher cell density were apparent. Encouragingly, the addition of amine-functionalised nanodiamond to ppAA appeared to control cell growth somewhat to similar levels experienced on PL, as would be expected due to the similar chemical environment.

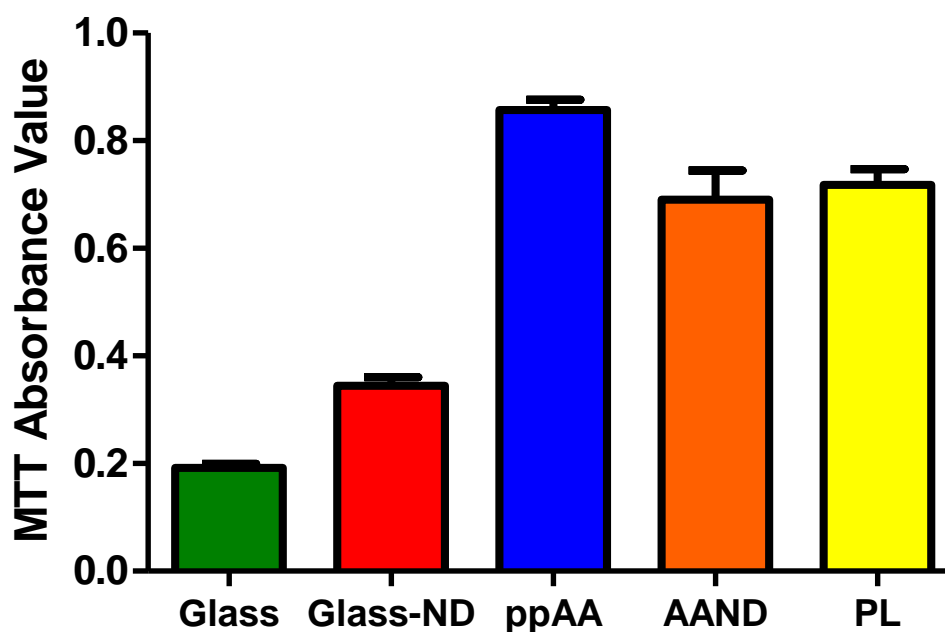


Figure 70: MTT assay absorbance values, measured at 570 nm and referenced at 630 nm, collated from NG108-15 cells cultured upon glass, glass-ND, ppAA, AAND and PL surfaces over a period of 7 days. Values were reported from the mean (\pm standard error) of three separate triplicate repeat experiments ($n=9$) with each triplicate utilising a different batch of cells ($N=3$). Complete statistical analysis of the mean dendrite length data is provided in table 9 overleaf

- Statistical Analysis Table – MTT data

	Glass-ND	ppAA	AAND	PL
Glass	*	***	***	***
Glass-ND		***	***	***
ppAA			*	*
AAND				N/S

*Table 9: Statistical significance data relating to figure 70 determined by Tukey's multiple comparison test and one way-anova, whereby; * $p < 0.05$, ** $p < 0.01$, *** $p < 0.001$ and N/S = no significant difference.*

4.4 Conclusion

The successful culture of neuronal and primary neural cells upon AAND, with results comparable to those recorded from conventional polylysine functionalised substrates illustrated the potential such surfaces could offer within the medical research sector. The beneficial neurocompatibility and coating stability ensured cells could continue to develop throughout the timescale of the experiment with both cell lines and primary cells demonstrating long processes, some in excess of 300 nm. AFM images proved that the coating procedure, although relatively simple, was successful. Additionally, XPS results illustrated the detection of the trifluoroacetic acid group of the TFAAD molecule proving that the UV-attachment of amines to hydrogenated ND was achievable.

The developments outlined in this results chapter may provide additional resources to benefit neuronal implants or applications where the incorporation of a neural interface may be required. The leaching of adsorbed PL upon exposure to liquids presents a hazard, whilst

covalently-bound functionalities do not pose such risks. ND particles have also been widely commented on for their biocompatibility and whilst their present applications remain restricted it is expected their use will expand as potential uses are realised.

Chapter Five: Carbon Nanoparticles (CNP) Study Results

5.0 Introduction

The development of effective fluorescent materials for *in vivo* and *in vitro* bioimaging applications has long been a research aim. Although the manufacture of quantum dots (QDs) has produced highly fluorescent nanoparticles, their intrinsic toxicity heavily restricts their use within *in vivo* related applications. Additionally the costly and inefficient production process and scarcity of raw materials involved in their synthesis further hampers their usability. Consequently, research has shifted towards the production of a new range of nanoparticles termed carbon dots which can emit similar levels of fluorescence as QDs but can be inexpensively mass-produced by simplistic synthesis routes. Numerous studies have also highlighted their biocompatibility and potential to be utilised in a wide range of further applications including drug delivery, biosensors, diagnostics and energy conversion [199].

The experiments outlined in this chapter revealed that carbon nanoparticles could be produced from a variety of saccharide sources, including alginate, glucose and sucrose. Although the stock solution utilised appeared to influence particle diameter and particle size distribution there appeared to be little difference in the effectiveness of the various CNPs produced to act as fluorescence tags. Indeed, the CNPs were shown to fluoresce over a wide range of visible excitation wavelengths, although slight differences in their specific fluorescent properties were observed. Additionally, although all CNPs were shown to be uptaken by the cells tested, those produced from a single saccharide source (i.e. alginate

CNPs, glucose CNPs, sucrose CNPs) were shown to have a greater cell internalisation efficiency than those produced from dual sources (i.e. glucose & sucrose CNPs). Furthermore, as reported previously by various research groups, cytotoxicity analysis of the CNPs listed in this chapter corroborated their biocompatibility and their effectiveness as inexpensive and versatile fluorescent tags. Where appropriate, all data in the following chapter will be quoted to three significant figures (3 s.f.).

5.1 Spectroscopy Analysis of CNPs

5.1.1 X-ray Photoelectron Spectroscopy (XPS) of Carbon nanoparticles and Precursor Solutions

Samples of glucose carbon nanoparticles (CNPs) and sucrose CNPs, and their respective precursor solutions, were analysed by XPS to assess differences in functionality following CNP formation. To produce CNPs, glucose or sucrose dissolved in glycerol and water was microwaved in a conventional microwave oven for 5 – 10 minutes until the solution resembled a black liquid. Several drops of these solutions were placed on separate glass cover slips, allowed to dry in a vacuum oven, and analysed with a Kratos AXIS Ultra DLD instrument. Data processing and charge correction were calculated using CasaXPS (ver.2.3.12 Casa Software Ltd.). CNPs derived from alginate were not analysed by XPS due to difficulties associated with drying out the CNP solution.

5.1.1.1 XPS of Dried Glycerol/Glucose Solution upon Glass

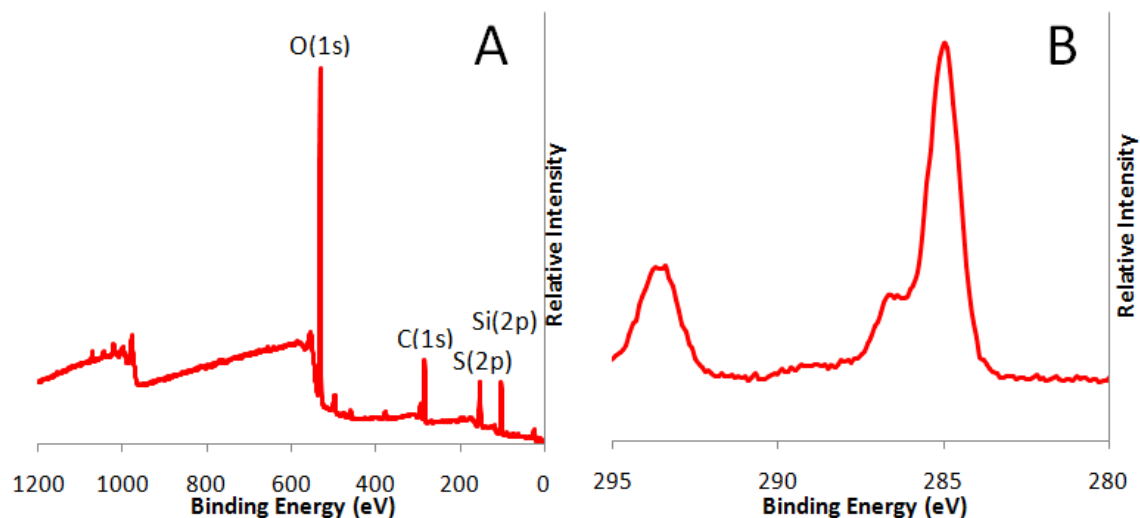


Figure 71: X-ray photoelectron spectra (XPS) depicting survey (A) and high resolution carbon (B) scans of glucose upon glass. For clarity, the S(2p) and Si(2p) peaks are located at 167 eV and 101 eV respectively.

5.1.1.2 XPS of Glucose CNPs upon Glass

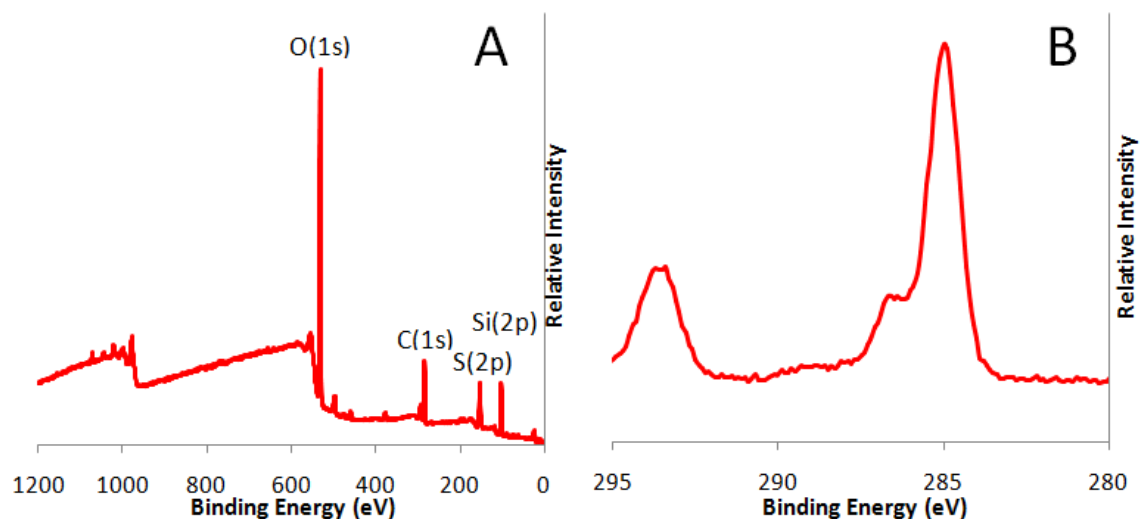


Figure 72: X-ray photoelectron spectra (XPS) depicting survey (A) and high resolution carbon (B) scans of glucose CNPs upon glass. For clarity, the S(2p) and Si(2p) peaks are located at 167 eV and 101 eV respectively.

Element	Binding Energy (eV)	Glucose Solution At %	Glucose CNPs At. %
O(1s)	533	48.6	32.8
C(1s)	285	25.9	59.0
Na(1s)	1072	0.500	0.600
B(1s)	190	1.50	1.00
Si(2p)	101	20.9	6.00
Al(2p)	74	2.40	0.600

Table 10: Elemental composition of the glucose precursor solution and glucose CNPs as analysed by XPS (figures 71 and 72).

Analysis of the survey spectra between glucose and the microwave synthesised CNPs revealed several differences (figures 71 and 72), the most prominent being the higher concentration of carbon present in the CNP sample (59.0%) compared to 25.9% within the dried glucose/glycerol mixture. This increased proportion of carbon appeared to be at the expense of the oxygen content within the CNPs, whereby the presence within the sample decreased from 48.6% before microwave treatment, to 32.8% afterwards once CNPs had been produced. The presence of a silicon peak within the survey spectra for both samples illustrated that the underlying glass substrate had been detected (dried glucose solution: 20.9%) (glucose CNPs: 6.00%), and was not a constituent of the glucose solution or glucose CNPs. Additionally, the trace presence of aluminium (average ~ 1.50%) and boron (average ~ 1.20%) may probably have resulted from inclusions within the glass that were detected and analysed.

5.1.1.3 XPS of Dried Glycerol/Sucrose Solution upon Glass

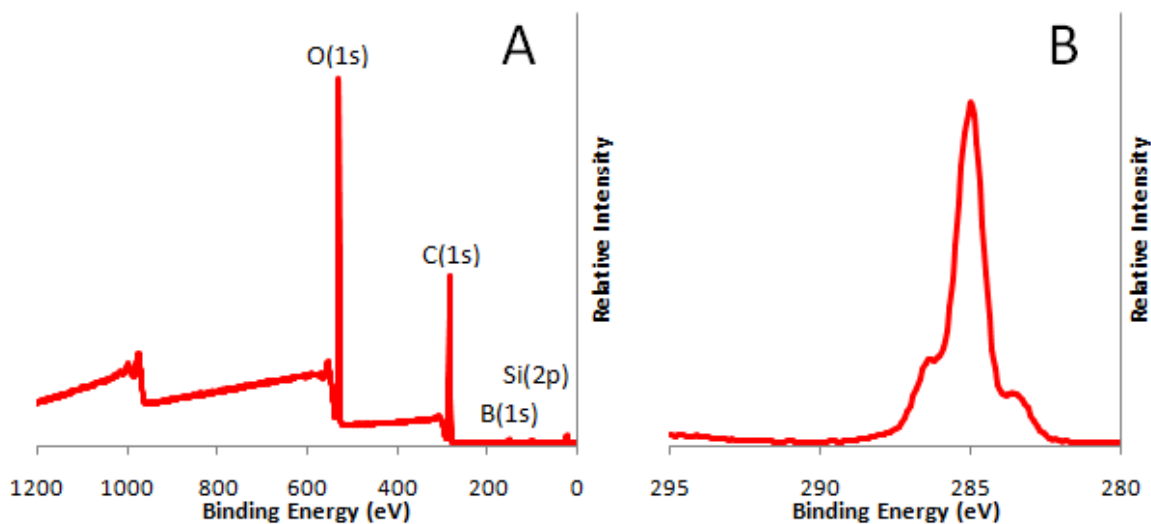


Figure 73: X-ray photoelectron spectra (XPS) depicting survey (A) and high resolution carbon (B) scans of dried glycerol/sucrose solution upon glass. For clarity, the B(1s) and Si(2p) peaks are located at 190 eV and 101 eV respectively

5.1.1.4 XPS of Sucrose CNPs upon Glass

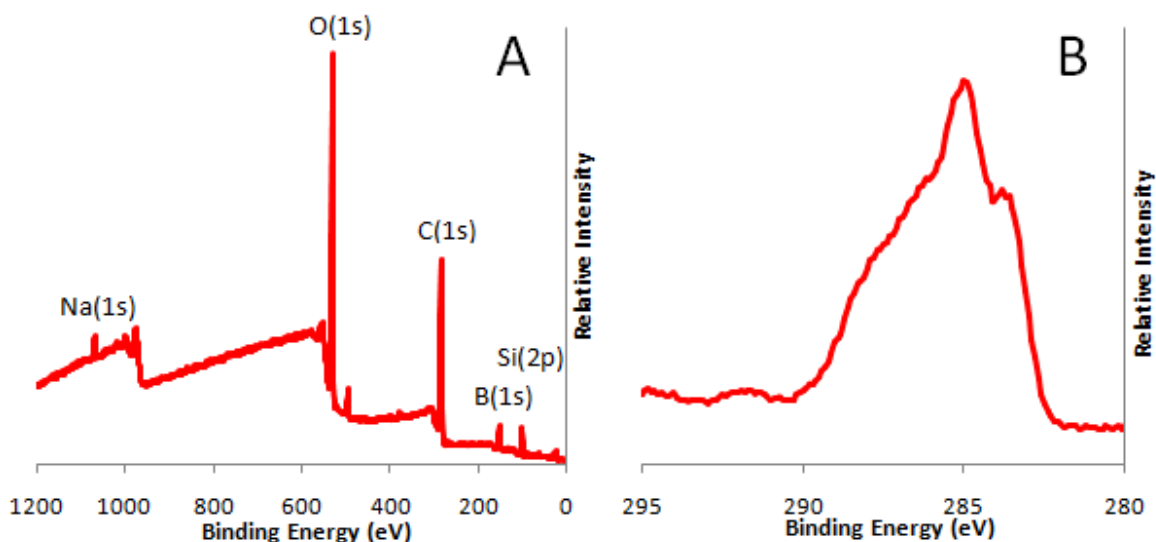


Figure 74: X-ray photoelectron spectra (XPS) depicting survey (A) and high resolution carbon (B) scans of sucrose CNPs upon glass. For clarity, the B(1s) and Si(2p) peaks are located at 190 eV and 101 eV respectively

Element	Binding Energy (eV)	Sucrose Solution At %	Sucrose CNPs At. %
O(1s)	533	59.7	34.8
C(1s)	285	38.2	56.2
Na(1s)	1072	-	0.700
B(1s)	190	1.10	1.20
Si(2p)	101	1.00	7.10
Al(2p)	74	-	-

Table 11: Elemental composition of the sucrose precursor solution and sucrose CNPs as analysed by XPS (figures 73 and 74).

Dried sucrose/glycerol solution and sucrose CNPs were analysed by XPS in much the same way as the glucose solutions/CNPs in sections 5.1.1.1 and 5.1.1.2. The surface formed by the dried sucrose/glycerol solution produced a survey spectrum free from impurities (figure 73). The only elements that were detected were carbon (38.2%), oxygen (59.7%), silicon (1.00%) and boron (1.10%) with this silicon and boron originating from the underlying glass substrate as in previous XPS studies.

The microwave synthesised sucrose CNPs produced a survey spectrum that contrasted with the precursor solution (figure 74). In much the same way as with the glucose solution / glucose CNPs analysed in sections 5.1.1.1 and 5.1.1.2, the main difference noted was the decreased proportion of oxygen present following CNP synthesis (34.8%) and an increased presence of carbon (56.2%). A greater proportion of silicon (7.10%) and boron (1.20%) was noted, but once these detections were discounted and the proportions of the remaining elements adjusted, the increase in carbon content was even more noticeable (60.9%) when compared to the original solution. The high resolution carbon scan produced from analysis of the glucose CNPs indicated a complex surface chemistry markedly different from the original

solution. The stretch of the C(1s) peak to approximately 290 eV indicated the presence of carboxyl and hydroxyl surface groups which displayed little if any presence within the glucose/glycerol precursor solution. The negative charge such groups convey are known to increase the hydrophilicity of CNPs which helps to deaggregate large CNP clusters. This benefits their use as a cell marker as single particles are more desirable for accurate and reproducible bioimaging capabilities.

5.1.2 Fluorescence Spectroscopy of CNPs

Once the CNP solutions had been produced they were analysed using fluorescence spectroscopy in an attempt to understand their fluorescence emission/excitation characteristics (figure 75). To facilitate analysis weak concentrations of CNPs within aqueous solutions were required, necessitating a sample of the original CNP solution being diluted ten-fold in distilled water. Fluorescence emission was detected using a FluroMax-4 spectrofluorometer.

All the produced CNPs were excited over a range of wavelengths from 420 nm to 470 nm, with most samples emitting a maximum intensity at approximately 500 nm when excited at 420 nm. This wavelength approaches that of green light in the visible spectrum. One exception to this were those CNPs produced from the 2.5M precursor glucose solution which emitted their maximal intensity when excited at 470 nm, whereas all other CNPs emitted their highest intensities of light at the lower wavelength of 420 nm. Additionally this intensity recorded from the 2.5M glucose CNPs was at a slightly higher wavelength than any other sample (552 nm), being closer to the yellow region of visible light and representing a blue-shift in the wavelengths of emitted light. Furthermore this maximum, however, was at an intensity more than four times smaller than that recorded from the CNPs produced from the lower concentration of glucose (1M).

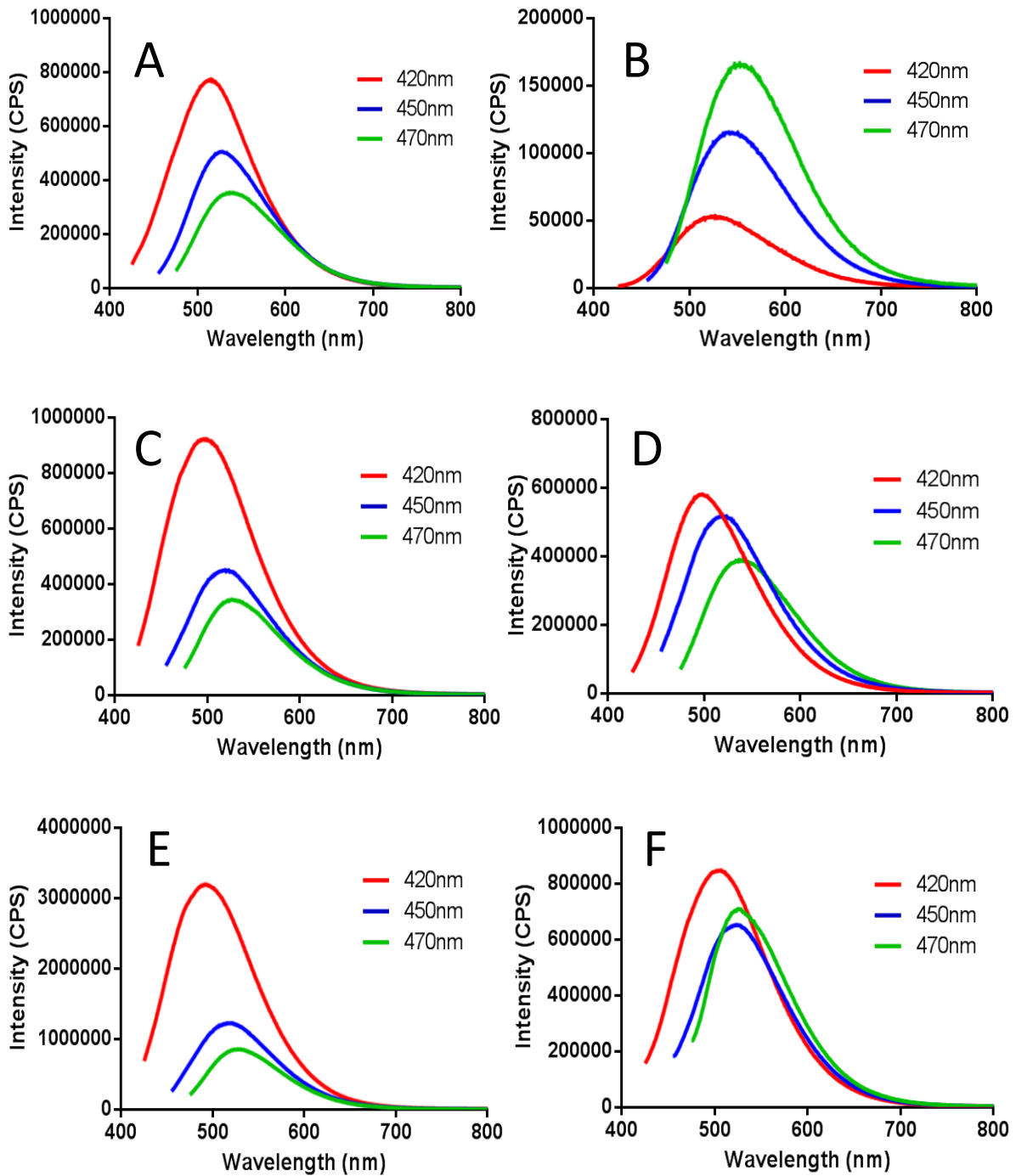


Figure 75: Fluorescence emission spectra of CNPs produced from (A) 1M and (B) 2.5M glucose:glycerol mixtures, (C) 1M alginate:glycerol mixtures, (D) 0.5M sucrose:glycerol mixtures, (E) 1M glucose: 0.5M alginate glycerol mixtures and (F) 0.5M sucrose: 0.5M alginate glycerol mixtures. CNPs were excited at three different wavelengths (420 nm, 450 nm and 470 nm).

	Glucose CNP (1M)	Glucose CNP (2.5M)	Alginate CNP	Sucrose CNP	Glucose / Alginate CNP	Sucrose / Alginate CNP
Maximum Emission Intensity (CPS)	772000	168000	922000	582000	847000	3190000
Emission Wavelength of Maximum Intensity (nm)	513	552	496	498	506	493
Excitation Wavelength of Maximum Intensity (nm)	420	470	420	420	420	420

Table 12: Maximum emission intensities (counts per second) observed from the CNPs produced during the study and the emission and excitation wavelengths observed during these maxima as recorded from the fluorescence spectra (figure 75).

Maximum emitted intensities varied widely across the samples, with the lowest average readings recorded by the CNPs produced from the 2.5M glucose solution, whereas the most intense fluorescent emissions were recorded from the hybrid glucose/alginate CNPs (table 12). This latter sample appeared to be highly sensitive to excited radiation since there appeared a three-fold decrease in emitted intensity following the excited wavelength of light shifting by 30 nm from 420 nm to 450 nm. A similar trend was also reported from alginate CNPs tested in this study, although the exact reasons for these patterns remain largely misunderstood although it is known that CNP fluorescence originates from the excitation of emissive energy traps upon the CNP surface [199].

5.1.3 Absorbance (UV/Visible) Spectroscopy CNPs

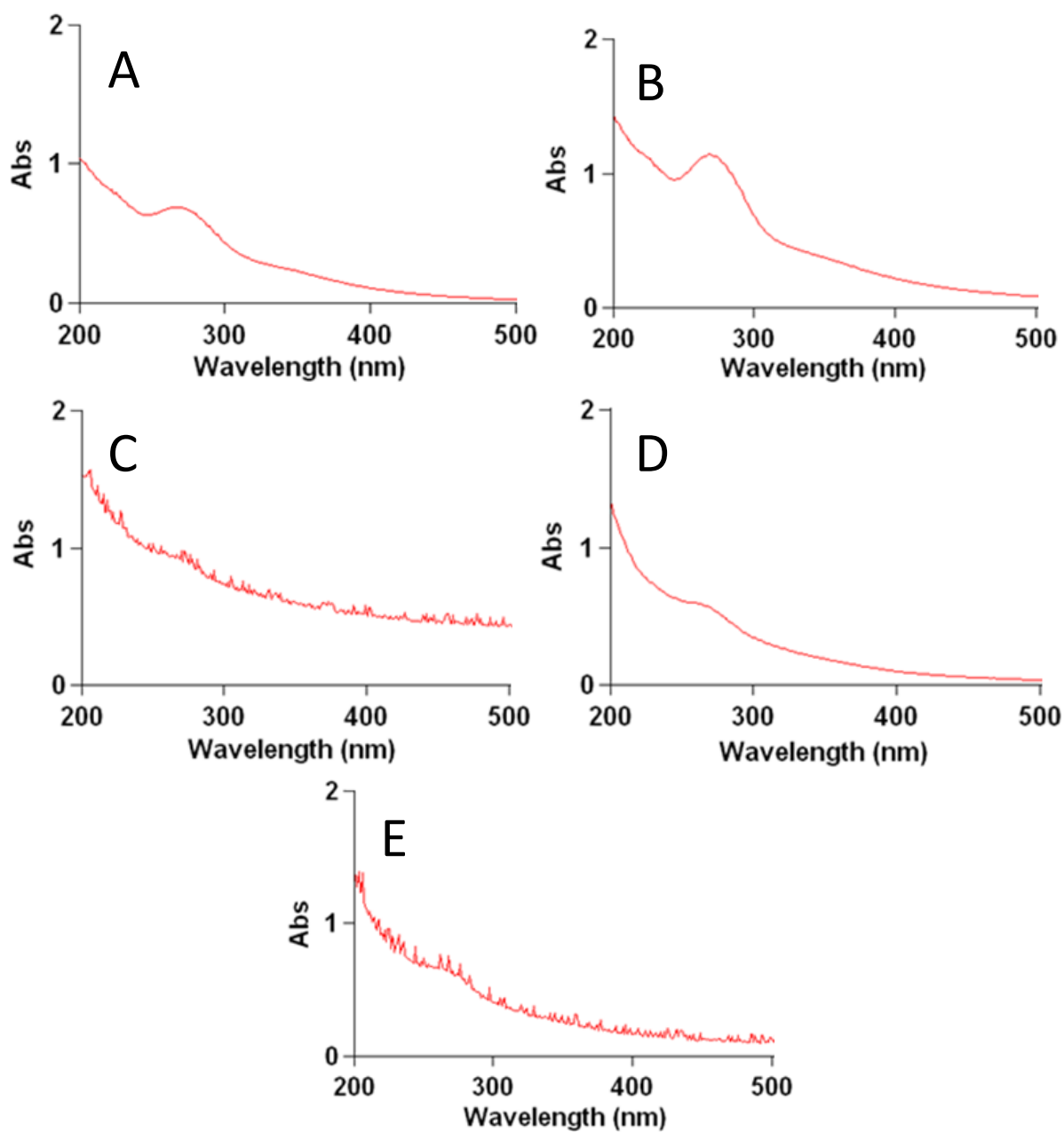


Figure 76: Absorption (Abs) spectra of (A) glucose CNPs produced from 1M glucose:glycerol mixture, (B) alginate CNPs produced from 1M alginate:glycerol mixture, (C) sucrose CNPs produced from 0.5M sucrose:glycerol mixture, (D) glucose/alginate CNPs produced from 1M glucose:0.5M alginate:glycerol mixture and (E) sucrose/alginate CNPs produced from 0.5M sucrose:0.5M alginate:glycerol mixture.

UV-vis spectroscopy aims to measure the ability with which a solution absorbs UV/visible light based upon the wavelength of the radiation being absorbed. To analyse the CNPs by this method a weak concentration of CNPs within an aqueous solution was required. It was therefore necessary to produce additional diluted quantities of the original CNP solutions within distilled water with absorbance (ultraviolet-visible) spectroscopy being performed using a Varian Cary 50b instrument.

The ultraviolet-visible (absorption) spectra illustrated in figure 76 depict a band within all the graphs which peaks in the region between 240 – 300 nm, this being the only discernible feature. This band has been recognised before as relating to a typical absorption peak for an aromatic π system, similar to those derived from polycyclic aromatic hydrocarbons [248]. The relatively large size of the bands may occur due to the overlap of several bands in the same region. It has been speculated before an additional band in the 264 nm region has been observed during analysis of CNPs originating from carbon soot. It was significant to note that the absorbance of the CNP solutions decreased as the wavelength of the absorbed light increased with the most significant absorption bands being recorded within glucose and alginate CNP samples (figure 76A & 76B).

5.2 Dynamic Light Scattering (Particle Sizing) Analysis of CNPs

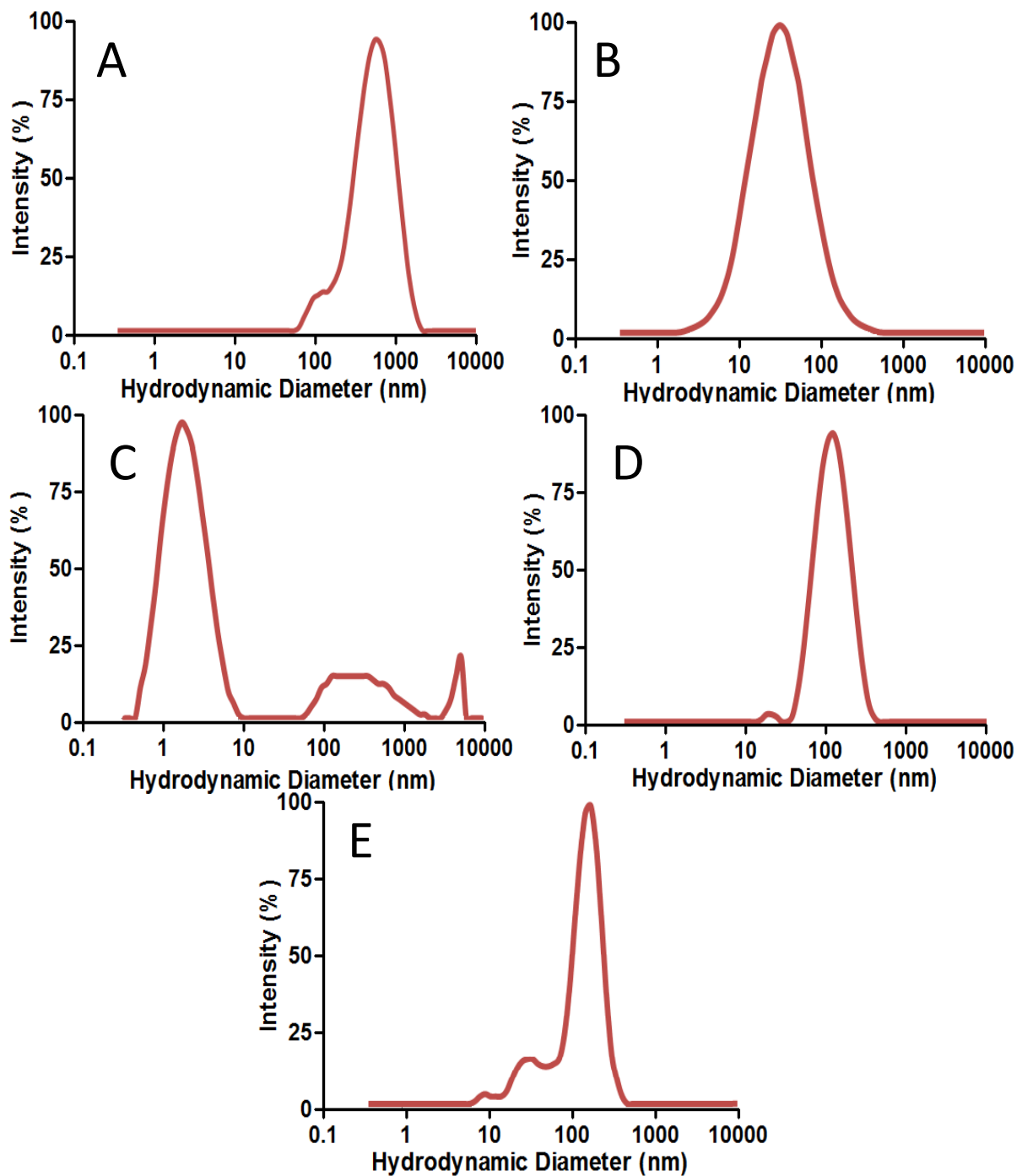


Figure 77: Dynamic light scattering (DLS) measurements of (A) glucose CNPs, (B) alginate CNPs, (C) sucrose CNPs, (D) alginate-sucrose CNPs and (E) alginate-glucose CNPs illustrating hydrodynamic diameter of the DLS data.

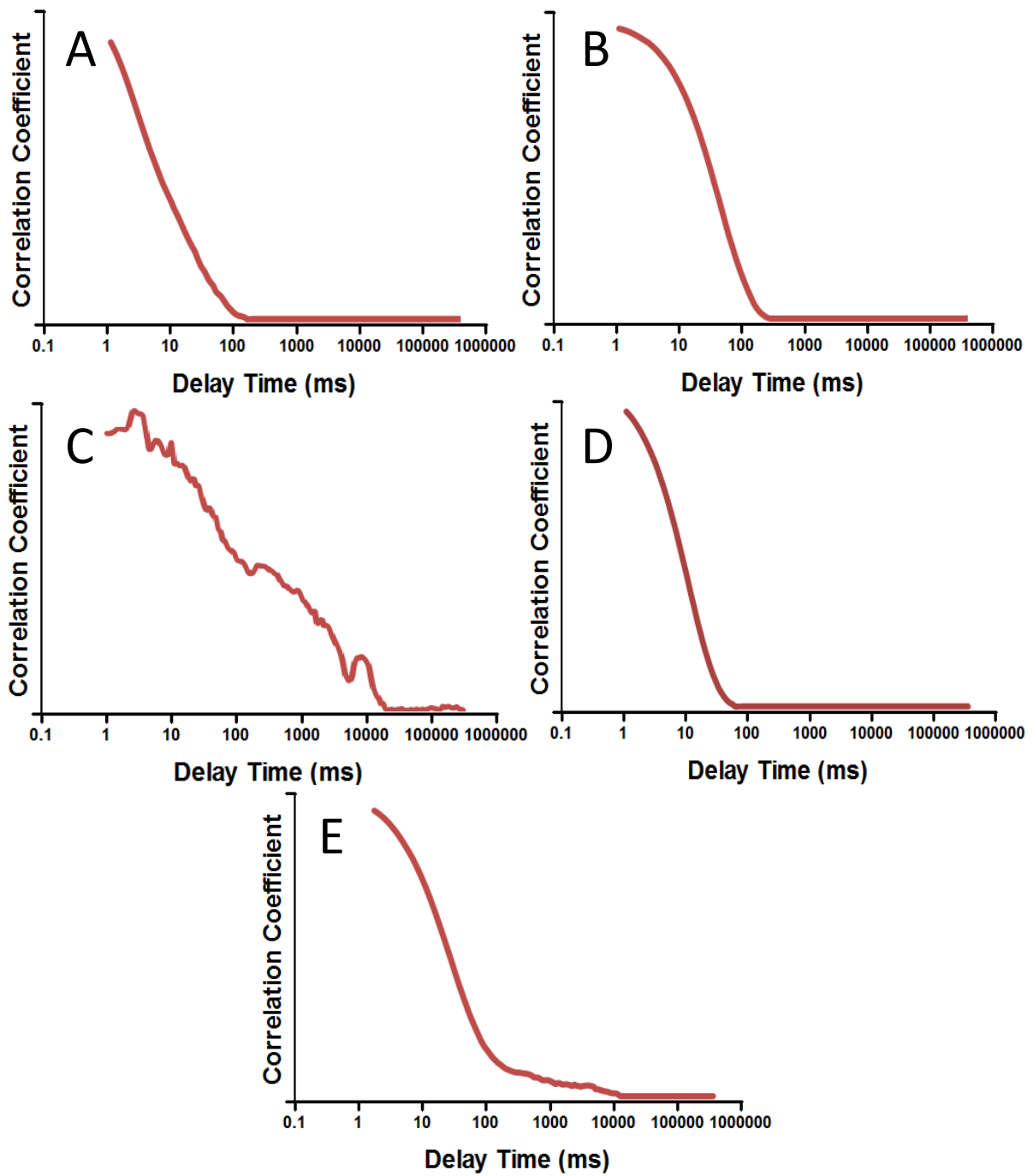


Figure 78: Dynamic light scattering (DLS) measurements of (A) glucose CNPs, (B) alginate CNPs, (C) sucrose CNPs, (D) alginate-sucrose CNPs and (E) alginate-glucose CNPs illustrating the correlation function of the DLS data.

	Glucose CNP	Alginate CNP	Sucrose CNP	Alginate/Sucrose CNP	Alginate/Glucose CNP
Particle Size Range (nm)	59 – 2310	3 – 600	0.6 – 5560	16 – 396	7 - 459
Hydrodynamic Diameter (nm)	417	22.9	38.3	106	199
Polydispersity	0.274	0.243	0.595	0.237	0.343

Table 13: The range of CNP sizes, hydrodynamic diameter and polydispersity readings recorded for each CNP sample as noted from the DLS results.

In order to understand the internalisation efficiency of the different CNPs it was important to derive the approximate CNP diameters produced by each carbon source. It is known that one of the factors that greatly affects the rate of nanoparticle uptake is CNP size with larger particles appearing to migrate across cell membranes at a quicker rate than those of a smaller diameter. Therefore, DLS measurements were gathered from all CNP samples utilised in the study to indicate their size distribution. Each sample was diluted ten-fold within distilled water before being subject to analysis using a Malvern Zetasizer Nano ZS instrument to produce particle size distributions and correlation functions.

This data enabled an approximate mean particle size to be calculated and also the size uniformity of the different CNPs. It is important to stress that DLS systems operate under several assumptions, the most salient of which is that the mean effective diameter of particles can only be accurately determined if the particle system being analysed is monodisperse. Polydisperse systems, which comprise a number of particle populations, are more difficult to characterise using DLS, thus resulting in any hydrodynamic diameters being subject to significantly higher errors unless appropriate corrections are taken into consideration.

The hydrodynamic data featured within figure 77 illustrated that alginate CNPs were the most favourable sample analysed due to the presence of a single population peak which indicated little/no sample agglomeration. This relatively normal population distribution was reflected in the low polydispersity reading of the sample solution (0.243). The hydrodynamic diameter of the sample could therefore be easily quantified as 22.9 nm and can be assumed to be a relatively accurate mean measurement of alginate CNP diameter. However the diameter recorded by DLS will also include any molecules, such as solvents, which have adsorbed onto the particle surface. Such molecules however would not be visible during transmission electron microscopy (TEM) analysis due to poor contrast, therefore leading to different diameter values being ascertained from different analytical techniques for the same sample of particles.

Additionally, glucose and alginate/sucrose CNPs also produced relatively uniform hydrodynamic diameter readings. The presence of a monodisperse CNP sample solution is preferable since it could not be ascertained which particular particle population was responsible for the findings observed if multiple populations were present. Furthermore, the presence of multiple CNP populations of varying sizes within the same sample may negatively impact cell internalisation efficiency since particles of larger size may be uptaken at the expense of smaller particles which are usually slower to internalise. However, as stated in the literature review, there are a plethora of other factors which affect CNP cellular translocation, including particle surface functionalisation, particle shape and particle concentration.

On the other hand, samples which were formed of multiple CNP population sizes, such as sucrose CNPs, were seen to display an erratic correlation coefficient graph with a relatively high polydispersity reading (0.595). The true particle diameter of this sample was therefore inherently difficult to ascertain through DLS due to the multiple population sizes present

within the sample. Although the mean hydrodynamic diameter was ascertained as 38.3 nm this could not be accepted as being an accurate representation of the true particle diameter size due to the aforementioned reasons. However, all of the particles tested for DLS analysis were later incubated in the presence of cells to test their *in vitro* cell uptake, translocation efficiency and fluorescence intensity.

5.3 Sodium dodecyl sulphate polyacrylamide gel electrophoresis (SDS-PAGE) of CNP solutions

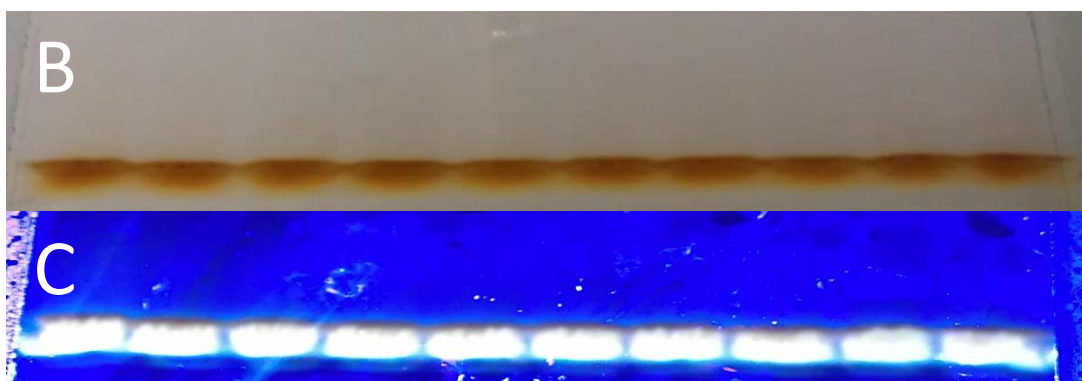


Figure 79: (A) SDS-PAGE of alginate CNPs within the electrophoresis chamber. (B) Bands of alginate CNPs formed after electrophoresis, with (C) autofluorescence achieved by UV irradiation.

Initially, alginate CNPs were selected for SDS-PAGE almost immediately after their production. The bands that formed in the acrylamide gel were then illuminated under UV light to display CNP autofluorescence properties (figure 79). Once three years had passed, further SDS-PAGE studies were conducted on the other CNPs utilised in the project, with further alginate CNPs being sampled to compare band formation and the intensity of fluorescence emission after exposure to UV radiation.

Although conventional SDS-PAGE allows for the separation of different protein fractions, the main reason for utilising the technique in this instance was to allow for easier visualisation of CNP autofluorescence upon exposure to UV light.

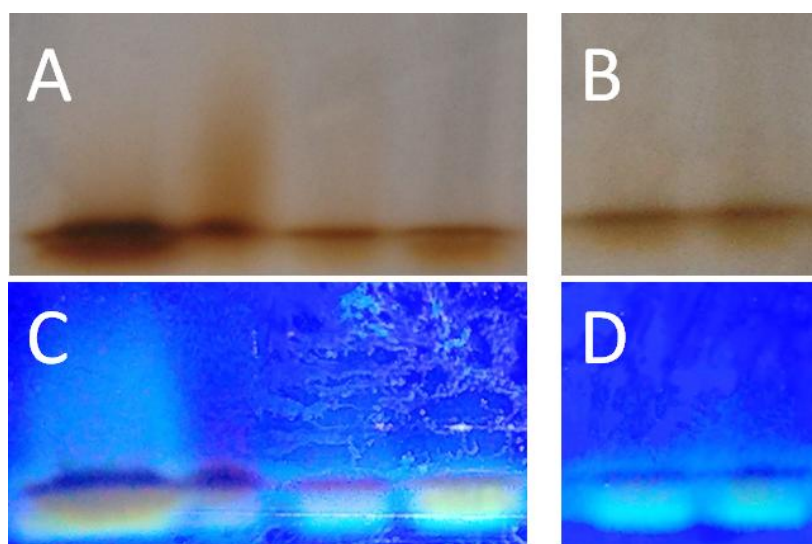


Figure 80: (A) SDS-PAGE of (left to right) alginate/sucrose, glucose, alginate/glucose, sucrose CNPs and (B) alginate CNPs. UV irradiation of the same acrylamide gels is displayed in (C) and (D) illustrating CNP autofluorescence. These CNP samples were analysed three years post manufacture.

Each CNP sample analysed was seen to produce only a single band within each lane, with all bands progressing through the gel at equal speed (figure 80A). Although some CNP samples produced greater sized bands than others (e.g. figure 80A: alginate/sucrose CNPs), this was

more a result of greater carbon concentration within a sample rather than any CNP-specific effect/property, since equal volumes of CNP solution were loaded into each lane of the stacking gel.

Maximum fluorescence intensities by CNPs excited by UV irradiation appeared to decrease with CNP ageing. It was seen that alginate CNPs subject to SDS-PAGE almost immediately following synthesis yielded bright autofluorescence (figure 79C) with emission levels seeming to decrease when the procedure was repeated three years later with the same sample of CNPs (figure 80D) indicating a decay in fluorescence potential.

5.4 Cell Culture

5.4.1 Fluorescence of CNPs within Cells

Primary human fibroblasts, primary rat Schwann cells, RN22 and NG108-15 neuroblastoma cells were cultured and exposed to CNPs produced from various sources. CNP incubation times varied between 2 hours and 2 days, after which cell uptake of the fluorescent CNPs was monitored by fluorescence microscopy.

	Excitation Wavelength (nm)	Emission Wavelength (nm)
FITC	495	519
Texas Red	590	615
DAPI	345	455

Table 14: Cells were incubated with CNPs and then imaged using an epifluorescence microscope. CNPs within the cells were excited under wavelengths which would normally stimulate FITC, Texas Red and DAPI to emit green, red and blue wavelengths of visible light respectively.

Most CNPs were excited using light of wavelengths 495 nm and 590 nm, causing emissions at 525 nm (green visible region) and 615 nm (red visible region) respectively (table 14). In some examples the CNPs within the cells were also excited at 345 nm, with emissions recorded at 455 nm (blue visible region). All images were recorded at X10 magnification. Since most CNP samples appeared to display the greatest fluorescence emissions after being excited with 420 nm light it would be expected that green and blue visible emissions would be more intense than the red emissions (figure 75 & table 12).

5.4.1.1 Glucose CNPs

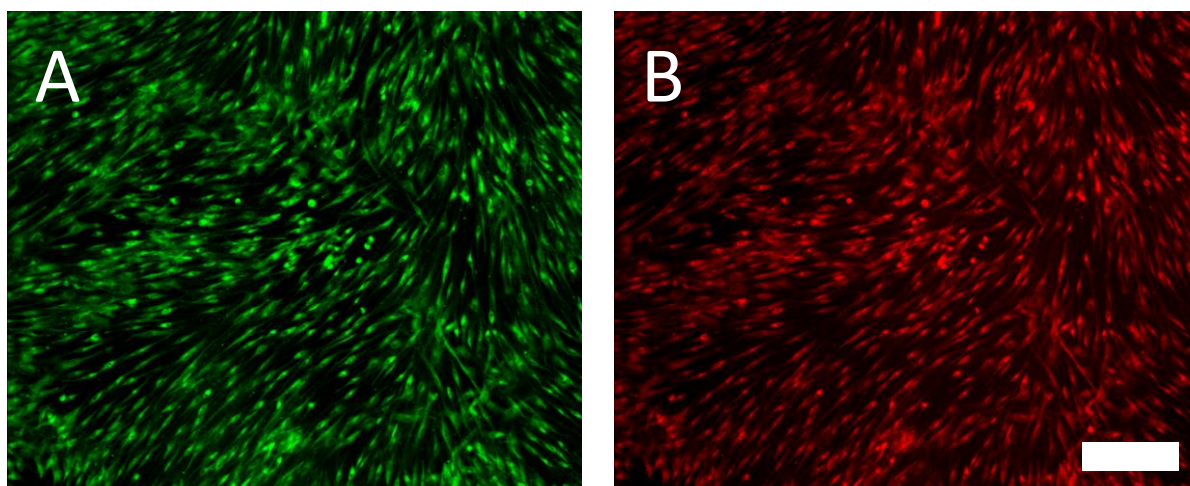


Figure 81: Fluorescence of glucose CNPs within primary human fibroblasts (passage 4) cultured for 7 days in cDMEM, supplemented with glucose CNPs for the final 2 hours (20 μ l CNP solution within 1 ml cDMEM). CNPs within the cells were excited with (A) 490 nm and (B) 570 nm light causing emissions at (A) 525 nm and (B) 590 nm. Three separate triplicate repeat experiments ($n=9$) were conducted with each triplicate utilising a different batch of cells ($N=3$). Scale bar: 200 μ m

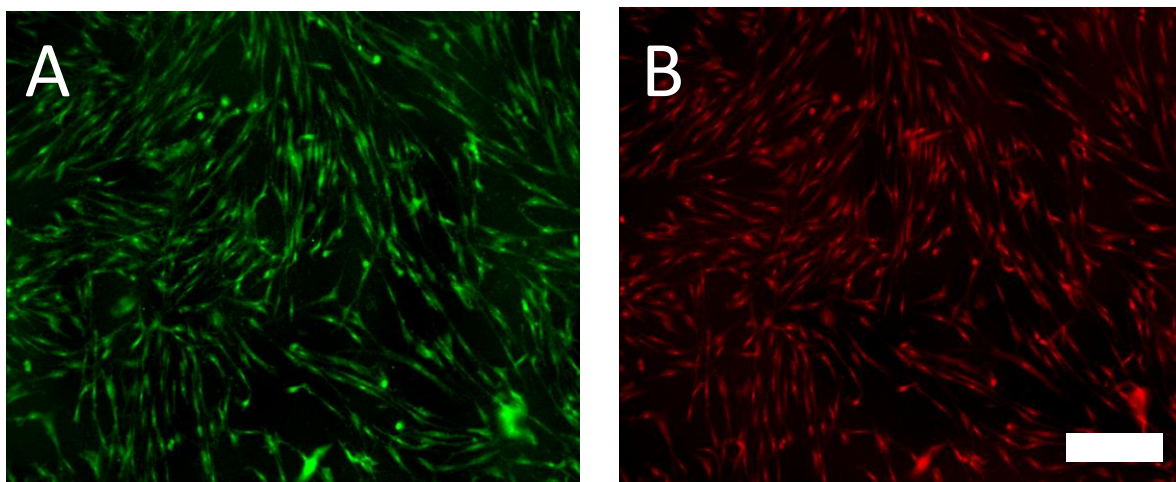


Figure 82: Fluorescence of glucose CNPs within primary human fibroblasts (passage 4) cultured for 7 days in cDMEM, supplemented with glucose CNPs for the final 48 hours (20 μ l CNP solution within 1 ml cDMEM). CNPs within the cells were excited with (A) 490 nm and (B) 570 nm light causing emissions at (A) 525 nm and (B) 590 nm. Three separate triplicate repeat experiments ($n=9$) were conducted with each triplicate utilising a different batch of cells ($N=3$). Scale bar: 200 μ m

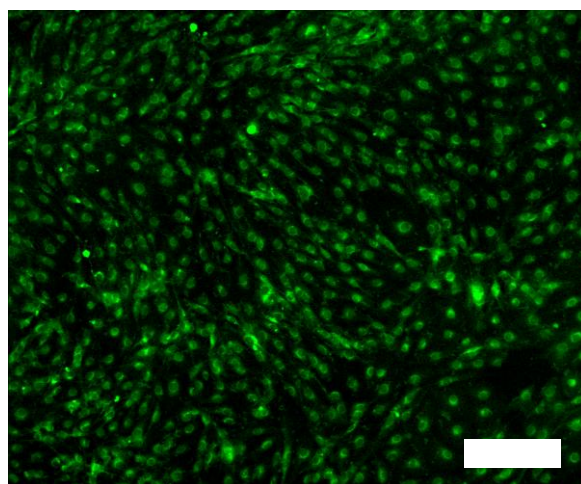


Figure 83: Fluorescence of glucose CNPs within primary rat Schwann cells (passage 3) cultured for 21 days in Schwann cell medium, supplemented with glucose CNPs for the final 2 hours (20 μ l CNP solution within 1 ml Schwann cell medium). CNPs within the cells were excited with 490 nm light causing emission at 525 nm. A triplicate experiment ($n=3$) was conducted using a single batch of cells ($N=3$). Scale bar: 200 μ m

Fibroblasts displayed great uptake of the CNPs over a short time scale as depicted by figure 81, whereby glucose CNP exposure over a period of 2 hours allowed complete visualisation of the cells, including the cell body and bipolar regions. However, in this short time period the CNPs did not enter the cell nuclei, which can clearly be seen as empty circular spaces within the cells. This enables the cell nuclei to be identified whilst illuminating the cytoplasm and cytoskeleton in relatively high definition, almost equivalent to conventional staining dyes such as phalloidin-FITC. The CNPs were able to emit radiation in the visible green (525 nm) and red (590 nm) regions, although the green appeared slightly more intense.

However, cells which were exposed to the CNPs for 48 hours (figure 82) did not fluoresce as intensely as those in figure 81. Despite the decreased fluorescence intensity the cells were still sufficiently labelled so that their morphology could be identified as being fibroblast-like.

In contrast to the primary human fibroblast cells, primary rat Schwann cells were illuminated comparatively poorly by the glucose CNPs. Although some CNPs were uptaken by the cells, not enough were distributed throughout the cytoplasm and cytoskeleton to allow a formal identification of the cell type to be ascertained. The CNPs resided mostly in the cell body of the PSCs within the first two hours, with little if any migrating to the dendritic regions. Again, CNP presence at this timescale within the nuclei was poor, allowing them to be easily identified within most PSCs. However, the intensity of the fluorescence emission was good and significantly better than the control images where cells can barely be recognised by cell autofluorescence alone.

5.4.1.2 Cell Autofluorescence – No CNPs present

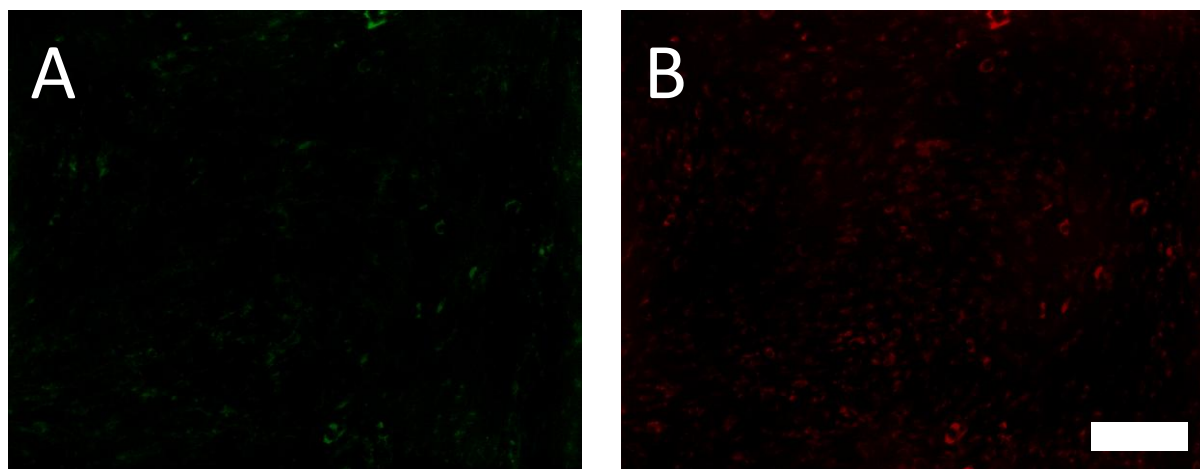


Figure 84: Autofluorescence of primary human fibroblasts (passage 4) cultured for 7 days in cDMEM. Cells were excited with (A) 490 nm and (B) 570 nm light causing emissions at (A) 525 nm and (B) 590 nm. Three separate triplicate repeat experiments ($n=9$) were conducted with each triplicate utilising a different batch of cells ($N=3$). Scale bar: 200 μm

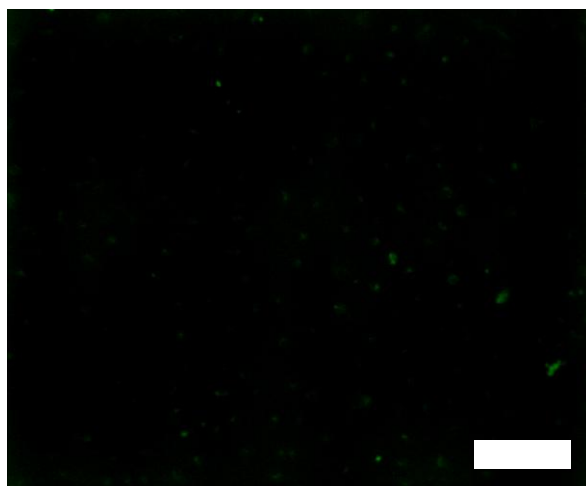


Figure 85: Autofluorescence of primary rat Schwann cells (passage 3) cultured for 21 days in Schwann cell medium. Cells were excited with 490 nm light causing emissions at 525 nm. A triplicate experiment ($n=3$) was conducted which utilised a single batch of cells ($N=1$). Scale bar: 200 μm

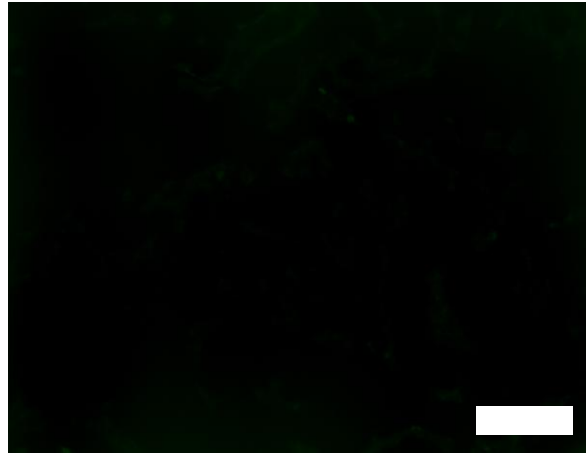


Figure 86: Autofluorescence of RN22 cells (passage 13) cultured for 5 days in cDMEM. Cells were excited with 490 nm light causing emissions at 525 nm. Three separate triplicate repeat experiments (n=9) were conducted with each triplicate utilising a different batch of cells (N=3). Scale bar: 200 μ m.



Figure 87: Autofluorescence of NG108-15 cells (passage 14) cultured for 5 days in serum-free DMEM. Cells were excited with 350 nm light causing emissions at 470 nm. Three separate triplicate repeat experiments (n=9) were conducted with each triplicate utilising a different batch of cells (N=3). Scale bar: 200 μ m.

These images illustrate that although cells sometimes display slight autofluorescence, they are mostly invisible without staining or other visualisation techniques/procedures. Some cells (PSC and RN22) do not fluoresce at all (figures 85 and 86 respectively), whereas fibroblast

and NG108-15 cells exhibited some fluorescence from the cell cytoplasm (figures 84 and 87 respectively). However this level of autofluorescence pales into insignificance when compared to the cell visibility illustrated using CNPs derived from alginate or glucose.

5.4.1.3 Thermally-decomposed glycerol

Without the addition of a further source of carbon (E.g. glucose, alginate or sucrose) it was thought necessary to investigate the fluorescence properties of pyrolysed glycerol upon cells. This would demonstrate whether the source of additional carbon was responsible for the fluorescence properties associated with the microwave generated CNPs or whether the glycerol itself was the cause.

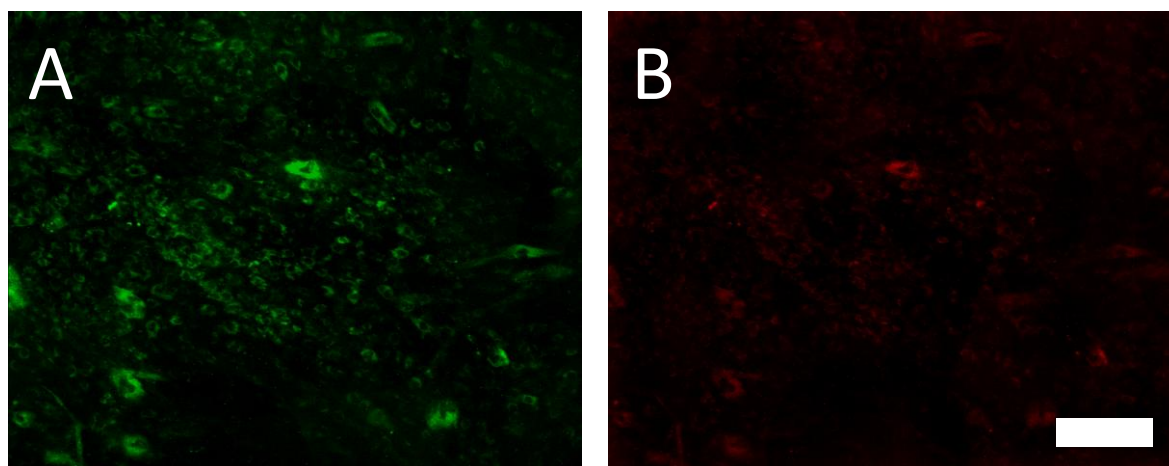


Figure 88: Fluorescence of primary human fibroblasts (passage 4) cultured for 7 days in cDMEM, supplemented with pyrolysed glycerol for the final 2 hours (20 μ l pyrolysed glycerol solution within 1 ml cDMEM). CNPs within the cells were excited with (A) 490 nm and (B) 570 nm light causing emissions at (A) 525 nm and (B) 590 nm. Three separate triplicate repeat experiments ($n=9$) were conducted with each triplicate utilising a different batch of cells ($N=3$). Scale bar: 200 μ m

Although an increase in fluorescence intensity was reported following incubation with pyrolysed glycerol (figure 88), this still produced an image where cell morphology was not

distinct and where cells could not be readily identified. The fluorescence emission intensity in the green visible region (525 nm) was fair, although only the cytoplasm of some cells could be identified, with the cytoskeleton failing to attract or retain associated CNPs. This implies that although microwave treatment of glycerol alone may produce fluorescent CNPs, they would not be of the quality or quantity required for cell imaging to be viable.

5.4.1.4 Alginate CNPs

Alginate CNPs were found to be one of the most amenable for cell imaging due to the quality of the fluorescence images attained, particularly in the cases of fibroblast and Schwann cells (Figures 89 & 90 and 91 respectively). Clear images of fibroblasts were attained in both the 2 hour and 48 hour incubation images. Additionally, in the case of the Schwann cells, long dendritic processes were identified, with details so fine that it was possible to measure their lengths accurately. Emission intensities at 525 nm and 590 nm were approximately equal.

However, visualisation of RN22 (figure 92) and NG108-15 cells (figure 93) was more troublesome, possibly due to the accelerated growth rate of these cells making clear identification difficult. Although the CNPs fluoresced once they were excited, quite vividly in the green region in the case of the RN22 cells, the morphology of the cells was difficult to decipher. The CNPs failed to pass into the nuclei within the 2 hour incubation period although an increased concentration of CNPs was identified at the edge of the cell nuclei within the RN22 cells.

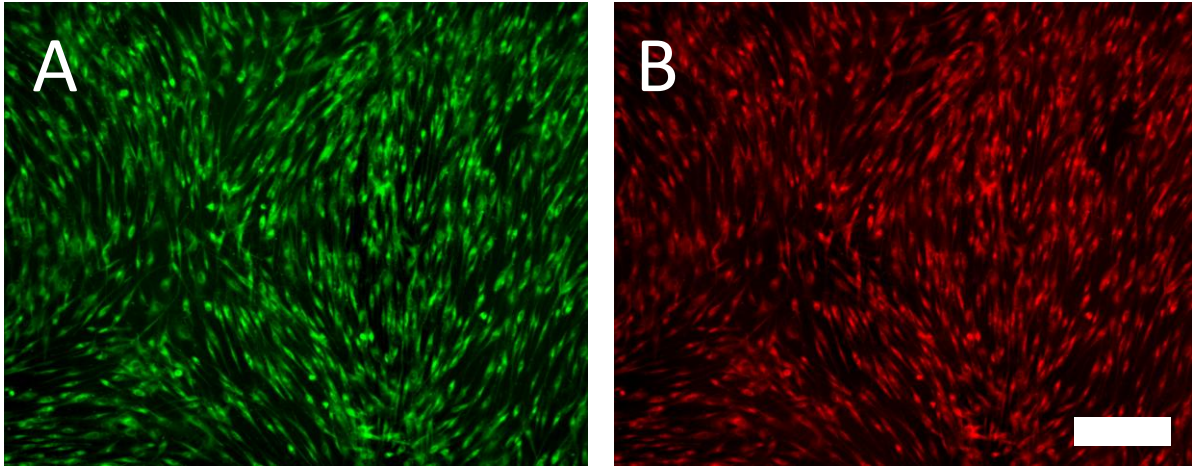


Figure 89: Fluorescence of alginate CNPs within primary human fibroblasts (passage 4) cultured for 7 days in cDMEM, supplemented with CNPs for the final 2 hours (20 μ l CNP solution within 1 ml cDMEM). CNPs within the cells were excited with (A) 490 nm and (B) 570 nm light causing emissions at (A) 525 nm and (B) 590 nm. Three separate triplicate repeat experiments ($n=9$) were conducted with each triplicate utilising a different batch of cells ($N=3$). Scale bar: 200 μ m

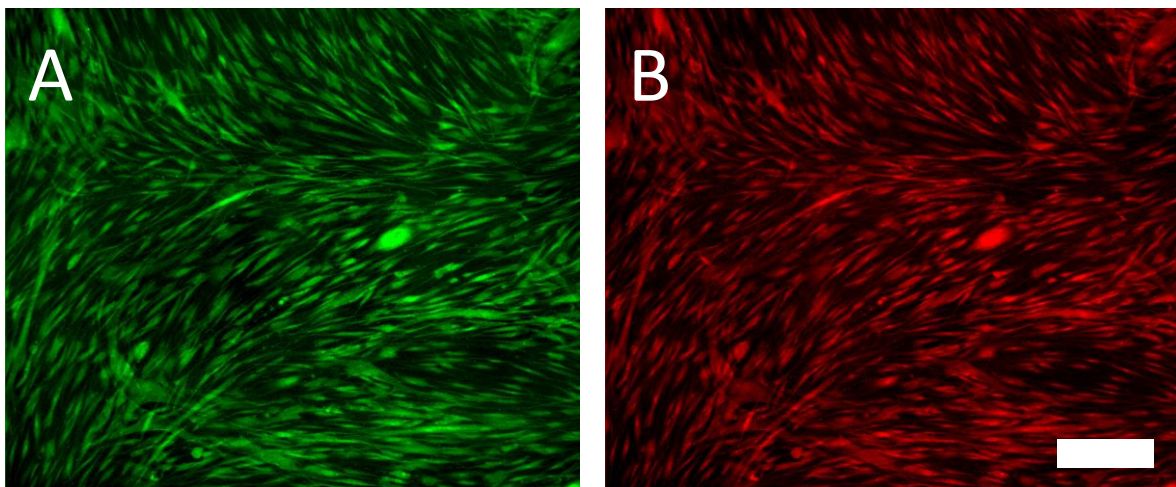


Figure 90: Fluorescence of alginate CNPs within primary human fibroblasts (passage 4) cultured for 7 days in cDMEM, supplemented with CNPs for the final 48 hours (20 μ l CNP solution within 1 ml cDMEM). CNPs within the cells were excited with (A) 490 nm and (B) 570 nm light causing emissions at (A) 525 nm and (B) 590 nm. Three separate triplicate repeat experiments ($n=9$) were conducted with each triplicate utilising a different batch of cells ($N=3$). Scale bar: 200 μ m

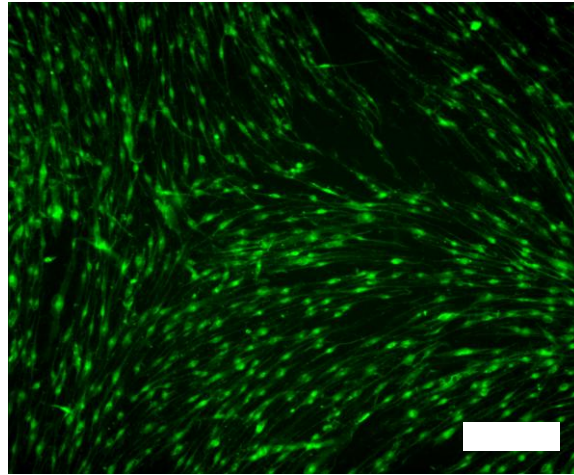


Figure 91: Fluorescence of alginate CNPs within primary rat Schwann cells (passage 3) cultured for 21 days in Schwann cell medium, supplemented with CNPs for the final 2 hours (20 μ l CNP solution within 1 ml Schwann cell medium). CNPs within the cells were excited with 490 nm light causing emission at 525 nm. A triplicate experiment ($n=3$) was conducted which utilised a single batch of cells ($N=1$). Scale bar: 200 μ m

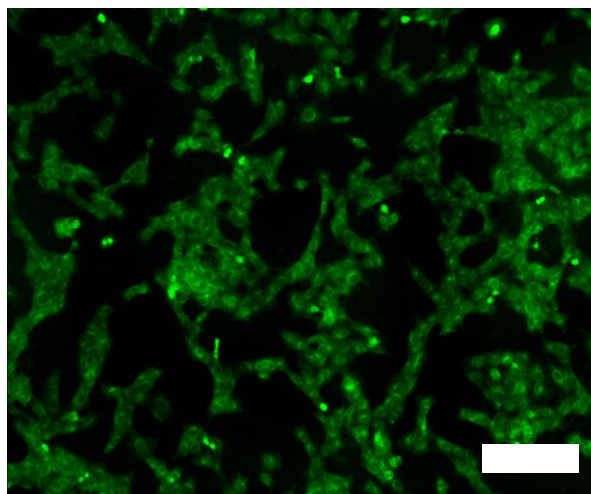


Figure 92: Fluorescence of alginate CNPs within RN22 cells (passage 13) cultured for 5 days in cDMEM, supplemented with CNPs for the final 2 hours (20 μ l CNP solution within 1 ml Schwann cell medium). CNPs within the cells were excited with 490 nm light causing emission at 525 nm. Three separate triplicate repeat experiments ($n=9$) were conducted with each triplicate utilising a different batch of cells ($N=3$). Scale bar: 200 μ m

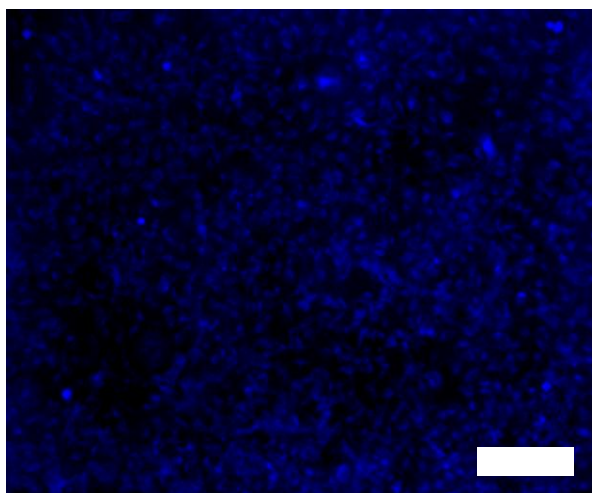


Figure 93: Fluorescence of alginate CNPs within NG108-15 cells (passage 14) cultured for 5 days in serum-free DMEM supplemented with CNPs for the final 2 hours (20 μ l CNP solution within 1 ml cDMEM). Cells within the cells were excited with 350 nm light causing emission at 470 nm. Three separate triplicate repeat experiments ($n=9$) were conducted with each triplicate utilising a different batch of cells ($N=3$). Scale bar: 200 μ m.

5.4.1.5 Sucrose CNPs

Vivid fluorescence was witnessed from sucrose CNPs uptaken by all of the cells in the study (figures 94 – 98), indicating that the particles can emit radiation in the red, blue and green visible regions. As was the case previously with alginate and glucose CNPs, clear images of fibroblast cells were attained following culture supplemented with sucrose CNPs for 2 hours and 48 hours. Although at the 2 hour timescale the emission intensity of the CNPs in the red and green visible regions appeared approximately equal, following 48 hours incubation emission in the green region was more intense than in the red (figure 95). Cell morphology appeared clearer in the images taken 2 hours post CNP addition as opposed to 48 hours.

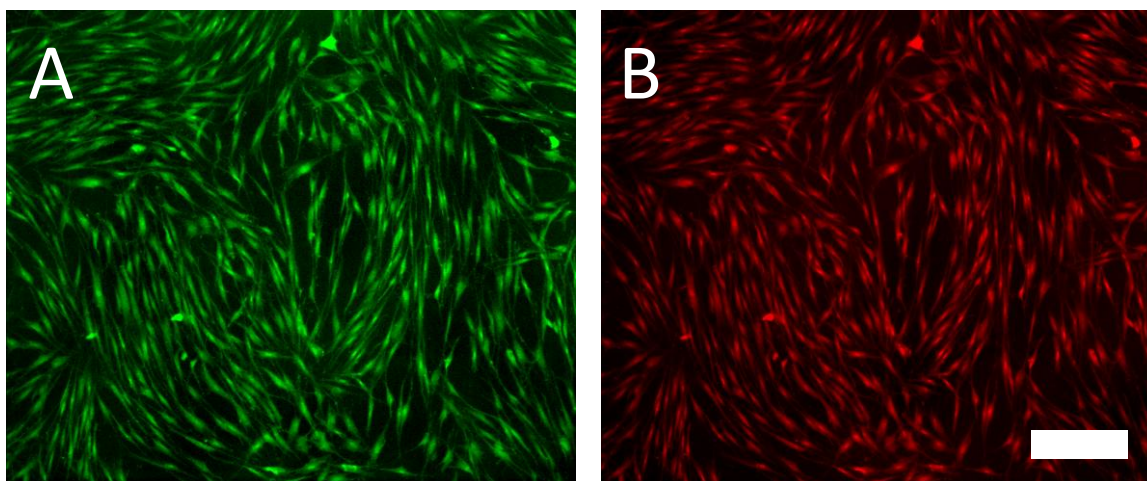


Figure 94: Fluorescence of sucrose CNPs within primary human fibroblasts (passage 4) cultured for 7 days in cDMEM, supplemented with CNPs for the final 2 hours (20 μ l CNP solution within 1 ml cDMEM). CNPs within the cells were excited with (A) 490 nm and (B) 570 nm light causing emissions at (A) 525 nm and (B) 590 nm. Three separate triplicate repeat experiments ($n=9$) were conducted with each triplicate utilising a different batch of cells ($N=3$). Scale bar: 200 μ m

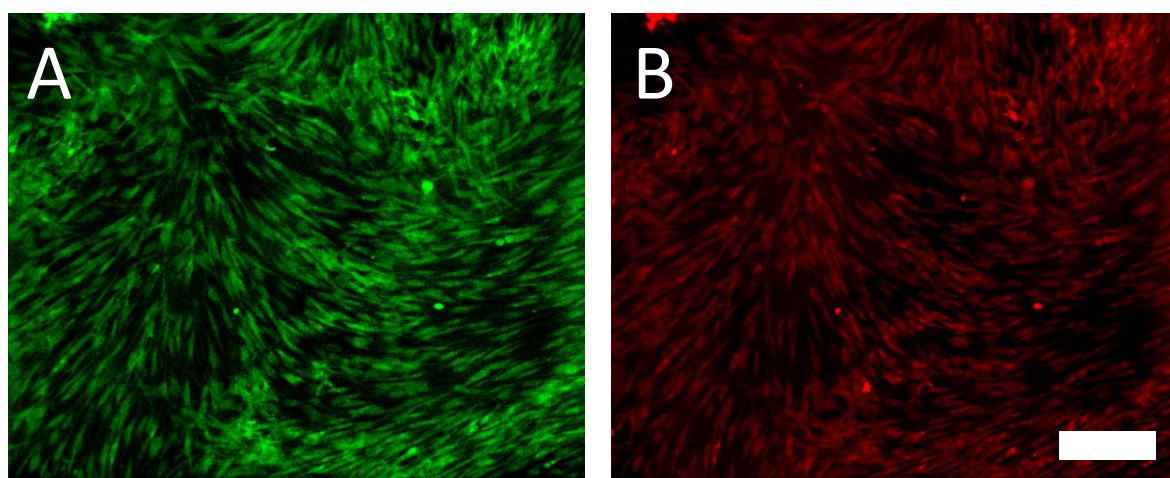


Figure 95: Fluorescence of sucrose CNPs within primary human fibroblasts (passage 4) cultured for 7 days in cDMEM, supplemented with CNPs for the final 48 hours (20 μ l CNP solution within 1 ml cDMEM). CNPs within the cells were excited with (A) 490 nm and (B) 570 nm light causing emissions at (A) 525 nm and (B) 590 nm. Three separate triplicate repeat experiments ($n=9$) were conducted with each triplicate utilising a different batch of cells ($N=3$). Scale bar: 200 μ m

Furthermore, sucrose CNPs fluoresced brightly once uptaken by RN22 (figure 97), NG108-15 (figure 98) and Schwann cells (figure 96) although cell morphology was difficult to identify in these cases, largely due to high cell confluency. Interestingly, sucrose CNPs which were uptaken by the NG108-15 and primary Schwann cells appeared to migrate into the cell nuclei, whereas they were characteristically absent from the nuclei of RN22 and fibroblast cells.

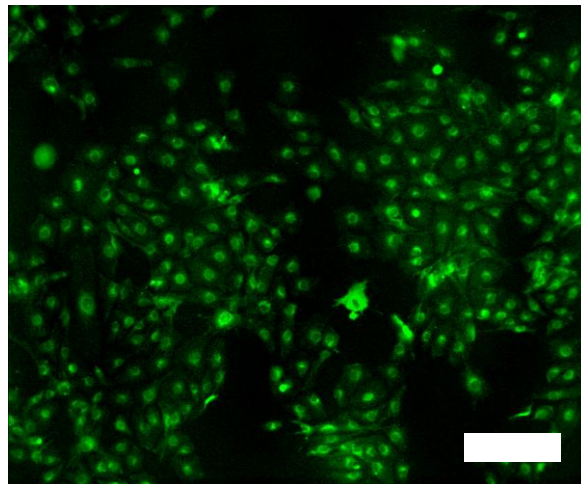


Figure 96: Fluorescence of sucrose CNPs within primary rat Schwann cells (passage 3) cultured for 21 days in Schwann cell medium, supplemented with CNPs for the final 2 hours (20 μ l CNP solution within 1 ml Schwann cell medium). CNPs within the cells were excited with 490 nm light causing emission at 525 nm. A triplicate experiments ($n=3$) was conducted which utilised a single batch of cells ($N=3$). Scale bar: 200 μ m

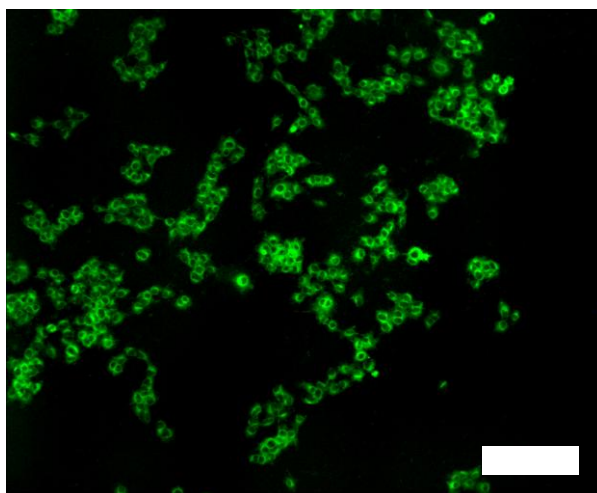


Figure 97: Fluorescence of sucrose CNPs within RN22 cells (passage 13) cultured for 5 days in cDMEM, supplemented with CNPs for the final 2 hours (20 μ l CNP solution within 1ml cDMEM). CNPs within the cells were excited with 490 nm light causing emission at 525 nm. Three separate triplicate repeat experiments (n=9) were conducted with each triplicate utilising a different batch of cells (N=3). Scale bar: 200 μ m

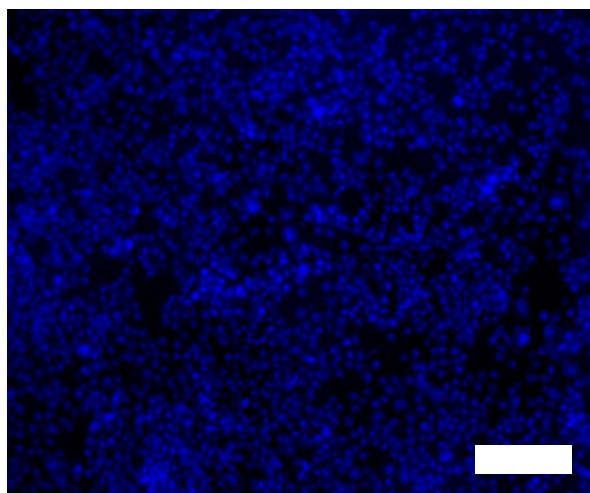


Figure 98: Fluorescence of sucrose CNPs within NG108-15 cells (passage 14) cultured for 5 days and supplemented with CNPs for the final 2 hours (20 μ l CNP solution within 1 ml cDMEM). Cells were excited at 350 nm causing light emission at 470 nm. Three separate triplicate repeat experiments (n=9) were conducted with each triplicate utilising a different batch of cells (N=3). Scale bar: 200 μ m.

5.4.1.6 Alginate/Sucrose CNPs

Alginate-sucrose CNPs fluoresced relatively intensely post-uptake by cells, but visualising cell features following CNP fluorescence appeared difficult. CNPs appeared to congregate around the outside region of the nuclei within fibroblast cells (figures 99 and 100), failing to distribute evenly within the cytoskeleton and cytoplasm contrasting with CNPs produced from single carbon sources. Emissions detected at 590 nm appeared even more indistinct than those recorded at 525 nm, possibly suggesting CNPs aggregating around the cell membrane and distorting the image. This pattern was also reported within RN22 cells exposed to the same type of CNPs (figure 102) whereby, although fairly intense fluorescence was observed, the CNPs did not appear to migrate through the cells evenly enough, to produce images of sufficient quality to rival existing laboratory cell imaging techniques.

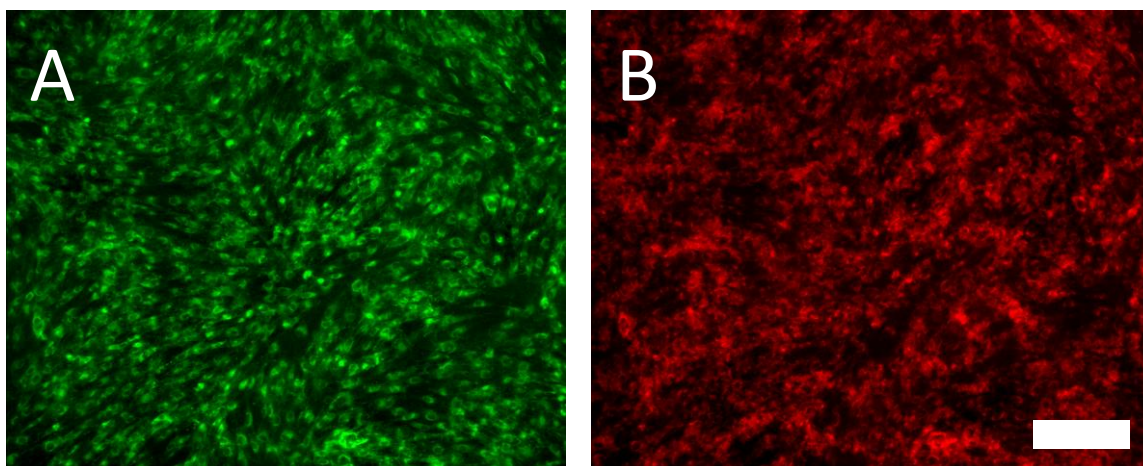


Figure 99: Fluorescence of alginate/sucrose CNPs within primary human fibroblasts (passage 4) cultured for 7 days in cDMEM, supplemented with CNPs for the final 2 hours (20 μ l CNP solution within 1 ml cDMEM). CNPs within the cells were excited with (A) 490 nm and (B) 570 nm light causing emissions at (A) 525 nm and (B) 590 nm. Three separate triplicate repeat experiments ($n=9$) were conducted with each triplicate utilising a different batch of cells ($N=3$). Scale bar: 200 μ m

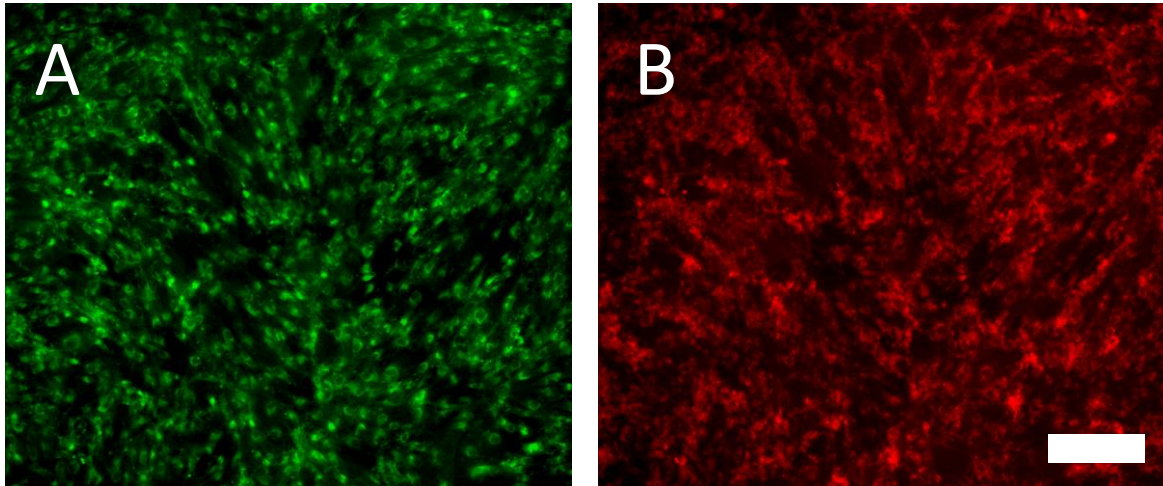


Figure 100: Fluorescence of alginate/sucrose CNPs within primary human fibroblasts (passage 4) cultured for 7 days in cDMEM, supplemented with CNPs for the final 48 hours (20 μ l CNP solution within 1 ml cDMEM). CNPs within the cells were excited with (A) 490 nm and (B) 570 nm light causing emissions at (A) 525 nm and (B) 590 nm. Three separate triplicate repeat experiments ($n=9$) were conducted with each triplicate utilising a different batch of cells ($N=3$). Scale bar: 200 μ m

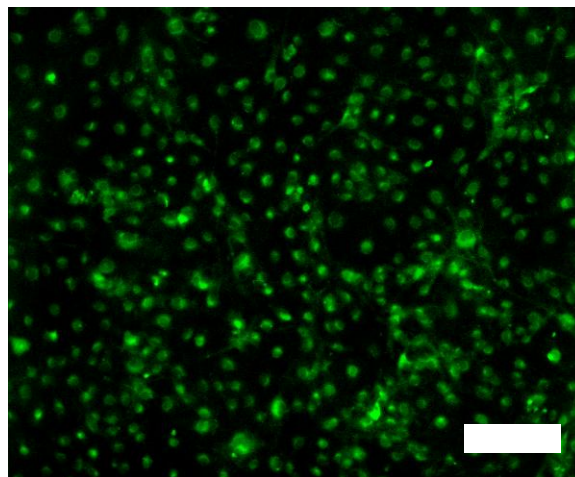


Figure 101: Fluorescence of alginate/sucrose CNPs within primary rat Schwann cells (passage 3) cultured for 21 days in Schwann cell medium, supplemented with CNPs for the final 2 hours (20 μ l CNP solution within 1 ml Schwann cell medium). CNPs within the cells were excited with 490 nm light causing emission at 525 nm. A triplicate experiment ($n=3$) was conducted which utilised a single batch of cells ($N=1$). Scale bar: 200 μ m

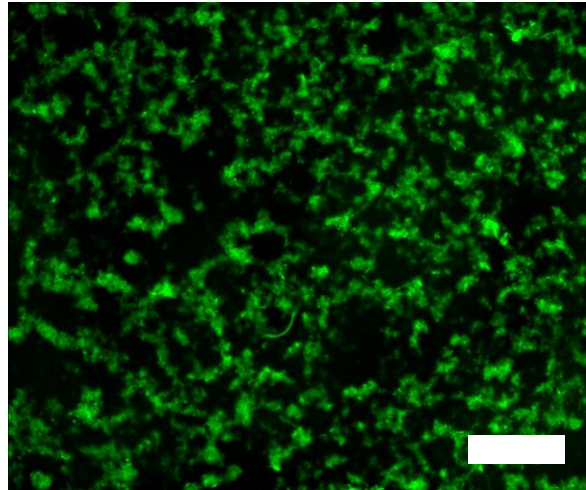


Figure 102: Fluorescence of alginate/sucrose CNPs within RN22 cells (passage 13) cultured for 5 days in cDMEM, supplemented with CNPs for the final 2 hours (20 μ l CNP solution within 1ml cDMEM). CNPs within the cells were excited with 490 nm light causing emission at 525 nm. Three separate triplicate repeat experiments (n=9) were conducted with each triplicate utilising a different batch of cells (N=3). Scale bar: 200 μ m

5.4.1.7 Alginate/Glucose CNPs

Alginate-glucose CNPs produced similar cell imaging results as with the alginate-sucrose CNPs. Unfortunately this sample also appeared not to be suitable for cell imaging due to the lack of clarity and definition in the cell images collated. In the fibroblast images (figures 103 and 104) the morphology of the cells did not appear clear, although the imaging of cells did seem to benefit from longer exposure times to CNPs, as the image collected 48 hours post CNP addition appeared more detailed and distinct than the image collated 2 hours post supplementation. However, a timescale such as 48 hours is not ideal, and images collated over shorter timescales with greater clarity were achieved using CNPs from a single carbon source (e.g. alginate – figure 89).

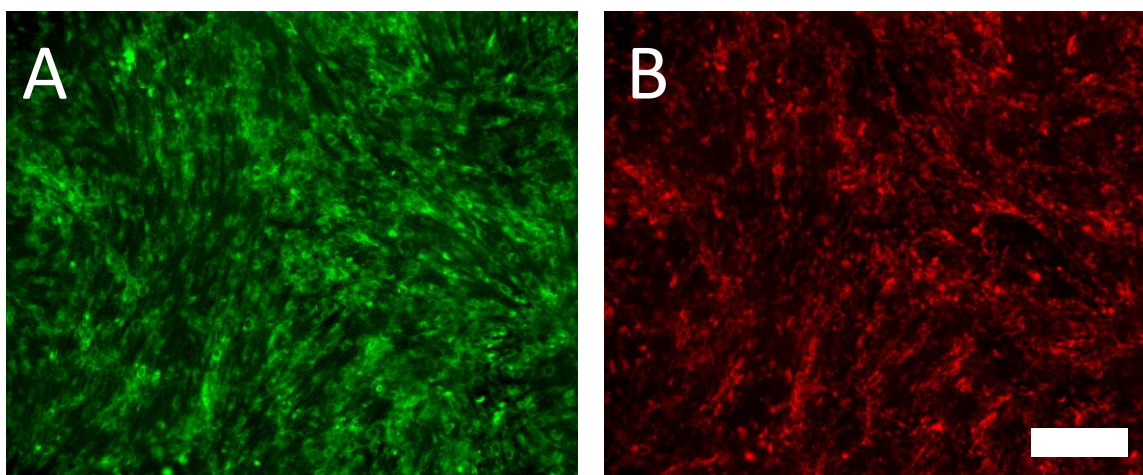


Figure 103: Fluorescence of alginate/glucose CNPs within primary human fibroblasts (passage 4) cultured for 7 days in cDMEM, supplemented with CNPs for the final 2 hours (20 μ l CNP solution within 1 ml cDMEM). CNPs within the cells were excited with (A) 490 nm and (B) 570 nm light causing emissions at (A) 525 nm and (B) 590 nm. Three separate triplicate repeat experiments (n=9) were conducted with each triplicate utilising a different batch of cells (N=3). Scale bar: 200 μ m

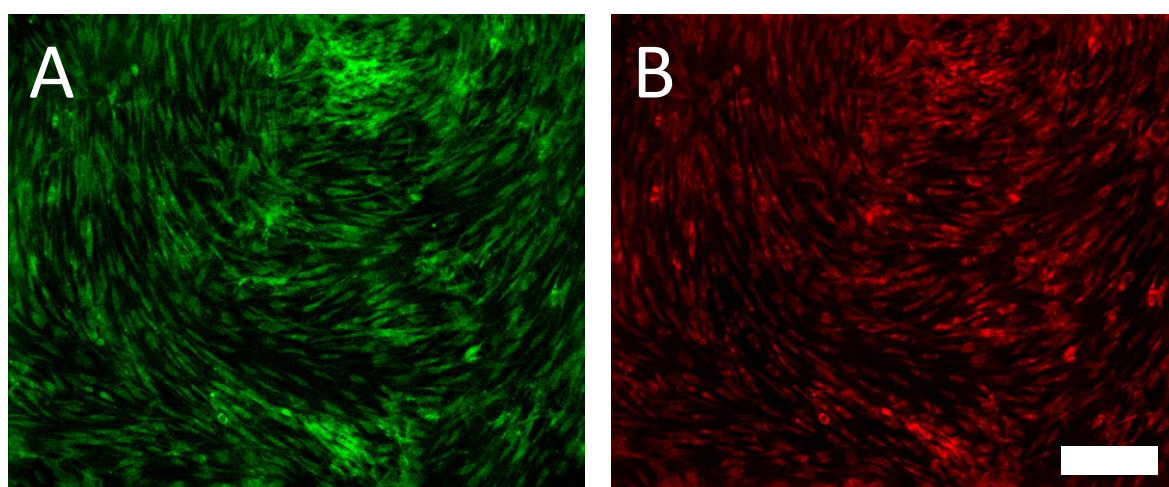


Figure 104: Fluorescence of alginate/glucose CNPs within primary human fibroblasts (passage 4) cultured for 7 days in cDMEM, supplemented with CNPs for the final 48 hours (20 μ l CNP solution within 1 ml cDMEM). CNPs within the cells were excited with (A) 490 nm and (B) 570 nm light causing emissions at (A) 525 nm and (B) 590 nm. Three separate triplicate repeat experiments (n=9) were conducted with each triplicate utilising a different batch of cells (N=3). Scale bar: 200 μ m

Although primary Schwann cells were also treated with alginate/glucose CNPs the image collected (figure 105) 2 hours after CNPs were added to the media appears only marginally better than the control image and seeks to reinforce the finding that CNPs produced from a combination of carbon sources may not be suitable for cell imaging purposes.

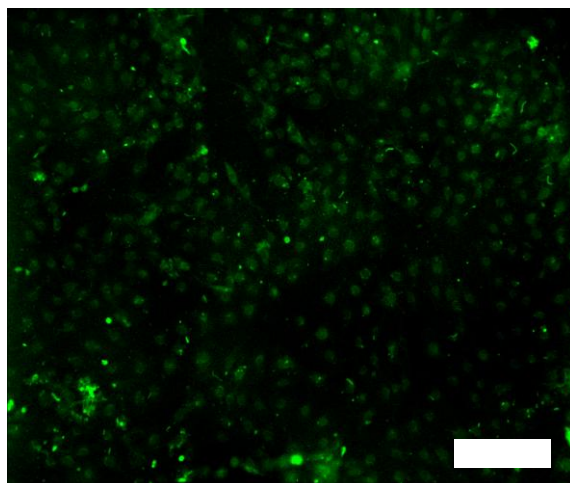


Figure 105: Fluorescence of alginate/glucose CNPs within primary rat Schwann cells (passage 3) cultured for 21 days in Schwann cell medium, supplemented with CNPs for the final 2 hours (20 μ l CNP solution within 1 ml Schwann cell medium). CNPs within the cells were excited with 490 nm light causing emission at 525 nm. A triplicate experiment (n=3) was conducted which utilised a single batch of cells (N=1). Scale bar: 200 μ m

A summary of the cell types and CNPs utilised in the aforementioned CNP luminescence experiments is stated in table 15.

	Control	CNPs				
		Glucose	Alginate	Sucrose	Alginate / Sucrose	Alginate / Glucose
Primary Fibroblasts	✓	✓	✓	✓	✓	✓
Primary Schwann Cells	✓	✓	✓	✓	✓	✓
RN22	✓	✗	✓	✓	✓	✗
NG108-15	✓	✗	✓	✓	✗	✗

Table 15: A summary of the luminescence experiments conducted in chapter 5, displaying the different types of cells tested with the various CNPs produced (✓ = positive result, ✗ = negative result). Testing was concentrated on utilising the primary cells available.

5.4.2 Live / dead imaging of fibroblast cells incubated with CNPs

In order to assess the cytotoxicity of the different CNPs utilised in the study a live/dead stain was conducted using fibroblast cells cultured to 75 – 90 % confluency. CNPs were incubated with the cells in the cDMEM for 48 hours prior to the commencement of staining using SYTO-9 and propidium iodide, which differentiated between live (green) and dead (red) cells respectively. The uptake of both dyes was monitored by fluorescence microscopy.

All fibroblast cells surveyed by the SYTO-9 / propidium iodide stain appeared alive with no signs of cell detachment or irregular characteristics (figure 106). Indeed, no cells appeared abnormal and careful washing of cells between each stage of the staining process ensured few, if any, dead cells were accidentally discarded.

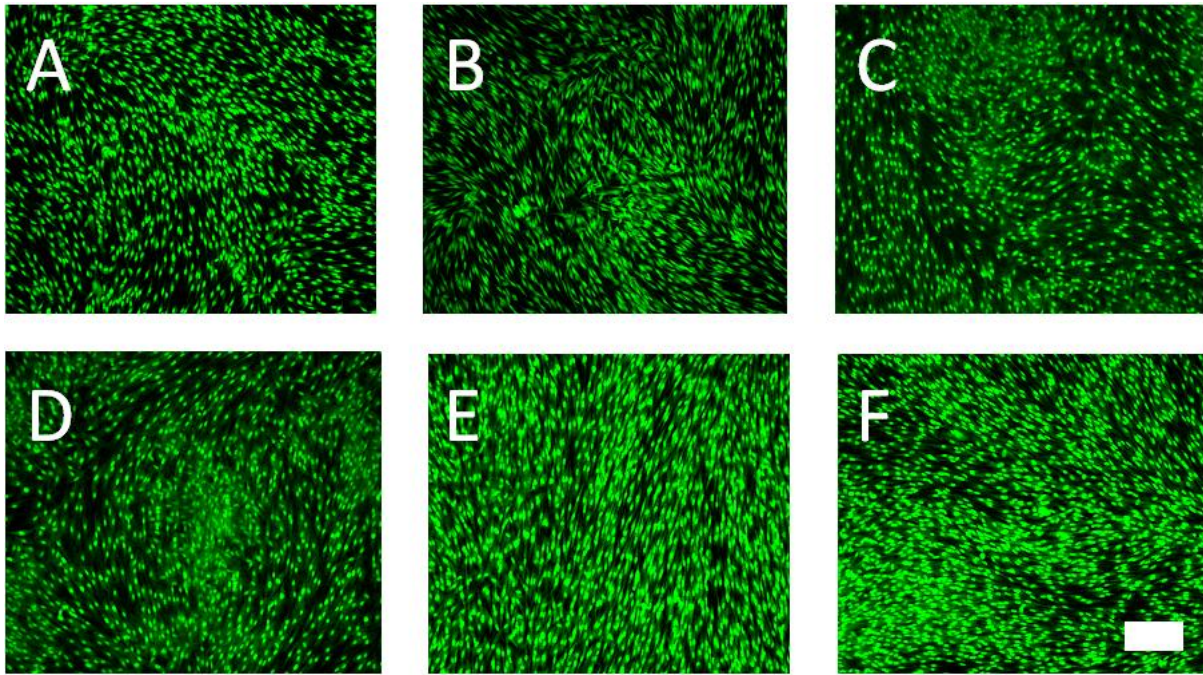


Figure 106: Primary human fibroblasts stained with SYTO-9 and propidium iodide after being incubated for 48 hours with (A) glucose, (B) alginate, (C) sucrose, (D) alginate/sucrose and (E) alginate/glucose CNPs. A control sample where the cells were not exposed to any CNPs was also analysed (F). A triplicate experiment ($n=3$) was conducted which utilised a single batch of cells ($N=1$). Scale bar: 200 μm

In addition, despite numerous different CNPs being added to the different fibroblast cultures, all cells displayed a normal fibroblastic morphology which demonstrated a lack of toxicity associated with microwave-generated CNPs.

5.4.3 MTT assay of fibroblast cells incubated with CNPs

A second method of assessing CNP cytotoxicity was an MTT assay, which was utilised across all CNP samples to test their effect on fibroblast metabolic activity. Cells were tested using MTT after being exposed to CNPs for either 2 hours or 48 hours once reaching at least 75% confluency. Additionally, the effect of utilising high and low initial concentrations of glucose within the CNP precursor mixture was also investigated.

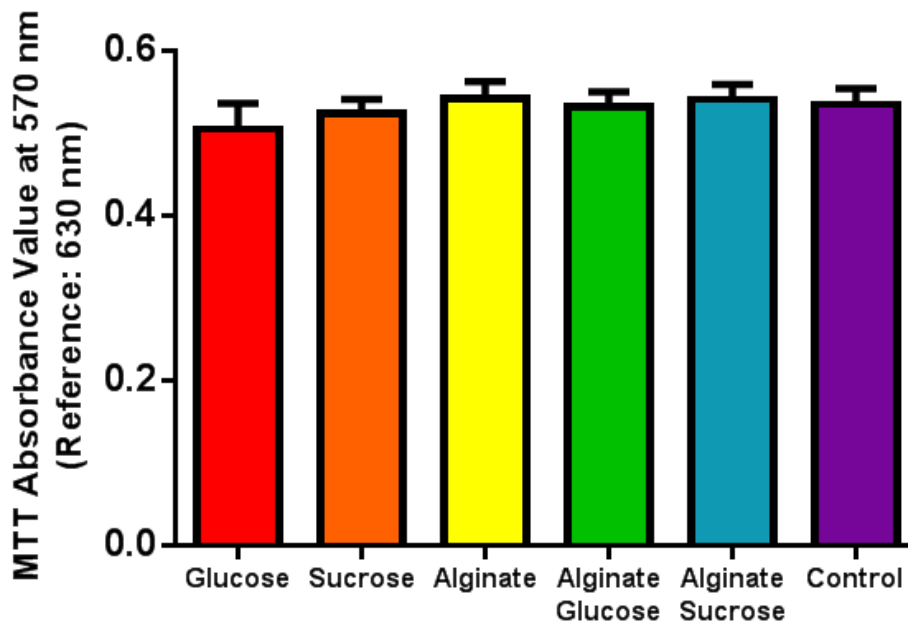


Figure 107: Fibroblast metabolic activity assessed by MTT assay upon cells cultured for 7 days which were exposed to CNPs (20 μ l within 1 ml cDMEM) for the final 2 hours. Values were reported from the mean (\pm standard error) of three separate triplicate repeat experiments ($n=9$) with each triplicate utilising a different batch of cells ($N=3$).

Following incubation with CNPs for 2 hours the MTT assay illustrated that there was no significant decrease in fibroblast metabolic activity compared with the control sample which was exposed to no CNPs (figure 107). The lowest mean metabolic activity was recorded by fibroblasts incubated with glucose CNPs (0.505 ± 0.0306) whilst the highest was recorded by cells in contact with alginate CNPs (0.542 ± 0.0207). All samples recorded remarkably similar assay values, highlighting the lack of cytotoxicity associated with these CNPs at short time scales.

An additional MTT assay to assess the effect of longer term contact (48 hours) of fibroblasts with CNPs also indicated no significant detrimental impact upon metabolic activity (figure 108). Although recorded assay values were lower than those recorded in the 2 hour experiment, the lower value also recorded for the 48 hour control sample illustrated that this

was not due to CNP exposure. Indeed, all assay values recorded from cells in contact with the CNPs for 48 hours were marginally higher than the control reading, although not significantly so. As with the cells incubated with CNPs for 2 hours, the highest assay reading in this sample was recorded by the cells in contact with alginate CNPs (0.503 ± 0.0381) whereas the control sample illustrated the lowest reading (0.447 ± 0.0171). This again demonstrated the lack of CNP cytotoxicity, whereby exposure of up to 48 hours was shown to have no adverse effect upon cell viability and corroborated the 100% live cell record demonstrated by the live/dead cell assay (figure 106).

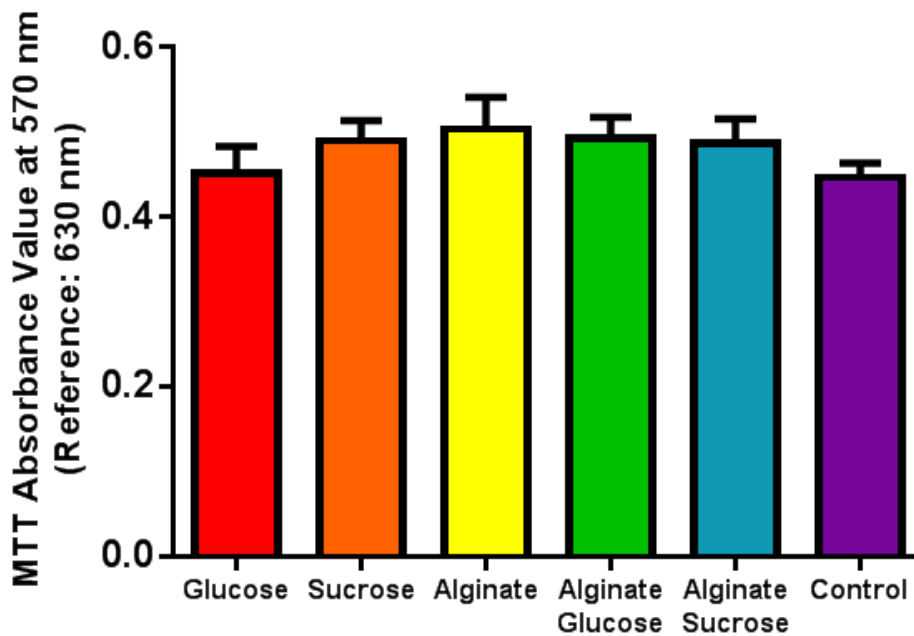


Figure 108: Fibroblast metabolic activity assessed by MTT assay upon cells cultured for 7 days which were exposed to CNPs (20 μ l within 1 ml cDMEM) for the final 48 hours. Values were reported from the mean (\pm standard error) of three separate triplicate repeat experiments ($n=9$) with each triplicate utilising a different batch of cells ($N=3$).

Furthermore, the initial ratio of the carbon source in relation to glycerol in the precursor mixture was also found to have no significant effect upon cell viability (figure 109). Although the MTT absorbance value was slightly higher for the lower glucose concentration

(1M: 0.478 ± 0.0158) in comparison to the CNPs produced from the 2.5M solution (0.452 ± 0.0318) this was not found to be a significant difference. These findings demonstrated that not only can biocompatible CNPs be produced relatively easily but the process is remarkably versatile and reliable.

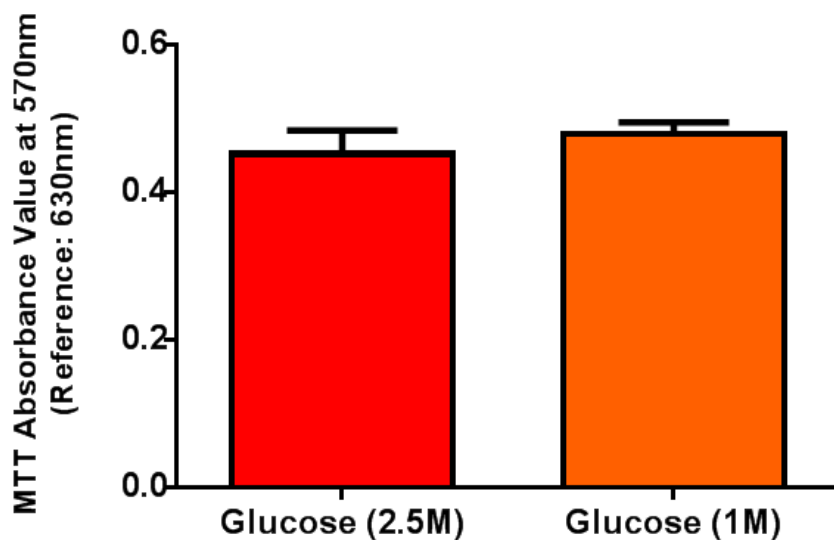


Figure 109: Fibroblast metabolic activity assessed by MTT assay upon cells cultured for 7 days which were exposed to glucose CNPs (20 μ l within 1 ml cDMEM) for the final 48 hours. Values were reported from the mean (\pm standard error) of three separate triplicate repeat experiments ($n=9$) with each triplicate utilising a different batch of cells ($N=3$). The ratio of glucose within the initial mixture, in relation to glycerol, was varied to assess the impact on cell viability

5.4.4. Summary of CNP Properties

	CNP				
	Glucose	Alginate	Sucrose	Alginate / Sucrose	Alginate / Glucose
CNP luminescence observed	✓	✓	✓	✓	✓
CNPs uptaken by cells	✓	✓	✓	✓	✓
Following CNP exposure cell morphology is discernible by microscopy	✓	✓	✓	✗	✗
Significant toxicity to cells detected following 2 hours CNP exposure	✗	✗	✗	✗	✗
Significant toxicity to cells detected following 48 hours CNP exposure	✗	✗	✗	✗	✗
Presence of dead cells detected by live / dead assay following CNP incubation	✗	✗	✗	✗	✗

Table 16: Summary of the findings associated with the experiments conducted in chapter 5 concerning the various CNPs produced (✓ = positive result, ✗ = negative result)

5.5 Conclusion

This chapter has illustrated the relative ease with which effective fluorescent carbon dots can be created from inexpensive and readily available materials. Their biocompatibility and swift internalisation enable them to be ideally suited as *in vitro* live cell markers, although the

degree to which cell uptake occurs appears to depend upon the CNP source material and the cell type themselves. Despite dual-origin CNPs failing to adequately internalise within cells to produce a clear fluorescent image, their bright emission upon excitation nevertheless proved that they are photofluorescent particles capable of emitting light across a range of visible wavelengths.

Chapter Six: Discussion

6.1 Introduction – DLC & ND discussion

The data in this thesis has demonstrated the ease with which DLC and ND can be functionalised with a wide range of chemical moieties, some of which have proven to be particularly effective for culturing neuronal and glial cells. The demand for alternative growth surfaces ameliorating the issues associated with conventional functionality provided by polylysine continues to grow [8, 51, 53, 91, 249]. This is especially apparent due to the need to create effective surfaces for a variety of *in vivo* neuronal based applications such as brain computer interfaces (BCIs) [250-252] and the bionic eye [253].

6.1.1 Discussion of DLC and ND related data

Numerous variables usually dictate the survival, growth and differentiation of neuronal cells *in vitro*, one of the most important of which is the culture substrate [249, 254]. The culture medium also plays a role, as does the dissociation technique if primary cells are utilised [254]. Substrates that have been commonly used in the culture of neuronal cells include polymers of basic amino acids such as polylysine (PL) and polyornithine [255, 256], whilst extracellular matrix constituents including laminin have also been applied, with collagen and fibronectin also being used to a lesser extent [257-260]. Such coatings have become widespread as a pre-treatment to neuronal cell culture since they promote cellular adhesion, survival and neurite outgrowth [249, 254, 256, 261].

One way it is assumed that substances such as PL, which contain amine groups, improve cell viability is to interact with specific receptors on neuronal cell membranes to enhance

adhesion to the substrate. Polycationic amino acids, on the other hand, are thought to act as positively charged bridges to electrostatically attach negatively charged cell membranes to the substrate surface [247, 256, 262]. Proteins originating from the serum component of the cell medium have also been highlighted as assisting cell adhesion, acting in a similar manner to extracellular matrix proteins [247].

PL surfaces have also been shown to develop a greater surface thickness of adsorbed proteins during cell culture compared to control surfaces, these either being secreted by the cells once attached, or adsorbed from the constituents of the cell medium [254]. Initial proteins which adsorb to PL denature and do not encourage neuronal adhesion; however subsequent proteins which bind to this denatured layer are envisaged to have their structure intact, thus encouraging the formation of a bound neuronal population. The fact that polylysine establishes a surface that is amenable to cell growth across a variety of cell media illustrates why it has been selected as a standard neuronal cell culture substrate.

Usually, although the coating of PL upon culture substrates is adequate to support the growth of neuronal cells *in vitro*, it is not envisaged to be desirable or permissible to introduce foreign-derived proteins such as PL for *in vivo* applications such as neural prosthetics [8]. Its inherent cytotoxicity also prevents its use across *in vivo* applications for which it would otherwise be suitable.

Transgressing the need for serum, AAND and amine-functionalised DLC (DLC-Amine) surfaces detailed within this thesis ensured neuronal survival despite the culture medium being serum-free. Although serum-free media enables experiments to be conducted in a chemically-controlled environment, with results being easier to repeat and interpret due to fewer variables, it has been traditionally more difficult to maintain neuronal survival in these conditions [263, 264]. It is therefore apparent that an inherent property, or combination of

surface features, associated with AAND/DLC-Amine substrates encourages neuronal adhesion to the extent that serum is no longer required. One possible explanation for this could be that the substrate helps stimulate greater ECM protein production from adhered cells. If true, this may bring greater opportunities for neural-based implants for *in vivo* applications due to the ability to produce a biomaterial without the need to supplement the surface with additional ECM proteins.

Certainly, although PL has been widely applied as a surface treatment for neuronal cell growth substrates it has been previously demonstrated that surface-bound amine groups can support neuronal adhesion and differentiation similarly without detrimental effects [265]. Although research in this area is ongoing it is envisaged that amines interact with cells through membrane-bound chondroitin sulphate proteoglycans (CSPGs). These proteoglycans exert significant influence over controlling neuronal differentiation via integrin mediated signalling illustrating the basic principle behind the neurocompatibility of amines [266, 267].

It is possible that by physically aminating culture surfaces it may enhance neural longevity in comparison to substrates non-covalently modified with PL. This finding, that furthers the case for a covalently functionalised surface such as am-DLC, demonstrated that significantly higher shear stresses were required to detach NG108-15 cells from covalently-modified amine surfaces, rather than those functionalised with ECM proteins [249]. This was corroborated by further research which concluded that chemically-adhered PL was far more effective at retaining adhered cells than the physically adsorbed alternative [256]. An additional benefit of chemisorbed functionalities is their lack of leaching into solution, contrasting with non-covalently bound PL whose gradual loss can result in cell dissociation [256]. All these factors hence demonstrate the advantages associated with chemisorbed functionalised substrates such as AAND/am-DLC compared to conventional functionalised substrates created by PL adsorption.

Intriguingly, an alternative to amine functionalised surfaces was discovered during the experiments conducted in this thesis through the effective use of aldehyde-terminated (10-undecenal) substrates for culturing neuronal cells. Although relatively little research has been undertaken regarding such functionalities for cell growth, aldehyde-terminated surfaces are regarded as being hydrophilic. In addition, plasma surfaces formed from aldehyde functionalities have been shown to support the growth and attachment of cells to a similar degree as those cultured upon tissue culture plastic (TCP) [230]. Additionally, aldehyde-functionalised substrates have been shown capable of immobilising proteins upon their surface to produce self assembled monolayers (SAMs) indicating that they may be applied to applications within the biosensor research field as well as within cell culture [268].

Within the DLC study of this thesis aldehyde-terminated surfaces supported neuronal cells to the extent that they were phenotypically similar to those cultured upon polylysine and DLC-Amine. The UV attachment of undecenal also appeared to occur significantly faster than the protected amine of TFAAD, where by the same proportion of functionalisation which occurred using TFAAD within 4 hours was achieved in just 20 minutes utilising the aldehyde. The dynamics and reasons for this are not entirely clear; however the variable reactivity of 1-alkenes with different distal functional groups has been commented upon before [191, 231]. Previously, three different alkenes of similar size (TFAAD, 1-dodecene and 10-*N*-Boc-aminodec-1-ene [tBoc]) were photografted upon hydrogenated silicon whereby TFAAD demonstrated approximately double the reactivity of 1-dodecene. It was suggested that UV radiation causes photoemission from the bulk substrate into the acceptor groups of the alkene molecules. This process causes the formation of a valence-band hole that encourages nucleophilic attack by the alkene. The rate-limiting step can essentially be a result of the electron affinity of the reactant alkene. It may therefore be the case that 10-undecenal

has greater electron-accepting potential than TFAAD but the dynamics and intricacies of this process are unfortunately beyond the scope of this project.

Additionally, it was discovered the termination of the substrate also determined the reactivity of alkenes [191]. Oxygenated amorphous carbon surfaces, richly functionalised with carbonyl groups, were shown to have an enhanced photochemical grafting capability compared with hydrogenated substrates. This occurs despite oxygen causing an increase in the work function. These differences, observed markedly upon binding dodecene and tBoc, relate to oxygenated surfaces exerting significantly greater influence upon the photoelectron emission reaction by their ability to ‘trap’ electrons which in turn helps initiate the grafting process. It is important to note that upon crystalline diamond surfaces however, hydrogen-terminated substrates remain the most desirable to achieve greatest reactivity with alkene molecules. This is due to the ability of the hydrogen terminations to reduce the energy barrier to electron emission from diamond to just below the UV photon energy. The increased work function of oxygen, however, takes greater precedence upon diamond surfaces than amorphous carbon and unfortunately negatively impacts upon its ability to photoemit upon exposure to UV. This renders oxygenated crystalline diamond surfaces less useful for photochemical functionalisation.

Helpfully, it seems apparent the polar component of the aldehyde group may enhance the attachment and growth of neuronal cells. Indeed, it is known that adhesion receptors within the cell membrane not only influence the adherence of cells but also mediate cellular growth and differentiation, highlighting the importance of creating a substrate that promotes cellular adhesion as a priority [269, 270].

Although these points highlight that functionalisation of the surface may appear important in encouraging cell growth and attachment, it could be argued the choice of the underlying

surface is equally as paramount. Within the studies detailed in this thesis DLC and ND-based substrates were selected for their suitability as possible coatings for nervous system implants and neuron:electrode interfaces due to several advantageous properties. One benefit of using diamond-based materials is their ability to be readily doped or functionalised to alter their characteristics to the greatest benefit of the desired application [18, 51, 68, 188, 197, 271]. Diamond materials have also been tested exhaustively to corroborate a lack of toxicity [17, 31, 124, 150, 190, 272]. With respect to industry the DLC/ND coating process offers a further advantage in that the size or shape of objects is of little consequence to the coating procedure. Most components and devices can be easily treated swiftly and at little expense to create a stable and robust surface layer [51, 170]. Additional positive attributes associated with ND surfaces include their bactericidal properties which may prove vital in restricting infections across *in vivo* and *in vitro* uses of the materials [273, 274] whilst the wear resistance of DLC could provide comparatively high longevity for any potential implants, reducing the need for intervention due to lower failures [51]. Indeed for some neural cell types, glass or DLC alone has been shown to support the growth of cells such as N2a neuroblastoma and PC12s [51]. However, cell culture studies conducted on pure DLC during the course of this thesis resulted in a lack of cell adhesion illustrating differences in cell growth behaviour. By day 7 of cell culture there with few if any cells remaining bound to pure DLC substrates.

Alternative methods of functionalising DLC to produce an effective nerve culture substrate have been trialled [51]. Attempts to make the surface more neurocompatible either by doping with phosphorous or by prolonged exposure to UV light have been met with success [51]. However, although irradiation may seem a simplistic manoeuvre the process did not favour the adhesion of neural cell lines (PC12) and it was discovered that UV-exposure partially removed the surface-bound DLC film due to oxidation. Whilst phosphorous-doped DLC appeared to be a highly effective neural culture substrate, the risk of dopant leaching which

could have severe implications over the lifespan of a long-term implant casts doubt over its future suitability [51]. Indeed, the non-dopant means of aminating nanodiamond and DLC demonstrated in this thesis will ensure that the efficacy of the surface would be unlikely to decrease in the long term.

Whilst the coating of DLC to glass undoubtedly produced a highly adherent surface layer, attempts to produce an equally as sturdy surface-bound ND layer were thought to be more challenging. To ensure the amine-functionalised nanodiamond would not detach following sonication the underlying glass substrate was coated with a plasma polymerised layer of acrylic acid (ppAA). This aimed to electrostatically attract the positively charged NDs to the surface. Although no long term studies into the stability of the acrylic acid / amine-nanodiamond bilayer were carried out, initial findings concerning the viability of the substrate were encouraging. The lack of cell detachment from the AAND samples following periods of cell culture of up to 21 days highlighted that the nanodiamond had formed a strong electrostatic bond to the underlying ppAA layer. This would have been of little use had the ppAA delaminated from the native glass substrate. However, through optimal manipulation of the parameters governing ppAA deposition during plasma polymerisation, namely the plasma power and monomeric flow rate, a coating was deposited that retained sufficient acidic functional groups to maintain nanodiamond attachment, whilst ensuring adequate polymer fragmentation to produce a strongly adherent surface layer.

This is not the first instance of ppAA being used to help fabricate a neuronal compatible growth substrate. Young *et al* [275] experimented with creating a poly(vinylidene fluoride) (PVDF) substrate which had been coated with ppAA upon which lysine, the basis for conventional polylysine surface coatings, was immobilised. Although limited analysis of cell compatibility upon the substrate was assessed, it was found that PC12 cell viability was greater upon substrates that had a greater ppAA density, due to the greater proportion of

immobilised lysine. Unfortunately, the lysine immobilisation yield was deemed insufficient to merit additional research due to the low efficiency of the amidation reaction between the carboxylic acid group of the ppAA and the amine group of lysine. Although numerous studies have been conducted to test how cells interact with plasma polymerised acrylic acid, little has been done to research its use as a base layer upon which to electrostatically attach particles [211, 233, 235]. However, although the choice of acrylic acid as a base layer was purely for convenience, there is little to suggest that alternative negatively charged surface layers wouldn't achieve a similar effect in creating a similar AAND substrate.

One further substratum property which has been postulated to influence cell behaviour *in vitro* is surface topography [247]. Varying studies have cited numerous cases where topographical surface features exert positive or negative impacts upon cell growth and survival [88, 91, 198, 276-282]

Although micron-scale surface roughness has been observed as affecting cell proliferation and morphology it is known that interactions between cells and the underlying substrate are usually governed by nanoscale mechanisms termed nanobiointeractions [277, 279, 280]. Indeed, since a cell's focal adhesions have a diameter of less than 200 nm, it is natural to derive that these small features may be highly influenced by nanoscale, rather than microscale, substrate topography [93].

Meanwhile, the adsorption of proteins to the culture surface, an initial step thought to preclude successful cell attachment, may indeed be a function of surface roughness. Although proteins are known to bind non-specifically to surfaces this phenomenon occurs much more readily upon surfaces that possess prominent nanoscale features, such as nanoparticles, which exhibit a high surface to volume ratio. These adsorbed proteins condition the surface and provide ligands from which integrins within the cell membrane can attach [283, 284]. The

initial surface properties determine the conformation, type and quantity of protein that is ultimately adsorbed [285].

Nanostructured surfaces have been reported to enhance the proliferation of cells such as osteoblasts with amine-functionalised silica nanoparticles also being proven to exert a similar effect upon endothelial and osteoblast cells [286]. These aminated nanoparticles also appeared to encourage cell spreading, a notion which may indicate a differentiated cell phenotype. Additionally, it was concluded that the presence of smaller nanoparticles (50 nm diameter) encouraged greater cell growth compared to surfaces composed of larger topographical features (100 nm - 300 nm particle diameter) [281]. Nanostructured surfaces have also been shown to enhance the proliferation and attachment of osteoblasts compared to those cells cultured upon flat control surfaces [278], further strengthening the beneficial concept of nanostructure upon neuronal cell growth.

On the other hand, a study stating the existence of a negative relationship between surface nanotopography and neuronal viability has also been published by Brunetti *et al* [95]. It was discovered that focal adhesion complexes may be negatively impacted by nanostructured surfaces, drastically reducing cell adhesion capability. Nanorough surfaces were also thought to contribute to the loss of neuronal polarity in these cells, the inadequate development of organelles such as golgi bodies and the formation of a weaker actin cytoskeleton. The lack of developed focal adhesions led to a cascade of events that eventually resulted in cell necrosis.

On first glance these findings may appear to discourage the use of AAND surfaces, these being based on nanodiamond. However, the mean roughness (Ra) of the substrates sampled in Brunetti's study were far higher (35 – 100 nm) than the mean roughness of AAND where Ra values were approximately 1 – 2 nm [95]. This low degree of AAND surface roughness implies that actually the surface nanotopography of the substrate may only have exerted

menial influence over neuronal cell adhesion. It therefore appears more likely that cells were influenced moreover by surface functionality alone. This would also account for the lack of noticeable differences in cell response to the AAND or DLC-Amine surfaces.

Indeed the findings published by Brunetti *et al* may be of little relevance to the research detailed within this thesis due to the use of only one cell line in the aforementioned study [95]. With no results confirming the impact of nanoroughness upon glial/neuronal primary cells it therefore presents a challenge to apply the conclusions from Brunetti's study to the findings listed in this thesis concerning AAND and DLC-Amine. Additionally, pure nanodiamond coated surfaces have been illustrated as being amenable to the culture of primary neuronal cells, whereby surface roughness values approaching 10 nm were noted, with no discernible negative impact upon neuronal adhesion, development or growth [8].

Relating these findings from the literature to the data collated within this thesis there appear to be few, if any, significant differences between neuronal and primary glial cells cultured upon either the nanostructured ND substrates, or the relatively flat DLC-Amine surfaces. Both substrates appeared to support the cells in a similar manner to PL, when analysing a wide range of parameters that assess neuronal compatibility such as neurite length and the neurite ratio per cell. Indeed, on the face of the data alone there seems to be little to choose from between the two diamond-based substrates.

On the other hand, despite AAND and DLC-Amine being equally as effective, both may not be suitable for all devices or surfaces which may require amination prior to neural seeding. Nanodiamond coating by ultrasonication may favour the functionalisation of intricate, detailed 3-dimensional objects whilst coating with DLC, with photoinitiated amine adsorption, would be more suited for flat surfaces requiring patterned or discriminate coating of a 2-dimensional surface. This latter coating method would be ideally suited to creating

hybrid neurocompatible/neurorepulsive surfaces where localised neuron development and growth could be controlled by surface properties, an asset highly sought in applications developing uniaxial neural outgrowth.

Neurorepulsive surfaces, such as hydrogen-terminated DLC, are known to inhibit neuronal growth due to the lack of adequate interaction sites to facilitate cell adhesion [91]. The hydrophobic nature of hydrogen functionalised substrates and the scarcity of electric field gradients ensures that cell attachment is greatly diminished. Indeed, analysis of cell culture upon hydrogenated nanodiamond detailed within this thesis indicated that the surface only supported neuronal based cells in the first stages of adhesion, whilst during the latter stages of the experiment (Days 5 and 7 of cell culture) cells appeared to rapidly dissociate from the surface either due to necrosis/apoptosis, substrate delamination or the severance of weak focal adhesions.

Despite the apparently hostile environment hydrogenated diamond surfaces pose towards neuronal cells, some limited studies have reported success in culturing cells upon hydrogenated-ND. Surfaces produced from monodispersed NDs which were then subjected to a surface hydrogenation treatment have been shown to support the short-term growth of primary neurons [251], although in this instance a very high initial seeding density was selected (100,000 cells / cm²) which may have influenced cell adhesion. In the absence of serum in the cell media neurons failed to attach however, which may corroborate the theory that ND particles encourage ECM adsorption. Unfortunately, the process whereby proteins would adsorb to a hydrophobic H-terminated ND surface, which would usually discourage cell adhesion is not fully understood. However, once a layer of ECM proteins adsorbs on to a surface, this being supplemented by cell secretions, the initial substrate functionalisation is thought to become less pertinent, with cell adhesion being determined moreover by the surface coverage of protein. The adhesion of cells, either to each other or to a substrate, is

known to be mediated by several different groups of receptors and proteins termed cell adhesion molecules (CAMs). These are known to include integrins which are heterodimeric molecules that govern both cell-cell adhesion and cell-substrate attachment and immunoglobulins and cadherins which generally govern cell-cell adhesion only [287]. Natural cell adhesion molecules are known to constitute the extracellular matrix and consist of proteins including collagen and fibronectin [288]. However, not all proteins that bind to substrates may encourage cell attachment. Indeed, some, such as alpha-1-antitrypsin are termed anti-adhesive proteins due to their ability to repel cell adhesion [289]. Although the presence of proteins within the media utilised in the amine-functionalised ND and DLC studies was not tested, it is envisaged that the concentration was fairly low since it was not supplemented with serum. However, this does not take into account the secretion of proteins from the cells themselves which may have affected their binding ability to the underlying substrate.

Additionally, similar results were attained by culturing hippocampal neurons upon oxygenated nanodiamond substrates [8], where culture of the primary cells was sustained for 7 days; this being comparable to cells grown upon conventional protein-coated materials (laminin/polyornithine). However, since AAND has been proven to provide an adequate cell culture surface for primary cells for at least 21 days this may indicate its better suitability for *in vivo* applications.

Indeed, whilst nanodiamond has been cited as supporting and promoting neuronal cells and the formation of neuronal networks and active synaptic connections [8] it had not yet been proven whether ND could also provide an acceptable growth environment for cells originating from the peripheral nervous system (PNS). The successful culture of primary rat Schwann cells upon AAND, as listed within this thesis, indicates that such surfaces may have beneficial applications for peripheral nerve repair. Importantly, to further exemplify the

coating's versatility and possible use within the PNS dorsal root ganglion (DRG) neurons were also successfully cultured, with cell development, spreading and phenotype being indistinguishable from those cultured upon the control PL surfaces. These promising results may provide the initial steps necessary towards incorporating amine-functionalised DLC/ND facile coatings into devices that provide an 'electronic bridge' with peripheral neurons such as advanced prosthetics.

As yet, it has been difficult to identify a single functionalisation method that would be ideally suited for the culture of cells from neuronal/glial lineages without the inherent disadvantages associated with PL. However, this preliminary work suggests AAND and amine-functionalised DLC substrates may fulfil this role.

6.2 Introduction – CNP Discussion

Nanoparticles, such as carbon dots (CNPs) produced by microwave pyrolysis, have been steadily growing in importance and prominence as their potential applications, ranging from bioimaging to drug delivery, have been realised [30, 32, 57, 199, 201, 203, 205, 212, 290-295]. The relatively simple method by which they can be manufactured, both cheaply and in plentiful quantities, has been reflected in the plethora of novel research currently being conducted in the area and the desire to create biocompatible equivalents to toxic quantum dots (QDs) [199]. For the purpose of this thesis, by producing carbon dots from a variety of different saccharide sources the most effective CNPs could be identified based upon their photoluminescence capabilities and cell uptake efficiency.

6.2.1 Discussion of Carbon Nanoparticle (CNP) Related Data

Bioimaging, either through the course of *in vitro* experiments or at the conclusion of *in vivo* studies, allows primarily for cell identification and observance of their morphology and

responses to stimuli. Although conventional bioimaging dyes are able to stain cells to allow for fluorescent visibility, some require the cell membrane to be permeabilised prior to the dye being applied to be effective. These multi-step procedures, which utilise Triton™ X-100, also require cells to be fixed beforehand so the ability to image living cells by fluorescence is limited. Additionally, the susceptibility of most fluorescent dyes to photobleaching reduces their effectiveness and restricts their shelf-life [199]. These factors have therefore led to research being conducted into suitable biocompatible alternatives.

The use of nano-sized particles for imaging purposes is not an alien concept; indeed nanodiamonds themselves have been noted as emitting bright fluorescence upon incorporation of nitrogen vacancy centres within the carbon lattice [35, 124, 150]. However, the specialist equipment required for creating fluorescent NDs and the lengthy synthesis procedure involved renders them expensive and cumbersome to produce. In addition, quantum dots (QDs) have been utilised as bioimaging agents in the past due to their bright fluorescence emission levels [199, 296]. However their cytotoxicity, due to most being produced from heavy metals, prevents their widespread use *in vivo* [199]. Alternatives, such as carbon nanoparticles outlined in this thesis, have been suggested due to their beneficial fluorescence emission, low cost of production, environmental sustainability and lack of cytotoxicity [199].

By contrast, carbon nanoparticles (CNPs) can be swiftly and cheaply produced by hydrothermal synthesis [292, 297]. Saccharide-derived CNPs, such as the ones produced during the course of this thesis study, can be produced in a matter of minutes through heating within a microwave oven [204]. It has been discovered that the diameters of the particles formed are influenced by temperature, the concentration of the carbon source and the reaction time, the latter of which is the most salient determining variable. For example, one study commented on a greater than 7-fold increase in the size of CNPs produced from a reaction

time of 10 hours as opposed to those produced over a 2 hour synthesis [297]. Within the CNP study outlined in this thesis microwave pyrolysis ensured the formation of CNPs was accelerated so that a reaction time of only 5 to 10 minutes was sufficient to precipitate particles of nanoscale dimensions.

The diameter of carbon dots is also one factor which is thought to affect their luminescence intensity; emission is thought to be improved in smaller particles [203]. Indeed, carbon dots that possess an ultrafine size (i.e. a diameter less than 20 nm) have an inherently disordered structure due to the swift pyrolysis reaction. This disordered structure favours the formation of a greater proportion of surface defect sites which act as emissive energy traps, thus giving rise to greater luminescence. However, these findings were not corroborated by the thesis study, whereby luminescence emission appeared to be independent of average particle size. Although several sub-population sizes of nanoparticles existed within each sample the relatively large distribution in diameter size across CNPs produced from different carbon sources seems to dispel the notion that only smaller nanoparticles could elicit meaningful levels of photoluminescence.

It has been assumed that the growth and development of CNPs in solution follows the LaMer model, whereby initial heating of a carbon solution leads to the formation of oligosaccharides and aromatic compounds [298]. What follows is an increase in solution viscosity ('polymerisation') and eventual carbonisation, resulting from cross-linking of oligosaccharides. These initial carbon spheres then grow isotropically due to the diffusion of solutes towards the surfaces of the particles until the final particle size is attained. Fourier transform infrared spectroscopy (FTIR) analysis of glucose-derived CNPs has confirmed the presence of C=O, C=C and C-OH groups, which supports the development of aromatic derivatives with large quantities of residual hydroxyl groups being retained following microwave treatment [299]. These alcohol and hydroxyl functionalities are known to improve

the hydrophilicity and stability of the formed CNPs, easily enabling them to be miscible in aqueous solutions [297, 300].

Despite the cytotoxicity issues associated with some carbon-based nanomaterials such as carbon nanotubes, research in the area of nanoparticles suggests few if any safety concerns surrounding CNPs. Numerous independent studies have been conducted which have concluded that CNPs pose minimal toxicity risks at concentrations permissible for bioimaging purposes [199]. Cytotoxicity analysis of the CNPs produced for this thesis also corroborated these findings, where no significant deviation in MTT assay readings was recorded between the control samples and cells cultured in the presence of CNPs. Despite the cell media being supplemented with concentrations of CNPs approximating 1 mg/ml the morphology of all cell types tested remained normal with live/dead assays indicating no presence of dead cells which was particularly encouraging. Research published by Sun *et al* also tested the *in vivo* effects of CNPs in a murine model with similarly positive results [212]. Mice were monitored up to 4 weeks following CNP intravenous exposure, whereby no adverse clinical signs were observed. At the conclusion of the experiment the organs were also found to have no abnormalities which in itself brings hope to further successful *in vivo* bioimaging trials of CNPs.

The ease with which CNPs appear to migrate through the body of animals during *in vivo* studies suggests numerous translocation processes may occur to permit their infiltration of cells and tissues. Although macrophage cells are able to practise phagocytosis to engulf nanoparticles and safely transport them this is not the preferred method of most cells which internalise nanoparticles through either active (pinocytotic) processes or via passive penetration of the plasma membrane [301, 302]. However, it has been discovered that a wide range of nanoparticle physico-chemical properties can determine the cellular uptake

efficiency of CNPs, these being their shape [303], size [303, 304], surface functionality [305-307] and surface charge [305, 308, 309].

Indeed, although these factors determine the ease with which CNPs pass through cells, it has been determined that the bare surface of the particles may be shrouded in a layer of adsorbed proteins, known as the protein corona, prior to encountering the cell plasma membrane. This surface bound layer of biomolecules has been known to affect the cellular uptake efficiency of CNPs. The adsorption of blood plasma proteins upon the surface of carboxylated NPs significantly suppressed their uptake by HeLa cells compared with bare NPs [310]. In an additional study it was concluded that the protein corona consisted of a protein monolayer of a thickness which suggested that the proteins had been absorbed in a highly specific manner (i.e. no significant denaturation occurred) [311]. Despite this, some cases have been documented where misfolding of some corona proteins occurred post adsorption, which led to a beneficial increase in the uptake of the NPs which otherwise would not have occurred [312]. This therefore illustrates that even factors indirectly associated with CNP physical and chemical properties may give rise to specific biological responses which may not have been foreseen.

One variable which is known to affect the internalisation pathway of nanoparticles within cells is NP diameter [313]. Whilst smaller nanoparticles (i.e. 10 nm diameter) are known to accumulate at the plasma membrane before incorporation [310], larger nanoparticles (i.e. 100 nm diameter) have been discovered in alternative studies to be immediately internalised without prior coating of the cell membrane [302]. This can be explained by the fact that smaller NPs have the ability to interact with a smaller number of receptors upon the plasma membrane, meaning several NPs may be required to activate pit formation and trigger endocytosis [313]. Additionally, as the concentration of NPs in solution decreases, the membrane-associated NP proportion also decreases linearly, whereas the intracellular

proportion decreases far more drastically. Furthermore, the conditions which are present within *in vitro* culture do not accurately represent what may happen *in vivo*; NP-uptake occurs more readily *in vitro* due to NP sedimentation in the immediate vicinity of the cultured cells [314]. Such factors need to be considered when translating *in vitro* models to *in vivo* situations and as such higher CNP concentrations may be required.

One peculiar aspect of CNP synthesis within the thesis study was that particles produced from more than one carbon source, such as glucose and sucrose, did not appear to be internalised by cells in the same manner as CNPs which were produced from only one carbon source (such as glucose alone). When visualising cells which were incubated in the presence of CNPs produced from multiple carbon sources the clarity of the images was poor, symbolising that although the CNPs were internalised by the cells, they were not distributed through the cytoplasm as efficiently as those CNPs produced from a single carbon source. This restricted intracellular translocation must, it is assumed, be a product of the different carbon sources utilised during pyrolysis which may affect the morphology of the CNPs synthesised. In turn, it has been discussed that the shape of CNPs determines their ability to penetrate the cell endosome to enter the cytoplasm, this sometimes taking precedence over functionality and chemical composition [315]. Future TEM analysis of CNP morphology would confirm this, whereby sharp-edged CNPs are more likely to remain within the cell cytoplasm and thus be difficult to exocytose [315].

In relation to the impact of manufacturing CNPs from variable carbon sources the slight visual differences in fluorescence intensities arising from the thesis CNPs is thought to be a disparity that may only be explained by the different molecular structures of the carbohydrates involved [297]. Glucose is a simple sugar which exists in solution as a six-membered ring containing a hemiacetal group. In comparison sucrose is a disaccharide which originates from the condensation of glucose and fructose which are linked together by a

glucosidic linkage. Additionally, the chemical compound sodium alginate which was utilised to produce alginate derived CNPs, exists as a natural polysaccharide and is a sodium salt of alginic acid being formed from mannuronate and guluronate sequences bonded by glycosidic linkages. It can therefore be gathered that the oxidation and carbonisation of sucrose, glucose and alginate, under hydrothermal conditions occurs differently due to the varying structures of the saccharides involved which is thought to affect the photoluminescence of the resulting CNPs.

A previous study attributed the presence of glycosidic linkages within carbohydrates to explain different characteristics of CNP photoluminescence [297]. Whilst it was shown that CNPs derived from carbohydrates with glycosidic linkages, such as sucrose and starch, were capable of emitting near infrared (NIR) radiation when excited with NIR, the same could not be said for CNPs produced from glucose, which has no such linkages. Although such findings were not corroborated in our study, He *et al* illustrated that different photoluminescence properties could also arise from the different additives used to create the precursor carbon solution prior to hydrothermal CNP synthesis [297]. Indeed, whilst glycerol and water were the main additives present in the thesis precursor solutions, He *et al* experimented with additions of hexamine, sodium hydroxide and hydrochloric acid, all of which drastically altered the fluorescence properties of each particular CNP sample [297]. Sucrose CNPs produced with additives of hexamine emitted blue light when excited with UV, whilst those produced with sodium hydroxide as an additive emitted green light under identical conditions. However the particles were not tested for their bioimaging effectiveness so it was not clear whether the particles in this prior study were suited for cell internalisation [297].

Furthermore, NPs with different functionalities have been shown to access the interior of cells via different endocytosis pathways. Carboxylated nanoparticles have been illustrated to cross the cell membrane more rapidly compared to unfunctionalised alternatives, having been

proven to be internalised via dynamin- and clathrin-dependent channels [302, 316, 317]. Indeed, the presence of oxygen rich functional groups also permits the NPs to be soluble in aqueous solutions to facilitate *in vivo* analysis [248]. These pathways exemplify that the degree of internalisation, and the rate of NP transfer, is at least partly related to NP surface functionality, with the specific interactions between NPs and cell surface receptors determining which pathway is chosen for intracellular access.

Certainly, XPS analysis of the sucrose CNPs and glucose CNPs created during the thesis study recorded significant oxygen retention. Although the proportion of oxygen present in the resulting CNP solutions was lower than in the precursors, spreading of the C(1s) peak towards a binding energy of 290 eV depicted greater quantities of oxygen-bound carbon atoms. In addition, the oxygen content of the CNP solutions produced was equivalent to that measured in previous studies, approximating 30-45 % [56, 318]. This possibly indicated the formation of oxygen defects or oxygen-derived functionalities upon the CNP surface, such as carboxyls, hydroxyls and alcohols, which have been cited as possible sources of the fluorescence phenomenon associated with CNPs [56, 199, 202].

Additionally, it has been postulated that the formation of polycyclic aromatic compounds within the CNPs upon their creation may also contribute to the unique photoluminescence properties that most carbon dots possess [299]. However, it is more likely that oxidation of the carbon source during pyrolysis facilitates the generation of oxide defects upon the CNP surface which produces a fluorescence mechanism. The introduction of complex surface states eventually generates fluorescence emission through the radiative recombination of excitons [56, 292]. Although some examples in the literature discussed the necessity of CNP passivation to activate the surface energy traps to produce photoluminescent emission [204], as with the thesis samples there are cases where carbon dots are shown to photoluminesce

without prior passivation [208]. This illustrates the regular and reproducible nature of the fluorescence emitted by these CNPs and their ease of manufacture.

The rationale of surface passivation remains poorly understood, but it is assumed that the role of these surface modifiers, such as polyethylene glycol (PEG), expose previously confined surface energy traps upon the CNP surface. Prior to passivation these would be inaccessible and thus the untreated carbon dots in these instances produce poor and unreliable luminescence. In addition to enhancing photoluminescence intensity it has been stated that passivation may provide CNPs with greater protection from fluorescence-quenching external factors that may result from solvent or pH changes [291]. It is therefore apparent that in some cases the CNP synthesis route may affect the density of exposed surface energy traps and thus whether surface passivation is necessary.

Of additional note, a plurality of literature has confirmed that photoluminescence originating from CNPs is not subject to photobleaching, unlike emissions from fluorophores which can readily decay following prolonged excitation. The lack of photobleaching, which was similarly observed in our experiments and those from other publications, illustrates the photostability of CNP fluorescence emission [210, 290, 319] and their long-term viability in comparison to conventional bioimaging dyes.

One seemingly counter-intuitive aspect of the thesis investigation was the discovery that slightly decreased levels of fluorescence were observed within cells incubated with CNPs for 48 hours, as opposed to those incubated for just 2 hours. This trend, which signifies that bioimaging utilising CNPs need not be a lengthy affair, is not related to decreased emission intensity from the CNPs themselves, but rather due to a lower proportion of CNPs present within the cells monitored 48 hours post CNP introduction. It has been discovered that the internalisation of nanoparticles during the initial 10 hours of uptake is not dependent upon the

stage of the cell cycle [320]. However, once cell division begins to occur, naturally the concentration of nanoparticles within the cells begins to decrease due to the intracellular nanoparticle accumulation being split between the two resulting daughter cells. Within tumour/cancer cells, which have an enhanced reproduction rate, the decline in intracellular nanoparticle concentration with increasing cell generation will be more pronounced, thus leading to lower concentrations of CNPs within cells and thus, lower photoluminescence emissions.

An additional factor that appears to affect the intensity of NP fluorescence is the CNP-solvent pH, with one study reporting that carbon dots produced from lampblack exhibited their brightest fluorescence output at pH 6 with recorded intensities gradually decreasing as the pH deviated from this optimal value [291]. Due to all CNPs within the thesis study being stored within aqueous solutions it followed that all CNP samples remained at a constant neutral pH; this being tested following purification to ensure contaminants had been eradicated. It was further discovered that the fluorescence intensity of NPs is also heavily-dependent upon the solvent used, whereby the fluorescence intensity of bare NPs has been shown to be approximately 7 times more intense than the same NPs stored within ethanol. On the other hand, NPs stored within acetone were shown to exhibit almost no fluorescence at all, whereas the use of water as a solvent, as chosen in our study, was illustrated not to detract from particle photoluminescence [291].

Indeed, the thesis study illustrated that even the initial concentration of the carbon source with respect to the additives used may drastically alter the luminescence properties of the synthesised CNPs. Fluorescence spectroscopy illustrated that lower concentrations of glucose with respect to glycerol (1M) saw the CNP fluorescence intensity increase when excited with shorter wavelengths of light (420 nm). However, as the concentration of glucose with respect to glycerol increased (2.5M) this trend reversed, with greater emitted intensities being

recorded from CNPs excited by longer wavelengths of light (470 nm). The understanding behind this is not entirely understood although since the additives utilised in the precursor solution are known to affect fluorescence properties it may actually be the concentration of this that affects the luminescence output. Indeed, it has been suggested that one of the roles of these additives, such as glycerol and nitric acid, is to generate energy traps upon the surfaces of the newly manufactured CNPs, which then emit radiation once stimulated [297].

All these points illustrate that, with so many external factors seeming to influence the photoluminescence properties of manufactured CNPs, it is inherently difficult to pinpoint the exact reasoning and understanding behind the complex mechanisms that seem to govern CNP photofluorescence. With variations observed in CNP photoluminescence efficiency being dictated by relatively minor deviations in sample preparation (i.e. solvent choice, reaction duration) it is not surprising that such different trends are observed across studies and as such emphasises the need for further research in the area to identify optimal CNP production pathways.

However, there are various beneficial advantages associated with utilising CNPs for *in vivo* and *in vitro* bioimaging applications which should see future research in the area continue to expand due to the great potential. Although further toxicity studies are required for *in vivo* analysis, especially median lethal dose measurements, it is expected that the biocompatibility of CNPs will approach that of conventional optical imaging agents which are currently used clinically such as indocyanine green [212].

Chapter Seven: Thesis Summary

7.1 Introduction

The original aims and objectives of the research are examined and compared with the findings detailed within the preceding chapters. Future work where it would be deemed beneficial to either continue or complement the existing findings is suggested.

7.2 Production of a neurocompatible substrate using diamond-like carbon (DLC) or nanodiamond (ND)

Although the application of polylysine has been promoted as being a competent surface treatment to promote the growth and attachment of neuronal cells it has limited appeal for *in vivo* applications. The tendency for polylysine to leach into solution, its cytotoxic tendencies and animal-derived origin all signify that an alternative functionalisation procedure would be desired.

The production of a suitable substrate capable of sustaining neuronal and glial type cells was discussed within the DLC and ND related chapters within this thesis. Although diamond-based surfaces for the culture of neural cells is not a novel concept in itself, with several authors commenting on the potential applications of diamond for neural-related applications, the utilisation of a functionalised DLC or ND derived surface is. It was demonstrated how a negatively-charged base coating, in this case composed of a plasma polymerised layer of acrylic acid, could electrostatically attract positively charged amine-functionalised nanodiamond particles during a ten to fifteen minute sonication procedure. This coating was then proven to remain stable for at least three weeks *in vitro* cell culture, whereas previous

diamond-related neural cell culture studies rarely progressed beyond one week experiments. This proved the versatility and stability of the AAND coating and the effectiveness it exhibited compared to the conventional polylysine control surface. During these *in vivo* cell culture studies primary and neuroblastoma cells exhibited long processes, some in excess of 300 μm . Such coatings may prove valuable in the search for an idealistic substrate for brain computer interfaces (BCI) or nerve guidance conduits (NGCs) where the ability for neurons to attach, proliferate and form functional connected networks is desirable.

7.3 Manufacture of carbon nanoparticles (CNPs) as bioimaging agents

The creation of CNPs produced from saccharide sources including glucose, sucrose and alginate was demonstrated to be successful by microwave pyrolysis. Although numerous research groups have conducted research in this field there has been little published regarding carbon dots manufactured from multiple carbon sources (i.e. sucrose and glucose). Such CNPs were demonstrated as being capable of emitting fluorescence although their limited intracellular translocation meant that, at present, their bioimaging capabilities are restricted. CNPs produced from single carbon sources were seen to be internalised by cells *in vitro* two hours post addition to the cell medium, visualisation being achieved across numerous visible wavelengths without the need for CNP passivation. The additional benefit that the fluorescence observed was not subject to photobleaching, a feature observed across most CNPs produced within previous studies, was a clear advantage compared with conventional bioimaging dyes. Furthermore, the ability of the CNPs to emit fluorescence upon excitation three years post-synthesis, albeit at slightly reduced intensity, illustrated the beneficial longevity that CNPs mentioned in this thesis possess. The internalisation of the particles by neuroblastoma and primary cells also showcased their versatility, although translocation ability appeared to vary depending on the cell type being tested.

7.4 Future Work

Although satisfactory results concerning *in vitro* cell culture upon the AAND and amine-functionalised DLC substrates was achieved no animal studies were conducted. These would be essential to determine the true effectiveness of the substrate at encouraging nerve growth and attachment within an *in vivo* environment. Additionally these experiments would be an essential requirement in verifying the possibility of utilising amine-functionalised diamond substrates towards producing implants and therapeutic products from the newly-created neural substrates.

It would be intriguing to undertake further cell studies upon the carbon-based functionalised substrates described in chapters three and four. The application of patterns to surfaces, possibly through shadow-mask techniques, could be easily accomplished to produce a substrate composed of neurophilic and neurophobic regions. This would enable the deposition and growth of neural cells in a highly specific manner which would be an essential prerequisite in the development of future *in vivo* devices for the BCI industry.

Furthermore, the ability to which the functionalised carbon substrates could encourage the differentiation of cells would also be intriguing. The long term study of Schwann cells upon the surfaces to study their differentiation and myelin production would be beneficial, as may be the potential differentiation of stem cells cultured on the functionalised surfaces. To encourage neural development it could be investigated whether the immobilisation of nerve growth factor positively enhances stem cell differentiation.

An additional avenue which would be beneficial to explore would be the further use of aldehyde-terminated DLC and ND for neuronal cell culture. The significantly diminished photoattachment duration compared to the amine-bound diamond surfaces makes it potentially a more lucrative alternative to polylysine or amine-terminated surfaces. Little if

any work has currently been completed investigating the influence aldehydes exert over neural and neuronal cells and greater research would be beneficial in establishing any future possible applications such functionalities may benefit.

The role which proteins play in assisting cell adherence to a substrate has long been documented yet in these experiments the effects proteins may have exerted has not been studied. In future work it would be valuable to understand exactly how neural cells adsorb to the amine functionalised substrates and which proteins assist this process, comparing this to control scenarios where cells would be cultured upon tissue culture plastic in the presence of serum.

Multiple studies regarding CNPs have cited the benefits of passivation to produce stronger fluorescence emission following excitation [212, 290, 321]. Although this was not deemed necessary in the present work due to the significant fluorescence emission recorded from cells incubated with the CNPs during fluorescence microscopy analysis it would nevertheless be intriguing to investigate the effect of PEGylation. If successful this would enable a lower concentration of CNPs to be effective for bioimaging purposes, thus conserving costs and supplies whilst improving efficiency. Additionally, it is also unknown whether the saccharide-derived CNPs produced would be as effective for bioimaging applications *in vivo* as they are *in vitro* although limited research conducted by other groups has suggested that CNPs pose no risk within animal studies.

The work presented within this thesis illustrates the benefits that both amine-functionalised diamond surfaces and saccharide-derived CNPs can bring to present research and the advantages they possess over the existing applications which can be improved through their possible implementation. It is anticipated that demand for neural implants will continue to grow as technology progresses and capabilities increase so that previously incurable disorders

or afflictions may be at least partially remedied. Meanwhile, the development of CNPs as future bioimaging agents could enable individual cells to be monitored morphologically in a much more cost-effective manner, a concept which is becoming increasingly important.

Appendix

1.1 XPS Data

1.1.1 XPS - Glass

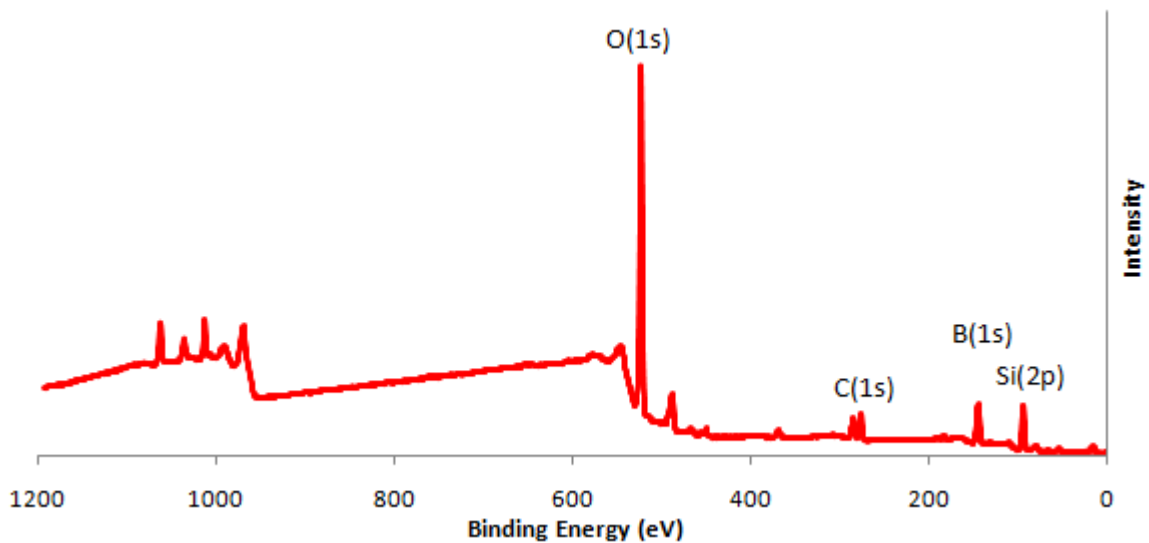


Figure A-1: X-ray photoelectron spectroscopy spectra (XPS) depicting survey scan of glass.

Borosilicate glass cover slips (Agar, UK) were used as a negative control in the study. XPS analysis of the glass surface (figure A-1) depicted a surface rich in oxygen ($60.19\% \pm 1.58\%$) and silicon ($24.23\% \pm 1.24\%$). Elements present in smaller quantities included boron ($1.96\% \pm 0.15\%$) and sodium ($2.19\% \pm 0.11\%$). This confirmed that the surface of the glass was mostly made up of silicon dioxide, with the glass composition approximating 80% SiO_2 , 4% Na_2O , 10% K_2O and 6% B_2O_3 . The presence of adventitious carbon is depicted by small peak on the survey scan at approximately 285.0 eV, which accounted for between 5 – 10% of the total signal detected. This is not representative of the material itself as carbon is not a constituent of borosilicate glass. This carbon presence is almost unavoidable, as all samples exposed to air will build up an instantaneous carbon film which is most probably derived

from CO and CO₂ species [322]. The presence of this carbon film has been shown to increase with greater exposure of the surface to air, with C:Si ratios in the borosilicate glass cover slips utilised in this study varying between 0.45-0.63. Previous studies have illustrated a C:Si ratio of 1.91 for glass samples exposed to air for one month, and 0.78 for those samples exposed for 8 days [323].

1.1.2 XPS - DLC created by SEM electron beam induced deposition (SEM-EBID) upon Si wafer

The creation of a surface layer of amorphous carbon, thought to be similar in character to that of DLC, is known to form upon samples exposed to the electron beam of secondary electron microscopes (SEMs). Normally considered a nuisance and surface contaminant, this carbon layer has been hitherto rarely scrutinised or characterised significantly, yet it may be functionalised in a similar manner to DLC. To assess possible future applications for this carbon film its ability to be functionalised by UV radiation was assessed alongside that of conventional DLC.

The concept of carbon films being created upon surfaces exposed to the focused electron beam of a secondary electron microscope (SEM) has been previously reported [324]. However, development of this adsorbed carbon layer for practical applications has yet to be adequately explored. Any device or apparatus that utilises a vacuum chamber is prone to the introduction of volatile hydrocarbon molecules primarily through the presence of atmospheric carbon. Although carbon adsorption upon the sample surface within the SEM vacuum chamber exerts little effect in itself, contact with ionising radiation such as that from the SEM electron beam causes the chemical structure of the carbon to change so that its sp³ content increases. Indeed, DLC itself is characterised by the significant presence of sp³ within its structure.

As time progresses, with increased exposure of the sample within the SEM chamber to radiation, greater quantities of hydrocarbon are adsorbed on to the surface to create a polymeric film of carbon. So to ascertain the suitability of SEM-EBID DLC for photo-functionalisation, carbon layers created from between 1 - 4 hours irradiation were tested using TFAAD.

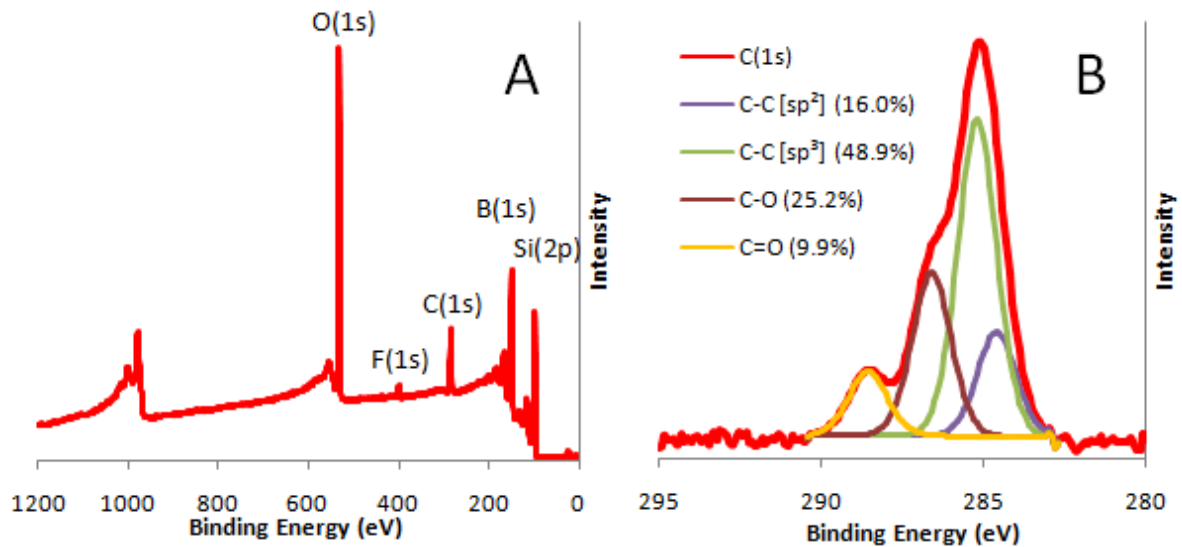


Figure A-2: X-ray photoelectron spectra (XPS) depicting (A) survey and (B) high resolution carbon scans of SEM-EBID DLC upon silicon wafer.

The carbon film created by the SEM electron beam was markedly different in composition and quality compared to DLC created by pulsed laser deposition (PLD). Silicon wafers which had an approximate area of 1 cm² were bombarded with the electron beam so that the entire surface area was exposed to radiation for 20 minutes. This procedure entailed 4 shots being directed equally across 4 quadrants of each sample, with each piece of silicon therefore requiring a treatment time of 80 minutes prior to photochemical functionalisation.

The different methods of producing DLC could also be readily distinguished from their respective XPS spectra. Indeed, the XPS survey scan of the SEM-EBID DLC surface (figure A-2A) displayed a much greater oxygen content (20.1%) compared to PLD DLC (8.2%)

whilst also possessing a much lower carbon content (15.6% as opposed to 87.2% for PLD DLC). These differences in surface composition were particularly obvious upon visual consultation of the survey XPS spectra for the two samples, whereby the carbon peak was far less conspicuous upon the SEM derived carbon coating. These figures signified the decreased thickness of SEM-EBID DLC with respect to PLD-DLC or that the surface coating of the former was not consistently applied. This could have a deleterious effect upon the ability of such a surface to be functionalised to the extent required to promote the attachment and growth of neuronal cells. Additionally, if the coating thickness was significantly smaller than that of PLD-DLC then this could have had implications upon coating longevity and its susceptibility to delamination.

In addition, whilst the underlying substrate upon each surface was silicon wafer, this was detected to the greatest degree upon the SEM-EBID DLC, whose XPS survey scan recorded a reading for Silicon [Si(2p)] twenty times greater (41.0%) than upon PLD-DLC (2.0%) signifying that the attenuation length of the XPS beam (typically 10 nm) exceeded the SEM-EBID DLC coating thickness. This again signified the decreased depth of the SEM-EBID DLC in comparison to PLD DLC. Significant traces of phosphorous (2.7 %) and boron (6.3 %) were also observed in the SEM derived carbon, all of which were otherwise absent from the PLD-DLC. Such constituents may have been the result of contamination.

The carbon high resolution scans of the two samples illustrated significant differences despite both samples supposedly demonstrating DLC surfaces (figures A-2B and 30B). Greater proportions of C-C [sp^3] binding environments were observed in the carbon created from the PLD beam (82.6%) with a significantly lower presence of sp^2 carbon (10.9%). On the other hand, within SEM-EBID DLC, although sp^3 carbon also predominated (48.9%) the proportion present was far lower, with a slightly increased presence of sp^2 carbon (16.0%). Furthermore, within the PLD-DLC only a small minority of carbon atoms were bound to

oxygen (6.5%), the remainder being bound to other carbon atoms. However, this figure was recorded as being over five times higher upon the SEM-EBID DLC (35.1%) signifying its potential impurity.

1.1.3 TFAAD bound to DLC created by SEM-EBID (1-4hrs)

XPS spectra gathered from photochemically functionalised SEM-EBID DLC films illustrated that although they could be functionalised, the ability to which this could be achieved was not predictable due to the erratic and variable composition of the DLC films deposited.

Within the first two hours of UV exposure, binding of trifluoroacetic acid protected 10-amino-dec-1-ene (TFAAD) to the SEM-EBID DLC film appeared weak, with only trace amounts of fluorine [F(1s)] being detected (Table A1: 0.2% at 1 hour and 0.2% at 2 hours) according to the survey spectra (figures A-3A and A-4A). Additionally only small levels of nitrogen (<1%), which would indicate amine attachment, were detected in samples exposed to UV light for 2 hours or less.

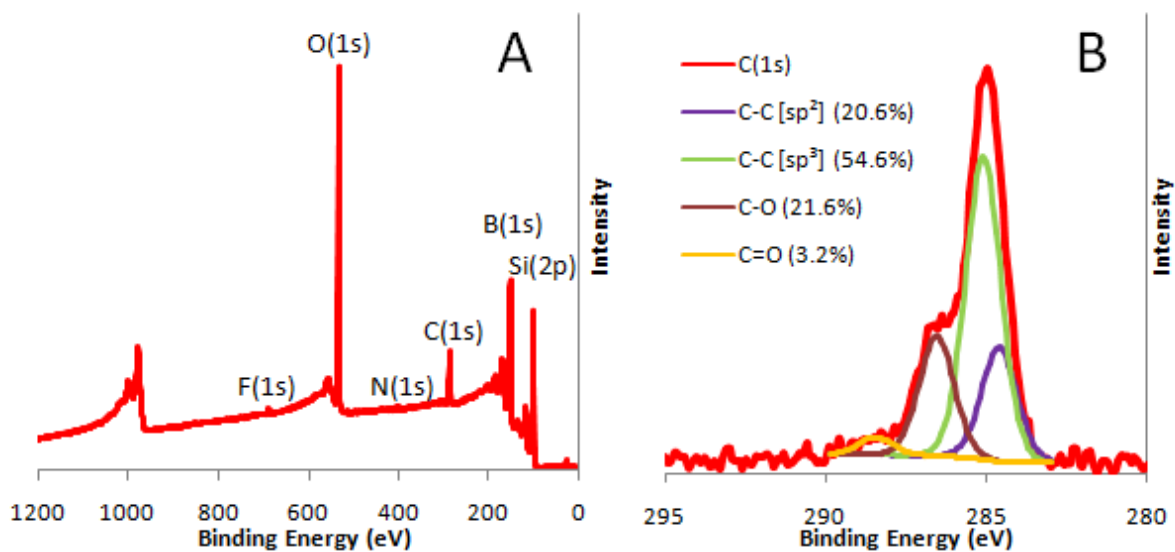


Figure A-3: X-ray photoelectron spectra (XPS) depicting survey (A) and high resolution carbon (B) scans of TFAAD photochemically bound to SEM-EBID DLC for 1 hour.

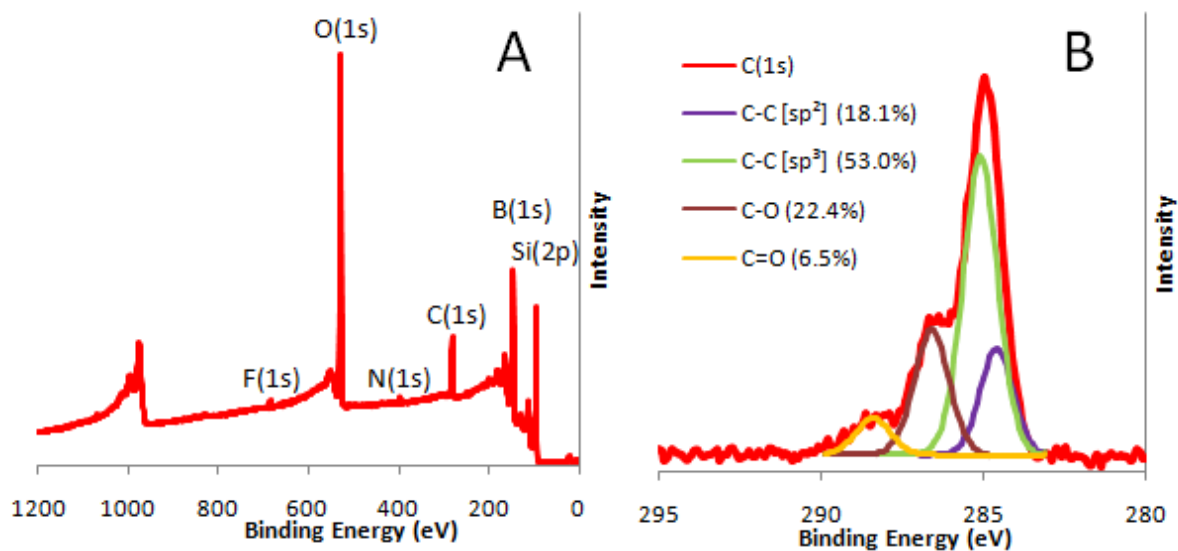


Figure A-4: X-ray photoelectron spectra (XPS) depicting survey (A) and high resolution carbon (B) scans of TFAAD photochemically bound to SEM-EBID DLC for 2 hours.

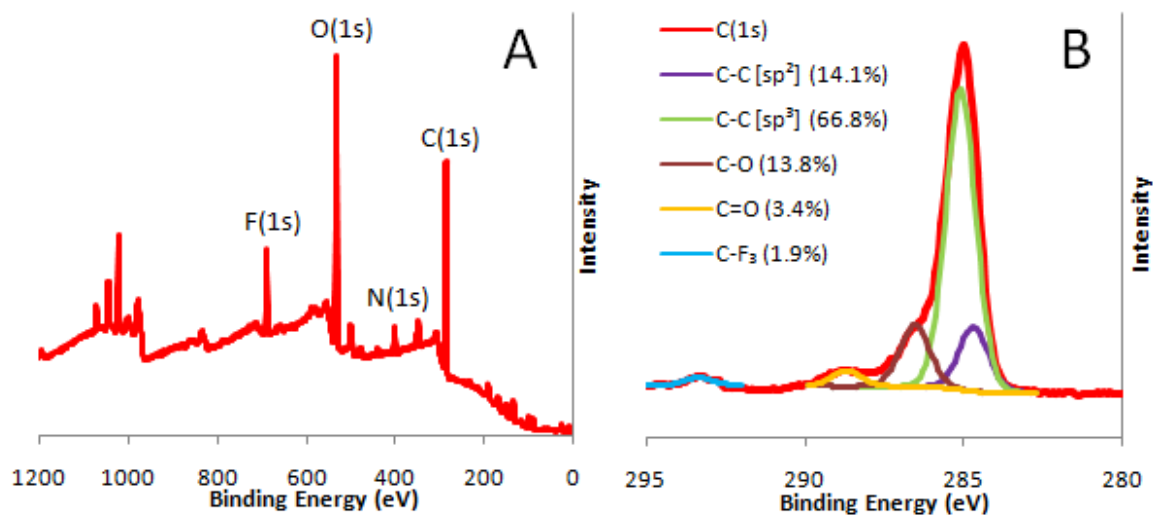


Figure A-5: X-ray photoelectron spectra (XPS) depicting survey (A) and high resolution carbon (B) scans of TFAAD photochemically bound to SEM-EBID DLC for 3 hours.

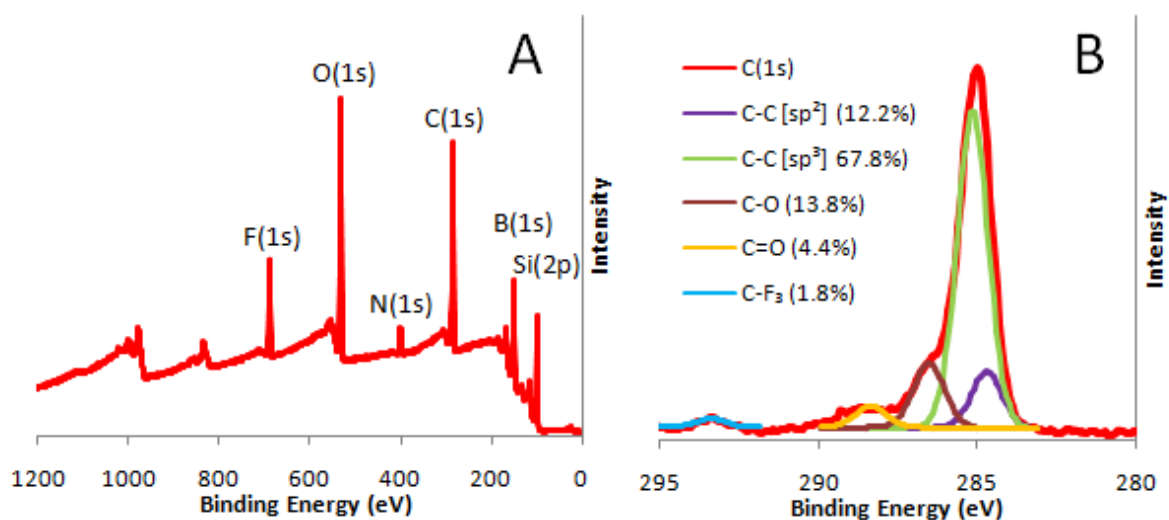


Figure A-6: X-ray photoelectron spectra (XPS) depicting survey (A) and high resolution carbon (B) scans of TFAAD photochemically bound to SEM-EBID DLC for 4 hours.

Element	Binding Energy (eV)	[Atomic Presence Within Each Sample (%)]				
		UV Irradiation Time (Hours)				
		0	1	2	3	4
O(1s)	533	20.1	19.0	19.6	19.4	14.3
C(1s)	285	15.6	11.8	14.4	48.2	38.1
N(1s)	400	1.20	0.400	0.700	3.40	2.80
F(1s)	686	0.400	0.200	0.200	3.40	3.70
P(2p)	134	-	4.50	4.64	3.30	2.90
B(1s)	190	14.3	12.3	13.3	9.40	8.80
Si(2p)	101	41.0	42.0	42.1	1.80	28.7

Table A-1: Atomic presence (%) of principal elements detected by XPS (survey spectra) from SEM-EBID DLC samples irradiated in the presence of TFAAD for 0, 1, 2, 3 or 4 hours.

Significant peaks which indicated the presence of boron were observed, with levels approaching 12% or 13% across samples exposed to UV for either one or two hours (figures A-3A to A-6A). The presence of carbon across these samples was also noticeably low, varying between 12 – 15% across the upper 10 nm of the surface. This most probably indicated the attachment of a thin surface layer of carbon which may not have been of sufficient thickness to permit widespread UV functionalisation. This was corroborated by the high levels of Si(2p) which accounted for 42.0% of the total signal in the one hour sample (figure A-3A) and 42.1% in the two hour sample (figure A-4A) indicating the underlying substrate was detected by the XPS apparatus.

In contrast, however, the samples exposed to TFAAD in the presence of UV light for periods of either 3 or 4 hours were functionalised to a significantly greater degree compared to those samples irradiated for 2 hours or less. Once exposed to 3 hours of irradiation, the level of contaminants such as boron and phosphorous decreased by 40 – 50% (the presence of boron decreased from 12.6% at 2 hours [figure A-3A] to 6.4% at 3 hours [figure A-4A], whilst

phosphorous reported a similar rate of decline, from 4.1% at 2 hours [figure A-3A] to 2.3% at 3 hours [figure A-4A]). In addition, the characteristic presence of the C-F₃ peak (293.3 eV) in figures A-5B and A-6B indicated the successful binding of TFAAD to the carbon film following at least 3 hours of UV irradiation. All these results were matched by a significant rise in the presence of surface carbon, increasing 3-4 fold between samples irradiated for 2 hours and 3 hours. This most probably was related to greater carbonisation from the SEM beam as some areas of the silicon samples may have been exposed to greater doses of the electron beam.

High resolution carbon spectra collated from the 3 and 4 hour samples illustrated these samples of SEM-EBID DLC were formed from greater proportions of sp³ carbon, signifying a greater resemblance to PLD-DLC which can be more readily functionalised (figures A-5B and A-6B). However, it may also be the case that since TFAAD binds to a surface by addition reactions the rate of functionalisation may not be linear. Indeed, the attachment of TFAAD upon a substrate can resemble the growth of a polymer-like layer with previous studies reporting attachment occurring in stages, between which the TFAAD layer undergoes cross-linking [236, 271].

Interestingly, although the sample selected for the four hour exposure appeared to have only a slightly lower presence of silicon (34.9%) (figure A-6A) than the one and two hour samples, the level of carbon recorded was far greater (38.1 %) with similar levels of fluorine being detected as in the 3 hour sample (3.5 %) (figure A-6A). Levels of nitrogen detected in the four hour sample were also far higher (2.8%) than upon those exposed to UV / TFAAD for less than two hours (typically 0.5%).

These results indicated the variability in the SEM-EBID DLC produced compared to the PLD-DLC and the difficulties experienced in adequately functionalising the former.

Although SEM-EBID DLC is still capable of supporting the photochemical attachment of alkene-containing functionalities, it appears to occur with less predictability and consistency since there was less control over the carbon deposition procedure. It was therefore decided to cease experimentation with SEM-EBID DLC so that greater results could be collated from PLD-DLC samples.

1.1.4 XPS - Detonation Nanodiamond

Nanodiamond is synthetically produced from the controlled detonation of explosives such as TNT within a sealed chamber under vacuum. The extreme pressure and thermal energy evolved produce nanodiamond particles of 5 – 10 nm in diameter. The nature of this synthesis route is known to produce an inhomogeneous surface functionality. The raw ND surface was composed of carbon ($58.70\% \pm 2.04\%$) and oxygen ($27.09\% \pm 2.10\%$) with various trace elements including aluminium, zinc, sodium and nitrogen being present at values of less than 2 At% each, indicative of the surface impurities present from the harsh formation conditions (figure A-7). Although a reading of approximately 10 At% of silicon was recorded, as stated previously, this is most probably due to the detection of the underlying glass substrate upon which the detonation nanodiamond was loaded for analysis and not indicative of the ND surface.

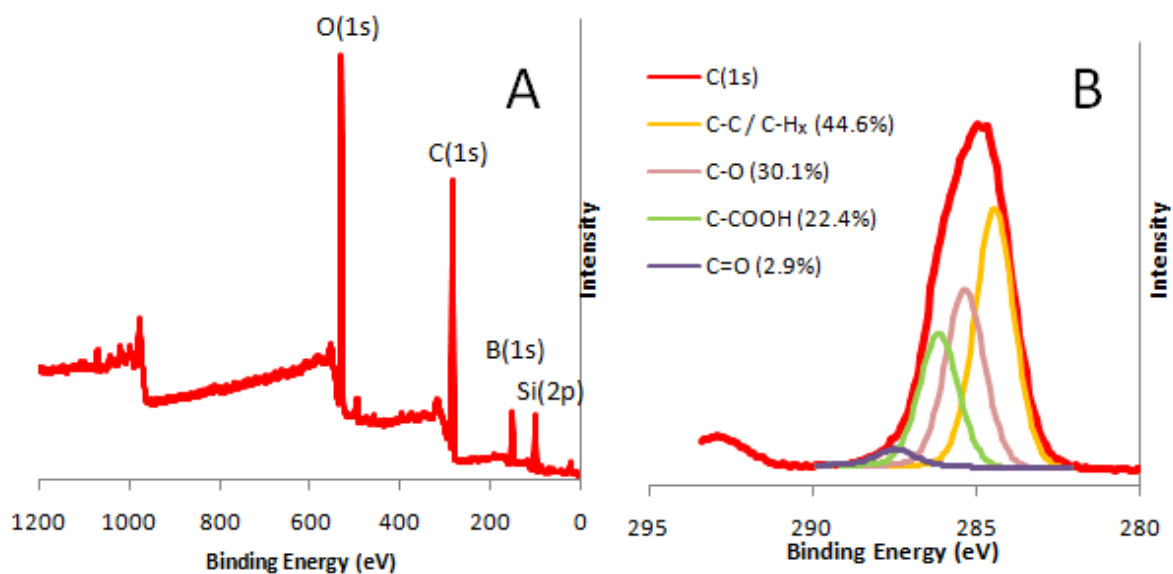


Figure A-7: X-ray photoelectron spectroscopy spectra (XPS) depicting survey scan (A) and high resolution C(1s) scan (B) of detonation nanodiamond.

The broad C(1s) peak observed (figure A-7B) for detonation nanodiamond resulted from the binding of surface carbon with either single (285.4 eV) or double oxygen bonds (287.8 eV) [40] with the contribution of each environment to the main C(1s) peak illustrated following deconvolution. Approximately 55% of carbon atoms were oxygenated, being formed from hydroxyl, ether, ketone or carboxyl groups. This indicated the need for hydrogenation so to achieve functional homogeneity of the surface.

1.1.5 XPS - Hydrogenated Nanodiamond (H-ND)

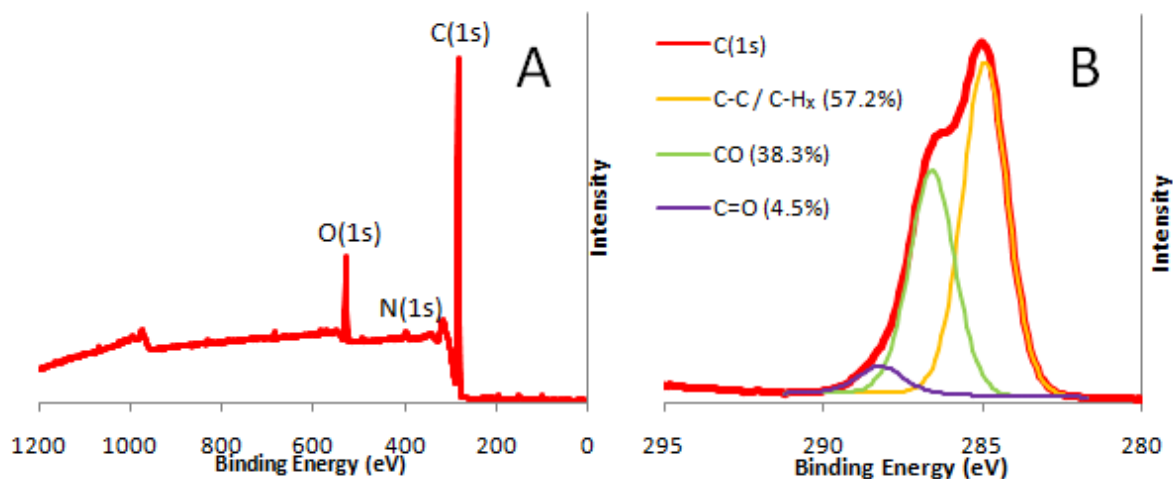


Figure A-8: X-ray photoelectron spectroscopy spectra (XPS) depicting survey scan (A) and high resolution C(1s) scan (B) of hydrogenated nanodiamond.

Hydrogenated nanodiamond was formed by the treatment of detonation ND within a hydrogen plasma. Analysis of the hydrogenated nanodiamond survey spectrum (figure A-8A) illustrated a surface that was dominated by carbon ($87.66\% \pm 2.45\%$) with a minority presence of oxygen ($6.52\% \pm 0.19\%$). This shows significant functional homogenisation of the surface chemistry when compared to the raw starting material (figure A-7), which is evident from the lower oxygen presence on the surface. Trace amounts of nitrogen ($0.48\% \pm 0.16\%$) and silicon ($3.12\% \pm 2.08\%$) were also identified, these again being detected due to the underlying glass substrate being situated within the depth that could be analysed by the XPS equipment.

It has been noted in the literature [40] that hydrogenated nanodiamond can reoxygenate over time if exposed to air for extended periods. This may also hold true for the sample of hydrogenated nanodiamond analysed within this thesis, which recorded approximately 43%

of surface carbons being bound to oxygen atoms (figure A-8B). However, the storage of the hydrogenated nanodiamond particles within distilled water may have restricted further oxidation and the level of oxidation recorded was far lower than that recorded from detonation ND (figure A-7). Indeed, the sharp decrease in oxygen bound carbons as indicated by the survey spectrum illustrated the effectiveness of hydrogenation at concealing the undesirable surface functionalities which have become associated with detonation ND.

1.1.6 XPS - Hydroxylated Nanodiamond (Fenton Treated)

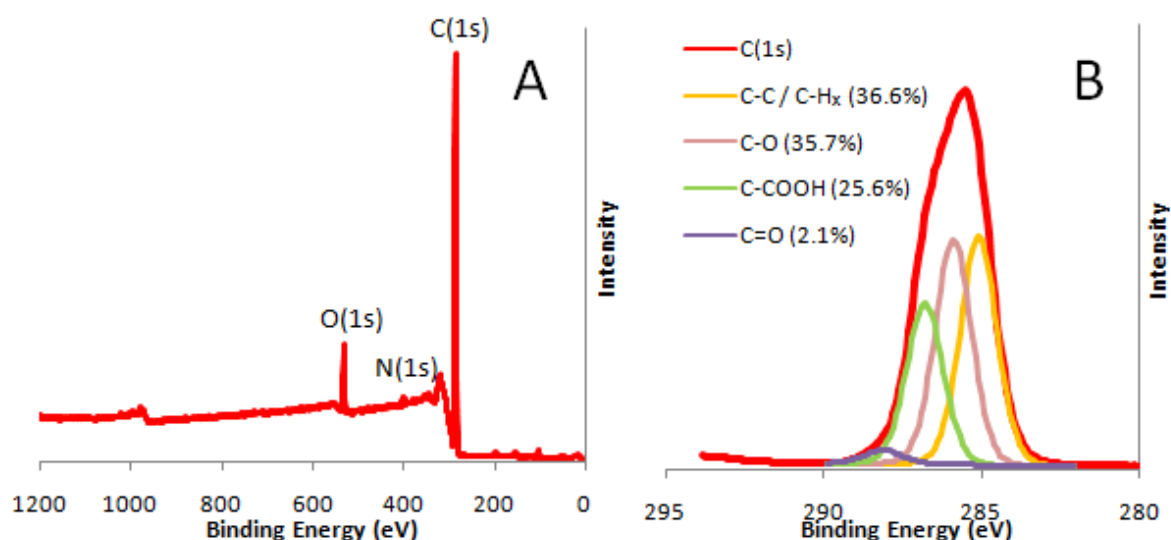


Figure A-9: X-ray photoelectron spectroscopy spectra (XPS) depicting survey scan (A) and high resolution C(1s) scan (B) of hydroxylated (Fenton-treated) ND.

The hydroxylation of detonation nanodiamond was attempted as a possible bypass to the requirement of using a hydrogen plasma to achieve functional homogeneity, since it was not possible to hydrogenate ND on site at the Kroto Institute. Once a surface had been hydroxylated it is possible to perform silanization or esterification to produce the desired functional group [325]. It has also been shown that alkenes will readily attach to surface –OH groups, paving the way for TFAAD to bind to hydroxylated surfaces [237, 326].

1.1.7 XPS - Hydroxylated Nanodiamond (Non-Fenton Treated)

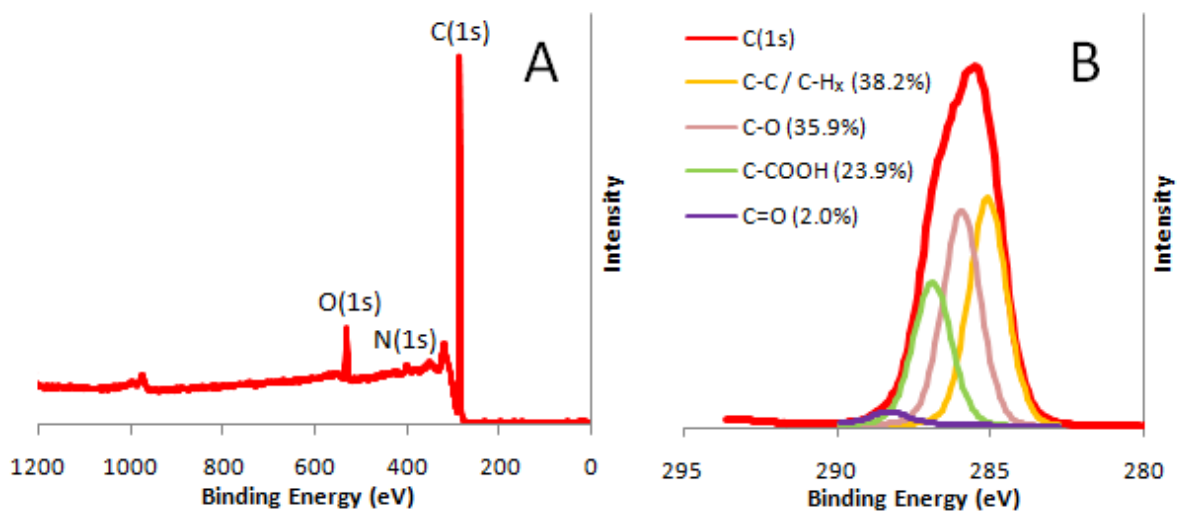


Figure A-10: X-ray photoelectron spectroscopy spectra (XPS) depicting survey scan (A) and high resolution C(1s) scan (B) of hydroxylated (Non-Fenton-treated) ND.

The Fenton method involved oxidation of the ND with the addition of iron sulphate, hydrogen peroxide and concentrated sulphuric acid over a period of 5 hours. The non-fenton reaction involved adding concentrated sulphuric acid and nitric acid to the ND slurry for 3 days, this being a gradual and less intense reaction.

This functionalisation of ND was also selected so to provide an alternative surface homogenisation route to hydrogenation. Once hydroxylated a surface can be photofunctionalised with TFAAD using UV radiation in much the same way as hydrogen-terminated substrates [20, 97, 193, 327]. This would enable the same functionalisation method to be utilised with the same functional molecule. Although hydroxylation was successful it was deemed simpler and more efficient to adopt ND-hydrogenation as a means for functional homogenation. It therefore follows that amination from hydroxylated ND was not attempted.

There were few differences between these two nanodiamonds in terms of surface chemistry, with both samples reporting carbon content in excess of 90 At% (figures A-9 & A-10). The oxygen content in both samples however, was much lower than that reported on detonation nanodiamond, with the treated nanodiamond reporting an oxygen atomic percentage in the region of 5% (figures A-9A & A-10A), whereas the raw nanodiamond indicated an oxygen content of 27% (figure A-7A). Although this represents a reduction in the proportion of oxygen present, it also coincides with the removal of undesirable functionalities and unwanted surface material from the raw ND. This is evidenced by the lack of peaks present in the survey spectra at binding energies higher than 600 eV.

In order to harmonise surface functionality it was paramount to separate the particle clusters as much as possible, so to ensure the greatest surface area could be functionalised by TFAAD. Deaggregation also resulted in a relatively flat cell culture surface as evidenced by the AFM images (figure 60). Although a degree of surface roughness has been demonstrated to encourage cell proliferation and growth for certain cell types [88, 95], it is anticipated that cell growth would be restricted by extremely rough surfaces such as those created by detonation nanodiamond clusters.

References

1. Tsugawa, K., et al., *Nanocrystalline diamond film growth on plastic substrates at temperatures below 100 degrees C from low-temperature plasma*. Physical Review B, 2010. **82**(12).
2. Shimkunas, R.A., et al., *Nanodiamond-insulin complexes as pH-dependent protein delivery vehicles*. Biomaterials, 2009. **30**(29): p. 5720-5728.
3. Chow, E.K., et al., *Nanodiamond Therapeutic Delivery Agents Mediate Enhanced Chemoresistant Tumor Treatment*. Science Translational Medicine, 2011. **3**(73): p. 73ra21.
4. Mostofizadeh, A., et al., *Synthesis, Properties, and Applications of Low-Dimensional Carbon-Related Nanomaterials*. Journal of Nanomaterials, 2011.
5. Narayan, R.J., R.D. Boehm, and A.V. Sumant, *Medical applications of diamond particles & surfaces*. Materials Today, 2011. **14**(4): p. 154-163.
6. Zhang, Q.W., et al., *Fluorescent PLLA-nanodiamond composites for bone tissue engineering*. Biomaterials, 2011. **32**(1): p. 87-94.
7. Xiao, X.C., et al., *In vitro and in vivo evaluation of ultrananocrystalline diamond for coating of implantable retinal microchips*. Journal of Biomedical Materials Research Part B-Applied Biomaterials, 2006. **77B**(2): p. 273-281.
8. Thalhammer, A., et al., *The use of nanodiamond monolayer coatings to promote the formation of functional neuronal networks*. Biomaterials, 2010. **31**(8): p. 2097-2104.
9. Allen, M., B. Myer, and N. Rushton, *In vitro and in vivo investigations into the biocompatibility of diamond-like carbon (DLC) coatings for orthopedic applications*. Journal of Biomedical Materials Research, 2001. **58**(3): p. 319-328.
10. Singh, A., et al., *Glial cell and fibroblast cytotoxicity study on plasma-deposited diamond-like carbon coatings*. Biomaterials, 2003. **24**(28): p. 5083-5089.
11. Shin, H.S., et al., *Biocompatible PEG Grafting on DLC-coated Nitinol Alloy for Vascular Stents*. Journal of Bioactive and Compatible Polymers, 2009. **24**(4): p. 316-328.
12. Mugeruma, T., et al., *Effects of a diamond-like carbon coating on the frictional properties of orthodontic wires*. Angle Orthodontist, 2011. **81**(1): p. 141-148.
13. Martin, R., et al., *Fenton-Treated Functionalized Diamond Nanoparticles as Gene Delivery System*. Acs Nano, 2010. **4**(1): p. 65-74.
14. Martin, R., et al., *Nano-Jewels in Biology. Gold and Platinum on Diamond Nanoparticles as Antioxidant Systems Against Cellular Oxidative Stress*. Acs Nano, 2010. **4**(11): p. 6957-6965.
15. Ho, D.A., *Beyond the Sparkle: The Impact of Nanodiamonds as Biolabeling and Therapeutic Agents*. Acs Nano, 2009. **3**(12): p. 3825-3829.
16. Grill, A., *Diamond-like carbon: state of the art*. Diamond and Related Materials, 1999. **8**(2-5): p. 428-434.
17. Liu, K.K., et al., *Biocompatible and detectable carboxylated nanodiamond on human cell*. Nanotechnology, 2007. **18**(32).
18. Neuville, S. and A. Matthews, *A perspective on the optimisation of hard carbon and related coatings for engineering applications*. Thin Solid Films, 2007. **515**(17): p. 6619-6653.
19. Kano, M., *Super low friction of DLC applied to engine cam follower lubricated with ester-containing oil*. Tribology International, 2006. **39**(12): p. 1682-1685.
20. Yang, W.S., et al., *DNA-modified nanocrystalline diamond thin-films as stable, biologically active substrates*. Nature Materials, 2002. **1**(4): p. 253-257.
21. Kong, X.L., et al., *Polylysine-coated diamond nanocrystals for MALDI-TOF mass analysis of DNA oligonucleotides*. Analytical Chemistry, 2005. **77**(13): p. 4273-4277.

22. Huang, H., et al., *Active nanodiamond hydrogels for chemotherapeutic delivery*. Nano Letters, 2007. **7**: p. 3305-3314.
23. Huang, H.J., et al., *Protein-mediated assembly of nanodiamond hydrogels into a biocompatible and biofunctional multilayer nanofilm*. ACS Nano, 2008. **2**(2): p. 203-212.
24. Merkel, T.J. and J.M. DeSimone, *Dodging Drug-Resistant Cancer with Diamonds*. Science Translational Medicine, 2011. **3**(73).
25. Ganesan, K., et al., *Diamond penetrating electrode array for Epi-Retinal Prosthesis*. Conf Proc IEEE Eng Med Biol Soc, 2010. **1**: p. 6757-60.
26. Intranuovo, F., et al., *Uniform cell colonization of porous 3-D scaffolds achieved using radial control of surface chemistry*. Acta Biomaterialia, 2011. **7**(9): p. 3336-3344.
27. Grill, A., *Diamond-like carbon coatings as biocompatible materials - an overview*. Diamond and Related Materials, 2003. **12**(2): p. 166-170.
28. Bondar, V.S., I.O. Pozdnyakova, and A.P. Puzyr, *Applications of nanodiamonds for separation and purification of proteins*. Physics of the Solid State, 2004. **46**(4): p. 758-760.
29. Huang, T.S., et al., *Immobilization of antibodies and bacterial binding on nanodiamond and carbon nanotubes for biosensor applications*. Diamond and Related Materials, 2004. **13**(4-8): p. 1098-1102.
30. Chung, P.H., et al., *Spectroscopic study of bio-functionalized nanodiamonds*. Diamond and Related Materials, 2006. **15**(4-8): p. 622-625.
31. Schrand, A.M., et al., *Differential biocompatibility of carbon nanotubes and nanodiamonds*. Diamond and Related Materials, 2007. **16**(12): p. 2118-2123.
32. Krueger, A., *New carbon materials: Biological applications of functionalized nanodiamond materials*. Chemistry-a European Journal, 2008. **14**(5): p. 1382-1390.
33. Liu, K.K., et al., *Endocytic carboxylated nanodiamond for the labeling and tracking of cell division and differentiation in cancer and stem cells*. Biomaterials, 2009. **30**(26): p. 4249-4259.
34. Chao, J.I., et al., *Protein-Nanodiamond Complexes for Cellular Surgery Nanodiamond and Its Bioapplications Using the Spectroscopic Properties as Probe for Biolabeling*. Nanodiamonds: Applications in Biology and Nanoscale Medicine, 2010: p. 189-224.
35. Cigler, P., et al., *Fluorescent Nanodiamonds: The New Platform For Constuction of Chemo- and Biosensors*. Nanocon 2010, 2nd International Conference, 2010: p. 188-190.
36. Tzeng, Y.K., et al., *Superresolution Imaging of Albumin-Conjugated Fluorescent Nanodiamonds in Cells by Stimulated Emission Depletion*. Angewandte Chemie-International Edition, 2011. **50**(10): p. 2262-2265.
37. Liu, Y., et al., *Functionalization of nanoscale diamond powder: Fluoro-, alkyl-, amino-, and amino acid-nanodiamond derivatives*. Chemistry of Materials, 2004. **16**(20): p. 3924-3930.
38. Krueger, A., et al., *Biotinylated nanodiamond: Simple and efficient functionalization of detonation diamond*. Langmuir, 2008. **24**(8): p. 4200-4204.
39. Yeap, W.S., S.M. Chen, and K.P. Loh, *Detonation Nanodiamond: An Organic Platform for the Suzuki Coupling of Organic Molecules*. Langmuir, 2009. **25**(1): p. 185-191.
40. Girard, H.A., et al., *Hydrogenation of nanodiamonds using MPCVD: A new route toward organic functionalization*. Diamond and Related Materials, 2010. **19**(7-9): p. 1117-1123.
41. Liang, Y.J., et al., *Deagglomeration and surface modification of thermally annealed nanoscale diamond*. Journal of Colloid and Interface Science, 2011. **354**(1): p. 23-30.
42. Meinhardt, T., et al., *Pushing the Functionality of Diamond Nanoparticles to New Horizons: Orthogonally Functionalized Nanodiamond Using Click Chemistry*. Advanced Functional Materials, 2011. **21**(3): p. 494-500.
43. Lockett, M.R. and L.M. Smith, *Fabrication and Characterization of DNA Arrays Prepared on Carbon-on-Metal Substrates*. Analytical Chemistry, 2009. **81**(15): p. 6429-6437.
44. Fu, C.C., et al., *Characterization and application of single fluorescent nanodiamonds as cellular biomarkers*. Proceedings of the National Academy of Sciences of the United States of America, 2007. **104**(3): p. 727-732.

45. Harrison, B.S. and A. Atala, *Carbon nanotube applications for tissue engineering*. *Biomaterials*, 2007. **28**(2): p. 344-353.
46. Shi Kam, N.W., et al., *Nanotube Molecular Transporters: Internalization of Carbon Nanotube-Protein Conjugates into Mammalian Cells*. *Journal of the American Chemical Society*, 2004. **126**(22): p. 6850-6851.
47. Yang, F., *Magnetic functionalised carbon nanotubes as drug vehicles for cancer lymph node metastasis treatment*. *European Journal of Cancer*, 2011. **47**: p. 1873-1882.
48. Kim, J.H., et al., *Comparison of diamond-like carbon-coated nitinol stents with or without polyethylene glycol grafting and uncoated nitinol stents in a canine iliac artery model*. *British Journal of Radiology*, 2011. **84**(999): p. 210-215.
49. Puertolas, J.A., et al., *Improved wear performance of ultra high molecular weight polyethylene coated with hydrogenated diamond like carbon*. *Wear*, 2010. **269**(5-6): p. 458-465.
50. Lockett, M.R., M.R. Shortreed, and L.M. Smith, *Aldehyde-terminated amorphous carbon substrates for the fabrication of biomolecule arrays*. *Langmuir*, 2008. **24**(17): p. 9198-9203.
51. Regan, E.M., et al., *Differential patterning of neuronal, glial and neural progenitor cells on phosphorus-doped and UV irradiated diamond-like carbon*. *Biomaterials*, 2010. **31**(2): p. 207-215.
52. Young, T.H., et al., *Surface modification of microporous PVDF membranes for neuron culture*. *Journal of Membrane Science*, 2010. **350**(1-2): p. 32-41.
53. Chen, Y.C., et al., *The effect of ultra-nanocrystalline diamond films on the proliferation and differentiation of neural stem cells*. *Biomaterials*, 2009. **30**(20): p. 3428-3435.
54. Kotov, N.A., *Inorganic Nanoparticles as Protein Mimics*. *Science*, 2010. **330**(6001): p. 188-189.
55. Morimune, S., et al., *Poly(vinyl alcohol) Nanocomposites with Nanodiamond*. *Macromolecules*, 2011. **44**(11): p. 4415-4421.
56. Ray, S.C., et al., *Fluorescent Carbon Nanoparticles: Synthesis, Characterization, and Bioimaging Application*. *Journal of Physical Chemistry C*, 2009. **113**(43): p. 18546-18551.
57. Yang, S.T., et al., *Carbon Dots for Optical Imaging in Vivo*. *Journal of the American Chemical Society*, 2009. **131**(32): p. 11308+.
58. Kong, X.L., et al., *High-affinity capture of proteins by diamond nanoparticles for mass spectrometric analysis*. *Analytical Chemistry*, 2005. **77**(1): p. 259-265.
59. Huang, L.C.L. and H.C. Chang, *Adsorption and immobilization of cytochrome c on nanodiamonds*. *Langmuir*, 2004. **20**(14): p. 5879-5884.
60. Steinmuller-Nethl, D., et al., *Strong binding of bioactive BMP-2 to nanocrystalline diamond by physisorption*. *Biomaterials*, 2006. **27**(26): p. 4547-4556.
61. Wang, H.D., et al., *Study on protein conformation and adsorption behaviors in nanodiamond particle-protein complexes*. *Nanotechnology*, 2011. **22**(14).
62. Kruger, A., et al., *Surface functionalisation of detonation diamond suitable for biological applications*. *Journal of Materials Chemistry*, 2006. **16**(24): p. 2322-2328.
63. Nichols, B.M., et al., *Electrical bias dependent photochemical functionalization of diamond surfaces*. *Journal of Physical Chemistry B*, 2006. **110**(33): p. 16535-16543.
64. Nichols, B.M., et al., *Photochemical functionalization of hydrogen-terminated diamond surfaces: A structural and mechanistic study*. *Journal of Physical Chemistry B*, 2005. **109**(44): p. 20938-20947.
65. Sun, B., et al., *Covalent photochemical functionalization of amorphous carbon thin films for integrated real-time biosensing*. *Langmuir*, 2006. **22**(23): p. 9598-9605.
66. Lud, S.Q., et al., *Chemical grafting of biphenyl self-assembled monolayers on ultrananocrystalline diamond*. *Journal of the American Chemical Society*, 2006. **128**(51): p. 16884-16891.
67. Baker, S.E., et al., *Covalent functionalization for biomolecular recognition on vertically aligned carbon nanofibers*. *Chemistry of Materials*, 2005. **17**(20): p. 4971-4978.

68. Kuo, T.C., R.L. McCreery, and G.M. Swain, *Electrochemical modification of boron-doped chemical vapor deposited diamond surfaces with covalently bonded monolayers*. *Electrochemical and Solid State Letters*, 1999. **2**(6): p. 288-290.
69. Brooksby, P.A. and A.J. Downard, *Multilayer nitroazobenzene films covalently attached to carbon. An AFM and electrochemical study*. *Journal of Physical Chemistry B*, 2005. **109**(18): p. 8791-8798.
70. Allongue, P., et al., *Covalent modification of carbon surfaces by aryl radicals generated from the electrochemical reduction of diazonium salts*. *Journal of the American Chemical Society*, 1997. **119**(1): p. 201-207.
71. Dolmatov, V.Y., *Detonation synthesis ultradispersed diamonds: Properties and applications*. *Uspekhi Khimii*, 2001. **70**(7): p. 687-708.
72. Spitsyn, B.V., et al., *Inroad to modification of detonation nanodiamond*. *Diamond and Related Materials*, 2006. **15**(2-3): p. 296-299.
73. Sotowa, K.I., et al., *Effect of treatment temperature on the amination of chlorinated diamond*. *Diamond and Related Materials*, 2004. **13**(1): p. 145-150.
74. Krueger, A., et al., *Biotinylated Nanodiamond: Simple and Efficient Functionalization of Detonation Diamond*. *Langmuir*, 2008. **24**(8): p. 4200-4204.
75. Martin, R., et al., *General Strategy for High-Density Covalent Functionalization of Diamond Nanoparticles Using Fenton Chemistry*. *Chemistry of Materials*, 2009. **21**(19): p. 4505-4514.
76. Osswald, S., et al., *Control of sp(2)/sp(3) carbon ratio and surface chemistry of nanodiamond powders by selective oxidation in air*. *Journal of the American Chemical Society*, 2006. **128**(35): p. 11635-11642.
77. Takeuchi, D., et al., *Negative electron affinity of diamond and its application to high voltage vacuum power switches*. *physica status solidi (a)*, 2013. **210**(10): p. 1961-1975.
78. Tiwari, R.N. and L. Chang, *Growth, microstructure, and field-emission properties of synthesized diamond film on adamantane-coated silicon substrate by microwave plasma chemical vapor deposition*. *Journal of Applied Physics*, 2010. **107**(10).
79. Ihara, M., et al., *Diamond Deposition on Silicon Surfaces Heated to Temperature as Low as 135-Degrees-C*. *Applied Physics Letters*, 1991. **59**(12): p. 1473-1475.
80. Gruen, D.M., *Nanocrystalline Diamond Films 1*. *Annual Review of Materials Science*, 1999. **29**(1): p. 211-259.
81. Chen, Y.C., et al., *Induction and regulation of differentiation in neural stem cells on ultrananocrystalline diamond films*. *Biomaterials*, 2010. **31**(21): p. 5575-5587.
82. Williams, O.A., et al., *Comparison of the growth and properties of ultrananocrystalline diamond and nanocrystalline diamond*. *Diamond and Related Materials*, 2006. **15**(4-8): p. 654-658.
83. Chong, K.F., et al., *Cell Adhesion Properties on Photochemically Functionalized Diamond*. *Langmuir*, 2007. **23**(10): p. 5615-5621.
84. Eckert, M., E. Neyts, and A. Bogaerts, *Differences between Ultrananocrystalline and Nanocrystalline Diamond Growth: Theoretical Investigation of CxHy Species at Diamond Step Edges*. *Crystal Growth & Design*, 2010. **10**(9): p. 4123-4134.
85. Chen, Y.C., et al., *Synthesis and characterization of smooth ultrananocrystalline diamond films via low pressure bias-enhanced nucleation and growth*. *Applied Physics Letters*, 2008. **92**(13).
86. Balda, M.S. and K. Matter, *Epithelial cell adhesion and the regulation of gene expression*. *Trends in Cell Biology*, 2003. **13**(6): p. 310-318.
87. Zutter, M.M., *Integrin-mediated adhesion: Tipping the balance between chemosensitivity and chemoresistance*. *Breast Cancer Chemosensitivity*, 2007. **608**: p. 87-100.
88. Khang, D., et al., *The role of nanometer and sub-micron surface features on vascular and bone cell adhesion on titanium*. *Biomaterials*, 2008. **29**(8): p. 970-983.
89. Armstrong, R.J.E. and C.N. Svendsen, *Neural stem cells: From cell biology to cell replacement*. *Cell Transplantation*, 2000. **9**(2): p. 139-152.

90. Bithell, A. and B.P. Williams, *Neural stem cells and cell replacement therapy: making the right cells*. Clinical Science, 2005. **108**(1): p. 13-22.
91. Lechleitner, T., et al., *The surface properties of nanocrystalline diamond and nanoparticulate diamond powder and their suitability as cell growth support surfaces*. Biomaterials, 2008. **29**(32): p. 4275-4284.
92. Clem, W.C., et al., *Mesenchymal stem cell interaction with ultra-smooth nanostructured diamond for wear-resistant orthopaedic implants*. Biomaterials, 2008. **29**(24-25): p. 3461-3468.
93. Arnold, M., et al., *Activation of Integrin Function by Nanopatterned Adhesive Interfaces*. ChemPhysChem, 2004. **5**(3): p. 383-388.
94. Amaral, M., et al., *Nanocrystalline diamond: In vitro biocompatibility assessment by MG63 and human bone marrow cells cultures*. Journal of Biomedical Materials Research Part A, 2008. **87A**(1): p. 91-99.
95. Brunetti, V., et al., *Neurons sense nanoscale roughness with nanometer sensitivity*. Proceedings of the National Academy of Sciences, 2010. **107**(14): p. 6264-6269.
96. Huang, H., et al., *Ultrananocrystalline Diamond Thin Films Functionalized with Therapeutically Active Collagen Networks*. The Journal of Physical Chemistry B, 2009. **113**(10): p. 2966-2971.
97. Hartl, A., et al., *Protein-modified nanocrystalline diamond thin films for biosensor applications*. Nat Mater, 2004. **3**(10): p. 736-742.
98. Stavis, C., et al., *Surface functionalization of thin-film diamond for highly stable and selective biological interfaces*. Proceedings of the National Academy of Sciences, 2011. **108**(3): p. 983-988.
99. Radadia, A.D., et al., *Control of Nanoscale Environment to Improve Stability of Immobilized Proteins on Diamond Surfaces*. Advanced Functional Materials, 2011. **21**(6): p. 1040-1050.
100. Abouzar, M.H., et al., *Penicillin detection with nanocrystalline-diamond field-effect sensor*. Physica Status Solidi a-Applications and Materials Science, 2008. **205**(9): p. 2141-2145.
101. Fischer, D., et al., *In vitro cytotoxicity testing of polycations: influence of polymer structure on cell viability and hemolysis*. Biomaterials, 2003. **24**(7): p. 1121-1131.
102. Danilenko, V.V., *On the history of the discovery of nanodiamond synthesis*. Physics of the Solid State, 2004. **46**(4): p. 595-599.
103. Greiner, N.R., et al., *Diamonds in Detonation Soot*. Nature, 1988. **333**(6172): p. 440-442.
104. Ozawa, M., et al., *Preparation and behavior of brownish, clear nanodiamond colloids*. Advanced Materials, 2007. **19**(9): p. 1201-+.
105. Chang, Y.-R., et al., *Mass production and dynamic imaging of fluorescent nanodiamonds*. Nature Nanotechnology, 2008. **3**(5): p. 284-288.
106. Mochalin, V.N. and Y. Gogotsi, *Wet Chemistry Route to Hydrophobic Blue Fluorescent Nanodiamond*. Journal of the American Chemical Society, 2009. **131**(13): p. 4594-+.
107. Maze, J.R., et al., *Nanoscale magnetic sensing with an individual electronic spin in diamond*. Nature, 2008. **455**(7213): p. 644-U41.
108. Krueger, A., *Diamond nanoparticles: Jewels for chemistry and physics*. Advanced Materials, 2008. **20**(12): p. 2445-+.
109. Zheng, W.-W., et al., *Organic functionalization of ultradispersed nanodiamond: synthesis and applications*. Journal of Materials Chemistry, 2009. **19**(44): p. 8432-8441.
110. Purtov, K.V., et al., *Nanodiamonds as Carriers for Address Delivery of Biologically Active Substances*. Nanoscale Research Letters, 2010. **5**(3): p. 631-636.
111. Alhaddad, A., et al., *Nanodiamond as a Vector for siRNA Delivery to Ewing Sarcoma Cells*. Small, 2011. **7**(21): p. 3087-3095.
112. Schrand, A.M., S.A.C. Hens, and O.A. Shenderova, *Nanodiamond Particles: Properties and Perspectives for Bioapplications*. Critical Reviews in Solid State and Materials Sciences, 2009. **34**(1-2): p. 18-74.

113. Schrand, A.M., et al., *Are diamond nanoparticles cytotoxic?* Journal of Physical Chemistry B, 2007. **111**(1): p. 2-7.
114. Danilenko, V.V., *Nanocarbon phase diagram and conditions for detonation nanodiamond formation.* Synthesis, Properties and Applications of Ultrananocrystalline Diamond, ed. D.M. Gruen, O.A. Shenderova, and A. Vul. Vol. 192. 2005. 181-198.
115. Mochalin, V.N., et al., *The properties and applications of nanodiamonds.* Nat Nano, 2012. **7**(1): p. 11-23.
116. Shenderova, O., et al., *Surface Chemistry and Properties of Ozone-Purified Detonation Nanodiamonds.* Journal of Physical Chemistry C, 2011. **115**(20): p. 9827-9837.
117. Williams, O.A., et al., *Size-Dependent Reactivity of Diamond Nanoparticles.* Acs Nano, 2010. **4**(8): p. 4824-4830.
118. Krueger, A. and T. Boedeker, *Deagglomeration and functionalisation of detonation nanodiamond with long alkyl chains.* Diamond and Related Materials, 2008. **17**(7-10): p. 1367-1370.
119. Liu, Y., V.N. Khabashesku, and N.J. Halas, *Fluorinated nanodiamond as a wet chemistry precursor for diamond coatings covalently bonded to glass surface.* Journal of the American Chemical Society, 2005. **127**(11): p. 3712-3713.
120. Lisichkin, G.V., et al., *Halogenation of detonation-synthesised nanodiamond surfaces.* Mendeleev Communications, 2009. **19**(6): p. 309-310.
121. Schrand, A.M., et al., *Cytotoxicity and Genotoxicity of Carbon Nanomaterials.* Safety of Nanoparticles: From Manufacturing to Medical Applications, ed. T.J. Webster. 2009. 159-187.
122. Schrand, A.M., et al., *Are diamond nanoparticles cytotoxic?* Journal of Physical Chemistry B, 2007. **111**(1): p. 2-7.
123. Yuan, Y., et al., *Pulmonary toxicity and translocation of nanodiamonds in mice.* Diamond and Related Materials, 2010. **19**(4): p. 291-299.
124. Mohan, N., et al., *In Vivo Imaging and Toxicity Assessments of Fluorescent Nanodiamonds in Caenorhabditis elegans.* Nano Letters, 2010. **10**(9): p. 3692-3699.
125. Chow, E.K., et al., *Nanodiamond Therapeutic Delivery Agents Mediate Enhanced Chemoresistant Tumor Treatment.* Science Translational Medicine, 2011. **3**(73).
126. Vista. *Vista Engineering: Diamond Research.* [cited 25 April 2011]; Available from: http://www.vistaeng.com/?page_id=81.
127. Manus, L.M., et al., *Gd(III)-Nanodiamond Conjugates for MRI Contrast Enhancement.* Nano Letters, 2010. **10**(2): p. 484-489.
128. Shenderova, O., S. Hens, and G. McGuire, *Seeding slurries based on detonation nanodiamond in DMSO.* Diamond and Related Materials, 2010. **19**(2-3): p. 260-267.
129. Saini, G., et al., *Core-Shell Diamond as a Support for Solid-Phase Extraction and High-Performance Liquid Chromatography.* Analytical Chemistry, 2010. **82**(11): p. 4448-4456.
130. Wu, C.-C., C.-C. Han, and H.-C. Chang, *Applications of Surface-Functionalized Diamond Nanoparticles for Mass-Spectrometry-Based Proteomics.* Journal of the Chinese Chemical Society, 2010. **57**(3B): p. 583-594.
131. Holt, K.B., *Diamond at the nanoscale: applications of diamond nanoparticles from cellular biomarkers to quantum computing.* Philosophical Transactions of the Royal Society a-Mathematical Physical and Engineering Sciences, 2007. **365**(1861): p. 2845-2861.
132. Lee, J.-Y., D.-P. Lim, and D.-S. Lim, *Tribological behavior of PTFE nanocomposite films reinforced with carbon nanoparticles.* Composites Part B-Engineering, 2007. **38**(7-8): p. 810-816.
133. Behler, K.D., et al., *Nanodiamond-Polymer Composite Fibers and Coatings.* Acs Nano, 2009. **3**(2): p. 363-369.
134. Mochalin, V.N., et al., *Covalent Incorporation of Aminated Nanodiamond into an Epoxy Polymer Network.* Acs Nano, 2011. **5**(9): p. 7494-7502.

135. Neitzel, I., et al., *Mechanical properties of epoxy composites with high contents of nanodiamond*. Composites Science and Technology, 2011. **71**(5): p. 710-716.
136. Maitra, U., et al., *Mechanical properties of nanodiamond-reinforced polymer-matrix composites*. Solid State Communications, 2009. **149**(39-40): p. 1693-1697.
137. Zhang, Q., et al., *Grafting polyimides from nanodiamonds*. Macromolecules, 2008. **41**(3): p. 536-538.
138. Stravato, A., et al., *HVOF-Sprayed Nylon-11+Nanodiamond Composite Coatings: Production & Characterization*. Journal of Thermal Spray Technology, 2008. **17**(5-6): p. 812-817.
139. Shenderova, O., et al., *Detonation nanodiamond and onion-like carbon: applications in composites*. Physica Status Solidi a-Applications and Materials Science, 2008. **205**(9): p. 2245-2251.
140. Shenderova, O., et al., *Nanodiamond and onion-like carbon polymer nanocomposites (vol 16, pg 1213, 2007)*. Diamond and Related Materials, 2007. **16**(9): p. 1770-1770.
141. Wang, D.H., et al., *In-Situ Nanocomposite Synthesis: Arylcarbonylation and Grafting of Primary Diamond Nanoparticles with a Poly(ether-ketone) in Polyphosphoric Acid*. Macromolecules, 2009. **42**(1): p. 114-124.
142. Li, L., J.L. Davidson, and C.M. Lukehart, *Surface functionalization of nanodiamond particles via atom transfer radical polymerization*. Carbon, 2006. **44**(11): p. 2308-2315.
143. Faklaris, O., et al., *Photoluminescent Diamond Nanoparticles for Cell Labeling: Study of the Uptake Mechanism in Mammalian Cells*. ACS Nano, 2009. **3**(12): p. 3955-3962.
144. McGuinness, L.P., et al., *Quantum measurement and orientation tracking of fluorescent nanodiamonds inside living cells*. Nature Nanotechnology, 2011. **6**(6): p. 358-363.
145. Rondin, L., et al., *Surface-induced charge state conversion of nitrogen-vacancy defects in nanodiamonds*. Physical Review B, 2010. **82**(11).
146. Boudou, J.-P., et al., *High yield fabrication of fluorescent nanodiamonds*. Nanotechnology, 2009. **20**(23).
147. Vlasov, I.I., et al., *Nitrogen and Luminescent Nitrogen-Vacancy Defects in Detonation Nanodiamond*. Small, 2010. **6**(5): p. 687-694.
148. Hens, S.C., et al., *Nanodiamond bioconjugate probes and their collection by electrophoresis*. Diamond and Related Materials, 2008. **17**(11): p. 1858-1866.
149. Schrand, A.M., et al., *Temporal and mechanistic tracking of cellular uptake dynamics with novel surface fluorophore-bound nanodiamonds*. Nanoscale, 2011. **3**(2): p. 435-445.
150. Yu, S.J., et al., *Bright fluorescent nanodiamonds: No photobleaching and low cytotoxicity*. Journal of the American Chemical Society, 2005. **127**(50): p. 17604-17605.
151. Huang, H., et al., *Active nanodiamond hydrogels for chemotherapeutic delivery*. Nano Letters, 2007. **7**(11): p. 3305-3314.
152. Zhang, X.-Q., et al., *Polymer-Functionalized Nanodiamond Platforms as Vehicles for Gene Delivery*. ACS Nano, 2009. **3**(9): p. 2609-2616.
153. Chen, M., et al., *Nanodiamond Vectors Functionalized with Polyethylenimine for siRNA Delivery*. Journal of Physical Chemistry Letters, 2010. **1**(21): p. 3167-3171.
154. Nair, V., *Retrovirus-induced oncogenesis and safety of retroviral vectors*. Current Opinion in Molecular Therapeutics, 2008. **10**(5): p. 431-438.
155. Weissmantel, C., et al., *Preparation and Properties of Hard I-C and I-BN Coatings*. Thin Solid Films, 1982. **96**(1): p. 31-44.
156. Koidl, P., Wild, C., Lacher, R., Sah, R.F., *Diamond and Diamond Like Films and Coatings*. 1991, New York, USA: Plenum Press.
157. Tamor, M.A., W.C. Vassell, and K.R. Carduner, *Atomic Constraint in Hydrogenated Diamond-Like Carbon*. Applied Physics Letters, 1991. **58**(6): p. 592-594.
158. Robertson, J., *Diamond-like amorphous carbon*. Materials Science and Engineering: R: Reports, 2002. **37**(4-6): p. 129-281.
159. Ladwig, A.M., et al., *Atmospheric plasma deposition of diamond-like carbon coatings*. Diamond and Related Materials, 2009. **18**(9): p. 1129-1133.

160. Izake, E.L., et al., *Characterization of reaction products and mechanisms in atmospheric pressure plasma deposition of carbon films from ethanol*. Journal of Materials Chemistry, 2005. **15**(2): p. 300-306.
161. Novikov, V.P. and V.P. Dymont, *Synthesis of diamondlike films by an electrochemical method at atmospheric pressure and low temperature*. Applied Physics Letters, 1997. **70**(2): p. 200-202.
162. Cappelli, E., et al., *Critical role of laser wavelength on carbon films grown by PLD of graphite*. Applied Physics A: Materials Science & Processing, 2008. **93**(3): p. 751-758.
163. Orlianges, J.C., et al., *Electrical properties of pure and metal doped pulsed laser deposited carbon films*. Thin Solid Films, 2004. **453-454**: p. 291-295.
164. Ronning, C., et al., *Ion beam deposition of fluorinated amorphous carbon*. Journal of Applied Physics, 2001. **90**(8): p. 4237-4245.
165. Hastas, N.A., et al., *Temperature dependence of the barrier at the tetrahedral amorphous carbon-silicon interface*. Semiconductor Science and Technology, 2001. **16**(6): p. 474-477.
166. Kahn, M., et al., *Accurate Raman spectroscopy of diamond-like carbon films deposited by an anode layer source*. Diamond and Related Materials, 2008. **17**(7-10): p. 1647-1651.
167. Kahn, M., et al., *Structural and mechanical properties of diamond-like carbon films deposited by an anode layer source*. Thin Solid Films, 2009. **517**(24): p. 6502-6507.
168. Kahn, M., et al., *Properties of DLC and Nitrogen-Doped DLC Films Deposited by DC Magnetron Sputtering*. Plasma Processes and Polymers, 2007. **4**: p. S200-S204.
169. Kahn, M., et al., *The relationship between structure and mechanical properties of hydrogenated amorphous carbon films*. Diamond and Related Materials, 2010. **19**(10): p. 1245-1248.
170. Kelly, S., et al., *Patterned growth of neuronal cells on modified diamond-like carbon substrates*. Biomaterials, 2008. **29**(17): p. 2573-2580.
171. Wang, H.Y., et al., *Mechanical and biological characteristics of diamond-like carbon coated poly aryl-ether-ether-ketone*. Biomaterials, 2010. **31**(32): p. 8181-8187.
172. Grill, A., *Tribology of diamondlike carbon and related materials: an updated review*. Surface & Coatings Technology, 1997. **94-5**(1-3): p. 507-513.
173. Erdemir, A., et al., *Characterization of transfer layers on steel surfaces sliding against diamond-like hydrocarbon films in dry nitrogen*. Surface & Coatings Technology, 1995. **76-77**(1-3): p. 559-563.
174. Petrmichl, R. (2009) *Diamond-Like Carbon as a Protective Coating for Decorative Glass*. Glass Performance Days 2009 Conference, 613.
175. Boutroy, N., et al., *Hydrogenated amorphous carbon film coating of PET bottles for gas diffusion barriers*. Diamond and Related Materials, 2006. **15**(4-8): p. 921-927.
176. Shirakura, A., et al., *Diamond-like carbon films for PET bottles and medical applications*. Thin Solid Films, 2006. **494**(1-2): p. 84-91.
177. Ueda, A., Nakachi, M., Goto, S., Yamakoshi, H., Shirakura, A., *High Speed and High Gas Barrier Rotary DLC Plasma Coating System for PET Bottles*. Mitsubishi Heavy Industries Ltd Technical Review, 2005. **42**(1): p. 1-3.
178. Burrow, S.J., *Friction and resistance to sliding in orthodontics: A critical review*. American Journal of Orthodontics and Dentofacial Orthopedics, 2009. **135**(4): p. 442-447.
179. Wichelhaus, A., et al., *The effect of surface treatment and clinical use on friction in NiTi orthodontic wires*. Dental Materials, 2005. **21**(10): p. 938-945.
180. Cobb, N.W., et al., *Efficiency of multi-strand steel, superelastic Ni-Ti and ion-implanted Ni-Ti archwires for initial alignment*. Clin Orthod Res, 1998. **1**(1): p. 12-9.
181. Kobayashi, S., et al., *Dissolution effect and cytotoxicity of diamond-like carbon coatings on orthodontic archwires*. Journal of Materials Science-Materials in Medicine, 2007. **18**: p. 2263-2268.
182. Schillinger, M., et al., *Caloon angioplasty versus implantation of nitinol stents in the superficial femoral artery*. New England Journal of Medicine, 2006. **354**(18): p. 1879-1888.

183. Duda, S.H., et al., *Sirolimus-eluting versus bare nitinol Stent for obstructive superficial femoral artery disease: The SIROCCO II trial*. Journal of Vascular and Interventional Radiology, 2005. **16**(3): p. 331-338.
184. Ponec, D., et al., *The nitinol SMART stent vs Wallstent for suboptimal iliac artery angioplasty: CRISP-US trial results*. Journal of Vascular and Interventional Radiology, 2004. **15**(9): p. 911-918.
185. Sinha, R.K., ed. *Hip Replacement: Current Trends and Controversies*. 2005, Marcel Dekker, Inc: New York, USA.
186. Kurtz, S.M., H.A. Gawel, and J.D. Patel, *History and Systematic Review of Wear and Osteolysis Outcomes for First-generation Highly Crosslinked Polyethylene*. Clinical Orthopaedics and Related Research, 2011. **469**(8): p. 2262-2277.
187. Lee, J.-H., et al., *Midterm Results of Primary Total Hip Arthroplasty Using Highly Cross-Linked Polyethylene*. Journal of Arthroplasty, 2011. **26**(7): p. 1014-1019.
188. Kwok, S.C.H., W. Jin, and P.K. Chu, *Surface energy, wettability, and blood compatibility phosphorus doped diamond-like carbon films*. Diamond and Related Materials, 2005. **14**(1): p. 78-85.
189. Ong, S.E., et al., *Influence of silicon concentration on the haemocompatibility of amorphous carbon*. Biomaterials, 2007. **28**(28): p. 4033-4038.
190. Ma, W.J., et al., *DLC coatings: Effects of physical and chemical properties on biological response*. Biomaterials, 2007. **28**(9): p. 1620-1628.
191. Colavita, P.E., et al., *Influence of Surface Termination and Electronic Structure on the Photochemical Grafting of Alkenes to Carbon Surfaces*. Journal of Physical Chemistry C, 2009. **113**(4): p. 1526-1535.
192. Hamers, R.J., et al., *Cycloaddition chemistry of organic molecules with semiconductor surfaces*. Accounts of Chemical Research, 2000. **33**(9): p. 617-624.
193. Strother, T., et al., *Photochemical functionalization of diamond films*. Langmuir, 2002. **18**(4): p. 968-971.
194. Phillips, M.F., et al., *In situ oligonucleotide synthesis on carbon materials: stable substrates for microarray fabrication*. Nucleic Acids Research, 2008. **36**(1).
195. Okpalugo, T.I.T., et al., *The MTT assays of bovine retinal pericytes and human microvascular endothelial cells on DLC and Si-DLC-coated TCPS*. Journal of Biomedical Materials Research Part A, 2004. **71A**(2): p. 201-208.
196. Kumari, T.V., et al., *In vitro cytocompatibility studies of Diamond Like Carbon coatings on titanium*. Bio-Medical Materials and Engineering, 2002. **12**(4): p. 329-338.
197. Kwok, S.C.H., et al., *Biocompatibility of calcium and phosphorus doped diamond-like carbon thin films synthesized by plasma immersion ion implantation and deposition*. Diamond and Related Materials, 2006. **15**(4-8): p. 893-897.
198. D'Angelo, F., et al., *Micropatterned and Hydrogenated Amorphous Carbon Guides Mesenchymal Stem Cells Towards Neuronal Differentiation*. European Cells & Materials, 2010. **20**: p. 231-244.
199. Baker, S.N. and G.A. Baker, *Luminescent Carbon Nanodots: Emergent Nanolights*. Angewandte Chemie-International Edition, 2010. **49**(38): p. 6726-6744.
200. Xu, X.Y., et al., *Electrophoretic analysis and purification of fluorescent single-walled carbon nanotube fragments*. Journal of the American Chemical Society, 2004. **126**(40): p. 12736-12737.
201. Cao, L., et al., *Carbon dots for multiphoton bioimaging*. Journal of the American Chemical Society, 2007. **129**(37): p. 11318+.
202. Lu, J., et al., *One-Pot Synthesis of Fluorescent Carbon Nanoribbons, Nanoparticles, and Graphene by the Exfoliation of Graphite in Ionic Liquids*. ACS Nano, 2009. **3**(8): p. 2367-2375.
203. Bourlinos, A.B., et al., *Surface functionalized carbogenic quantum dots*. Small, 2008. **4**(4): p. 455-458.

204. Zhu, H., et al., *Microwave synthesis of fluorescent carbon nanoparticles with electrochemiluminescence properties*. Chem Commun (Camb), 2009(34): p. 5118-20.
205. Liu, R.L., et al., *An Aqueous Route to Multicolor Photoluminescent Carbon Dots Using Silica Spheres as Carriers*. Angewandte Chemie-International Edition, 2009. **48**(25): p. 4598-4601.
206. Zhai, X.Y., et al., *Highly luminescent carbon nanodots by microwave-assisted pyrolysis*. Chemical Communications, 2012. **48**(64): p. 7955-7957.
207. Wei, W., et al., *Non-Enzymatic-Browning-Reaction: A Versatile Route for Production of Nitrogen-Doped Carbon Dots with Tunable Multicolor Luminescent Display*. Scientific Reports, 2014. **4**.
208. Zhou, J.G., et al., *An electrochemical avenue to blue luminescent nanocrystals from multiwalled carbon nanotubes (MWCNTs)*. Journal of the American Chemical Society, 2007. **129**: p. 744-745.
209. Hu, S.L., et al., *One-step synthesis of fluorescent carbon nanoparticles by laser irradiation*. Journal of Materials Chemistry, 2009. **19**(4): p. 484-488.
210. Peng, H. and J. Travas-Sejdic, *Simple Aqueous Solution Route to Luminescent Carbogenic Dots from Carbohydrates*. Chemistry of Materials, 2009. **21**(23): p. 5563-5565.
211. Colley, H.E., et al., *Plasma Polymer Coatings to Support Mesenchymal Stem Cell Adhesion, Growth and Differentiation on Variable Stiffness Silicone Elastomers*. Plasma Processes and Polymers, 2009. **6**(12): p. 831-839.
212. Yang, S.T., et al., *Carbon Dots as Nontoxic and High-Performance Fluorescence Imaging Agents*. Journal of Physical Chemistry C, 2009. **113**(42): p. 18110-18114.
213. Li, S.D., *7th International Symposium on Polymer Therapeutics, Valencia, Spain*. American Chemical Society, 2007: p. 496.
214. Kaewkhaw, R., A.M. Scutt, and J.W. Haycock, *Anatomical site influences the differentiation of adipose-derived stem cells for Schwann-cell phenotype and function*. Glia, 2011. **59**(5): p. 734-749.
215. Plumb, L.A., *Cell sensitivity assays: The MTT assay*. Cancer Cell Culture: Methods and Protocols, 2004. **88**: p. 165-169.
216. Yuan, Y. and T.R. Lee, *Contact Angle and Wetting Properties*, in *Surface Science Techniques*, G. Bracco and B. Holst, Editors. 2013, Springer Berlin Heidelberg. p. 3-34.
217. Siegbahn, K. and K. Edvarson, *β -Ray spectroscopy in the precision range of 1 : 105*. Nuclear Physics, 1956. **1**(8): p. 137-159.
218. Hagström, S., C. Nordling, and K. Siegbahn, *Electron spectroscopy for chemical analyses*. Physics Letters, 1964. **9**(3): p. 235-236.
219. McArthur, S.L., *Applications of XPS in bioengineering*. Surface and Interface Analysis, 2006. **38**(11): p. 1380-1385.
220. McArthur, S.L., et al., *XPS and surface-MALDI-MS characterisation of worn HEMA-based contact lenses*. Biomaterials, 2001. **22**(24): p. 3295-3304.
221. Gengenbach, T.R., et al., *A multi-technique study of the spontaneous oxidation of N-hexane plasma polymers*. Journal of Polymer Science Part A: Polymer Chemistry, 1994. **32**(8): p. 1399-1414.
222. Beck, A.J., et al., *Plasma Co-Polymerisation of Two Strongly Interacting Monomers: Acrylic Acid and Allylamine*. Plasma Processes and Polymers, 2005. **2**(8): p. 641-649.
223. Pennycook, S.J., et al., *Transmission electron microscopy: Overview and challenges, in Characterization and Metrology for Ulsi Technology*, D.G. Seiler, et al., Editors. 2003. p. 627-633.
224. Binnig, G., C.F. Quate, and C. Gerber, *Atomic Force Microscope*. Physical Review Letters, 1986. **56**(9): p. 930-933.
225. Seo, Y. and W. Jhe, *Atomic force microscopy and spectroscopy*. Reports on Progress in Physics, 2008. **71**(1).

226. Ralston, D.R., et al., *Keratinocytes contract human dermal extracellular matrix and reduce soluble fibronectin production by fibroblasts in a skin composite model*. British Journal of Plastic Surgery, 1997. **50**(6): p. 408-415.
227. Smith, L.E., S. Rimmer, and S. MacNeil, *Examination of the effects of poly(N-vinylpyrrolidinone) hydrogels in direct and indirect contact with cells*. Biomaterials, 2006. **27**(14): p. 2806-2812.
228. Nobbmann, U., et al., *Dynamic light scattering as a relative tool for assessing the molecular integrity and stability of monoclonal antibodies*. Biotechnology & genetic engineering reviews, 2007. **24**: p. 117-28.
229. Yang, N., et al., *Amine-layer growth and electronic properties on H-terminated undoped single crystalline CVD diamond*. Diamond and Related Materials, 2008. **17**(4-5): p. 892-895.
230. Siow, K.S., et al., *Plasma methods for the generation of chemically reactive surfaces for biomolecule immobilization and cell colonization - A review*. Plasma Processes and Polymers, 2006. **3**(6-7): p. 392-418.
231. Wang, X., et al., *UV-Induced Grafting of Alkenes to Silicon Surfaces: Photoemission versus Excitons*. Journal of the American Chemical Society, 2010. **132**(12): p. 4048-+.
232. Seidman, K.J.N., et al., *Differentiation of NG108-15 neuroblastoma cells by serum starvation or dimethyl sulfoxide results in marked differences in angiotensin II receptor subtype expression*. Journal of Neurochemistry, 1996. **66**(3): p. 1011-1018.
233. He, T., et al., *Enhanced endothelialization guided by fibronectin functionalized plasma polymerized acrylic acid film*. Materials Science & Engineering C-Materials for Biological Applications, 2012. **32**(5): p. 1025-1031.
234. Feng, J.C., et al., *Deposition of well-defined fluoropolymer nanospheres on PET substrate by plasma polymerization of heptadecafluorodecyl acrylate and their potential application as a protective layer*. Plasma Processes and Polymers, 2005. **2**(2): p. 127-135.
235. Carton, O., et al., *Plasma Polymerization of Acrylic Acid by Atmospheric Pressure Nitrogen Plasma Jet for Biomedical Applications*. Plasma Processes and Polymers, 2012. **9**(10): p. 984-993.
236. Yang, N., et al., *Photochemical Amine Layer Formation on H-Terminated Single-Crystalline CVD Diamond*. Chemistry of Materials, 2007. **19**(11): p. 2852-2859.
237. Li, B., et al., *Photochemical Grafting and Patterning of Biomolecular Layers onto TiO₂ Thin Films*. Acs Applied Materials & Interfaces, 2009. **1**(5): p. 1013-1022.
238. Harsch, A., et al., *Pulsed plasma deposition of allylamine on polysiloxane: a stable surface for neuronal cell adhesion*. Journal of Neuroscience Methods, 2000. **98**(2): p. 135-144.
239. Keilhoff, G., et al., *Neuroma: a donor-age independent source of human Schwann cells for tissue engineered nerve grafts*. Neuroreport, 2000. **11**(17): p. 3805-3809.
240. Vleggeert-Lankamp, C., et al., *Adhesion and proliferation of human Schwann cells on adhesive coatings*. Biomaterials, 2004. **25**(14): p. 2741-2751.
241. Ko, Y.-M., K. Lee, and B.-H. Kim, *Bone like apatite formation on modified Ti surfaces with COOH, NH₂, and OH functional groups by plasma polymerization*. Thin Solid Films, 2012. **521**: p. 128-131.
242. Bisson, I., et al., *Acrylic acid grafting and collagen immobilization on poly(ethylene terephthalate) surfaces for adherence and growth of human bladder smooth muscle cells*. Biomaterials, 2002. **23**(15): p. 3149-3158.
243. Cheng, Z.Y. and S.H. Teoh, *Surface modification of ultra thin poly (epsilon-caprolactone) films using acrylic acid and collagen*. Biomaterials, 2004. **25**(11): p. 1991-2001.
244. Morgan, D.M.L., V.L. Larvin, and J.D. Pearson, *Biochemical-Characterization of Polycation-Induced Cyto-toxicity to Human Vascular Endothelial-Cells*. Journal of Cell Science, 1989. **94**: p. 553-559.
245. Arnold, L.J., et al., *Anti-Neoplastic Activity of Poly(L-Lysine) With Some Ascites Tumor-Cells*. Proceedings of the National Academy of Sciences of the United States of America, 1979. **76**(7): p. 3246-3250.

246. Kim, S.W., *Polylysine copolymers for gene delivery*. Cold Spring Harbor protocols, 2012. **2012**(4): p. 433-8.
247. Harnett, E.M., J. Alderman, and T. Wood, *The surface energy of various biomaterials coated with adhesion molecules used in cell culture*. Colloids and Surfaces B-Biointerfaces, 2007. **55**(1): p. 90-97.
248. Li, H., et al., *Fluorescent carbon nanoparticles: electrochemical synthesis and their pH sensitive photoluminescence properties*. New Journal of Chemistry, 2011. **35**(11): p. 2666-2670.
249. Cargill li, R.S., K.C. Dee, and S. Malcolm, *An assessment of the strength of NG108-15 cell adhesion to chemically modified surfaces*. Biomaterials, 1999. **20**(23-24): p. 2417-2425.
250. Regan, E.M., et al., *Spatially Controlling Neuronal Adhesion and Inflammatory Reactions on Implantable Diamond*. Ieee Journal on Emerging and Selected Topics in Circuits and Systems, 2011. **1**(4): p. 557-565.
251. Edgington, R.J., et al., *Patterned neuronal networks using nanodiamonds and the effect of varying nanodiamond properties on neuronal adhesion and outgrowth*. Journal of Neural Engineering, 2013. **10**(5).
252. May, P.W., et al., *Spatially controlling neuronal adhesion on CVD diamond*. Diamond and Related Materials, 2012. **23**: p. 100-104.
253. Auciello, O. and B. Shi, *Science and Technology of Bio-Inert Thin Films as Hermetic-Encapsulating Coatings for Implantable Biomedical Devices: Application to Implantable Microchip in the Eye for the Artificial Retina*, in *Implantable Neural Prostheses 2: Techniques and Engineering Approaches*, D.D. Zhou and E. Greenbaum, Editors. 2010. p. 63-84.
254. Schaffner, A.E., et al., *Investigation of the factors necessary for growth of hippocampal neurons in a defined system*. Journal of Neuroscience Methods, 1995. **62**(1-2): p. 111-119.
255. Yavin, E. and Z. Yavin, *Attachment and Culture of Dissociated Cells From Rat Embryo Cerebral Hemispheres on Polylysine-Coated Surface*. Journal of Cell Biology, 1974. **62**(2): p. 540-546.
256. Kim, Y.H., et al., *Enhancement of neuronal cell adhesion by covalent binding of poly-D-lysine*. Journal of Neuroscience Methods, 2011. **202**(1): p. 38-44.
257. Elsdale, T. and J. Bard, *Collagen Substrata For Studies on Cell Behavior*. Journal of Cell Biology, 1972. **54**(3): p. 626-&.
258. Carbonetto, S., M.M. Gruver, and D.C. Turner, *Nerve-Fiber Growth in Culture on Fibronectin, Collagen, and Glycosaminoglycan Substrates*. Journal of Neuroscience, 1983. **3**(11): p. 2324-2335.
259. Lein, P.J., G.A. Banker, and D. Higgins, *Laminin selectively enhances axonal growth and accelerates the development of polarity by hippocampal neurons in culture*. Brain research. Developmental brain research, 1992. **69**(2): p. 191-7.
260. Lochter, A. and M. Schachner, *Tenascin and Extracellular-Matrix Glycoproteins - From Promotion To Polarization of Neurite Growth In-Vitro*. Journal of Neuroscience, 1993. **13**(9): p. 3986-4000.
261. James, C.D., et al., *Aligned microcontact printing of micrometer-scale poly-L-lysine structures for controlled growth of cultured neurons on planar microelectrode arrays*. Ieee Transactions on Biomedical Engineering, 2000. **47**(1): p. 17-21.
262. Lieberman, I. and P. Ove, *Protein Growth Factor for Mammalian Cells in Culture*. Journal of Biological Chemistry, 1958. **233**(3): p. 637-642.
263. Romijn, H.J., *Development and Advantages of Serum-Free, Chemically Defined Nutrient Media for Culturing of Nerve-Tissue*. Biology of the Cell, 1988. **63**(3): p. 263-268.
264. Ohsawa, F., et al., *Response of Embryonic Rat Hippocampal-Neurons in Culture to Neurotrophin-3, Brain-Derived Neurotrophic Factor and Basic Fibroblast Growth Factor*. Neuroscience, 1993. **57**(1): p. 67-77.
265. Wang, J.-H., et al., *Change in neuron aggregation and neurite fasciculation on EVAL membranes modified with different diamines*. Journal of Biomedical Materials Research Part A, 2010. **94A**(2): p. 489-498.

266. Massia, S.P. and J.A. Hubbell, *Immobilised Amines and Basic-Amino-Acids as Mimetic Heparin-Binding Domains for Cell-Surface Proteoglycan-Mediated Adhesion*. Journal of Biological Chemistry, 1992. **267**(14): p. 10133-10141.
267. Gu, W.-L., et al., *Chondroitin sulfate proteoglycans regulate the growth, differentiation and migration of multipotent neural precursor cells through the integrin signaling pathway*. Bmc Neuroscience, 2009. **10**.
268. Hahn, C.D., et al., *Self-Assembled Monolayers with Latent Aldehydes for Protein Immobilization*. Bioconjugate Chemistry, 2006. **18**(1): p. 247-253.
269. Agrez, M.V. and R.C. Bates, *Colorectal-Cancer And The Integrin Family Of Cell-Adhesion Receptors - Current Status And Future-Directions*. European Journal of Cancer, 1994. **30A**(14): p. 2166-2170.
270. Basora, N., et al., *Relation between integrin alpha 7B beta 1 expression in human intestinal cells and enterocytic differentiation*. Gastroenterology, 1997. **113**(5): p. 1510-1521.
271. Yang, N., et al., *Photochemical attachment of amine-layers on H-terminated undoped single crystalline CVD diamonds*. Diamond and Related Materials, 2008. **17**(7-10): p. 1376-1379.
272. Hinuber, C., et al., *Biocompatibility and mechanical properties of diamond-like coatings on cobalt-chromium-molybdenum steel and titanium-aluminum-vanadium biomedical alloys*. Journal of Biomedical Materials Research Part A, 2010. **95A**(2): p. 388-400.
273. Medina, O., et al., *Bactericide and bacterial anti-adhesive properties of the nanocrystalline diamond surface*. Diamond and Related Materials, 2012. **22**: p. 77-81.
274. Beranová, J., et al., *Antibacterial behavior of diamond nanoparticles against Escherichia coli*. physica status solidi (b), 2012. **249**(12): p. 2581-2584.
275. Young, T.-H., et al., *Immobilization of l-lysine on dense and porous poly(vinylidene fluoride) surfaces for neuron culture*. Desalination, 2008. **234**(1-3): p. 134-143.
276. Brunetti, V., et al., *Neurons sense nanoscale roughness with nanometer sensitivity*. Proceedings of the National Academy of Sciences of the United States of America, 2010. **107**(14): p. 6264-6269.
277. Brunette, D.M. and B. Chehroudi, *The effects of the surface topography of micromachined titanium substrata on cell behavior in vitro and in vivo*. Journal of Biomechanical Engineering-Transactions of the Asme, 1999. **121**(1): p. 49-57.
278. Zhu, X.L., et al., *Effects of topography and composition of titanium surface oxides on osteoblast responses*. Biomaterials, 2004. **25**(18): p. 4087-4103.
279. Karuri, N.W., et al., *Biological length scale topography enhances cell-substratum adhesion of human corneal epithelial cells*. Journal of Cell Science, 2004. **117**(15): p. 3153-3164.
280. Curtis, A.S.G., M. Dalby, and N. Gadegaard, *Cell signaling arising from nanotopography: implications for nanomedical devices*. Nanomedicine, 2006. **1**(1): p. 67-72.
281. Choi, C.-H., et al., *Cell interaction with three-dimensional sharp-tip nanotopography*. Biomaterials, 2007. **28**(9): p. 1672-1679.
282. Hamilton, D.W., F. Jamshidi, and D.M. Brunette, *Focal adhesion mediated intracellular signaling, Stat3 translocation and osteoblast differentiation: regulation by substratum topography*. Materialwissenschaft Und Werkstofftechnik, 2009. **40**(1-2): p. 101-107.
283. Anderson, J.M., A. Rodriguez, and D.T. Chang, *Foreign body reaction to biomaterials*. Seminars in Immunology, 2008. **20**(2): p. 86-100.
284. Walczyk, D., et al., *What the Cell "Sees" in Bionanoscience*. Journal of the American Chemical Society, 2010. **132**(16): p. 5761-5768.
285. Castner, D.G. and B.D. Ratner, *Biomedical surface science: Foundations to frontiers*. Surface Science, 2002. **500**(1-3): p. 28-60.
286. Lipski, A.M., et al., *Nanoscale engineering of biomaterial surfaces*. Advanced Materials, 2007. **19**(4): p. 553-+.
287. Albelda, S.M. and C.A. Buck, *Integrins and other cell adhesion molecules*. The FASEB Journal, 1990. **4**(11): p. 2868-80.

288. Pelham, R.J. and Y.-I. Wang, *Cell locomotion and focal adhesions are regulated by substrate flexibility*. Proceedings of the National Academy of Sciences of the United States of America, 1997. **94**(25): p. 13661-13665.
289. Curtis, A.S. and J.V. Forrester, *The competitive effects of serum proteins on cell adhesion*. Journal of Cell Science, 1984. **71**(1): p. 17-35.
290. Sun, Y.P., et al., *Quantum-sized carbon dots for bright and colorful photoluminescence*. Journal of the American Chemical Society, 2006. **128**(24): p. 7756-7757.
291. Mao, X.-J., et al., *Study on the fluorescence characteristics of carbon dots*. Spectrochimica Acta Part a-Molecular and Biomolecular Spectroscopy, 2010. **75**(2): p. 553-557.
292. Wang, Q., et al., *Microwave-hydrothermal synthesis of fluorescent carbon dots from graphite oxide*. Carbon, 2011. **49**(9): p. 3134-3140.
293. Tan, M.Q., et al., *Enhanced photoluminescence and characterization of multicolor carbon dots using plant soot as a carbon source*. Talanta, 2013. **115**: p. 950-956.
294. Kumar, V., G. Toffoli, and F. Rizzolio, *Fluorescent Carbon Nanoparticles in Medicine for Cancer Therapy*. ACS Medicinal Chemistry Letters, 2013. **4**(11): p. 1012-1013.
295. Huang, H., et al., *Facile and green synthesis of photoluminescent carbon nanoparticles for cellular imaging*. New Journal of Chemistry, 2014. **38**(2): p. 784-789.
296. Michalet, X., et al., *Quantum dots for live cells, in vivo imaging, and diagnostics*. Science, 2005. **307**(5709): p. 538-544.
297. He, X., et al., *Water soluble carbon nanoparticles: Hydrothermal synthesis and excellent photoluminescence properties*. Colloids and Surfaces B-Biointerfaces, 2011. **87**(2): p. 326-332.
298. Lamer, V.K., *Nucleation in Phase Transitions*. Industrial and Engineering Chemistry, 1952. **44**(6): p. 1270-1277.
299. Sun, X.M. and Y.D. Li, *Colloidal carbon spheres and their core/shell structures with noble-metal nanoparticles*. Angewandte Chemie-International Edition, 2004. **43**(5): p. 597-601.
300. Hsu, P.-C. and H.-T. Chang, *Synthesis of high-quality carbon nanodots from hydrophilic compounds: role of functional groups*. Chemical Communications, 2012. **48**(33): p. 3984-3986.
301. Conner, S.D. and S.L. Schmid, *Regulated portals of entry into the cell*. Nature, 2003. **422**(6927): p. 37-44.
302. Jiang, X., et al., *Specific effects of surface carboxyl groups on anionic polystyrene particles in their interactions with mesenchymal stem cells*. Nanoscale, 2011. **3**(5): p. 2028-2035.
303. Chithrani, B.D., A.A. Ghazani, and W.C.W. Chan, *Determining the size and shape dependence of gold nanoparticle uptake into mammalian cells*. Nano Letters, 2006. **6**(4): p. 662-668.
304. Rejman, J., et al., *Size-dependent internalization of particles via the pathways of clathrin- and caveolae-mediated endocytosis*. Biochemical Journal, 2004. **377**: p. 159-169.
305. Labhasetwar, V., et al., *Arterial uptake of biodegradable nanoparticles: Effect of surface modifications*. Journal of Pharmaceutical Sciences, 1998. **87**(10): p. 1229-1234.
306. Nativo, P., I.A. Prior, and M. Brust, *Uptake and intracellular fate of surface-modified gold nanoparticles*. ACS Nano, 2008. **2**(8): p. 1639-1644.
307. Holzapfel, V., et al., *Synthesis and biomedical applications of functionalized fluorescent and magnetic dual reporter nanoparticles as obtained in the miniemulsion process*. Journal of Physics-Condensed Matter, 2006. **18**(38): p. S2581-S2594.
308. Arbab, A.S., et al., *Characterization of biophysical and metabolic properties of cells labeled with superparamagnetic iron oxide nanoparticles and transfection agent for cellular MR imaging*. Radiology, 2003. **229**(3): p. 838-846.
309. Sun, X.K., et al., *An assessment of the effects of shell cross-linked nanoparticle size, core composition, and surface PEGylation on in vivo biodistribution*. Biomacromolecules, 2005. **6**(5): p. 2541-2554.
310. Jiang, X., et al., *Quantitative analysis of the protein corona on FePt nanoparticles formed by transferrin binding*. Journal of the Royal Society Interface, 2010. **7**: p. S5-S13.

311. Maffre, P., et al., *Characterization of protein adsorption onto FePt nanoparticles using dual-focus fluorescence correlation spectroscopy*. Beilstein Journal of Nanotechnology, 2011. **2**: p. 374-383.
312. Prapainop, K., D.P. Witter, and P. Wentworth, Jr., *A Chemical Approach for Cell-Specific Targeting of Nanomaterials: Small-Molecule-Initiated Misfolding of Nanoparticle Corona Proteins*. Journal of the American Chemical Society, 2012. **134**(9): p. 4100-4103.
313. Treuel, L., X. Jiang, and G.U. Nienhaus, *New views on cellular uptake and trafficking of manufactured nanoparticles*. Journal of the Royal Society Interface, 2013. **10**(82).
314. Cho, E.C., Q. Zhang, and Y. Xia, *The effect of sedimentation and diffusion on cellular uptake of gold nanoparticles*. Nature Nanotechnology, 2011. **6**(6): p. 385-391.
315. Chu, Z., et al., *Unambiguous observation of shape effects on cellular fate of nanoparticles*. Scientific Reports, 2014. **4**.
316. Macia, E., et al., *Dynasore, a cell-permeable inhibitor of dynamin*. Developmental Cell, 2006. **10**(6): p. 839-850.
317. Wang, L.H., K.G. Rothberg, and R.G.W. Anderson, *Mis-Assembly of Clathrin Lattices on Endosomes Reveals a Regulatory Switch for Coated Pit Formation*. Journal of Cell Biology, 1993. **123**(5): p. 1107-1117.
318. Liu, H., T. Ye, and C. Mao, *Fluorescent carbon nanoparticles derived from candle soot*. Angewandte Chemie-International Edition, 2007. **46**(34): p. 6473-6475.
319. Zhao, Q.-L., et al., *Facile preparation of low cytotoxicity fluorescent carbon nanocrystals by electrooxidation of graphite*. Chemical Communications, 2008(41): p. 5116-5118.
320. Kim, J.A., et al., *Role of cell cycle on the cellular uptake and dilution of nanoparticles in a cell population*. Nature Nanotechnology, 2012. **7**(1): p. 62-68.
321. Sun, Y.-P., et al., *Doped carbon nanoparticles as a new platform for highly photoluminescent dots*. The Journal of Physical Chemistry C, 2008. **112**(47): p. 18295-18298.
322. Barr, T.L. and S. Seal, *Nature of the Use of Adventitious Carbon as a Binding-Energy Standard*. Journal of Vacuum Science & Technology a-Vacuum Surfaces and Films, 1995. **13**(3): p. 1239-1246.
323. So, L., et al., *X-ray photoelectron spectroscopic study of the surface chemistry of soda-lime glass in vacuum*. Surface and Interface Analysis, 2006. **38**(4): p. 648-651.
324. Lau, D., et al., *Electron-Beam-Induced Carbon Contamination on Silicon: Characterization Using Raman Spectroscopy and Atomic Force Microscopy*. Microscopy and Microanalysis, 2010. **16**(01): p. 13-20.
325. Szunerits, S. and R. Boukherroub, *Different strategies for functionalization of diamond surfaces*. Journal of Solid State Electrochemistry, 2008. **12**(10): p. 1205-1218.
326. Franking, R.A., E.C. Landis, and R.J. Hamers, *Highly Stable Molecular Layers on Nanocrystalline Anatase TiO₂ through Photochemical Grafting*. Langmuir, 2009. **25**(18): p. 10676-10684.
327. Mooney, J.F., et al., *Patterning of functional antibodies and other proteins by photolithography of silane monolayers*. Proceedings of the National Academy of Sciences of the United States of America, 1996. **93**(22): p. 12287-12291.